UNIVERSIDAD COMPLUTENSE DE MADRID

FACULTAD DE FARMACIA

DEPARTAMENTO DE QUÍMICA INORGÁNICA Y BIOINORGÁNICA

TESIS DOCTORAL

Una nueva biocerámica *nanocomposite* para regeneración tisular ósea

MEMORIA PARA OPTAR AL GRADO DE DOCTORA

PRESENTADA POR

Mónica Cicuéndez Maroto

Directoras

Isabel Izquierdo Barba
María Teresa Portolés Pérez

Madrid, 2014

UNIVERSIDAD COMPLUTENSE DE MADRID
Departamento de Química Inorgánica y Bioinorgánica

Una nueva biocerámica *nanocomposite* para regeneración tisular ósea

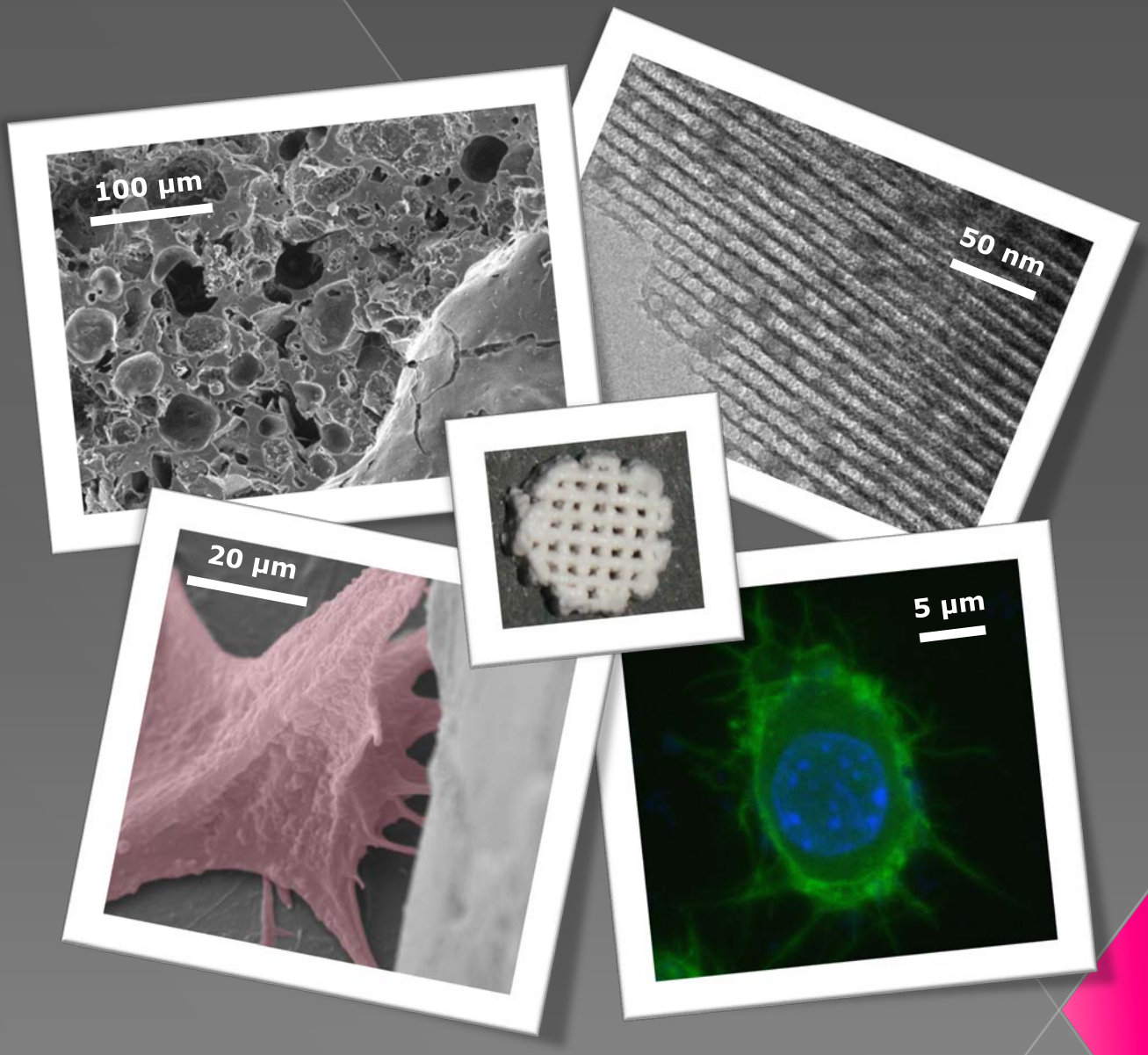

Mónica Cicuéndez Maroto

TESIS DOCTORAL mención DOCTOR EUROPEO

MADRID, 2014

UNIVERSIDAD COMPLUTENSE DE MADRID

FACULTA DE FARMACIA

Departamento de Química Inorgánica y Bioinorgánica

UNA NUEVA BIOCERÁMICA *NANOCOMPOSITE* PARA REGENERACIÓN TISULAR ÓSEA

Mónica Cicuéndez Maroto

Memoria para optar al Grado de Doctor - mención Doctor Europeo - por la Universidad Complutense de Madrid

DIRECTORAS

Dra. Isabel Izquierdo Barba

Prof. Dra. María Teresa Portolés Pérez

Madrid, 2014

Dra. **Isabel Izquierdo Barba,** Profesora Contratada Doctor del Departamento de Química Inorgánica y Bioinorgánica de la Facultad de Farmacia de la Universidad Complutense de Madrid

Prof. Dra. **Mª Teresa Portolés Pérez**, Catedrática del Departamento de Bioquímica y Biología Molecular I de la Facultad de Ciencias Químicas de la Universidad Complutense de Madrid

CERTIFICAN:

Que la presente Memoria, titulada **"Una nueva biocerámica *nanocomposite* para regeneración tisular ósea"** ha sido realizada por la doctoranda **Mónica Cicuéndez Maroto** en el Departamento de Química Inorgánica y Bioinorgánica de la Facultad de Farmacia de la Universidad Complutense de Madrid, bajo nuestra dirección y autorizamos su presentación para que sea calificada como Tesis Doctoral dado que reúne las condiciones necesarias para su defensa.

En Madrid, a 17 de Febrero de 2014

Fdo.: Dra. Isabel Izquierdo Barba Fdo.: Prof. Dra. Mª Teresa Portolés Pérez

ABREVIATURAS

Síntesis y caracterización de materiales

MBG	Vidrio bioactivo mesoporoso, del inglés *Mesoporous Bioactive Glasses*
TG	Vidrio con plantilla, del inglés *Template Glasses*
TEM	Microscopia electrónica de transmisión, del inglés *Transmission Electron Microscopy*
HRTEM	Microscopia electrónica de transmisión de alta resolución, del inglés *High Resolution Transmission Electron Microscopy*
SGG	Vidrios convencionales sol-gel, del inglés *Sol-Gel Glasses*
S_{BET}	Superficie específica calculada por el método B.E.T. del inglés *Brunauer, Emmer, Teller*
V_p	Volumen de poro
D_p	Diámetro de poro
EISA	Autoensamblaje inducido por evaporación, del inglés *Evaporation-induced self-assembly*
SBF	Fluido corporal simulado, del inglés *Simulated Body Fluid*
ACP	Fosfato de calcio amorfo, del inglés *Amorphous Calcium Phosphate*
OCP	Fosfato octacálcico, del inglés *Octa Calcium Phosphate*
NMR	Resonancia magnética nuclear, del inglés Nuclear Magnetic Resonance
XRD	Difracción de rayos-X, del inglés *X- Ray Diffraction*
XRF	Fluorescencia de rayos-X, del inglés *X- Ray Fluorescence*
FTIR	Espectroscopia infrarroja con transformada de Fourier, del inglés *Infrared Fourier Transform Spectroscopy*
FT	Transformada de Fourier, del inglés *Fourier Transform*
TEOS	Tetraetilortosilicato
TEP	Trietilfofato
P123	*Pluronic P123*
F127	*Pluronic F127*

Cultivos celulares y microbiológicos

DMEM	Medio de cultivo Eagle modificado por Dulbecco, del inglés *Dulbecco's Modified Eagle Medium*
BSA	Proteína sérica albúmina, del inglés *Bovine Serum Albumine*
PCC	Espacio pericelular, del inglés *PeriCellular Cell*
APC	Célula presentadora de antígeno, del inglés *Antigen Presenting Cell*
TNFα	Factor de necrosis tumoral α, del inglés *Tumor Necrosis Factor α*
INFγ	Interferón γ, del inglés *Interferon γ*
ROS	Especies reactivas de óxigeno, del inglés *Reactive Oxygen Species*
MHC	Complejo mayor de histocompatibilidad, del inglés *Mayor Histocompatibility Complex*
TCR	Receptor específico de célula T, del inglés *T-Cell Receptor*
PBS	Disolución tampón de fosfatos, del inglés *Phosphate Buffer Saline*
IP	Impregnación, del inglés *ImPregnation*
OP	*One Pot*
CFU	Unidad formadora de colonias, del inglés *Colony Forming Unit*
CMI	Concentración Mínima Inhibitoria
Levo	Levofloxacino

ÍNDICE GENERAL

Resumen

Summary

RESUMEN

El comienzo del nuevo milenio se ha caracterizado por una mayor aplicación de dispositivos médicos en todos los campos de la medicina destinados principalmente al diagnóstico, a la reparación y a la regeneración de tejidos dañados. Para estos fines son imprescindibles diferentes biomateriales que han de ser biocompatibles y poder combinarse con células, factores de crecimiento, fármacos u otras moléculas bioactivas, buscando su integración en el microambiente natural del organismo y la estimulación de la regeneración tisular. Los avances científicos y tecnológicos actuales han conducido al más alto nivel de refinamiento y optimización tanto en la selección de los biomateriales más adecuados como en el diseño de su estructura a escala macro, micro, e incluso recientemente, nanométrica. Los logros sustanciales en términos de biocompatibilidad asociados a un riesgo siempre menor de fracaso y a la creciente demanda de atención médica de una población que ha visto incrementada su esperanza de vida, han contribuido a la expansión exitosa de la utilización de biomateriales con fines biomédicos, existiendo actualmente alrededor de 2.700 tipos de dispositivos médicos.

El desarrollo de nuevos biomateriales se basa en la innovación multidisciplinar y en cierta medida en la capacidad de “imaginar” sus aplicaciones. La multidisciplinaridad es un requisito esencial de la investigación biomédica que avanza rápidamente gracias a la convergencia de científicos procedentes de diferentes áreas como física, matemáticas, ingeniería, biología y medicina. La evolución de los biomateriales queda reflejada en cómo ha ido modificándose su definición. Si inicialmente se consideró el término biomaterial como un material que debe entrar en contacto con los tejidos del organismo sin producir toxicidad, este concepto ha sido redefinido como "una sustancia diseñada para dirigir el curso de cualquier procedimiento terapéutico o diagnóstico en medicina o veterinaria mediante el control de las interacciones con componentes de los sistemas vivos". El tipo de biomaterial elegido para cada terapia o diagnóstico, su forma y propiedades dependerán de la función que deba realizar y de los tipos celulares con los que entrará en contacto en el tejido en el que vaya a ser colocado.

La ingeniería tisular requiere la utilización de andamios que actúen como soportes para la formación del nuevo tejido, permitiendo sobre su superficie los

procesos de adhesión, proliferación y diferenciación celular, sin inducir reacciones del sistema inmune que podrían ralentizar el proceso de cicatrización, o incluso, provocar el rechazo del implante por el organismo. De esta manera, la composición, arquitectura, porosidad, topografía y química de superficie, así como las propiedades mecánicas de estos andamios desempeñan un papel crucial en el éxito de los implantes. Recientemente, las investigaciones van encaminadas a "imitar" la escala nanométrica de los tejidos y órganos ya que influye de forma muy importante en la respuesta celular y es fundamental para garantizar su éxito. En este sentido, el rápido crecimiento de la nanotecnología ha aportado numerosos avances en el diseño de nuevas biocerámicas nanoestructuradas para regeneración ósea. La hidroxiapatita nanocristalina, debido a su cercana similitud con el componente mineral óseo, a sus propiedades osteoconductivas y a su excelente biocompatibilidad, ocupa una posición clave con respecto a otras biocerámicas. Por otra parte, los materiales mesoestructurados con base silícica (entre los que destacamos los vidrios biactivos mesoporosos) formados por canales de poros ordenados capaces de albergar diferentes biomoléculas en su interior, constituyen otra familia importante de biocerámicas nanoestructuradas con un gran potencial en ingeniería tisular gracias a sus fascinantes propiedades bioactivas y a su capacidad como sistemas de liberación local controlada de fármacos. Por ello, estos materiales son prometedores candidatos para evitar el riesgo de una posible de infección tras su implantación, al poder albergar en su interior agentes antimicrobianos y liberarlos de manera controlada.

En la actualidad los materiales *nanocomposites*, formados por dos componentes, uno de ellos *nanocristalino* distribuido homogéneamente en matrices mesoestructuradas de naturaleza amorfa, son objeto de una intensa investigación en diferentes disciplinas debido a la sinergia de sus componentes, potenciando así sus propiedades finales y su funcionalidad.

Por todo ello, en la presente Tesis Doctoral se ha realizado el diseño, la síntesis, la caracterización y la evaluación biológica de un nuevo *nanocomposite* MGHA, formado por hidroxiapatita nanocristalina embebida en una matriz mesoporosa. Dicho material ha sido preparado en forma pulverizada y como andamios macroporosos 3D, analizando su interacción con diferentes tipos celulares implicados en la formación de tejido óseo (preosteoblastos, osteoblastos, fibroblastos) y en la respuesta inmune

(macrófagos, linfocitos T y B, células *natural killer*). Asimismo se ha llevado a cabo la carga y liberación de levofloxacino en el material MGHA, evaluando su acción sobre *Staphylococcus aureus* y *Escherichia coli* y la influencia del pH en la cinética de liberación.

La **Figura 1** esquematiza los diferentes puntos de mira de esta Tesis Doctoral desarrollados a lo largo de los tres capítulos de esta Memoria. El primer capítulo describe la síntesis, caracterización y evaluación biológica de un nuevo sistema *nanocomposite* MGHA formado por hidroxiapatita nanocristalina embebida en una matriz mesoporosa de composición SiO_2-CaO-P_2O_5. El segundo capítulo comprende desde el conformado en forma de andamios tridimensionales (3D) macroporosos del nuevo *nanocomposite* y la aminofuncionalización de su superficie hasta el estudio de la interacción de estos andamios con células óseas y células del sistema inmune. Por último el tercer capítulo está dedicado al estudio de diferentes estrategias de carga y liberación de levofloxacino en el material MGHA para el tratamiento y la prevención de una infección ósea, analizando sus efectos *in vitro* sobre distintas cepas bacterianas y su posible efecto citotóxico sobre osteoblastos y fibroblastos.

Los resultados obtenidos han demostrado las excelentes propiedades de este nuevo *nanocomposite* MGHA que permiten proponerlo como candidato para ser utilizado en ingeniería tisular ósea.

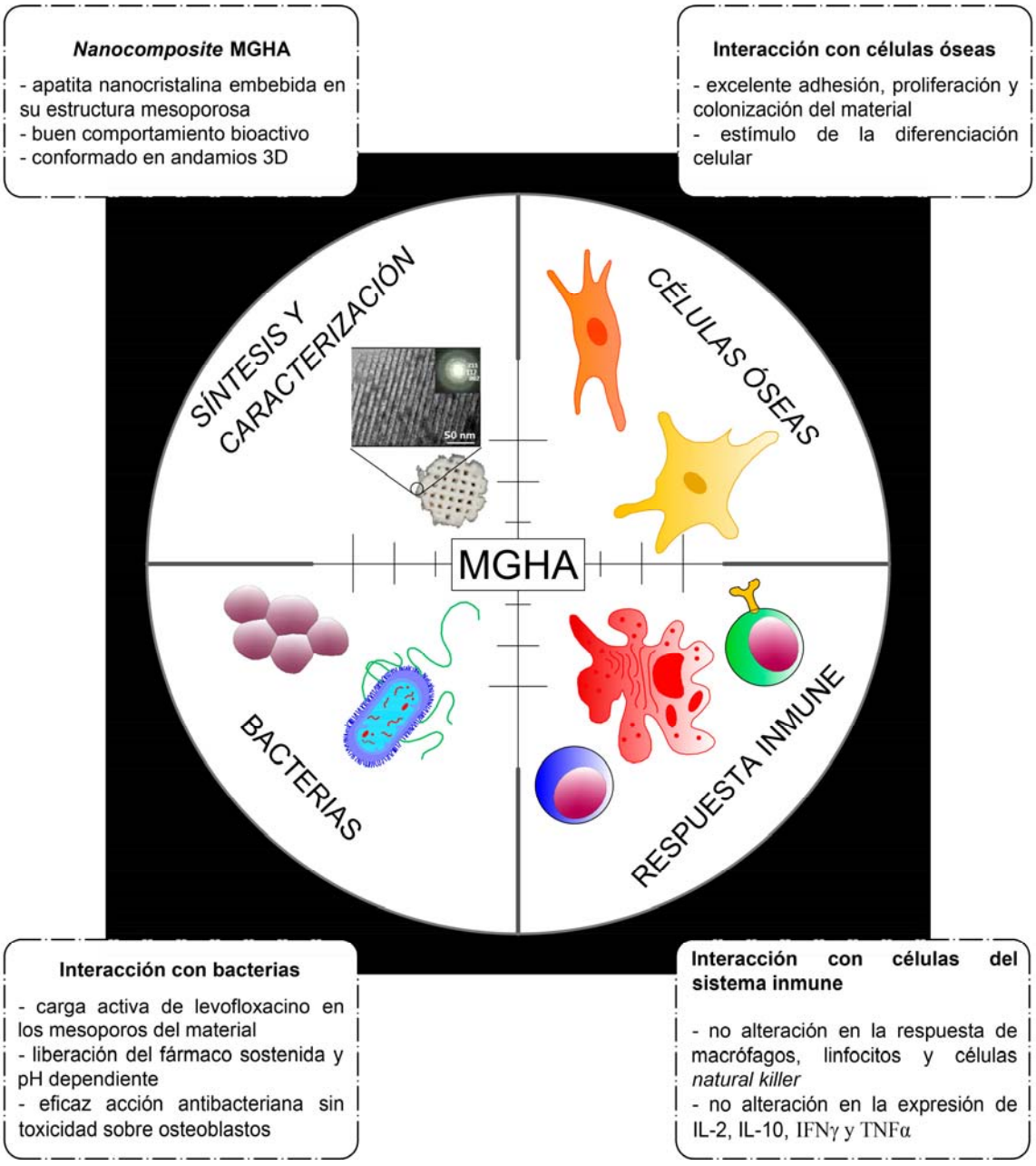

Figura 1. Esquema de los distintos puntos de mira desarrollados durante la presente Tesis Doctoral.

SUMMARY

The beginning of the new millennium has been characterized by the increased application of medical devices in all fields of medicine, principally for the diagnosis, repair and regeneration of damaged tissues. For these purposes, different biomaterials are essential, which have to be biocompatible and which can be combined with cells, growth factors, drugs or other bioactive molecules, seeking the integration into natural body microenvironment and the stimulation of tissue regeneration. The current scientific and technological advances have led to the highest level of refinement and optimization in the selection of the most appropriate biomaterials and the design of its structure at the macro, micro, and even recently, nanometer levels. The substantial gains in terms of biocompatibility associated to a lower risk of failure and the growing demand for medical care of a population that has increased life expectancy, have contributed to the successful expansion of the biomaterial use for biomedical purposes, and currently, about 2,700 types of medical devices exist.

The development of new biomaterials is based on the multidisciplinary innovation and on the ability to "imagine" their applications. The multidisciplinary approach is an essential requirement of the biomedical research, which rapidly advances through the convergence of scientists from different areas such as physics, mathematics, engineering, biology and medicine. The evolution of the biomaterials is reflected in how its definition has been modified. If the term biomaterial was initially considered as a material that should contact body tissues without producing toxicity, this concept has been redefined as "a substance designed to direct the course of any therapeutic or diagnostic procedure in veterinary or medicine by controlling the interactions with components of living systems". The type of biomaterial chosen for each therapy or diagnosis, its shape and its properties depend on the function to be performed and on the cell types which will come into contact in the tissue in which it is to be placed.

Tissue engineering requires the use of scaffolds that act as supports for the formation of new tissue, allowing on its surface the adhesion, proliferation and differentiation processes, without inducing immune reactions that may slow the healing process, or even cause graft rejection by the body. For this reason, composition,

architecture, porosity, topography and chemistry of surface, as well as mechanical properties of these scaffolds play a crucial role in the success of the implants. Recently, researches are focused to "imitate" the nanoscale of tissues and organs since it determines significantly the cellular response and is critical ~~to~~ for ensuring their success. In this sense, the rapid growth of nanotechnology has provided numerous advances in the design of new nanostructured bioceramics for bone regeneration. Nanocrystalline hydroxyapatite, due to its close similarity to the bone mineral component, its osteoconductivas properties and its excellent biocompatibility, plays a key position in respect to other bioceramics. On the other hand, mesostructured silica based materials (as the mesoporous bioactive glasses) formed by channels of ordered pores capable of hosting different biomolecules inside, constitute another important family of nanostructured bioceramics with great potential in tissue engineering, thanks to its excellent bioactive properties and its capacity as controlled local drug release systems. Therefore, these materials are promising candidates to avoid the risk of a possible infection after its implantation, to accommodate inside antimicrobial agents and to release them in a controlled manner.

Nowadays, *nanocomposites* materials, consisting of two components, being one of them nanocrystalline homogeneously distributed into mesostructured amorphous matrix, are subject of intense research in different fields due to the synergy of its components, thus enhancing its final properties and functionality.

Therefore, in this Ph.D. Thesis the synthesis, characterization and evaluation of a new MGHA *nanocomposite* has been carried out. This new material is formed by nanocrystalline hydroxyapatite particles embedded in a mesoporous matrix and it has been prepared in powdered form and as macroporous 3D scaffolds, analyzing their interaction with different cell types involved in the formation of bone tissue (preosteoblasts, osteoblasts, fibroblasts) and in the immune response (macrophages, T and B lymphocytes, *natural killer* cell). Moreover, the loading and release of levofloxacin from MGHA material has been performed evaluating their action on *Staphylococcus aureus* and *Escherichia coli*, and the influence of pH on the release kinetics.

Figure 1 outlines the different points of aim developed in this **Ph.D. Thesis** along the three chapters of this report. The first chapter describes the synthesis, characterization and biological evaluation of a new MGHA *nanocomposite* system formed by nanocrystalline hydroxyapatite particles embedded in a mesoporous matrix with SiO_2-CaO-P_2O_5 composition. The second section comprises the shaped of macroporous MGHA three-dimensional scaffolds (3D) and the aminofunctionalization of its surface to study the interaction of these scaffolds with bone cells and immune cells. Finally, the third chapter is devoted to the study of different strategies of levofloxacin loading and release from the MGHA material for the treatment and prevention of bone infection, analyzing the *in vitro* effects on various bacterial strains and the possible cytotoxic effect on osteoblasts and fibroblasts.

The results have shown the excellent properties of this new MGHA *nanocomposite* which allow to propose it as a candidate to be used in bone tissue engineering.

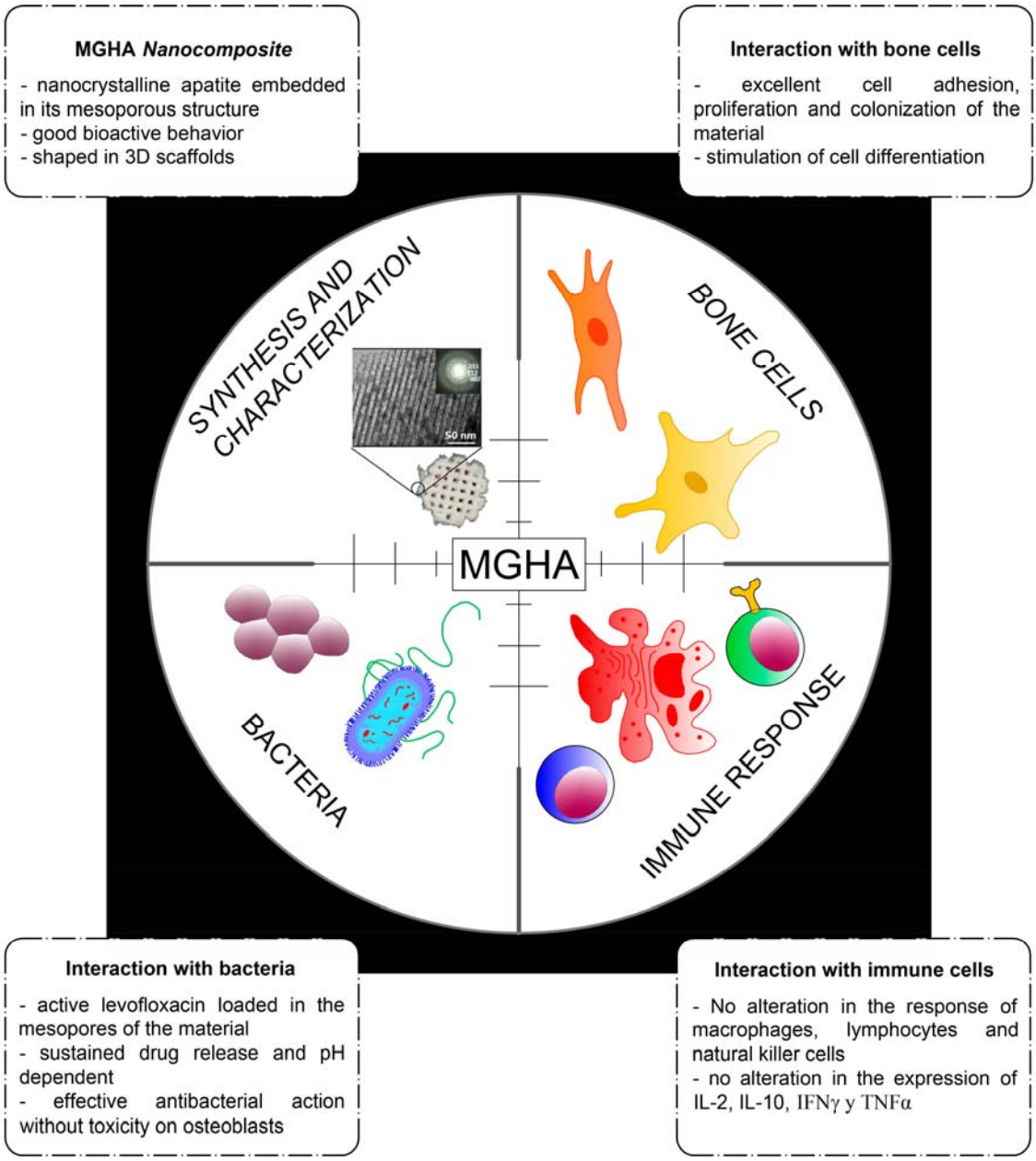

Figure 1. Scheme of different crosshairs developed during this Ph.D. Thesis.

Objetivos

OBJETIVOS

1. Con el fin de potenciar la excelente biocompatibilidad de la apatita nanocristalina y la acelerada bioactividad/propiedades texturales de los vidrios mesoporosos uno de los objetivos ha sido sintetizar un material *nanocomposite* formado por un vidrio bioactivo mesoporoso de composición SiO_2-P_2O_5-CaO con partículas de hidroxiapatita nanocristalina embebidas en las paredes del mesoporo. Tras una exhaustiva caracterización del nuevo material y para comprobar la sinergia de sus componentes, se han realizado estudios *in vitro* de bioactividad y biocompatibilidad con diferentes líneas celulares.

2. Una vez evaluadas las propiedades de este nuevo *nanocomposite,* se han fabricado andamios tridimensionales de porosidad jerarquizada a diferentes escalas de magnitud (meso y macroporosidad) analizando *in vitro* su posible aplicación para Ingeniería Tisular ósea. Con este objetivo se ha llevado a cabo la optimización de la superficie mediante funcionalización con grupos amino y se han realizado estudios con tipos celulares específicos implicados en la regeneración de tejido óseo (preosteoblastos) y en la aceptación del implante (macrófagos, linfocitos T y B, células *natural killer*).

3. Puesto que la infección es un factor clave que determina en muchos casos el rechazo de un implante, se han llevado a cabo distintas estrategias de carga y liberación de levofloxacino a partir del nuevo *nanocomposite*, analizando la biocompatibilidad de las diferentes matrices y su actividad antimicrobiana frente a *E. coli* y *S. aureus*. Los posibles efectos nocivos de la liberación del fármaco se han evaluado en osteoblastos. Finalmente, se ha analizado la influencia del pH en la cinética de liberación de levofloxacino desde andamios tridimensionales de dicho *nanocomposite*, evaluando los efectos antimicrobianos y la biocompatibilidad de las muestras.

Capítulo 1

CAPÍTULO 1. SÍNTESIS, CARACTERIZACIÓN Y EVALUACIÓN BIOLÓGICA DEL *NANOCOMPOSITE* MGHA VIDRIO MESOPOROSO/ HIDROXIAPATITA NANOCRISTALINA

1.1. Vidrios bioactivos mesoporosos: antesala hacia la síntesis de sistemas *nanocomposites*

Los vidrios bioactivos mesoporosos (MBG) también denominados vidrios con plantilla (TG) han despertado un gran interés en la comunidad científica gracias a sus excelentes propiedades estructurales, texturales y bioactivas [1]. Estos materiales han sido preparados tanto en forma de polvo [2,3,4,5], como en microesferas [6,7,8,9], cementos [10] y andamios tridimensionales (3D) para regeneración tisular [11,12,13,14,15,16,17], lo que ha aumentado aún más su potencial aplicabilidad. A esto se le suma su gran capacidad para poder ser funcionalizados [18,19], su actividad hemostática [20] y sus propiedades como sistemas de liberación controlada de fármacos [21,22,23,24,25,26]. La **Figura 1.1.** representa el número de citas anuales relativas al término "*vidrio bioactivo mesoporoso*" desde su descubrimiento en el año 2004 por el grupo del Prof. Zhao (Fundan University) hasta la actualidad [2].

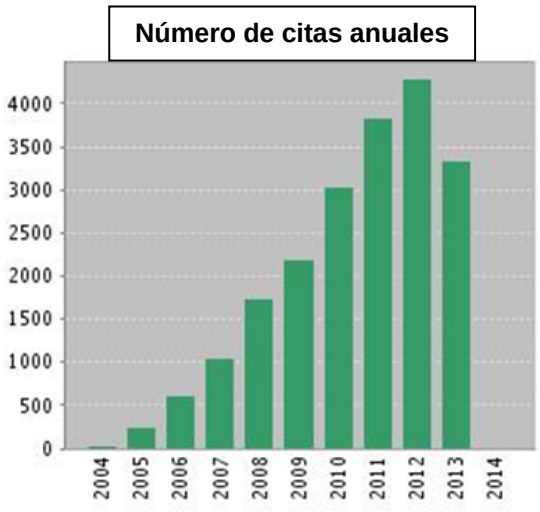

Figura 1.1. Número de citas anuales recibidas desde el año 2004 para el término "*vidrio bioactivo mesoporoso*" obtenido a través de la fuente web of Knowledge[SM].

Un MBG se caracteriza por presentar orden a escala mesoscópica (2-10 nm) y desorden a escala atómica [27]. La **Figura 1.2.** representa dos imágenes de TEM mostrando las dos escalas de magnitud: la *mesoescala* donde existen canales de poros ordenados en el sistema 2D-hexagonal (grupo planar, *P6mm*) y la *escala atómica* representada por las paredes de estos mesoporos con una estructura desordenada (amorfa) característica de un vidrio. Este ordenamiento mesoporoso proporciona unos valores de superficie de área y volumen de poro significativamente mayores que los obtenidos en los vidrios convencionales sol-gel (SGGs) con la misma composición, tal y como se representa en la **Tabla 1.1.**

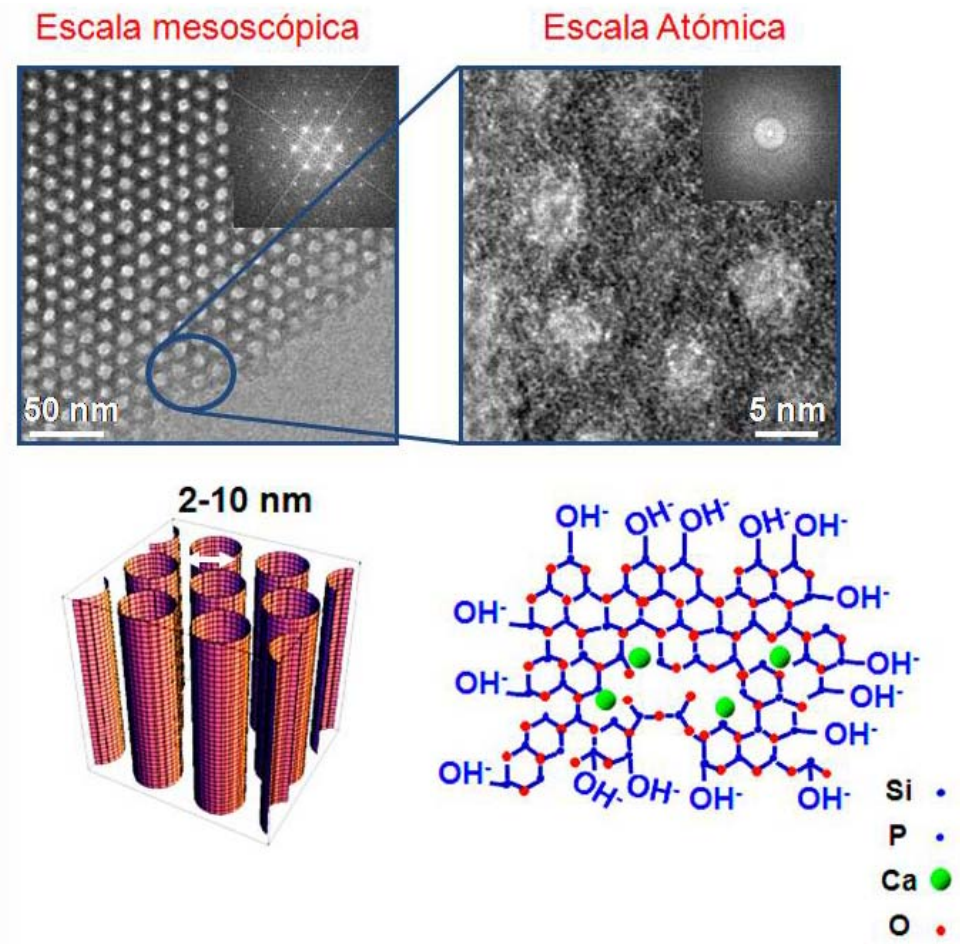

Figura 1.2. Características estructurales de los vidrios bioactivos mesoporosos a diferentes escalas de magnitud. Parte superior-izquierda: imagen de TEM mostrando poros ordenados en un sistema 2D-hexagonal (la imagen está tomada con el haz de electrones paralelo a estos canales de poro). Parte inferior-izquierda: reconstrucción 3D de esta estructura. Parte superior-derecha: imagen de HRTEM mostrando un detalle de las paredes de los poros, exhibiendo el carácter amorfo de un vidrio de composición SiO_2-CaO-P_2O_5. Adaptada de la referencia [1].

Tabla 1.1. Propiedades texturales y estructurales de diferentes composiciones de MBGs comparadas con las de SGGs convencionales [28].

	Composición	S_{BET}	V_p	D_p	Estructura mesoporosa
MBG-S58	$58SiO_2$-$37CaO$-$5P_2O_5$	195	0.46	9.5	*P6mm+wormlike*
MBG-S75	$75SiO_2$-$20CaO$-$5P_2O_5$	393	0.59	6.0	*P6mm+P2mm*
MBG-S85	$85SiO_2$-$10CaO$-$5P_2O_5$	427	0.61	5.7	*Ia-3d*
SGG-S58	$58SiO_2$-$37CaO$-$5P_2O_5$	95	0.35	-	No
SGG-S75	$75SiO_2$-$20CaO$-$5P_2O_5$	117	0.21	-	No
SGG-S85	$85SiO_2$-$10CaO$-$5P_2O_5$	227	0.24	-	No

En la síntesis de los MBGs se combinan la *química sol-gel*, para la síntesis de vidrios sol-gel utilizando alcóxidos en medio hidroalcohólico [29], con la *química supramolecular*, que utiliza surfactantes como agentes directores de la mesoestructura [30]. Esta síntesis se realiza a través de un método de autoensamblaje inducido por evaporación (EISA), que permite obtener una distribución homogénea de todos los componentes [31]. El autoensamblaje comienza con una solución homogénea de los precursores del vidrio junto con el surfactante, en una relación solvente etanol/agua muy elevada. De esta manera, la concentración inicial es muy inferior a la concentración micelar crítica (c_i <<< cmc), permitiendo así una mayor homogeneidad en el sistema. A continuación, la concentración del sistema va incrementando progresivamente debido a la evaporación del etanol, conduciendo así al autoensamblaje de las micelas de surfactante. Éstas interaccionan con las especies inorgánicas, dando lugar a la formación de la mesofase líquida cristalina correspondiente. Por la complejidad del sistema multicomponente (Si-Ca-P), tanto las propiedades estructurales finales del material como el entorno químico de cada uno de sus elementos son muy difíciles de predecir. La **Figura 1.3.** esquematiza el proceso de formación de un MBG en el sistema SiO_2-CaO-P_2O_5.

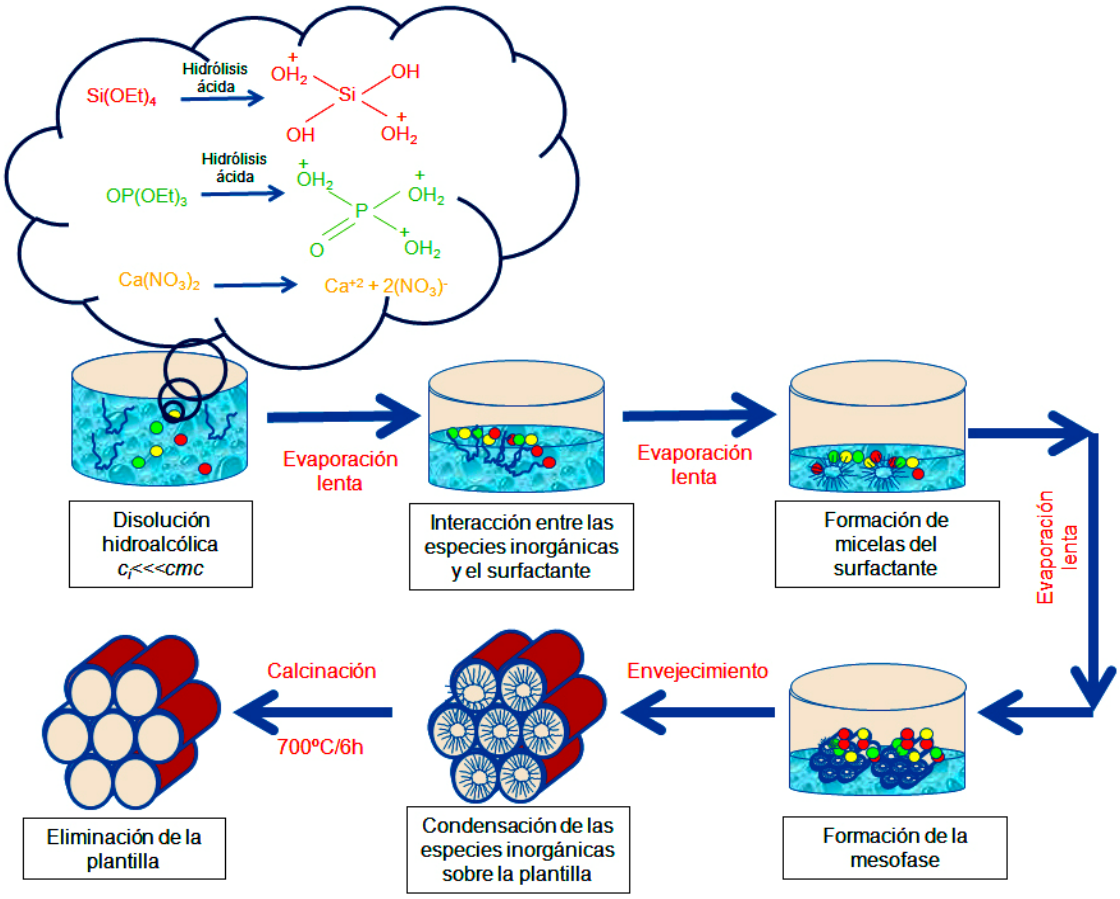

Figura 1.3. Proceso de síntesis de un MBG en el sistema SiO_2-P_2O_5-CaO.

Este proceso de síntesis permite controlar las características texturales y estructurales de estos materiales, las cuales ejercen una importante influencia en su comportamiento bioactivo, tal y como se describe posteriormente. Son muchos los factores que intervienen en tal síntesis: la naturaleza y concentración del surfactante, el solvente, los aditivos, el pH, la temperatura, composición etc. [2,2,32,33,34,35]. En cuanto a la composición, se ha demostrado que la cantidad de calcio presente en la estructura del vidrio ejerce un papel importante en las características estructurales y texturales finales. De esta manera, en trabajos previos se ha demostrado que, variando la cantidad de CaO incorporada durante el proceso de síntesis de vidrios bioactivos SiO_2-CaO-P_2O_5, la estructura mesoporosa se puede controlar desde estructuras 3D-cúbicas a estructuras 2D-hexagonales (ver **Tabla 1.1.**) [2]. Estas modificaciones estructurales se explican en términos de la influencia de los iones Ca^{2+} en la condensación de la sílice, ya que dichos iones actúan como modificadores de la red, disminuyendo la conectividad de la red de sílice. Como consecuencia, la relación Volumen inorgánico/Volumen

orgánico (V_{inorg}/V_{org}) se incrementa con el contenido de Ca^{2+}, disminuyendo así el radio de curvatura de las micelas de surfactante, y contribuyendo a la formación de fases hexagonales en lugar de fases cúbicas.

En cuanto al comportamiento bioactivo *in vitro* de los MBGs, sus cinéticas de formación de la capa de hidroxiapatita (HA) son mucho más aceleradas que en el caso de los SGGs con similar composición. Dicho proceso de formación transcurre en *horas* en lugar de *días* como ocurre en los SGGs. Estos resultados se deben fundamentalmente a la sinergia de sus propiedades: composición química, muy similar a la de los SGGs con superficies y porosidades 5 veces superiores. Sin embargo, existe una gran controversia entre los factores que verdaderamente rigen los procesos de bioactividad de estos MBGs, los cuales son objeto de debate. Esto es consecuencia de que la composición y las propiedades estructurales/texturales de los MBGs están íntimamente relacionadas entre sí. Estudios de bioactividad *in vitro* han mostrado que una disminución del contenido en calcio en un MBG no conduce a una disminución en su cinética de bioactividad, como ocurre en los SGGs, sino todo lo contrario. Esto es debido a que al disminuir el contenido en calcio se incrementan los valores de superficie específica y volumen de poro (propiedades texturales) favoreciendo la formación de estructuras 3D-cúbicas bicontínuas. Dichas estructuras, permiten una mayor accesibilidad de los fluidos a través de su estructura interconectada, lo que podría favorecer los procesos de bioactividad (**Figura 1.4.**) [36].

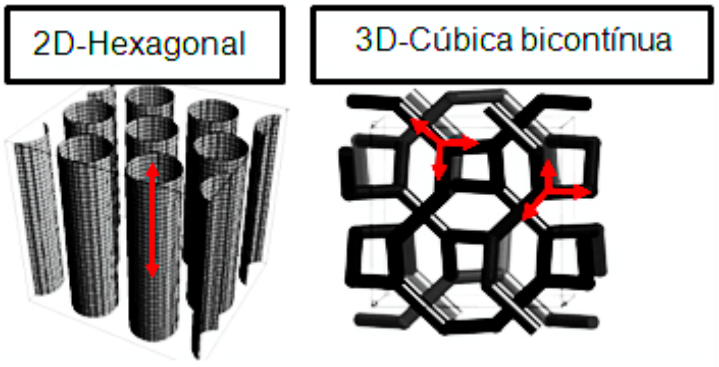

Figura 1.4. Esquema representando los canales correspondientes a una estructura 2D-hexagonal y una 3D-cúbica bicontínua. Adaptada de la referencia [38].

La **Figura 1.5.** muestra el estudio por TEM de un MBG con bajo contenido en calcio (S85) y con mesoestructura 3D-cúbica, después de 4 horas de inmersión en un

fluido corporal simulado (SBF), observándose la formación de cristales aciculares de HA en su superficie [37]. Dicha composición es la que ha presentado las cinéticas de bioactividad más rápidas, jamás mostradas por otra biocerámica. Estos resultados se han atribuido a las propiedades texturales (427 m^2/g de superficie específica) y a las características estructurales (3D-cúbica biocontínua).

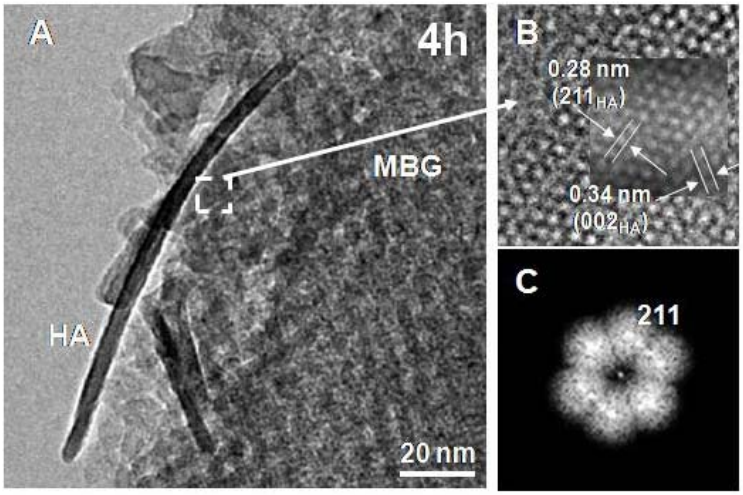

Figura 1.5. Estudio por TEM de un MBG de composición S85 después de permanecer 4 h en SBF. A. Imagen de TEM mostrando la formación de cristales aciculares de HA sobre su superficie. B. Imagen de HRTEM mostrando espaciados a 0.28 y 0.34 nm correspondientes a los planos (211) y (002) de una fase HA. C. Transformada de Fourier (FT) de la zona B. Adaptada de la referencia [38].

Esta familia de MBGs con ordenamiento mesoestructural 2D-hexagonal, también ha evidenciado particularidades en su reactividad/bioactividad cuando su contenido en calcio es elevado (S58). En este caso, dichas composiciones muestran una maduración secuencial en SBF desde fosfato de calcio amorfo (ACP), a fosfato octacálcico (OCP) y finalmente a una HA carbonatada deficiente en calcio (**Figura 1.6.**). Esta maduración secuencial constituye una ventaja muy importante para regeneración tisular ya que dicha secuencia es la misma que tiene lugar en el hueso natural [39].

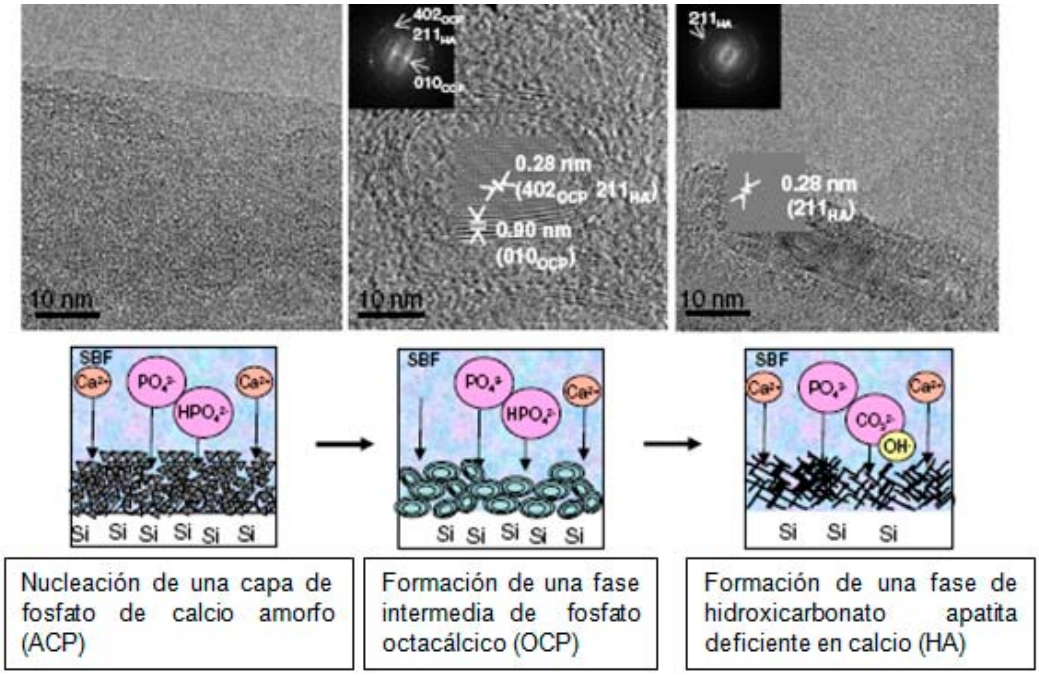

Figura 1.6. Estudio por TEM del proceso de bioactividad de un MBG S58 a diferentes tiempos de incubación en SBF. Adaptada de la referencia [38].

Estudios por NMR de estos MBG han sido necesarios para determinar su estructura a nivel atómico y el entorno químico de cada uno de sus componentes [40,41,42,43]. Dichos estudios han evidenciado por primera vez, la presencia de *clusters* de fosfato de calcio amorfo (ACP) distribuidos homogéneamente dentro de una red mayoritariamente constituida por SiO_2-CaO. Dichos *clusters* podrían actuar como centros de nucleación de la capa de HA, que al quedar distribuidos dentro de la red mesoporosa explicaría el fascinante comportamiento bioactivo de estos materiales. En la Figura **1.7.** se representa un esquema de la estructura de un MBG por NMR.

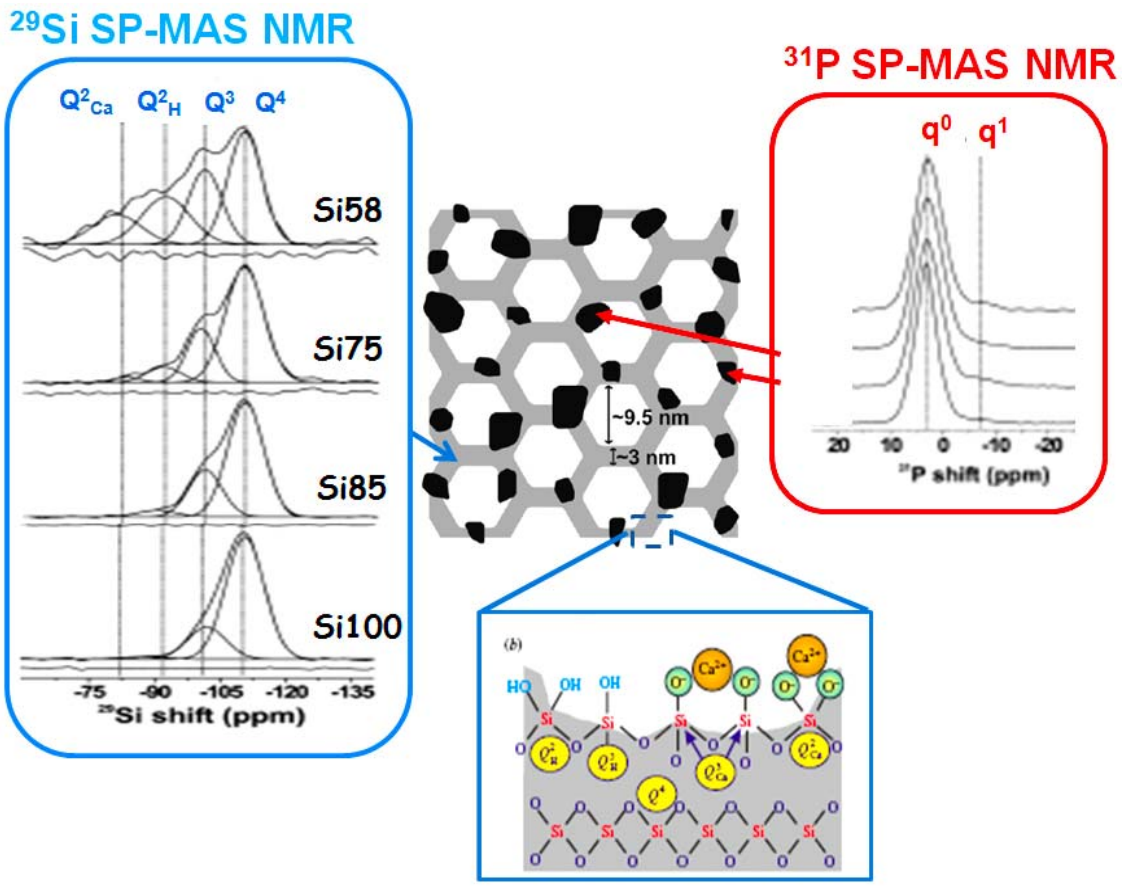

Figura 1.7. Estudio a nivel atómico de un MBG a través de la técnica de RMN. Adaptada de las referencias [41, 42].

Sin embargo, el conjunto de todos los resultados mostrados y su posible influencia en su comportamiento bioactivo plantea demasiadas incógnitas: *¿Son las propiedades texturales o la propia estructura de los vidrios bioactivos mesoporosos factores clave en el proceso bioactivo?*, *¿cuál es el papel fundamental de cada componente en la estructura y comportamiento bioactivo final? ¿son los clusters de ACP esenciales en el comportamiento bioactivo?*

Con el fin de dar respuesta a todas estas incógnitas y así poder determinar el papel fundamental de cada uno de los componentes en las propiedades estructurales/texturales y en el comportamiento bioactivo de los MBG, se prepararon diferentes composiciones de MBGs en los sistemas $100SiO_2$, $95SiO_2$-$5P_2O_5$ y $90SiO_2$-10CaO (% mol) en idénticas condiciones de síntesis, manteniendo siempre constante la relación molar *P123*/formadores de red (SiO_2+P_2O_5). Por otra parte, teniendo en cuenta que la temperatura de envejecimiento juega un papel importante en la mesoestructura

final, por primera vez, se ha preparado un MBG de composición $85SiO_2$-$10CaO$-$5P_2O_5$ con idénticas propiedades texturales pero exhibiendo diferentes propiedades estructurales (3D-cúbica y 2D-hexagonal) mediante un exhaustivo control de la temperatura de envejecimiento durante el proceso de síntesis. Estos resultados han permitido discriminar, entre los demás parámetros, el papel de las propiedades estructurales en el comportamiento bioactivo. Todos los resultados se recogen en el siguiente artículo de investigación:

"***Essential Role of Calcium Phosphate Heterogeneities in 2D-Hexagonal and 3D-Cubic SiO_2-CaO-P_2O_5 Mesoporous Bioactive Glasses***" A. García, **M. Cicuéndez**, I. Izquierdo-Barba, D. Arcos and M. Vallet-Regí. ***Chemistry of Materials 2009, 21, 5474-5484.***

Este Trabajo evidencia el papel fundamental del calcio y del fósforo en las propiedades estructurales y bioactivas finales de los MBGs, en base a un exhaustivo estudio por NMR y TEM. La **Figura 1.8.** esquematiza las propiedades de cada uno de los elementos derivadas de este trabajo. Estos resultados no han sido incluidos en las conclusiones de esta Tesis Doctoral, pero sí han constituido el punto de partida para el diseño y síntesis del nuevo material *nanocomposite* vidrio mesoporoso-hidroxiapatita, eje principal de dicha Tesis.

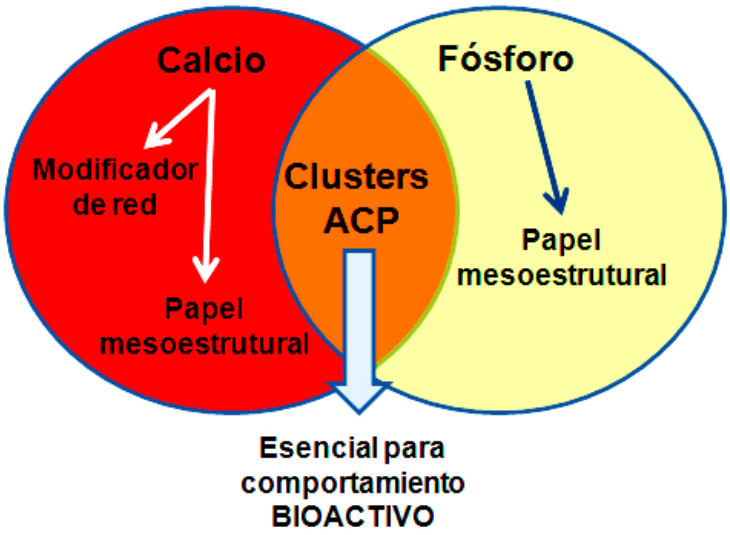

Figura 1.8. Esquema mostrando el papel de cada uno de los componentes de un vidrio mesoporoso en sus propiedades estructurales y bioactivas.

En el caso del ***CaO***, este componente ejerce un importante papel tanto en las propiedades estructurales como en las propiedades bioactivas. Un estudio combinado por NMR de ^{29}Si en SP y CP y TEM, muestra que el Ca^{2+} actúa como modificador de la red de sílice, disminuyendo notablemente su grado de conectividad. Consecuentemente, la fase inorgánica tiene menor densidad, incrementándose así la relación V_{inorg}/V_{org} de la micela lo que favorece la formación de estructuras más hidrofílicas (2D-Hexagonales). Por el contrario, la presencia conjunta de CaO y P_2O_5, en un MBG de composición $85SiO_2$-$10CaO$-$5P_2O_5$, conduce a la formación de *clusters* de ACP localizados en la superficie de la pared vítrea. En este caso, debido a que los cationes Ca^{2+} son consumidos para formar *clusters* de ACP, no contribuyen a disminuir la conectividad de la red de sílice y por tanto la relación de V_{inor}/V_{org} es más baja, favoreciendo así estructuras más hidrofóbicas (3D-cúbica bicontínua). Con respecto al comportamiento bioactivo, se observaron importantes diferencias al comparar el sistema binario $90SiO_2$-$10CaO$ con la composición ternaria $85SiO_2$-$10CaO$-$5P_2O_5$. Ambos vidrios presentan propiedades texturales muy similares, sin embargo, el vidrio ternario exhibe una respuesta bioactiva notablemente mayor. Estos resultados ponen de manifiesto el papel esencial de los *clusters* de ACP en el comportamiento bioactivo.

En cuanto al ***P_2O_5***, este componente también tiene importantes implicaciones en la estructura y más aún en las propiedades bioactivas de los vidrios mesoporosos. En el caso del vidrio de composición $95SiO_2$-$5P_2O_5$, los estudios por NMR muestran que las unidades de P_2O_5 se distribuyen tanto como tetraedros independientes dentro de la red de sílice (formador de red), que como cadenas de polifosfatos situadas en la superficie de la sílice. Sin embargo, cuando las unidades de P_2O_5 forman parte de un sistema ternario $85SiO_2$-$10CaO$-$5P_2O_5$, su papel cambia completamente. La presencia de unidades CaO y P_2O_5 conduce a la formación de *clusters* de ACP localizados en la superficie de la pared vítrea.

En el proceso EISA, la ***temperatura de envejecimiento*** ejerce un papel primordial en las características estructurales finales. En este trabajo, se ha demostrado por primera vez, que es posible sintetizar MBGs en el sistema ternario $85SiO_2$-$10CaO$-$5P_2O_5$ con idéntica composición y propiedades texturales, pero exhibiendo diferentes estructuras mesoporosas tales como, 3D-cúbica bicontínua (*Ia-3d*) y 2D-hexagonal (*P6mm*), modificando la temperatura de evaporación del solvente dentro de un intervalo

de temperatura de 20-40ºC. Estos resultados demuestran que la estructura mesoporosa se puede cambiar mediante un riguroso control de la temperatura de evaporación del solvente durante la formación de la mesofase, resultando en las fases *p6mm*, la coexistencia de fases *p6mm/Ia-3d* y fases *Ia-3d* para 20, 30 y 40ºC, respectivamente. Estos resultados han permitido discriminar el papel de la estructura mesoporosa en el proceso bioactivo, de otros factores como la composición y las propiedades texturales. Los resultados mostraron que la estructura mesoporosa no es un factor determinante en el comportamiento bioactivo de MBGs, cuando la composición y propiedades texturales son similares. Esta observación indica que la composición química, las propiedades texturales y la presencia de *clusters* de ACP accesibles determinan el comportamiento bioactivo *in vitro* de un MBG, independientemente de su estructura mesoporosa.

5474 *Chem. Mater.* **2009,** *21,* 5474–5484
DOI:10.1021/cm9022776

CHEMISTRY OF MATERIALS
Article

Essential Role of Calcium Phosphate Heterogeneities in 2D-Hexagonal and 3D-Cubic $SiO_2-CaO-P_2O_5$ Mesoporous Bioactive Glasses

A. García,[†,‡] M. Cicuéndez,[†,‡] I. Izquierdo-Barba,[†,‡] D. Arcos,*[,†,‡] and M. Vallet-Regí*[,†,‡]

[†]*Departamento Química Inorgánica y Bioinorgánica, Facultad de Farmacia, Universidad Complutense de Madrid, Plaza Ramón y Cajal s/n, 28040 Madrid, Spain, and* [‡]*Networking Research Center on Bioengineering, Biomaterials and Nanomedicine* (*CIBER-BBN*), *Madrid, Spain*

Received July 24, 2009. Revised Manuscript Received October 5, 2009

Mesoporous bioactive glasses (MBGs) with a compoisition of $85SiO_2-10CaO-5P_2O_5$ (mol %) have been prepared through the evaporation-induced self-assembly (EISA) method, using P123 as a structure directing agent. For the first time, $SiO_2-CaO-P_2O_5$ MBGs with identical composition and textural properties, but exhibiting different bicontinuous 3D-cubic and 2D-hexagonal structures, have been prepared. These materials allow us to discriminate the role of the structure on the bioactivity, from other parameters. To understand the role of each component on the mesostructure, local environment, and bioactive behavior, mesoporous $100SiO_2$, $95SiO_2-5P_2O_5$, and $90SiO_2-10CaO$ (mol %) materials were also prepared under the same conditions. The results demonstrate that the joint presence of CaO and P_2O_5 results in amorphous calcium phosphate (ACP) clusters sited at the pore wall surface. This heterogeneity highly improves the bioactive behavior of these materials. In addition, the presence of ACP clusters within the silica network leads to different mesoporous structures. The mesoporous order can be tuned through a rigorous control of the solvent evaporation temperature during the mesophase formation, resulting in *p6mm*, *p6mm*/*Ia*$\bar{3}$*d* coexistence, and *Ia*$\bar{3}$*d* phases for 20, 30, and 40 °C, respectively. Preliminary results indicate that, in the case of identical composition and textural properties, the mesoporous structure does not have influence on the apatite formation, although initial ionic exchange is slightly enhanced for 3D cubic bicontinuous structures.

Introduction

Mesoporous bioactive glasses (MBGs) are a new generation of bioactive materials that are intended for use to heal and restore bone tissue in orthopedic and periodontal diseases. MBGs were prepared for the first time by Zhao et al. in 2004,[1] and they can be considered as enhanced derivatives of conventional $SiO_2-CaO-P_2O_5$ sol−gel glasses.[2−5] In fact, MBGs preparation is based on the principles of sol−gel processes and supramolecular chemistry of surfactants acting as structure directing agents.[6,7] The results are a new family of compounds with outstanding *in vitro* bioactive behavior. This fact is due to the chemical composition, which is similar to sol−gel bioactive glasses classically prepared,[8−12] together with surfaces and porosities 3−5 times higher than those of conventional sol−gel glasses. In addition, the mesopore ordering provides a final product suitable to be used as a delivery system of drugs and osteogenic agents.[13−15]

During the last five years, MBGs have attracted the attention of many researchers. In this sense, not only powdered MBGs,[16,17] but also microspheres,[18,19] cements,[20]

*Author to whom correspondence should be addressed. E-mails: vallet@farm.ucm.es (M.V.-R.), arcosd@farm.ucm.es (D.A.).

(1) Yan, X. X.; Yu, C. Z.; Zhou, X. F.; Tang, J. W.; Zhao, D. Y. *Angew. Chem., Int. Ed.* **2004**, *43*, 5980–5984.
(2) Li, R.; Clark, A. E.; Hench, L. L. *J. Appl. Biomater.* **1991**, *2*, 231–239.
(3) Peltola, T.; Jokinen, M.; Rahiala, H.; Levänen, E.; Rosenholm, J. B.; Kangasniemi, I.; Yli-Urpo, A. *J. Biomed. Mater. Res.* **1999**, *44*, 12–21.
(4) Vallet-Regí, M.; Ragel, C. V.; Salinas, A. J. *Eur. J. Inorg. Chem.* **2003**, 1029–1042.
(5) Vallet-Regí, M. *Dalton Trans.* **2006**, *44*, 5211–5220.
(6) Hench, L. L.; West, J. K. *Chem. Rev.* **1990**, *90*, 33–72.
(7) Mann, S.; Burkett, S. L.; Davis, S. A.; Fowler, C. E.; Mendelson, N. H.; Sims, S. D.; Walsh, D.; Whilton, N. T. *Chem. Mater.* **1997**, *9*, 2300–2310.
(8) Pereira, M. M.; Clark, A. E.; Hench, L. L. *J. Biomed. Mater. Res.* **1994**, *28*, 693–698.
(9) Vallet-Regí, M.; Arcos, D.; Pérez-Pariente, J. *J. Biomed. Mater. Res.* **2000**, *51*, 23–28.
(10) Izquierdo-Barba, I; Salinas, A. J.; Vallet-Regí, M. *J. Biomed. Mater. Res.* **1999**, *47*, 243–250.
(11) Jones, J. R.; Hench, L. L. *J. Mater. Sci.* **2003**, *38*, 3783–3790.
(12) Jokinen, M.; Rahiala, H.; Rosenholm, J. B.; Peltola, T.; Kangasniemi, I. *J. Sol-Gel Sci. Technol.* **1998**, *12*, 159–167.
(13) Vallet-Regí, M.; Balas, F.; Arcos, D. *Angew. Chem., Int. Ed.* **2007**, *46*, 7548.
(14) Vallet-Regí, M.; Colilla, M.; Izquierdo-Barba, I. *J. Biomed. Nanotechnol.* **2008**, *4*, 1–15.
(15) Vallet-Regí, M.; Balas, F.; Colilla, M.; Manzano, M. *Prog. Solid State Chem.* **2008**, *36*, 163–191.
(16) Yan, X. X.; Deng, H. X.; Huang, X. H.; Lu, G. Q.; Qiao, S. Z.; Zhao, D. Y.; Yu, C. Z. *J. Non-Cryst. Solids* **2005**, *351*, 3209–3217.
(17) Yan, X. X.; Huang, H. H.; Yu, C. Z.; Deng, H. X.; Wang, Y.; Zhang, A. D.; Qiao, S. Z.; Lu, G. Q.; Zhao, D. Y. *Biomaterials* **2006**, *27*, 3396–3403.
(18) Arcos, D.; López-Noriega, A.; Ruiz-Hernández, E.; Terasaki, O.; Vallet-Regí, M. *Chem. Mater.* **2009**, *21*, 1000–1009.
(19) Li, X.; Zhang, L. X; Dong, X. P.; Liang, J.; Shi, J. L. *Microporous Mesoporous Mater.* **2007**, *102*, 151–158.
(20) Shi, Q. H.; Wang, J. F.; Zhang, J. P.; Fan, J.; Stucky, G. D. *Adv. Mater.* **2006**, *18*, 1038–1042.

Published on Web 10/21/2009

and scaffolds[21,22] have been prepared. In addition, functionalization,[23] drug delivery properties,[24,25] and hemostatic activity[26] have been also considered for potential applications of MBGs.

The preparation of MBGs in the $SiO_2-CaO-P_2O_5$ system requires synthesis strategies that lead to robust mesoporous structures. The presence of a multicomponent inorganic system, including CaO, makes it difficult to obtain ordered structures when conventional methods are used for mesoporus materials syntheses. In this sense, the evaporation-induced self-assembly (EISA) method[27] is the best choice to prepare these types of MBGs. This method is based on the preferential evaporation of the organic solvents used initially to homogenize the solution of precursors and surfactant, thus enriching the concentrations of nonvolatile constituents. The consequence is the formation of more-stable mesoporous structures.

Because of the complexity of multicomponent systems during the mesophase formation, the final mesoporous structure is difficult to predict, as well as the local environment of each component. Besides, the role of the pore ordering on the bioactive behavior of MBGs is still unclear. For instance, Yan et al. have reported on the homogeneous Ca distribution within 2D-hexagonal MBGs, because of the nanometric size of the pore walls,[1,16] thus avoiding aggregates or calcium phosphate clusters formation. Hexagonal MBGs have been also obtained using P123 and F127 triblock copolymers and the mesophase formation has been followed via small-angle X-ray diffraction (SAXRD),[28] indicating that the mesophase formation occurs via a complicated process that involves a Si−O−Ca−P−O complex. Yun et al. have also shown the possibilities of preparing MBGs with cubic $Im\bar{3}m$ cage-type structures when F127 is added as a surfactant,[29,30] whereas P123 addition commonly results in 2D-hexagonal *p6mm* structures. However, in 2006, it was demonstrated that bicontinuous 3D-cubic structures could be also been prepared with P123 in the same system, under very similar conditions.[31] The mesoporous structure could be modified by changing the SiO_2/CaO ratio. By varying this ratio, 3D-cubic to 2D-hexagonal evolution could be observed as the amount of CaO increased. Moreover, it was thereafter demonstrated that the bioactive behavior showed special particularities, depending on the molar composition and mesoporous ordering in $SiO_2-CaO-P_2O_5$ system.[32]

It has been hypothesized that 3D-cubic bicontinuous structures can facilitate the bioactive process, because of the better fluids accessibility through an interconnected porous structure.[30,32] However, the mesoporous arrangement is commonly associated to the chemical composition or textural properties in MBGs. Consequently, the different bioactive behavior between 3D-cubic or 2D-hexagonal structures cannot be discriminated from chemical and textural factors or even with the homogeneity degree of Ca^{2+} cations into the silica network, which is also a controversial subject in this field.[33]

For the first time, we have prepared $SiO_2-CaO-P_2O_5$ MBGs with identical composition and textural properties that exhibit different bicontinuous 3D-cubic and 2D-hexagonal structures. We have chosen the composition $85SiO_2-10CaO-5P_2O_5$ (mol %) because of its excellent bioactive behavior without altering the surrounding fluids.[32] These materials allow us to discriminate the role of the structure from other parameters. This paper also reveals the fundamental role of P_2O_5 over the local environment of Ca^{2+}, demonstrating the importance of the calcium phosphate heterogeneities on the final mesoporous structure and bioactive behavior in these compounds.

Materials and Methods

Synthesis. Highly ordered mesoporous materials were synthesized using a nonionic surfactant Pluronic P123 (BASF) as a structure directing agent and evaporation-induced self-assembly (EISA) method. P123 is an amphiphilic triblock polymer that has the following sequence: $EO_{20}PO_{70}EO_{20}$, where EO is poly(ethylene oxide) and PO is poly(propylene oxide). Tetraethyl orthosilicate (TEOS), triethyl phosphate (TEP), and calcium nitrate tetrahydrate ($Ca(NO_3)_2 \cdot 4H_2O$) were used as SiO_2, P_2O_5, and CaO sources, respectively. Four different compositions, denoted as Si100, Si95P5, Si90Ca10, and Si85Ca10P5, were prepared according to the nominal composition (on a mol % basis) of SiO_2 (Si), P_2O_5 (P), and CaO (Ca), respectively.

In a typical synthesis, 16 g of P123 were dissolved in 240 mL of ethanol with 4 mL of 0.5 M HCl solution at room temperature. Afterward, the appropriate amount of TEOS, TEP, and/or $Ca(NO_3)_2 \cdot 4H_2O$ was added under continuous stirring in 3 h intervals. The different amounts of reactive are shown in Table S1 of the Supporting Information. The resulting colorless sols were stirred at room temperature for 24 h, and then they were transferred into Petri dishes (9 cm in diameter). Six aliquots (*ca.* 50 mL) were obtained for each composition and evaporated at three different temperatures (20, 30, and 40 °C) for ~7 days. With this synthesis scheme,

(21) Yun, H.; Kim, S.; Hyeon, Y. *Chem. Commun.* **2007**, 2139–2141.
(22) Li, X.; Shi, J. L.; Dong, X. P.; Zhang, L. X.; Zeng, H. Y. *J. Biomed. Mater. Res.* **2008**, *84A*, 84–91.
(23) Sun, J.; Li, Y. S.; Li, L.; Zhao, W.; Li, L.; Gao, J. H.; Ruan, M. L.; Shi, J. L. *J. Non-Cryst. Solids* **2008**, *354*, 3799–3805.
(24) Zhao, L. Z.; Yan, X. X.; Zhou, X. F.; Zhou, L.; Wang, H. N.; Tang, J. W.; Yu, C. Z. *Microporous Mesoporous Mater.* **2008**, *109*, 210–215.
(25) Xia, W.; Chang, J. *J. Controlled Release* **2006**, *110*, 522–530.
(26) Ostomel, T. A.; Shi, Q.; Tsung, C. K.; Liang, H.; Stucky, G. D. *Small* **2006**, *2*, 1261–1265.
(27) Brinker, C. J.; Lu, Y. F.; Sellinger, A.; Fan, H. Y. *Adv. Mater.* **1999**, *11*, 579–585.
(28) Zhao, Y. F.; Loo, S. C. J.; Chen, Y. Z.; Boey, F. Y. C.; Ma, J. *J. Biomed. Mater. Res.* **2008**, *85A*, 1032–1042.
(29) Yun, H.; Kim, S.; Hyun, Y. *Solid State Sci.* **2008**, *10*, 1083–1092.
(30) Yun, H.; Kim, S.; Hyeon, Y. *Mater. Lett.* **2007**, *61*, 4569–4572.
(31) López-Noriega, A.; Arcos, D.; Izquierdo-Barba, I.; Sakamoto, Y.; Terasaki, O.; Vallet-Regí, M. *Chem. Mater.* **2006**, *18*, 3137–3144.
(32) Izquierdo-Barba, I.; Arcos, D.; Sakamoto, Y.; Terasaki, O.; López-Noriega, A.; Vallet-Regí, M. *Chem. Mater.* **2008**, *20*, 3191–3198.
(33) Leonova, E.; Izquierdo-Barba, I.; Arcos, D.; López-Noriega, A.; Hedin, N.; Vallet-Regí, M.; Edén, M. *J. Phys. Chem. C* **2008**, *112*, 5552–5562.

we modify the thermal conditions at which mesophase formation occurs, thus changing the final mesoporous structure (see below). Finally, homogeneous membranes were obtained and calcined in air at 700 °C for 6 h to obtain ordered mesoporous powders with different chemical compositions.

Characterization. Powder X-ray diffraction (XRD) patterns were recorded in a Philips Model X'Pert diffractometer that used Cu Kα radiation (wavelength of 1.5406 Å). XRD patterns were collected in the 2θ range of 0.6°−8°, with a step size of 0.02° and a counting time of 0.5 s per step.

Transmission electron microscopy (TEM) was performed with a JEOL Model 3000 FEG electron microscope that had been fitted with a double-tilting goniometer stage (±45°) and with an Oxford LINK EDS analyzer. TEM images were recorded using a charge-coupled device (CCD) camera (MultiScan model 794, Gatan, 1024 × 1024 pixels, 24 μm × 24 μm in size) using low-dose condition. Fourier transform (FT) patterns were conducted using Digital Micrograph (Gatan).

The textural properties of the calcined materials were determined by nitrogen adsorption/desorption analyses at −196 °C on a Micromeritics Model ASAP 2020 instrument (Micromeritics Co, Norcross, GA). To perform the N_2 adsorption measurements, 100−150 mg of materials were previously degassed under vacuum for 24 h at 200 °C. The surface area was determined using the Brunauer−Emmett−Teller (BET) method. The pore size distribution in the range of 0.5−40 nm was determined from the desorption branch of the isotherm by means of the Barrett−Joyner−Halenda (BJH) method.

$^{1}H \rightarrow {}^{29}Si$ and $^{1}H \rightarrow {}^{31}P$ CP (cross-polarization)/MAS (magic-angle-spinning) and single-pulse (SP) solid-state nuclear magnetic resonance (NMR) measurements were performed to evaluate the different silicon and phosphorus environments in the synthesized samples. The NMR spectra were recorded on a Bruker Model Avance 400 spectrometer. Samples were spun at 10 kHz for ^{29}Si and 6 kHz in the case of ^{31}P. Spectrometer frequencies were set to 79.49 and 161.97 MHz for ^{29}Si and ^{31}P, respectively. Chemical shift values were referenced to tetramethylsilane (TMS) and H_3PO_4 for ^{29}Si and ^{31}P, respectively. All spectra were obtained using a proton-enhanced CP method, using a contact time of 1 ms. The time period between successive accumulations was 5 and 4 s for ^{29}Si and ^{31}P, respectively, and the number of scans was 10 000 for all spectra.

***In Vitro* Bioactivity Test.** The assessment of *in vitro* bioactivity was performed in a SBF solution, proposed by Kokubo et al.[34] The simulated body fluid (SBF) solution has a composition and concentration similar to those of the inorganic part of human plasma, prepared by dissolving NaCl, KCl, $NaHCO_3$, $K_2HPO_4 \cdot 3H_2O$, $MgCl_2 \cdot 6H_2O$, $CaCl_2$, and Na_2SO_4 into distilled water and buffering at pH 7.4 with tris(hydroxymethyl)aminomethane $NH_2C(CH_2OH)_3$ and HCl.

The four samples with different chemical compositions were used to investigate the composition−bioactivity correlation. For this purpose, 1 g of powder was immersed in 50 mL of filtered SBF in polyethylene containers under sterile conditions. The containers were treated at 37 °C under continuous orbital stirring in an Ecotron HT incubator. After soaking, the powders were collected from the SBF via filtration and air-dried at room temperature. Bioactive behavior was followed over powdered samples by Fourier transform infrared (FTIR) spectroscopy after different soaking periods to determine the formation of an apatite like-phase, according to the method proposed by Warren, Clark, and Hench[35] for bioactive glasses. FTIR spectra were collected in a Thermo Nicolet Model Nexus system that was equipped with a Goldengate attenuated total reflectance (ATR) device and using the KBr pellet method. XRD patterns were collected before and after soaking in SBF with a Philips Model X'pert diffractometer using the Kα Cu radiation. Finally, the Ca^{2+} content and pH evolution of the SBF were tested as a function of MBGs soaking by means of an Ilyte ion analyzer.

Results. Figure 1 shows low-angle XRD patterns of the calcined pure silica sample, Si100, and calcined samples comprised of $SiO_2-P_2O_5$ (Si95P5) and SiO_2-CaO (Si90Ca10), which have been evaporated at 40 °C. Samples exclusively synthesized with network formers (i.e., Si100 and Si95P5) show an intense diffraction maxima at $2\theta = 1.17°$ and 1.18° for Si100 and Si95P5, respectively. These maxima can be indexed as the 211 reflection of a 3D-cubic phase with space group $Ia\bar{3}d$, based on TEM results. A weak shoulder at $2\theta°$ values of ∼2.22° could be assigned to the 400 reflection of the same phase, considering the TEM results (see below). The unit-cell parameters calculated from the 211 peak positions are 18.5 and 18.3 nm for Si100 and Si95P5, respectively. Identical XRD patterns were obtained for these samples, independent of the evaporation temperature at 20, 30, or 40 °C (see Table 1).

When 10% mol of CaO is incorporated (Si90Ca10), the XRD pattern shows two weak peaks beside the first intense peak, which can be indexed assuming a typical 2D-hexagonal *p6mm* structure. The well-resolved peaks can be indexed as 10, 11, and 20 reflections of a more hydrophilic hexagonal structure with a unit-cell parameter of 8.2 nm (see TEM results below). This composition also showed identical mesopore ordering that was independent of evaporation temperature (see Table 1), noting that the presence or absence of CaO as a network modifier can determine the formation of more hydrophilic (*p6mm*) or hydrophobic ($Ia\bar{3}d$) structures, respectively.

Figure 2 shows the XRD patterns of the calcined Si85Ca10P5 sample, when the EISA process was performed at 20, 30, and 40 °C. In this case, the mesopore structure is

(34) Kokubo, T.; Kushitani, H.; Sakka, S.; Kitsugi, T.; Yamamuro, T. *J. Biomed. Mater. Res.* **1990**, *24*, 721–734.

(35) Warren, L. D.; Clark, A. E.; Hench, L. L. *J. Biomed. Mater. Res.: Appl. Biomat.* **1989**, *23*, 201–209.

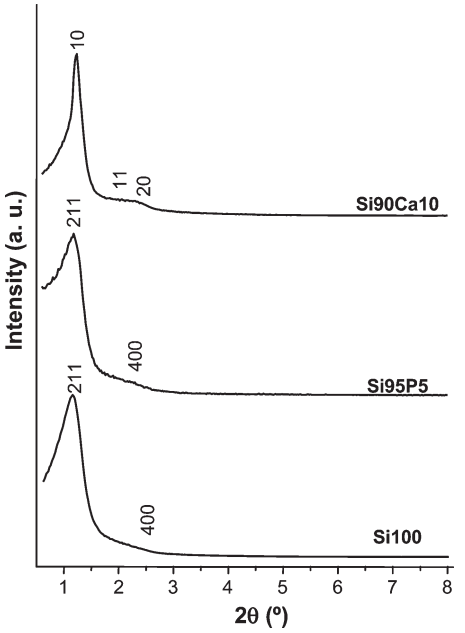

Figure 1. Low-angle powder X-ray diffraction (XRD) patterns obtained for calcined Si100, Si95P5, and Si90Ca10 compositions evaporated at 40 °C. Miller indexes for the corresponding cubic or hexagonal phases are indicated. Samples evaporated at 20 and 30 °C showed almost identical patterns.

Table 1. Mesoporous Structure (Space Groups) Observed for the Different Chemical Compositions and Solvent Evaporation Temperatures by XRD and TEM Studies

	Space Group		
sample	20 °C	30 °C	40 °C
Si100	$Ia\bar{3}d$	$Ia\bar{3}d$	$Ia\bar{3}d$
Si95P5	$Ia\bar{3}d$	$Ia\bar{3}d$	$Ia\bar{3}d$
Si90Ca10	*p6mm*	*p6mm*	*p6mm*
Si85Ca10P5	*p6mm*	*p6mm*/$Ia\bar{3}d$	$Ia\bar{3}d$

clearly dependent on the self-assembling temperature, evolving from a hydrophilic 2D-hexagonal phase *p6mm* toward a more hydrophobic $Ia\bar{3}d$ 3D-cubic bicontinuous structure, as the temperature increases. The XRD pattern for Si85Ca10P5 prepared at 20 °C clearly shows diffraction maxima at 1.18°, 2.02°, and 2.30°, which are assigned to reflections 10, 11, and 20, respectively, of a *p6mm* hexagonal phase. Si85Ca10P5 prepared at 30 °C exhibits a XRD pattern with maxima that cannot be assigned to a spatial group without a certain degree of ambiguity. In fact, the main peak at $2\theta = 1.14°$ exhibits a profile intermediate between the characteristic 10 reflection of a 2D-hexagonal phase and the 211 reflection of a 3D-cubic phase. In addition, the scattering observed between $2\theta = 1.8°$ and 2.4° cannot be clearly assigned to the 11 and 20 reflections of a *p6mm* planar group, or the 400 and 332 reflections of an $Ia\bar{3}d$ cubic phase. Further TEM studies were performed to provide a satisfactory answer. Finally, the XRD pattern for the calcined Si85Ca10P5 prepared at 40 °C shows diffraction maxima assignable to the 211, 400, and 332 reflections, respectively of a 3D-cubic $Ia\bar{3}d$ symmetry.

TEM studies confirm the results obtained by XRD. Figure 3 displays TEM images and the Fourier patterns

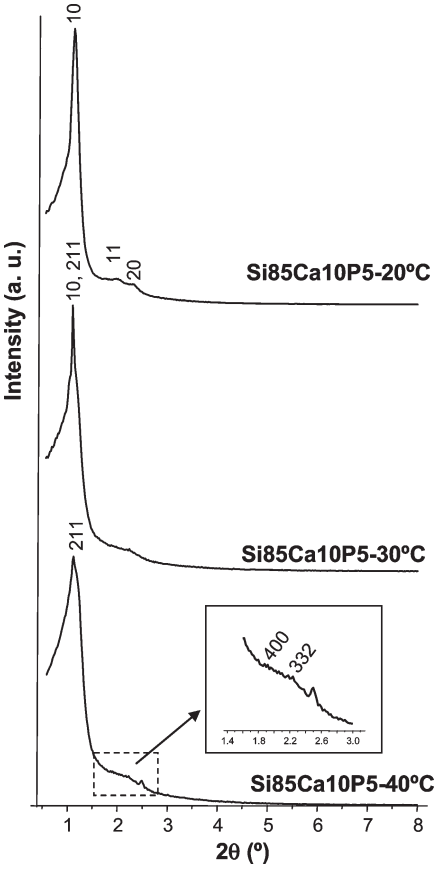

Figure 2. Low-angle powder X-ray diffraction (XRD) patterns obtained for calcined Si85Ca10P5 samples evaporated at 20, 30, and 40 °C. Miller indexes for the corresponding cubic or hexagonal phases are indicated.

obtained for Si100 (see Figure 3a) and Si95P5 (see Figure 3b) synthesized at 40 °C, showing typical images taken along the [111] direction of an $Ia\bar{3}d$ structure,[36] in agreement with XRD patterns. In contrast, the TEM image and the Fourier pattern for the Si90Ca10 sample (see Figure 3c) clearly evidence the formation of a 2D-hexagonal *p6mm* mesoporous structure. Identical results were observed for each composition, in the case of samples evaporated at 20 and 30 °C.

Figure 4 shows the TEM images for calcined Si85-Ca10P5 samples evaporated at 20, 30, and 40 °C during the self-assembly process. TEM images evidence the change of the mesoporous structure as a function of the self-assembly temperature. The Si85Ca10P5 sample obtained at 20 °C clearly evidences a 2D-hexagonal channel structure taken along the direction perpendicular to the channels, showing parallel planes with a *d*-spacing of 6.9 nm. When the evaporated temperature is 30 °C, the TEM images (see Figure 4b) show two certain domains. One domain (denoted as number 1 in Figure 4b) corresponds to the typical TEM image taken along the [111] direction of an $Ia\bar{3}d$ structure, showing values of $d_{211} = 7.9$ nm and $d_{220} = 6.9$ nm. In contrast, the second domain shows a typical 2D-hexagonal arrangement in the direction perpendicular to the channels with a value of $d_{10} = 6.9$ nm.

(36) Sakamoto, Y.; Kim, T. W.; Ryoo, R.; Terasaki, O. *Angew. Chem., Int. Ed.* **2004**, *43*, 5231–5234.

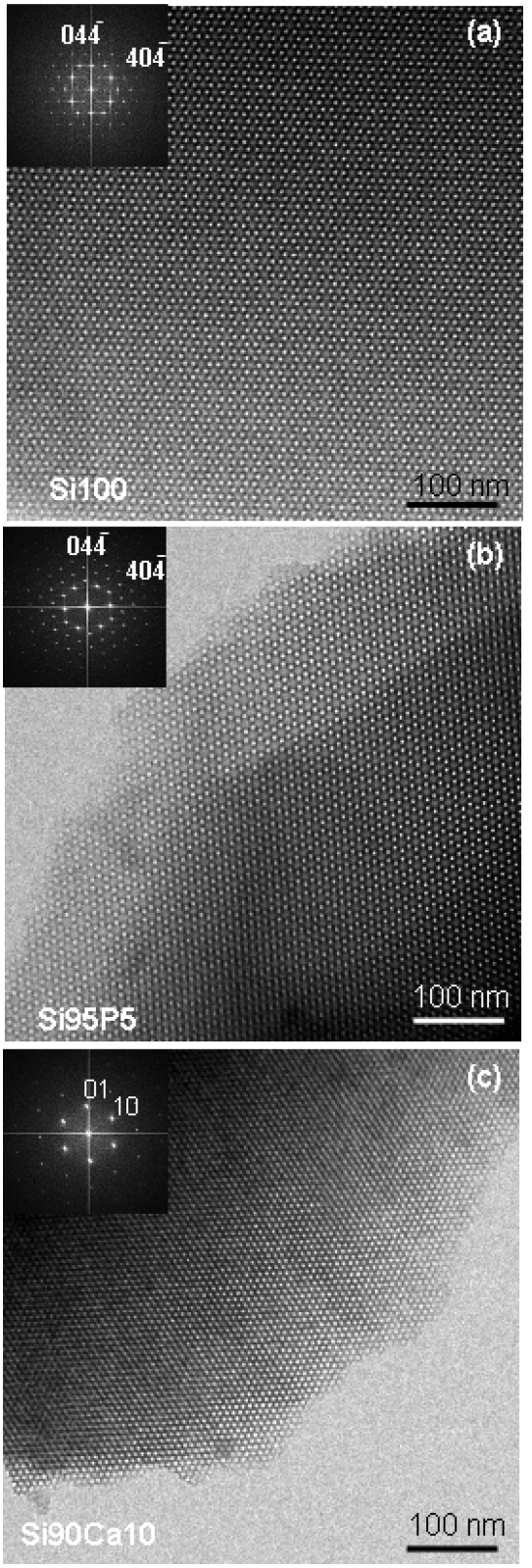

Figure 3. TEM images and Fourier patterns for calcined (a) Si100, (b) Si95P5, and (c) Si90Ca10 samples evaporated at 40 °C. Similar results were observed for each composition evaporated at 20 and 30 °C.

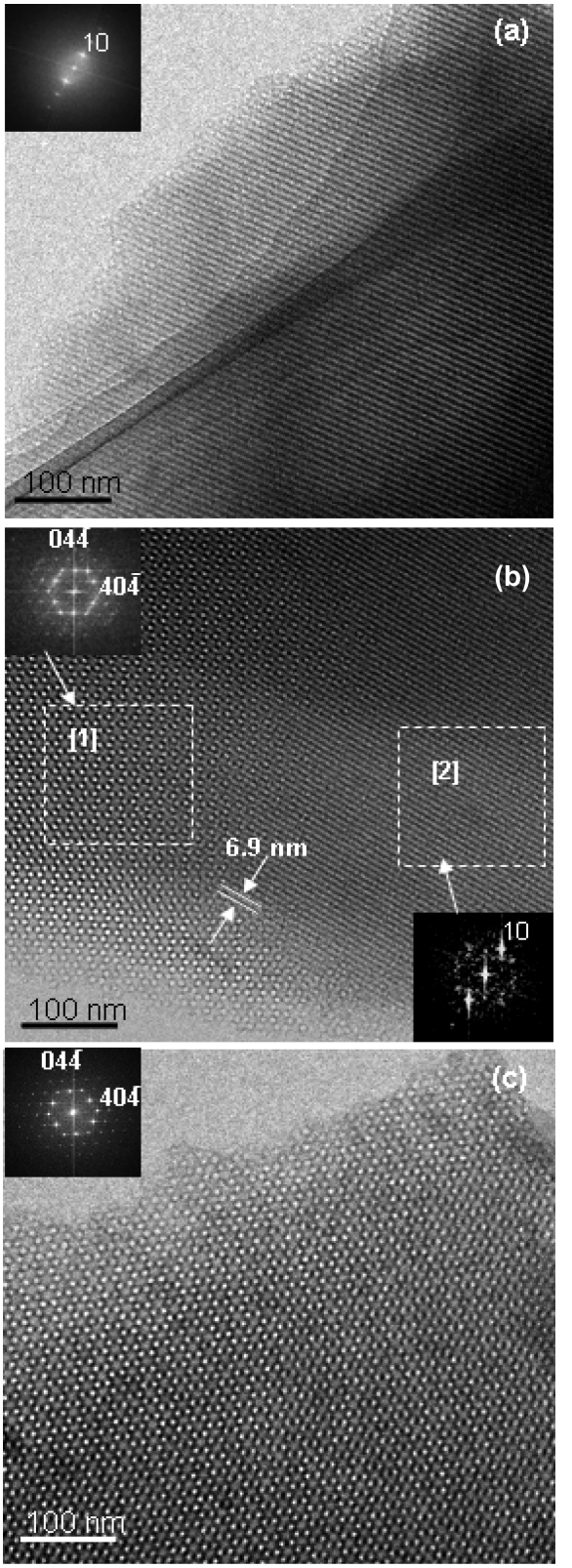

Figure 4. TEM images and Fourier patterns for calcined Si85Ca10P5 samples evaporated at (a) 20, (b) 30, and (c) 40 °C. Panel (a) shows a TEM image corresponding to a 2D-hexagonal structure. Panel (b) is a TEM image showing two well-defined domains (framed in dotted lines). FT patterns were obtained from these framed areas showing an $Ia\bar{3}d$ structure and a *p6mm* structure, respectively. Panel (c) shows TEM images that correspond to the [111] direction of a 3D-cubic structure.

Therefore, TEM results demonstrate the phase transition occurred through the formation of a mixed ordering. In this transition, *p6mm* structure evolves toward a cubic $Ia\bar{3}d$ through the transformation of the 10 reflection of a 2D-hexagonal to the 220 reflection of the 3D-cubic structure.

This observation is consistent with the peak profiles observed by XRD for this sample, because the reflections

Table 2. Textural Properties of the Mesoporous Materials Prepared

sample	symmetry	space group	surface area, S_{BET} (m^2/g)[a]	total pore volume, V_p (cm^3/g)	pore diameter, D_P (nm)[b]	unit-cell parameter, a_0 (nm)[c]	wall thickness, t_{wall} (nm)
Si100	3D-cubic	$Ia\bar{3}d$	389.42	0.62	6.39	18.5	2.78
Si95P5	3D-cubic	$Ia\bar{3}d$	454.29	0.73	6.43	18.3	2.70
Si90Ca10	2D-hexagonal	*p6mm*	467.54	0.63	5.37	8.2	2.83
Si85Ca10P5−20 °C	2D-hexagonal	*p6mm*	472.74	0.63	5.37	8.6	3.23
Si85Ca10P5−40 °C	3D-cubic	$Ia\bar{3}d$	479.99	0.64	5.38	19.0	3.46

[a] Determined using the BET method. [b] Calculated using the BJH method. [c] Calculated by XRD.

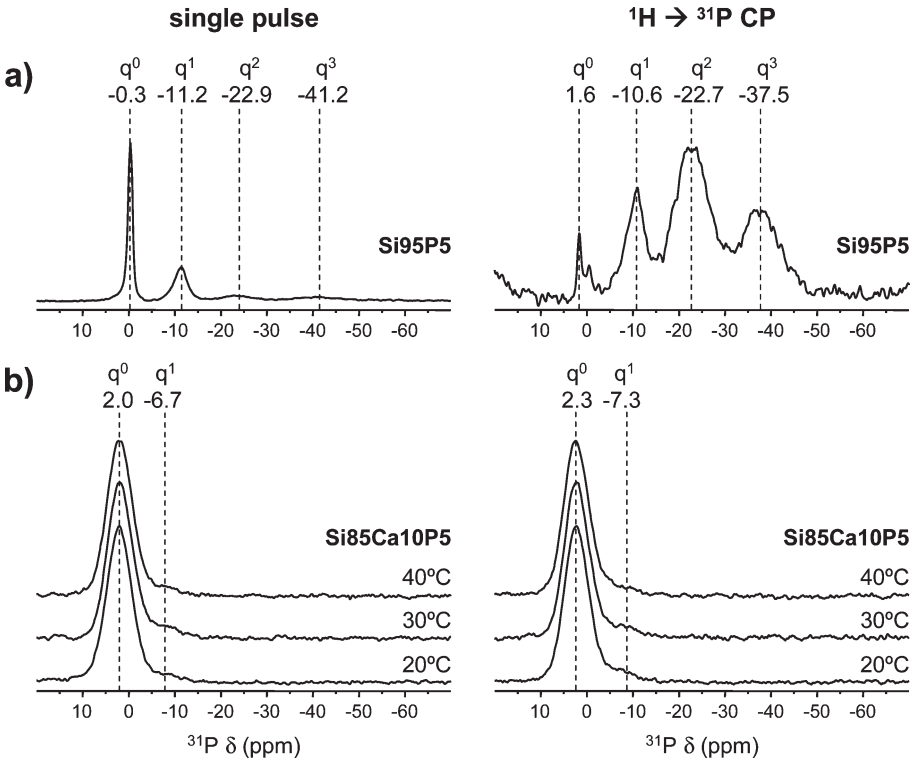

Figure 5. Solid-state ^{31}P single-pulse (left) and cross-polarization (right) MAS NMR spectra (with their respective q^n phosphorus environments shown at the top) of the (a) Si95P5 and (b) Si85Ca10P5 samples evaporated at 20, 30, and 40 °C.

observed must be a convolution of both coexisting phases. Finally, TEM observations of the Si85Ca10P5 sample at 40 °C evidence a cubic $Ia\bar{3}d$ mesoporous structure, as can be seen in Figure 4c, taken with an incidence beam parallel to the [111] direction, showing values of $d_{211} = 7.9$ and $d_{220} = 6.9$ nm.

Textural properties of the mesoporous glasses are collected in Table 2. All the isotherms showed curves characteristic of porous materials with type H1 hysteresis loops that correspond to cylindrical pores (see Figure S1 in the Supporting Information). The mesoporous glasses exhibit surface areas in the range of 390−480 m^2/g, similar to other MBGs previously reported.[1,31] Special attention should be given to the smaller pore diameters of the calcium-containing compositions (Si90Ca10 and Si85Ca10P5). These results are in clear agreement with an increase of the pore wall thickness, indicating a volume increase of the inorganic component during the mesophase formation. It must be highlighted that 2D-hexagonal Si85Ca10P5−20 °C and 3D-cubic Si85Ca10P5−40 °C show almost identical adsorption isotherms and pore size distributions, as well as S_{BET} and pore volume values (see Figure S2 in the Supporting Information).

^{31}P NMR. ^{31}P NMR spectroscopy was used to evaluate the local environment of P atoms, thus elucidating the phosphate species that is contained in the Si95P5 and Si85Ca10P5 (20, 30, and 40 °C) samples. Figure 5 shows the solid-stage ^{31}P MAS NMR spectra for both compositions. Spectra were recorded by single-pulse excitation (left) and by $^1H \rightarrow ^{31}P$ cross-polarization (right).

The spectrum that was recorded by single pulse for the Si95P5 sample shows four signals assignable to q^0, q^1, q^2, and q^3 phosphorus environments. In this case, q^0, q^1, q^2, and q^3 represent phosphorus atoms (denoted P*) present in the PO_4^{3-} species, $(NBO)_3P^*-(OP)$, $(NBO)_2-P^*-(OP_2)$, and $(NBO)-P^*(OP)_3$, respectively (NBO denotes a nonbonding oxygen, relative to another P atom). The presence of all these resonances in the Si95P5 spectrum indicates that an important amount of PO_4 tetrahedrons are forming ramified chains, thus acting as network formers, together with the SiO_2 network. However, the high percentage of q^0 also signifies that most of the P atoms are included as independent PO_4 tetrahedrons

Table 3. Chemical Shifts, Relative Peak Areas, and Silica Connectivity Obtained by Solid-State Single Pulse ^{29}Si MAS NMR

	Q^2		Q^3		Q^4		
	chemical shift	relative peak area	chemical shift	relative peak area	chemical shift	relative peak area	network connectivity
Si100			−101.0	14.6	−110.7	85.4	3.85
Si95P5	−94.1	4.7	−102.0	17.2	−110.6	78.1	3.73*
Si90Ca10	−91.8	3.6	−100.7	20.1	−109.9	76.3	3.72
Si85Ca10P5−20 °C	−93.1	2.2	−101.2	18.2	−110.4	79.6	3.77

* Network connectivity is underestimated for this sample, because only SiO_4 units (and not PO_4) have been considered as network formers in these calculations.

within the silica network. The $^1H \rightarrow ^{31}P$ CP spectrum for the Si95P5 sample emphasizes resonances for q^2 and q^3, signifying that ramified polyphosphate chains are placed close to the protons (that is, at the material surface). Considering both spectra (SP and CP) for the Si95P5 sample, the results would agree with two main environments for the P_2O_5 into these materials. The first one would consist of individual PO_4 tetrahedrons (q^0) sited within the SiO_2 wall and bonded to four SiO_4 tetrahedrons in a regular environment (full width at half-maximum height (fwhm), equal to 1.2 ppm). The second one would consist of ramified polyphosphates, bonded to the end of silica chains and sited at the material surface. This situation can be explained in terms of the slower hydrolysis kinetic of the TEP, compared with TEOS.

Single-pulse excitation and $^1H \rightarrow ^{31}P$ CP spectra for the Si85Ca10P5 samples show similar patterns. All the Si85Ca10P5 samples show a mean maximum of ∼2 ppm assigned at the q^0 environment. This signal shows a fwhm of *ca.* 6 ppm, which is typical of an amorphous orthophosphate. A second weak signal sited around −7 ppm appears for these samples. This resonance falls in the range of q^1 tetrahedra[37] and can be assigned to P−O−P or P−O−Si environments. Previous studies lead us to conclude that this signal is preferently attributed to a P−O−Si environment.[33] Both single-pulse and $^1H \rightarrow ^{31}P$ CP spectra show very similar results. This fact indicates that, independent of the self-assembling temperature, the CaO presence in this system leads to the nucleation of an amorphous calcium phosphate (ACP), consuming all of the P_2O_5 and thus avoiding polyphosphate formation. To determine whether ACP clusters occur during the self-assembling of the Si85Ca10P5 sample or after surfactant calcinations, ^{31}P NMR spectra were recorded for this composition, evaporated at 20, 30, and 40 °C before calcination. The three spectra only showed one resonance that corresponded to the q^0 environment, thus indicating that calcium orthophosphate is formed before the subsequent thermal treatment (see Figure S3 in the Supporting Information), without the presence of other polyphosphate species.

^{29}Si NMR. ^{29}Si NMR spectroscopy was used to evaluate the network connectivity of MBGs as a function of chemical composition. Q^2, Q^3, and Q^4 represent the silicon atoms (denoted Si*) in $(NBO)_2Si^*-(OSi)_2$, $(NBO)Si^*-(OSi)_3$, and $Si^*(OSi)_4$ (NBO = nonbonding oxygen), respectively. (See Scheme S1 in the Supporting Information to facilitate an understanding of these resonances.) The signals in the region of −109 ppm to −111 ppm comes from Q^4; −100 ppm to −102 ppm comes from Q^3; and resonances at approximately −92 ppm comes from Q^2. Table 3 shows the chemical shifts, deconvoluted peak areas, and silica network connectivity for each composition.

One of the most determinant factors concerning mesoporous structure and bioactive behavior of MBGs, is the role of Ca^{2+} cations as network modifiers through the decreasing SiO_2 network density (see Table 3). Figure 6a shows the ^{29}Si NMR spectra recorded by single-pulse (left) and $^1H \rightarrow ^{29}Si$ CP (right) analysis for the Si90Ca10 sample. SP ^{29}Si NMR spectrum shows two intense resonances, at −109.9 ppm and −100.7 ppm, corresponding to the Q^4 and $Q^3{}_H$ environments. In addition, there is a small shoulder at −91.8 ppm that could be assigned to $Q^3{}_{Ca}$, which is slightly more intense in the single-pulse spectrum (3.6 area %). More importantly, the proportion of Q^3 is lower in the environment close to protons (see the $^1H \rightarrow ^{29}Si$ CP spectrum), indicating that Ca^{2+} cations responsible of Q^3 units are mostly sited within the silica walls (that is, well-distributed within the SiO_2 network of the Si90Ca10 sample).

The single-pulse ^{29}Si NMR spectrum for Si85Ca10P5−20 °C shows resonances corresponding to Q^4, Q^3, and $Q^2{}_H$ (see Table 3 and Figure 3b). No significant differences were observed in the spectra of the Si85Ca10P5 sample that was evaporated at 30 and 40 °C. The signal at −93.1 ppm is mainly assigned to the $Q^2{}_H$ (not to $Q^3{}_{Ca}$) environment attending to these criteria: (1) Ca^{2+} cations are mainly entrapped as ACP and (2) the $^1H \rightarrow ^{29}Si$ CP spectrum shows this signal clearly emphasized. The small amount of free CaO (not entrapped as ACP) in this composition does not allow observing $Q^2{}_{Ca}$ environments when the spectrum is recorded by SP. However, $^1H \rightarrow ^{29}Si$ CP spectrum shows a small signal at −85.4 ppm assigned to the $Q^2{}_{Ca}$ environment, highlighting the presence of this species close to the protons sited at the material surface. Contrary to the Si90Ca10 sample, the Si85Ca10P5 sample evidences a much more disrupted network at the surface (16.0% and 83.7% of Q^4 units for the Si85Ca10P5 and Si90Ca10 samples, respectively). This is clearly indicative of the joint presence of Ca^{2+} and $PO_4{}^{3-}$, resulting in calcium

(37) MacKenzie, K. J. D.; Smith, M. E. *Multinuclear Solid-State NMR of Inorganic Materials*; Pergamon Press: Amsterdam, 2002.

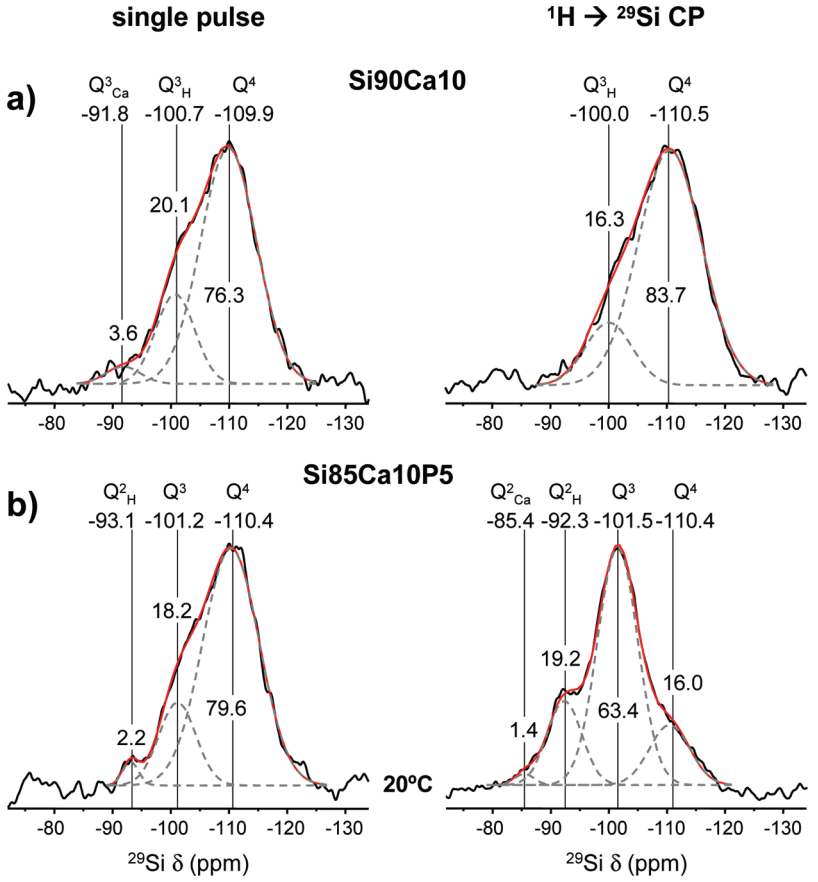

Figure 6. Solid-state ^{29}Si single-pulse (left) and cross-polarization (right) MAS NMR spectra of Si90Ca10 and Si85Ca10P5 (at 40 °C) samples. The areas for the Q^n units were calculated by Gaussian line-shape deconvolutions and are displayed by gray dotted lines (their relative populations are expressed as percentages).

phosphate clusters located at the wall surface, in agreement with the model previously reported for these types of materials.[33]

***In Vitro* Bioactivity Tests.** The surface reactivity of the mesoporous glasses was followed as a function of soaking time in SBF. *In vitro* bioactivity was assessed by analyzing the absorption band at the 560−600 cm^{-1} doublet in the FTIR spectra, corresponding to the phosphate formation in a crystalline environment. This method was proposed by Hench et al.,[35] and it is widely accepted for the assessment of bioactivity in SiO_2-based bioactive glasses. The Si100 and Si95P5 samples do not show bioactive behavior after one week in SBF (see Figure S4 in the Supporting Information). Figure 7 shows the FTIR spectra for the Si90Ca10 sample and the Si85Ca10P5 sample prepared at 20 and 40 °C (i.e., with *p6mm* hexagonal and $Ia\bar{3}d$ cubic structures). The Si90Ca10 sample (see Figure 7a) exhibits slow *in vitro* bioactive behavior under the conditions set for this study. After 24 h, a very weak absorption band is observed at 560 cm^{-1}, signifying the slight formation of amorphous calcium phosphate. After 7 days in SBF, a weak doublet at 560−600 cm^{-1} evidences the formation of a crystalline environment for the phosphate, which is indicative of the formation of an apatite-like phase. Si85Ca10P5−20 °C (Figure 7b) exhibits faster and more intense bioactive behavior. After 6 h, the singlet at 560 cm^{-1} is observed and only 8 h are needed for the observation of the PO_4^{3-} doublet, which is characteristic of the apatite formation. Figure 7c shows the *in vitro* bioactive behavior of the Si85Ca10P5−40 °C sample. As described previously, this sample is almost equivalent to the Si85Ca10P5−20 °C sample, with regard to the chemical composition and textural properties. In contrast, both samples show very different mesoporous structures. As can be observed from Figures 7b and 7c, the *in vitro* bioactive behaviors are almost identical. These results were confirmed with additional surface analyses with XRD, as a function of soaking time (see Figures S5 and S6 in the Supporting Information). In both cases, diffraction maxima can be assigned to the 211 and 002 reflections of an apatite phase that appear in the patterns without significant differences, in terms of peak intensity or profile.

Since the *in vitro* bioactive behavior results from the reaction between the material surface with the surrounding fluid, the ionic exchange between Ca^{2+} cations and H^+ from the SBF was determined. Figure 8 shows that a slight but significant $Ca^{2+}-H^+$ exchange can be observed for the Si85Ca10P5−40 °C sample, relative to the Si85Ca10P5−20 °C sample. These data signify that the pore ordering in bicontinuous cubic structures enhances the ionic exchange, relative to 2D hexagonal ones.

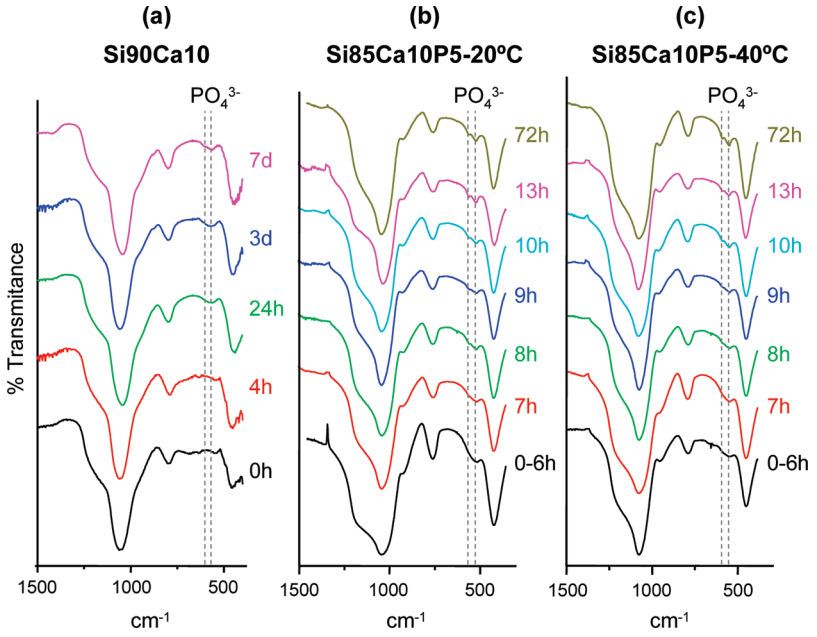

Figure 7. FTIR spectra obtained for the (a) Si90Ca10, (b) Si85Ca10P5−20 °C, and (c) Si85Ca10P5−40 °C samples soaked in SBF, as a function of time.

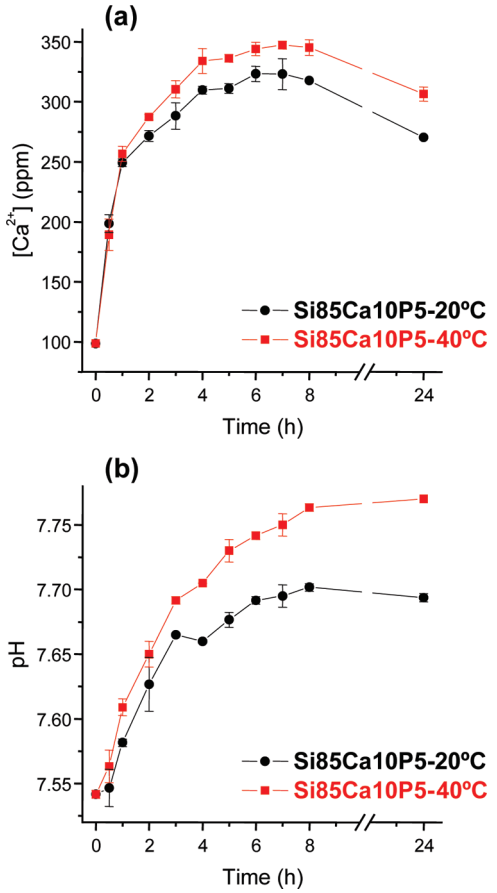

Figure 8. Variations of (a) Ca^{2+} content and (b) pH values of the SBF after soaking (−●−) the Si85Ca10P5−20 °C sample and (−■−) the Si85Ca10P5−40 °C sample.

Discussion

The results presented in this work demonstrate the fundamental role of amorphous calcium phosphate (ACP) on the mesoporous structure and bioactive behavior of SiO_2−CaO−P_2O_5 MBGs. In addition, the evaporation temperature during the EISA process seems to be an effective parameter to control the final mesostructure for a given ternary composition. Preparing ordered mesoporous glasses in a ternary system is not obvious. SiO_2−CaO−P_2O_5 contains both network formers (SiO_2 and P_2O_5) and a modifier (CaO) that disrupt the mesophase formation during the self-assembling of surfactant and inorganic species. For this reason, a more robust method, such as the EISA process, is required to prepare highly ordered materials in these systems. The EISA process occurs during the evaporation of the volatile solvent (in this case, ethanol) at low temperature (commonly "room temperature"). Our results demonstrate that strict control on the environmental conditions is required to prepare the desired MBGs.

In previous works, our research group has demonstrated that, by varying the CaO amount in SiO_2−CaO−P_2O_5, we can control the porous structure.[31] In this one, we demonstrate that, for the same composition ($85SiO_2$−$10CaO$−$5P_2O_5$, mol %), we can prepare MBGs with different mesoporous structures by changing the evaporation temperature within the 20−40 °C interval. The studies of the mesoporous structures of our materials demonstrates that, with the inorganic species/organic surfactant ratio used in this work, the systems exhibit a V_{inorg}/V_{org} ratio that was low enough to form hydrophobic structures with space groups such as $Ia\bar{3}d$. This is clear for highly dense inorganic phases exclusively prepared with network formers (SiO_2 and P_2O_5). The incorporation of 10% CaO (Si90Ca10), involves a lower connectivity index, as revealed by ^{29}Si NMR and, consequently, leads to inorganic phases with lower density. Because the V_{inorg}/V_{org} ratio increases in the Si90Ca10 composition, the mesophase arranges in a more hydrophilic structure that exhibits a 2D-hexagonal *p6mm* phase for any evaporation temperature.

On the other hand, the role of P_2O_5 is determinant in two aspects: mesoporous structure and bioactive behavior. In the case of the CaO-free composition (i.e., Si95P5), P_2O_5 is distributed as both PO_4 independent tetrahedrons within the silica network and polyphosphate chains at the silica surface. This second situation can be explained because of the slower hydrolysis of the P precursor (TEP), compared to the Si precursor (TEOS). Nevertheless, both situations involve a contribution to the network connectivity, resulting in hydrophobic 3D-cubic structures without bioactive behavior (i.e., the same situation as that for pure SiO_2 mesoporous material (Si100)). However, when P_2O_5 is part of the ternary system, its role changes completely. This is clear when comparing Si90Ca10 with Si85Ca10P5 MBGs. Si90Ca10 exhibits a 2D-hexagonal *p6mm* structure, as a consequence of the higher V_{inorg}/V_{org} ratio. Moreover, the combined studies of single-pulse and $^1H \rightarrow ^{29}Si$ CP NMR spectra indicate that Ca^{2+} cations are distributed within the inorganic silica walls but are not accumulated at the surface. In contrast, in the case of the Si85Ca10P5 sample, the presence of CaO and P_2O_5 leads to the formation of ACP clusters that are accumulated at the surface. In addition, the porous structure is not always 2D-hexagonal and is dependent on the evaporation temperature during the EISA process. Because Ca^{2+} is consumed to form ACP clusters, Ca^{2+} cations do not contribute to decrease SiO_2 connectivity and the hydrophobic 3D-cubic $Ia\bar{3}d$ phase can be formed, as a function of the evaporation temperature. It must be highlighted that 3D-cubic and 2D-hexagonal structures can coexist in the same material when an intermediate temperature (30 °C) is applied for evaporation. Certainly, ACP clusters also contribute to increase the inorganic volume. This is clear when calculating the wall thickness by N_2 adsorption porosimetry. However, the efficacy to create NBOs is lower than that provide by "free" Ca^{2+} cations. Consequently, hydrophobic phases can only occur at temperatures of < 30 °C.

The dependence of a mesoporous structure on the evaporation temperature can be explained in terms of a reduction of hydrogen interactions. In the case of nonionic triblock copolymers such as P123, the micelle size is strongly dependent on the hydrogen-bond interactions with the solvent, which becomes greater when hydrogen interactions are reduced. Consequently, the hydrophilic/hydrophobic ratio is reduced, favoring hydrophobic mesostructures such as cubic $Ia\bar{3}d$, as previously indicated by Zhao and co-workers for pure silica mesoporous materials obtained via the hydrothermal method.[38]

The main motivation for the synthesis and development of MBGs is their excellent bioactive behavior. In fact, the high textural properties of these compounds lead to long-term *in vitro* bioactivity, even for the calcium-free composition.[39] However, MBGs exhibit their maximum potential when CaO and P_2O_5 are both incorporated into the system. Recently, we have observed the fast kinetics of bonelike apatite formation onto these materials. For some compositions, < 1 h is sufficient for the nucleation of newly formed apatite under *in vitro* conditions.[32] To establish measurable differences between different compositions, we have set new conditions to increase the time for apatite crystallization. For this purpose, bioactivity tests were performed with MBG powders instead of compacted bodies, because the proximity of apatite nuclei enhances the apatite layer formation onto compact pieces. Under these conditions, important differences could be observed when comparing the binary system Si90Ca10 with the ternary composition Si85Ca10P5. The latest composition exhibits a much higher bioactive response, although the network former/modifier is identical. The difference is reflected in the local structure in both materials. The Si90Ca10 composition contains the Ca^{2+} cations distributed within the silica network, whereas the Si85Ca10P5 composition contains Ca^{2+} as calcium phosphate clusters at the wall surface. This involves two features: first, Ca^{2+} cations are more accessible to the surrounding fluids to initiate the bioactivity reaction cascade, and, second, the ACP clusters act as nucleation sites of the newly formed apatite.

By modifying the evaporation temperature of the Si85Ca10P5 composition, MBGs with the same composition and textural properties, but different porous structure, have been synthesized for the first time. In addition, MBGs with coexisting cubic and hexagonal phases have been isolated, as is the case of the Si85Ca10P5−30 °C sample. Recently, the influence of pore structure has been hypothesized as a factor that affects the bioactive behavior of MBGs. However, to date, different pore ordering in the SiO_2−CaO−P_2O_5 systems also has involved changes in molar composition and/or textural differences. Our bioactivity studies with 3D-cubic and 2D-hexagonal Si85Ca10P5 samples allow us to discriminate the pore array from other factors and show that differences in mesopore ordering are not determining the bioactive behavior of MBGs, when composition and texture are equivalent factors. Both *in vitro* bioactive processes exhibit equivalent behavior along the study, for 3D-cubic and 2D-hexagonal phases of the Si85Ca10P5 composition. The amount and accessibility of Ca^{2+} cations to the surrounding fluids, the presence of ACP clusters, the chemical composition, and the textural properties are the material-related factors that determine the *in vitro* bioactivity, independent of the mesopore ordering.

Conclusions

The mesoporous bioactive glass (MBG) $85SiO_2$−$10CaO$−$5P_2O_5$ (mol %) is formed by a silica network and amorphous calcium phosphate (ACP) clusters sited at the pore wall surface. In this system, the formation of hydrophilic 2D-hexagonal, hydrophobic 3D-cubic, or even mixed mesoporous structures is dependent on the solvent evaporation temperature.

The presence of CaO determines the *in vitro* bioactive behavior of multicomponent mesoporous glasses. Very

(38) Li, Z.; Chen, D. H.; Tu, B.; Zhao, D. Y. *Microporous Mesoporous Mater.* **2007**, *105*, 34–40.
(39) Izquierdo-Barba, I.; Ruiz-González, L.; Doadrio, J. C.; González-Calbet, J. M.; Vallet-Regí, M. *Solid State Sci.* **2005**, *7*, 983–989.

important kinetic differences are observed when Ca^{2+} cations are dispersed into the SiO_2 network or are forming segregated calcium orthophosphate clusters at the surface.

2D-hexagonal Si85Ca10P5 and 3D-cubic Si85Ca10P5 samples exhibit almost identical *in vitro* bioactive behavior, although a slight but significant $Ca^{2+}-H^{+}$ exchange can be observed for the bicontinuous cubic sample, with respect to the hexagonal one. This observation indicates that chemical composition, textural properties, and the presence of accessible ACP clusters determine the *in vitro* bioactive behavior, independent of the mesopore structure.

Acknowledgment. This work was supported by the Spanish CICYT (through Project No. MAT2008-00736) and by the Comunidad Autónoma de Madrid (through Project No. S-0505/MAT/0324). We also thank to the CAI Electron Microscopy Center, CAI Nuclear Magnetic Resonance and Fernando Conde (CAI X-ray Diffraction), Universidad Complutense de Madrid, for their valuable technical assistance.

Supporting Information Available: Nominal compositions and reactants used to prepare mesoporous materials in MBGs (Table S1). Isotherms of mesoporous materials in this work (Figures S1 and S2). NMR studies of the Si85Ca10P5 composition before calcination (Figure S3). Negative bioactivity tests for Si100 and Si95P5 samples (Figure S4). Powder XRD patterns of Si85Ca10P5 evaporated at 20 and 40 °C after soaking in simulated body fluid (SBF) (Figures S5 and S6). Schematic depiction of Q^n_H and Q^n_{Ca} assignments in solid-state ^{29}Si NMR (Scheme 1). (PDF) This material is available free of charge via the Internet at http://pubs.acs.org.

SUPPORTING INFORMATION

Nominal compositions and reactants used for the preparation of mesoporous materials in the systems SiO_2, SiO_2-P_2O_5, SiO_2-CaO and SiO_2-CaO-P_2O_5. The design of this experiment is based on the assumption that SiO_2 and P_2O_5 are network formers and CaO is a network modifier that disrupts the SiO_2 (or SiO_2-P_2O_5) network. All the syntheses were carried out with 16 g of P123, 4 mL of HCl 0.5 M and 240 mL of EtOH absolute. In this way, the ratio network formers: surfactant is kept constant for all the samples.

Table S1. Nominal composition (% mol) and amounts of reactants (g) of ordered mesoporous materials.

Sample	Nominal composition (% mol)	TEOS (g)	TEP (g)	$Ca(NO_3)_2 \cdot 4H_2O$ (g)
Si100	100 SiO_2	33.04	--	--
Si95P5	95 SiO_2 – 5 P_2O_5	29.60	2.72	--
Si90Ca10	90 SiO_2 – 10 CaO	32.72	--	3.92
Si85Ca10P5	85 SiO_2 – 10 CaO – 5 P_2O_5	29.60	2.72	3.92

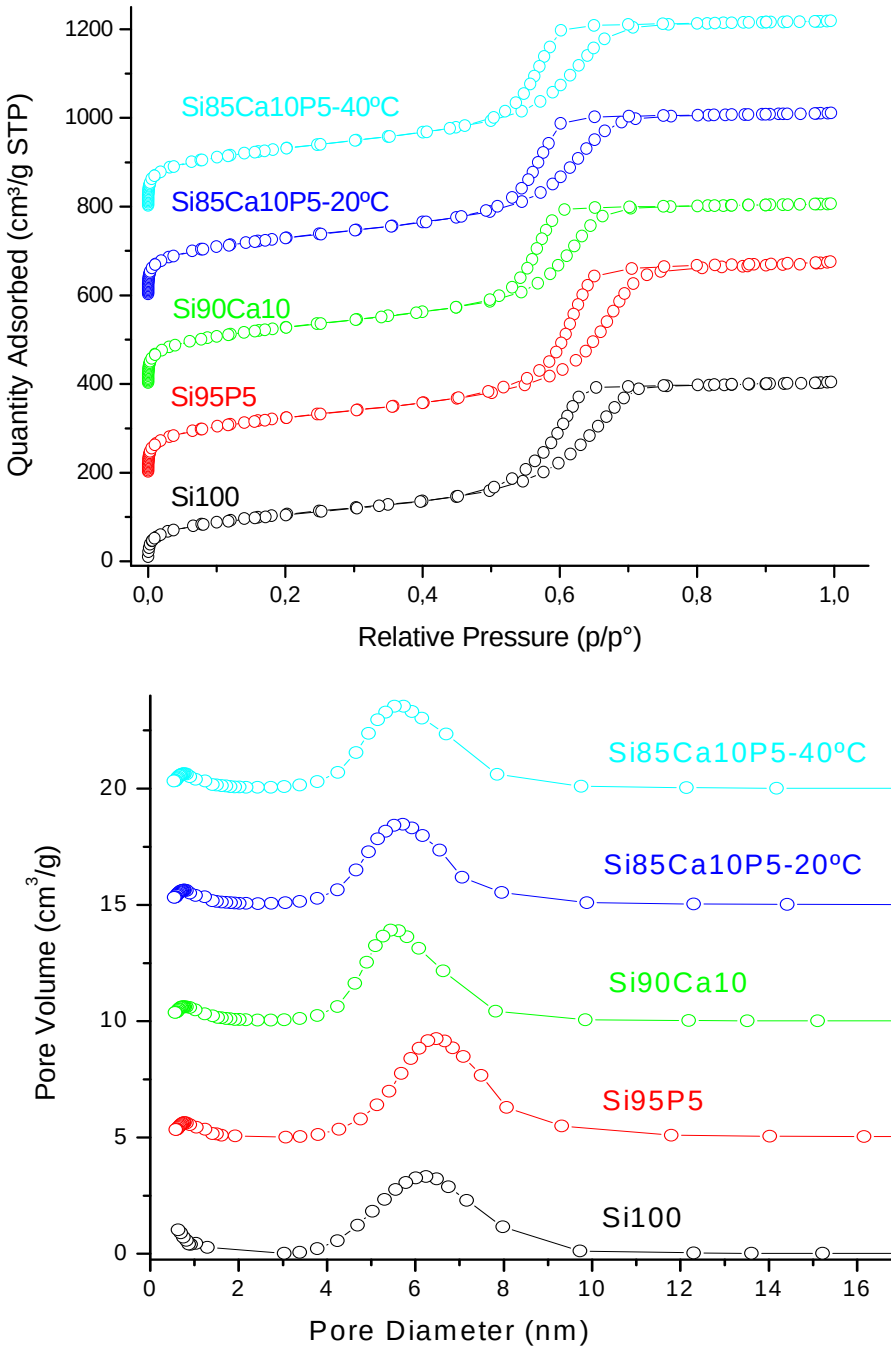

Figure S1. Top) N_2 adsorption isotherms of the mesoporous materials prepared in this work. Textural parameters calculated from these plots are displayed in Table 2 in the manuscript. Bottom) Pore size distribution of the different mesoporous materials prepared.

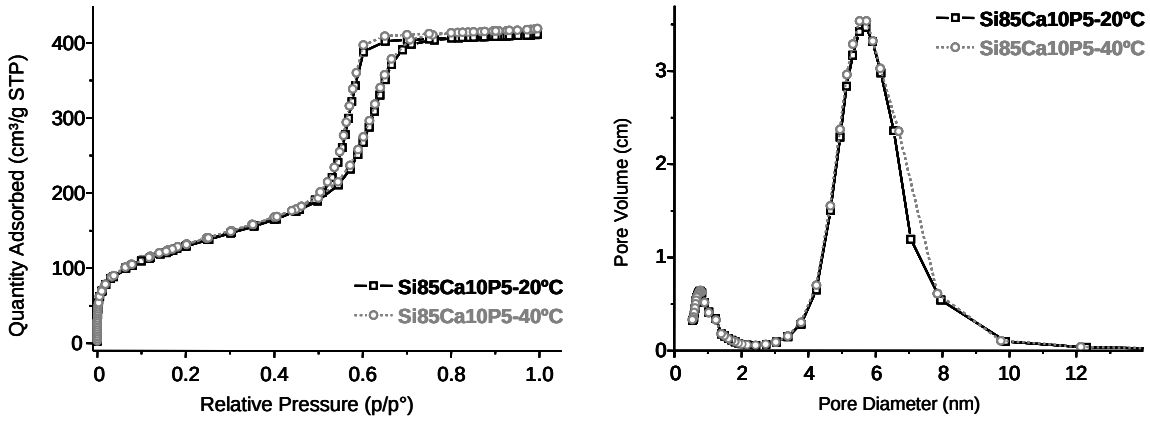

Figure S2. Adsorption isotherms and pore distribution for 2D-hexagonal (Si85Ca10P5-20ºC) and 3D-cubic (Si85Ca10P5-40ºC) materials. It can be observed that both plots are almost equivalent, pointing out the close similitude of textural properties presented by these samples.

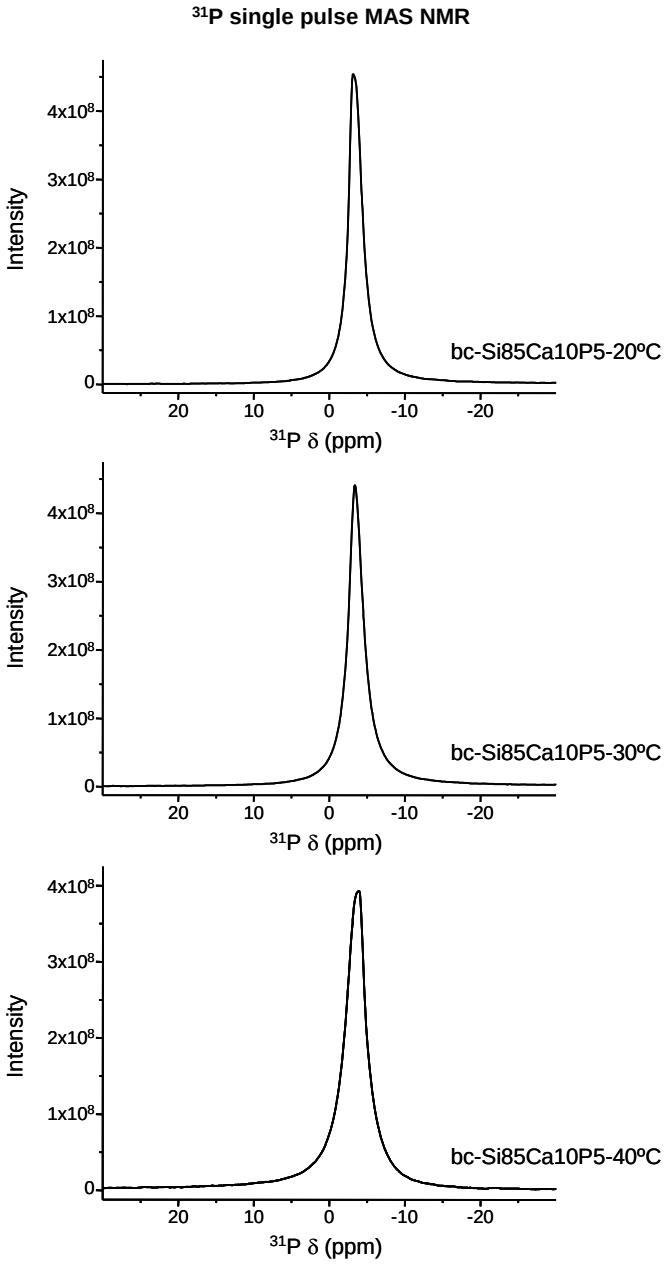

Figure S3. ^{31}P-NMR studies before calcinations for Si85Ca10P5 evaporated at 20, 30 and 40ºC. In the three cases, the phosphate units are assigned to q^0 environment, indicating that calcium orthophosphates are formed during the self-assembling.

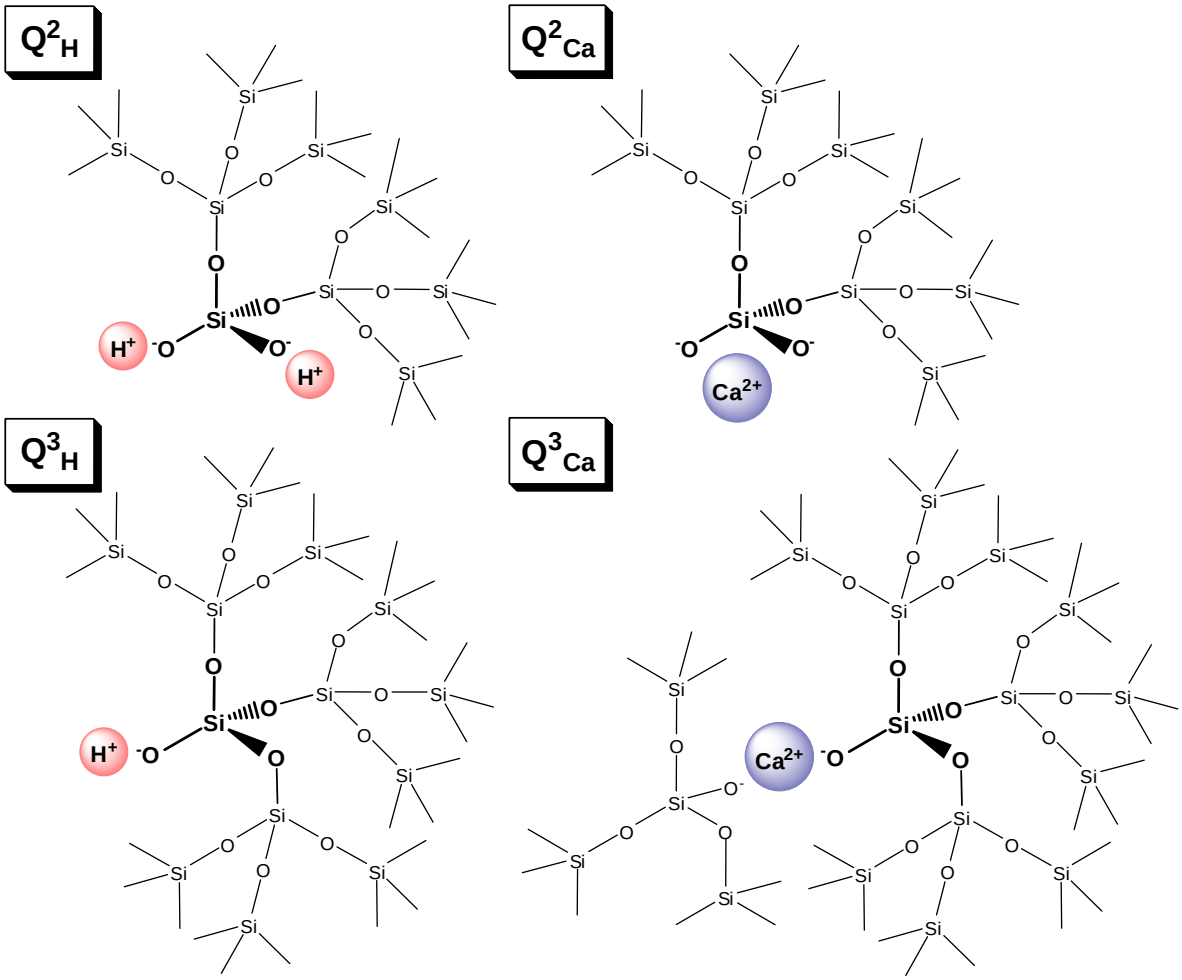

Scheme 1. Schematic view of Q^n_H and Q^n_{Ca} (n = 2, 3) assignments in solid-stage ^{29}Si MAS NMR.

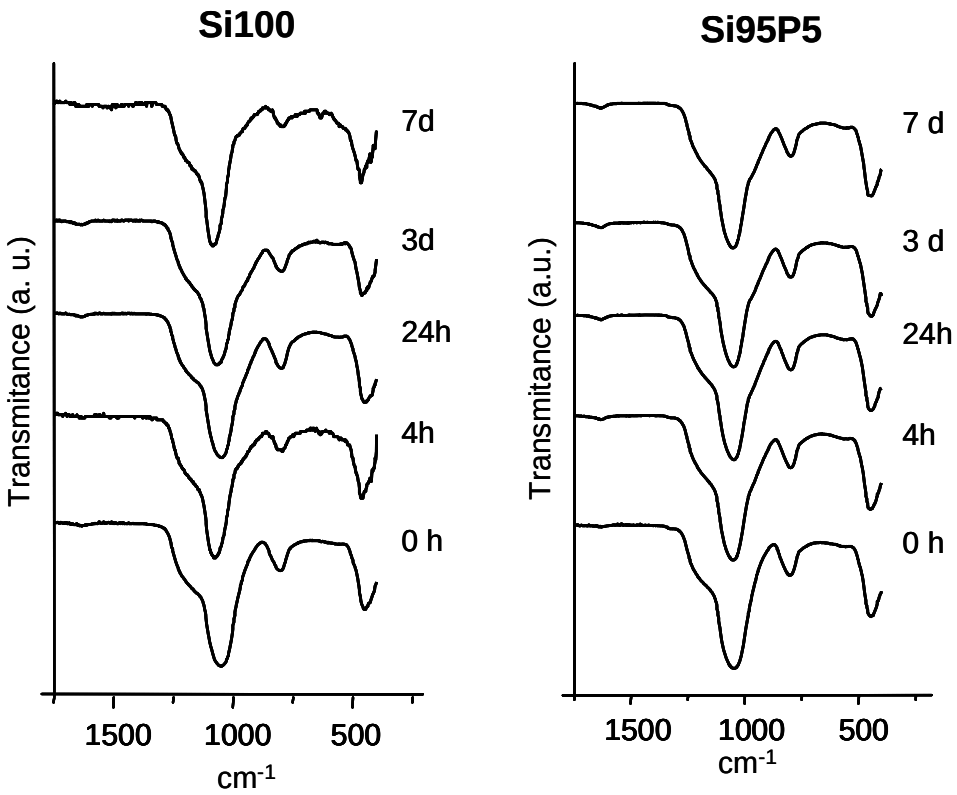

Figure S4. Negative bioactivity test for Si100 and Si95P5 samples.

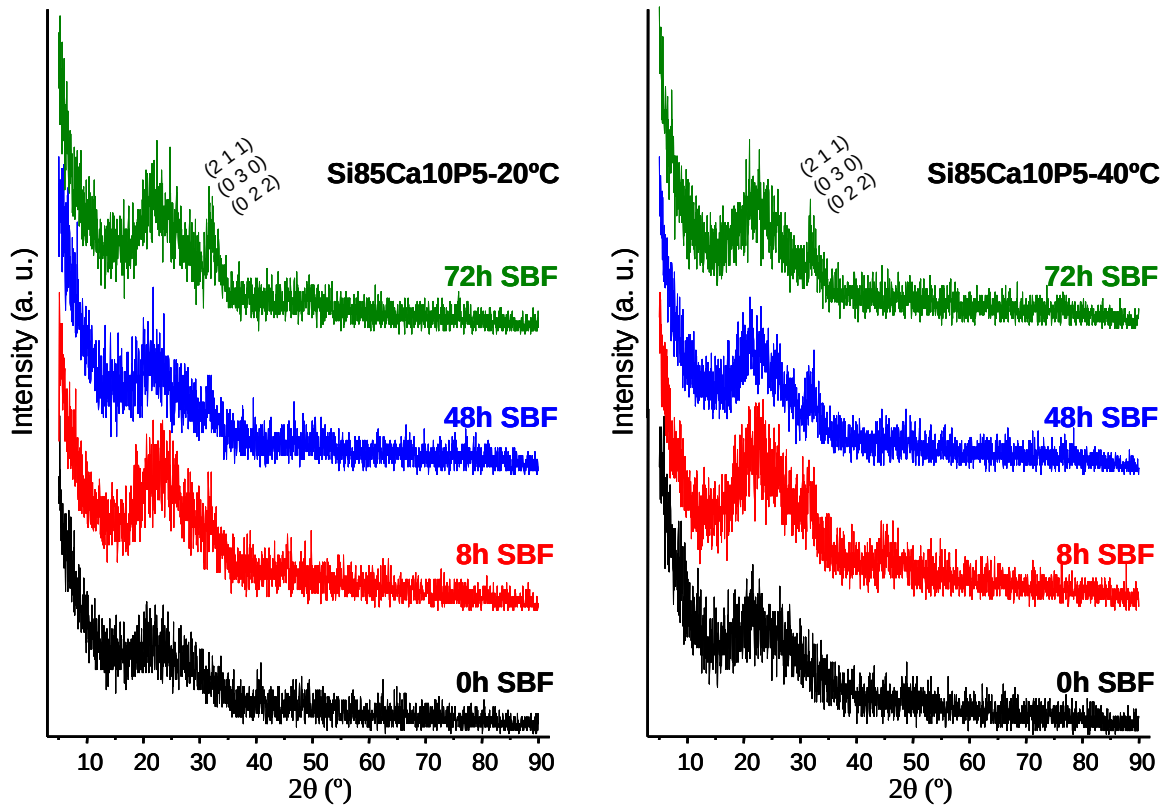

Figure S5. Powder XRD diffraction patterns of hexagonal (left) and cubic (right) Si85Ca10P5 collected before and after soaking in SBF for several times. The evolution of a new apatite like phase can be followed by the maxima centered at 2θ ≈ 32º. Similar behavior as a function of time is observed for both samples. XRD patterns were collected in the 2θ range between 5º and 90º with a step size of 0.04º and counting time of 1 s per step.

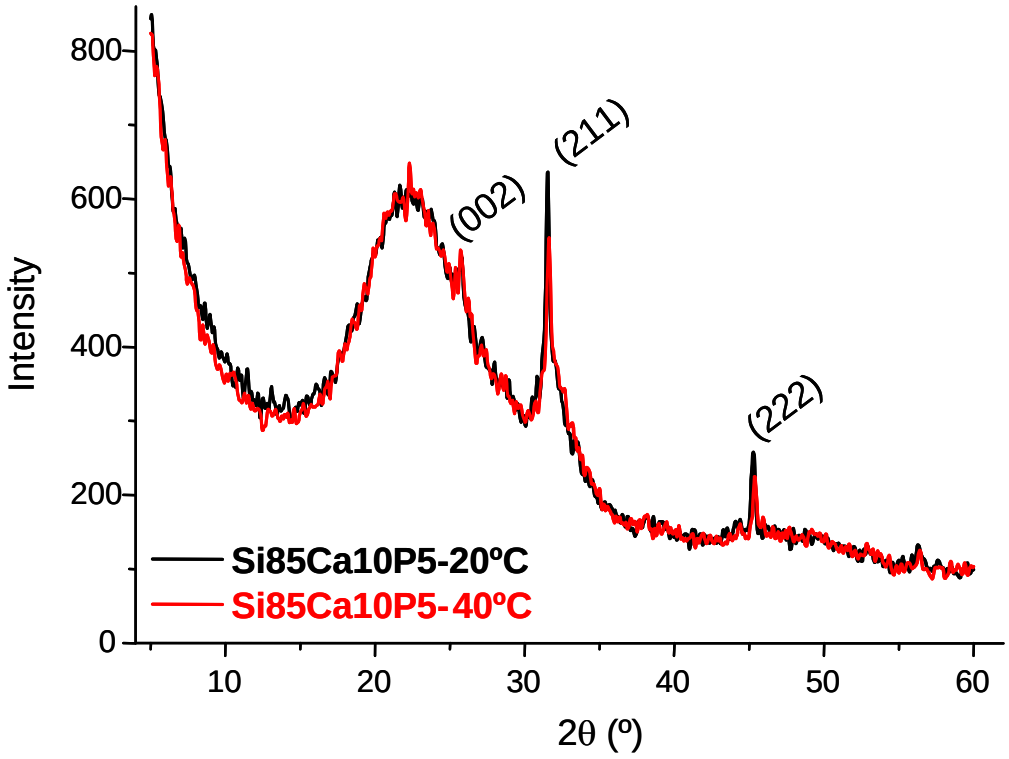

Figure S6. Powder XRD diffraction patterns for 2D-hexagonal (Si85Ca10P5-20ºC) and cubic (Si85Ca10P5-40ºC) samples after 8 hours soaking in SBF. XRD conditions measurements was modified increasing the counting time of 10 s per step. Similar behavior is observed for both samples.

En la actualidad los materiales *nanocomposites* formados por nanopartículas cristalinas distribuidas homogéneamente en matrices mesoestructuradas de naturaleza amorfa, son objeto de una intensa investigación, ya que combinan las propiedades de sus dos componentes, incrementando su funcionalidad más allá de la presentada por cada uno de ellos por separado [44,45]. La **Tabla 1.2.** muestra los ejemplos más representativos de estos *nanocomposites* propuestos en diferentes disciplinas, desde la electroquímica y la catálisis hasta su posible utilización como biomateriales en aplicaciones biomédicas. La **Figura 1.9.** representa a modo de ejemplo un *nanocomposite* formado por un material de sílice mesoporosa (SBA-15) y nanotubos de carbono (CNTs). Este material, debido a la sinergia entre sus componentes, exhibe una elevada proliferación de osteoblastos en su superficie junto con su capacidad para liberar el fármaco cargado [48].

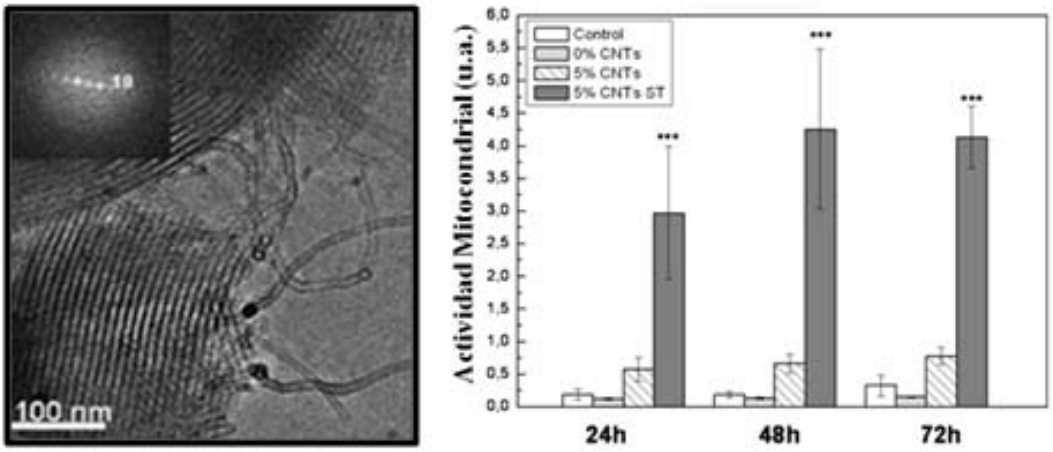

Figura 1.9. ***Nanocomposite*** **SBA-15/CNTs**. Izquierda: imagen de TEM mostrando su estructura. Derecha: respuesta de osteoblastos al *nanocomposite*. La sinergia de sus dos componentes induce una mejora considerable en la proliferación celular con respecto a la obtenida por cada uno de sus componentes por separado. Adaptada de la referencia [49].

Tabla 1.2. Ejemplos de materiales *nanocomposites* con diferentes aplicaciones

Nanocomposites	**Propiedades**	**Aplicaciones**	**Ref**
Sílice mesoporosa-NPs de Au	Conductividad de las NP de Au con propiedades ópticas y excelentes propiedades texturales de la sílice mesoporosa	Sensores y catálisis	[46]
Sílice mesoporosa-NPs de TiO_2	Propiedades antibacterianas del TiO_2 con la estabilidad térmica, porosidad y excelentes propiedades ópticas proporcionadas por la sílice mesoporosa	Capacidad de auto-limpieza y alta eficiencia fotocatalítica en reacciones en fase gaseosa	[47]
Sílice mesoporosa nanotubos de carbono	Conductividad eléctrica de los CNTs con las propiedades texturales y estructurales de la sílice mesoporosa	Biomateriales	[48]
Sílice mesoporosa-NPs de Fe_3O_4	Propiedades magnéticas de las NPs de hierro con las propiedades texturales y estructurales de la sílice mesoporosa	Biomateriales	[49,50]
Sílice mesoporosa-NPs de magnetita	Propiedades magnéticas del componente magnetita con la excelentes propiedades texturales de la sílice	Bioseparaciones magnéticas	[51]
Sílice mesoporosa-NPs de Ag	Propiedades antibacterianas de la Ag y las propiedades texturales y estructurales de la sílice mesoporosa	Biomateriales	[52]
Sílice mesoporosa-NPs de hidroxiapatita	Excelente biocompatibilidad de la HA con las propiedades texturales y estructurales de la sílice	Biomateriales	[53]
Carbono mesoporoso- NPs de MnO (Si) (ZrO_2)	Alta porosidad con conductividad eléctrica. Transporte del ion Li favorecido a través de los canales mesoporosos. Superior ciclavilidad. ZrO_2 NPs ofrece la posibilidad del anclaje estable de organofosfonatos.	Electroquímica Baterias Li	[54,55,56]

La síntesis de sistemas *nanocomposites* constituye una ardua tarea donde se requiere: (i) una distribución homogénea de ambos componentes preservando las propiedades intrínsecas de cada uno de ellos, (ii) gran capacidad de albergar la mayor cantidad posible de componente nanocristalino dentro de la matriz mesoporosa, (iii) control de la cristalinidad y de las propiedades texturales del material final, evitando el colapso de la mesoestructura durante el proceso de síntesis [44].

En general, se han descrito diferentes estrategias para la síntesis de estos *nanocomposites*, las cuales se esquematizan en la **Figura 1.10.** Una de ellas, denominada "*Brick and Mortar*", se basa principalmente en la incorporación de las nanopartículas (NPs) cristalinas preformadas durante el proceso de síntesis del componente mesoestructurado amorfo. En este caso, el surfactante se elimina bien por calcinación o bien por extracción, ya que la fase cristalina ha sido previamente formada [47,48]. Esta síntesis requiere un riguroso control del tamaño de las nanopartículas (NPs) para que sean compatibles con el tamaño del mesoporo resultante [47].

El segundo método de síntesis se basa en la incorporación de los precursores de ambos componentes a la vez, seguido de un proceso de cristalización de una de las fases mediante un proceso de calcinación [44]. Este método requiere un alto control en la formación de ambas fases (una amorfa y otra cristalina). En general, se requiere que los procesos sean más lentos con el fin de controlar la formación y una distribución homogénea de ambas fases. Por ello, se utiliza el método de evaporación de autoensamblaje inducido (EISA) [57], descrito en la sección anterior, ya que permite ralentizar los procesos de formación de ambas fases lo que conduce a una mayor homogeneidad de ambas. Asimismo, la naturaleza del surfactante también juega un papel fundamental en la homogeneidad de ambos componentes [47]. Se ha descrito que surfactantes con cadenas hidrofílicas más largas, permiten una mayor homogeneidad de estos sistemas al exhibir mayor superficie para la incorporación de las NPs.

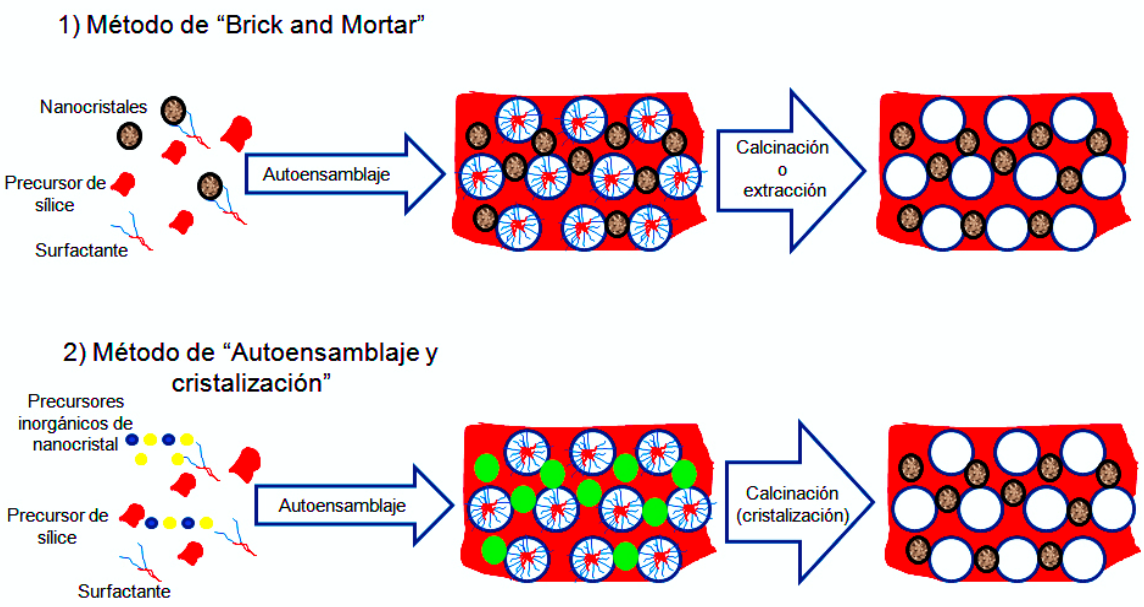

Figura 1.10. Estrategias de síntesis de materiales *nanocomposites*.

Respecto a las *biocerámicas de 3ª generación*, el rápido crecimiento de la *nanotecnología* en este campo ha aportado numerosos avances en el diseño de nuevas biocerámicas nanoestructuradas para regeneración ósea. Una biocerámica clave es la HA nanocristalina, la cual está recibiendo una considerable atención en el reemplazamiento y reconstrucciones de tejidos duros, debido a su cercana similitud con el componente mineral óseo, a sus propiedades osteoconductivas y a su excelente biocompatibilidad con respecto a otras biocerámicas [58,59,60,61].

Por otra parte, tal y como se ha indicado en la sección anterior, los vidrios bioactivos mesoporosos son materiales prometedores en regeneración ósea gracias a sus excelentes propiedades texturales y estructurales que permiten aceleradas cinéticas de bioactividad jamás mostradas por otro material. Su ordenamiento mesoporoso y su composición química (fundamentalmente la gran presencia de grupos silanoles) les confiere un valor añadido al poder actuar como reservorio de matrices de liberación controlada de moléculas biológicamente activas. En este sentido, el diseño de un sistema *nanocomposite* formado por partículas de HA nanocristalina embebidas uniformemente dentro de una red amorfa de un MBG, constituiría una mejora con respecto a cada uno de sus componentes por separado. Así, se combinarían sus

propiedades, e incluso se potenciarían las propiedades de la HA nanocristalina al quedar distribuidas dentro de una matriz amorfa con superficies específicas altas.

1.2. Sistema *nanocomposite* MGHA vidrio mesoporoso/hidroxiapatita: excelente candidato como biocerámica de tercera generación

Diferentes autores han descrito la síntesis de materiales *nanocomposite*s formados por nanocristales de HA y sílice mesoporosa, mediante la incorporación de partículas preformadas de HA durante el proceso de síntesis de la matriz mesoporosa amorfa de sílice. Sin embargo, los resultados mostrados sugieren una segregación de las fases, viendo comprometida la funcionalidad de estos materiales en futuras aplicaciones [53,62].

Teniendo en cuenta el proceso de síntesis de MBGs y la formación de *clusters* de ACP (precursor de HA) en sus paredes, parece lógico pensar que la aceleración de los procesos de cristalización de la HA durante la síntesis mediante una severa acidificación del sistema, podría ser una vía para obtener *clusters* de HA en lugar de ACP. Por ello, se ha incrementado la relación molar [HCl/TEOS + TEP] desde 0.013 a 0.287. La problemática que se platea es que al acelerar el proceso de cristalización de la HA, es posible que la estructura mesoporosa colapse quedando ambas fases distribuidas heterogéneamente. Por ello, con el fin de homogeneizar dicho sistema, se han introducido tres variables más durante la síntesis:

a) Cambio de la fuente de calcio, utilizando $CaCl_2$ en vez de $Ca(NO_3)_2$, ya que la fácil eliminación del $CaCl_2$ durante el proceso de calcinación evitaría el colapso de la estructura mesoporosa.
b) Aumento del volumen de etanol para ralentizar la formación del componente mesoestructurado y permitir una mayor integración de los nanocristales de HA dentro de la matriz amorfa.
c) Cambio del surfactante *P123* por *F127* con cadenas hidrofílicas más largas permitiendo una mayor homogeneidad del sistema.

El trabajo de investigación que se muestra a continuación describe la síntesis, caracterización y evaluación *in vitro* de la bioactividad y biocompatibilidad de un

material *nanocomposite* formado por nanocristales de HA embebidos homogéneamente dentro de la estructura de un vidrio mesoporoso de composición SiO_2-CaO-P_2O_5.

New Nanocomposite System with Nanocrystalline Apatite Embedded into Mesoporous Bioactive Glass. **M. Cicuéndez**, M.T. Portolés, I. Izquierdo-Barba, and M. Vallet-Regí. ***Chemistry of Materials 2012, 24, 1100-1106.***

El proceso de síntesis del material *nanocomposite* se ha optimizado a partir de la síntesis de un MBG [2]. Concretamente, la composición molar elegida ha sido la 85SiO_2-10CaO-5P_2O_5 (**Si85**), por sus propiedades bioactivas. A partir de ella, se han ido variando diferentes parámetros, los cuales se recopilan en la **Tabla 1.3.** Para confirmar, el éxito de la síntesis, los materiales calcinados fueron caracterizados por TEM.

Tabla 1.3. Composición molar de reactivos utilizados en las diferentes síntesis del material *nanocomposite,* en comparación con la del MBG 85SiO_2-10CaO-5P_2O_5 (Si85).

Material	Surfactante	HCl	TEOS	TEP	Fuente de calcio	Etanol
MBG (Si85)	*P123* 2.76×10^{-3}	2.0×10^{-3}	0.141	0.015	$Ca(NO_3)_2{\cdot}4H_2O$ 0.016	5.22
$MGHA_1$	*P123* 2.76×10^{-3}	0.045	0.141	0.015	$Ca(NO_3)_2{\cdot}4H_2O$ 0.016	5.22
$MGHA_2$	*P123* 2.76×10^{-3}	0.045	0.141	0.015	$CaCl_2{\cdot}4H_2O$ 0.016	6.52
$MGHA_3$	*F127* 1.38×10^{-3}	0.045	0.141	0.015	$CaCl_2{\cdot}4H_2O$ 0.016	6.52

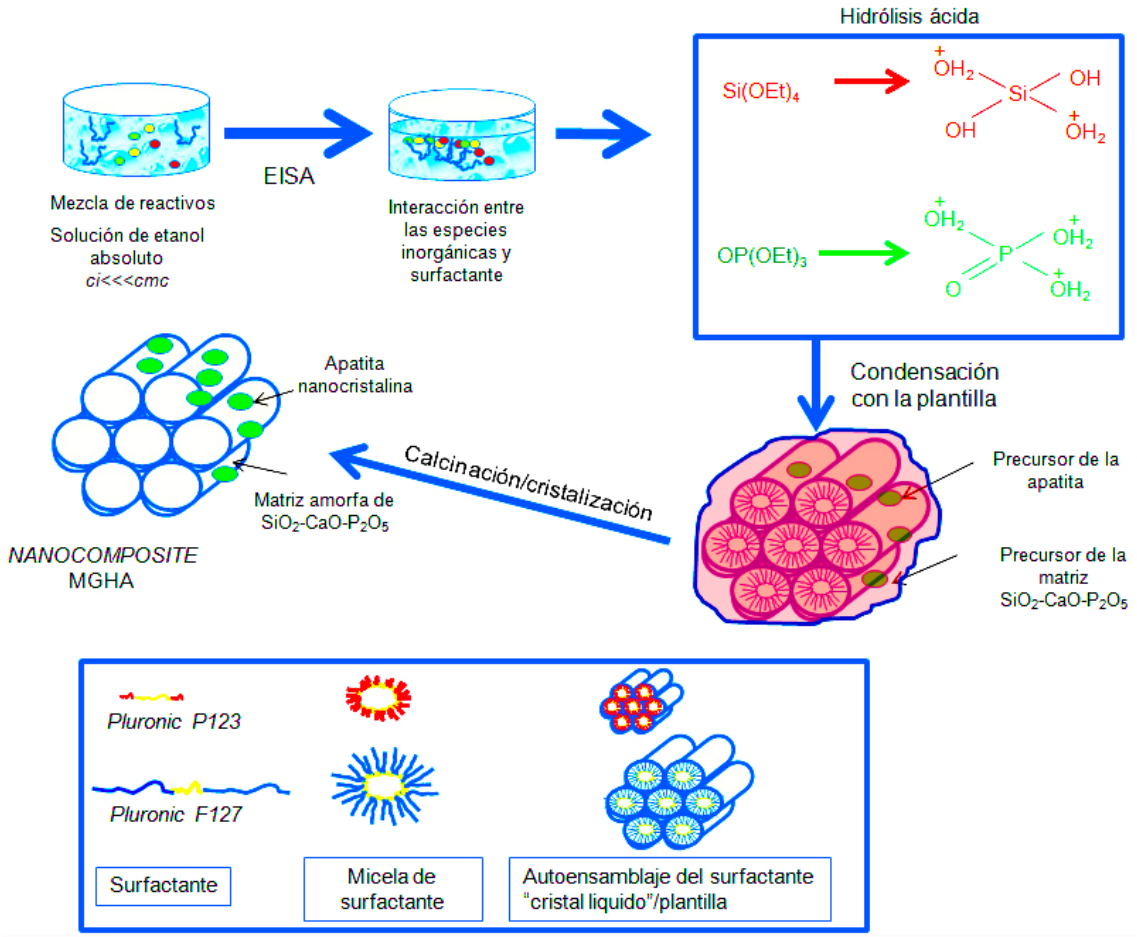

Figura 1.11. Proceso de síntesis del material *nanocomposite* MGHA. Esquema comparativo entre el surfactante *P123* y *F127* con cadenas hidrofílicas más largas que permiten una mayor integración de los nanocristales de HA en la red mesoporosa.

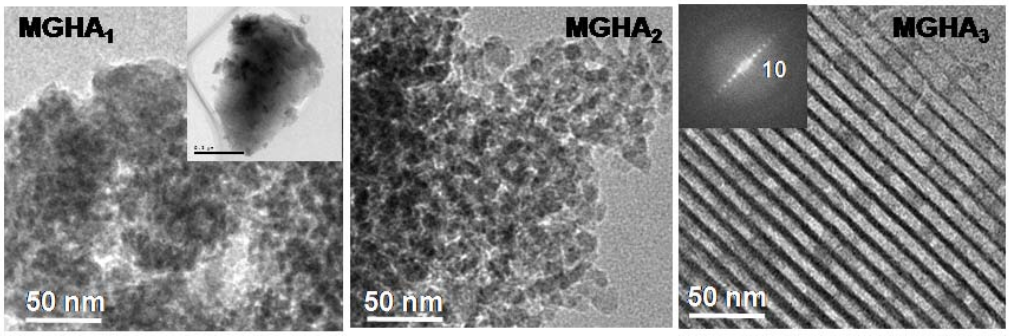

Figura 1.12. Imágenes de TEM correspondientes a los materiales $MGHA_1$, $MGHA_2$ y $MGHA_3$.

La **Figura 1.12.** muestra los resultados por TEM de los diferentes materiales mostrados en la **Tabla 1.3.** Las imágenes de TEM de las muestras $MGHA_1$ y $MGHA_2$ ponen de manifiesto una distribución heterogénea de ambas fases, con colapso de la estructura mesoporosa. Estos resultados evidencian que el aumento de la acidez del sistema es suficiente para la formación de HA nanocristalina. Sin embargo, su formación interfiere en la de la estructura mesoporosa, colapsándola. Por el contrario, los resultados de TEM de la muestra $MGHA_3$, en la cual se ha utilizado *F127* como agente director de la estructura, muestran una estructura mesoporosa en el sistema 2D-hexagonal con partículas de contraste más oscuro correspondientes a una fase apatita. Estas partículas están distribuidas homogéneamente dentro de la red mesoporosa. Los resultados ponen de manifiesto que la utilización de *F127* con cadenas hidrofílicas más largas que el surfactante *P123* permite una mejor incorporación de los cristales de HA formados, aumentando la homogeneidad del sistema, tal y como se ha reportado para otras composiciones de *nanocomposites* [47].

El artículo ***Chem. Mater. 2012, 24, 1100-1106***, mostrado a continuación, comprende una completa caracterización físico-química del material $MGHA_3$, por diferentes técnicas: DRX, TEM, RMN, Adsorción/Desorción de N_2, FTIR, XRF y análisis químico elemental. Para simplificar la nomenclatura, el material sintetizado se ha denominado MGHA. Dicha caracterización se ha realizado con el fin de determinar la estructura completa del material y poder así entender mejor las propiedades finales de éste. Los resultados obtenidos evidencian el éxito de la síntesis mostrando un material mesoestructurado con canales distribuidos en un sistema 2D-hexagonal, donde se encuentran embebidas partículas de apatita nanocristalina. El comportamiento bioactivo y la biocompatibilidad del material *nanocomposite* MGHA, fueron estudiados *in vitro* de forma comparativa con los vidrios bioactivos mesoporosos. Los ensayos de bioactividad muestran una rápida formación de la fase apatita, después de 8 horas de ensayo, similar a la mostrada por los vidrios bioactivos mesoporosos. La respuesta celular al material *nanocomposite* fue evaluada a través de diferentes parámetros: proliferación, morfología, viabilidad y apoptosis celular, utilizando como líneas celulares fibroblastos L929 y osteoblastos Saos-2. Los resultados obtenidos muestran elevados valores de proliferación de los dos tipos celulares en presencia del material MGHA, no existiendo diferencias significativas entre las células tratadas y los cultivos control en ausencia del material ($p > 0.05$). Estudios previos utilizando vidrios

bioactivos mesoporosos, con la misma composición $85SiO_2$-$10CaO$-$5P_2O_5$, también mostraron resultados de biocompatibilidad satisfactorios. Sin embargo, en dichos estudios se observó un efecto citostático, basado en la reducción de la proliferación celular [63]. La ausencia de este efecto citostático cuando el material MGHA se añadió a los cultivos celulares puede ser debido a la presencia de la apatita nanocristalina distribuida en la red mesoporosa amorfa, confirmando que las células son suficientemente sensibles a cambios a nivel de escala atómica [59].

El conjunto de todos los resultados obtenidos pone de manifiesto que este nuevo material *nanocomposite* ofrece una sinergia de sus dos componentes, vidrio bioactivo mesoporoso y apatita nanocristalina, mejorando las propiedades de cada componente y convirtiéndolo en un potencial candidato para regeneración tisular ósea.

CHEMISTRY OF MATERIALS

Article

pubs.acs.org/cm

New Nanocomposite System with Nanocrystalline Apatite Embedded into Mesoporous Bioactive Glass

Mónica Cicuéndez,[†,‡] María Teresa Portolés,[§] Isabel Izquierdo-Barba,*[,†,‡] and María Vallet-Regí*[,†,‡]

[†]Departamento de Química Inorgánica y Bioinorgánica, Facultad de Farmacia, Universidad Complutense de Madrid, Plaza Ramón y Cajal s/n, 28040 Madrid, Spain

[‡]Networking Research Center on Bioengineering, Biomaterials and Nanomedicine (CIBER-BBN), Madrid, Spain

[§]Department of Biochemistry and Molecular Biology I, Faculty of Chemistry, Universidad Complutense de Madrid, Ciudad Universitaria s/n, 28040-Madrid, Spain

Supporting Information

ABSTRACT: Crystalline nanoparticles are very attractive building blocks for the preparation of nanostructured materials. These particles can be dispersed in different noncrystalline mesostructured matrixes in order to obtain *nanocomposite* systems which combine the properties of both components broadening their functionality. In the present study, a novel *nanocomposite* bioceramic formed by nanocrystalline apatite particles uniformly embedded into a mesostructured $SiO_2-CaO-P_2O_5$ glass wall has been synthesized through the evaporation-induced self-assembly (EISA) method, commonly used for mesoporous bioactive glass synthesis, but accelerating the sol–gel apatite crystallization rate by strong acidification. Moreover, the use of F127 surfactant as a structure directing agent in this synthesis has allowed the homogeneous nanocrystalline apatite particles incorporation inside of the amorphous mesoporous glass. *In vitro* bioactive assays have shown a fast apatite-like phase formation similar to that exhibited by mesoporous bioactive glasses. Furthermore, the response of L929 fibroblasts and Saos-2 osteoblasts to this new *nanocomposite* has indicated a significant improvement in its biocompatibility compared with conventional mesoporous bioactive glasses.

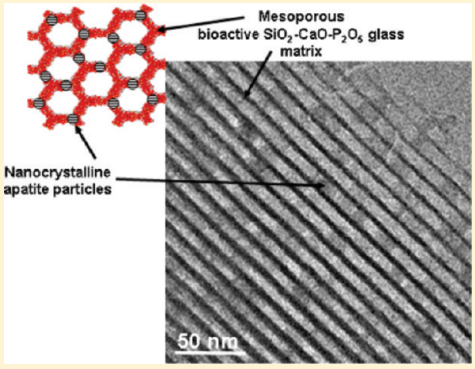

KEYWORDS: *nanocomposite system, nanocrystalline apatite particles, mesoporous bioactive glasses, biocompatibility, cell response*

1. INTRODUCTION

A great challenge for the scientific community in the field of biomaterials is the design of novel and advanced third generation bioceramics which promote bone tissue regeneration, accelerating the healing processes.[1,2] The rapid growth of nanotechnology has allowed numerous advances in this field since nanosized and nanocrystalline bioceramics clearly represent a promising class of orthopedic and dental implant formulations with improved biological and biomechanical properties.[3−5] In this sense, nanocrystalline hydroxyapatite constitutes a revolutionary bioceramic with better properties than coarser crystals.[6] Furthermore, due to its close similarities with bone mineral component, bioactivity, exceptional biocompatibility, and osteoconduction, this nanobioceramic receives considerable attention in hard tissue replacement and reconstruction applications.[6,7]

On the other hand, mesostructured bioactive glasses (MBGs) have recently been suggested as excellent candidates for bone tissue regeneration.[2,8−10] Their structural and textural properties offer higher surface/volume ratios and a chemical synergistic effect which provoke the most accelerated bioactive kinetics shown up to date. Moreover, their mesoporous arrangement and chemical composition confer them the ability to act as excellent matrixes for local drug delivery.[11−14]

"*Nanocomposite systems*" in which nanocrystals are dispersed in different noncrystalline matrixes are currently the subject of intensive research activity because they combine the properties of both components, thus broadening their functionality beyond the pure materials.[15,16] To guarantee such functionality, the synthesis process of such systems requires a homogeneous distribution of both components, preserving the intrinsic characteristics of each constituent. In this sense, the design of a *nanocomposite* material formed by nanocrystalline apatite particles embedded into an MBG mesoporous wall would allow to obtain a novel third generation bioceramic with an enhanced functionality. Several routes toward the preparation of silica mesoporous–apatite composite have been explored.[17−21] The most common methods are based in grafting apatite precursors on preformed silica mesoporous material or coating apatite particles with mesoporous silica films. However, such routes do not satisfy the requirements for preserving the properties of

Received: November 16, 2011
Revised: February 21, 2012
Published: February 22, 2012

both components, and the materials obtained in the process present very heterogeneous distribution and phase segregation.[19−21]

Exploring new routes to obtain this new *nanocomposite* and taking into account that during the synthesis of evaporation-induced self-assembly (EISA)-derived MBGs, *clusters* of amorphous calcium phosphate (ACP) are formed into the mesoporous wall;[22,23] a modification of such process in order to increase the crystallinity of this ACP to apatite could be an alternative. However, the incorporation of nanocrystalline particles into noncrystalline matrixes is a challenging task where the surfactant plays an important role. Thus, the use of F127 surfactant, whose molecules are larger in the hydrophilic region than Pluronic P123, produces a homogeneous distribution of the nanocrystalline particles into amorphous mesoporous matrixes, avoiding phase segregation, as it has been demonstrated in other nanocomposite systems.[24]

Therefore, in the present study, we report the synthesis of a *nanocomposite* material (MG-HA) formed by nanocrystalline apatite particles embedded into SiO_2−CaO−P_2O_5 mesoporous glass. The synthesis has been carried out through EISA method using F127 as surfactant in very acidic conditions, which will lead to acceleratation of the crystallization rate of sol−gel apatite. A deep physicochemical characterization of MG-HA material has been performed to determine its final properties. On the other hand, its *in vitro* bioactive response as well as its biocompatibility on both murine L929 fibroblasts and human Saos-2 osteoblasts have been evaluated.

2. EXPERIMENTAL SECTION

2.1. Synthesis of MG-HA *Nanocomposite*. Highly mesostructured *nanocomposite* (MG-HA) material formed by nanocrystalline apatite particles embedded into SiO_2−CaO−P_2O_5 mesporous glass wall has been synthesized through the evaporation-induced self-assembly (EISA) method[25] using a nonionic surfactant, Pluronic F127 (BASF), and tetraethyl orthosilicate (TEOS, 98%, Sigma−Aldrich), triethyl phosphate (TEP, 99.8%, Sigma−Aldrich), and calcium chloride[26] ($CaCl_2.4H_2O$, 99%, Sigma−Aldrich) as SiO_2, P_2O_5, and CaO sources, respectively. The synthesis of the *nanocomposite* MG-HA material is based mainly on the synthesis of MBGs in the SiO_2−CaO−P_2O_5 system[9] but with specific modifications: (i) by an increase of molar ratio of [HCl/TEOS + TEP] from 0.013 to 0.287, which will lead to an acceleration in the hydrolysis of different alkoxides as well as the sol−gel apatite crystallization[28−30] and (ii) the use of surfactant Pluronic F127 instead of Pluronic P123 to facilitate the incorporation and homogeneous distribution of nanocrystalline apatite nanoparticles within the amorphous mesostructured glassy matrix. In this synthesis, the evaporation self-assembly starts with a homogeneous solution of nanocomposite precursors and surfactant prepared in ethanol/water solvent with $c_0 \ll$ cmc, with cmc being the critical micellar concentration. The concentration of the system is progressively increasing by ethanol evaporation which drives to self-assembly of silica−surfactant micelles and further organization into liquid crystalline mesophase. This process goes at 30 °C in air atmosphere.[25]

A mesoporous material containing only silica and denoted Si100 sample has also been synthesized in the same conditions in order to compare with MG-HA (see summary characterization in Supporting Information, S1). Briefly, 19.5 g of F127 was dissolved in 168.6 mL of absolute ethanol (99.5%, Panreac) with 12.8 mL of 1.0 M HCl (prepared from 37% HCl, Panreac) solution and 19.4 mL of Milli-Q water. Afterward, the appropriate amounts of TEOS, TEP, and $CaCl_2$ were added in 1 h intervals under continuous stirring during 4 h at 40 °C and subsequently maintained in static conditions at the same temperature overnight. Note that, to prepare Si100 sample, only TEOS was added in the synthesis process. The resulting sols were cast in Petri dishes (9 cm diameter) to undergo the EISA method at 30 °C.

Table 1. Amounts of Reactants Used in the Synthesis of MG-HA Material[a]

Reactants					
TEOS (mL)			TEP (mL)	$CaCl_2$ (g)	
37.2			2.6	2.1	
Final composition					
χ_{Si}[b]	χ_{Ca}[b]	χ_P[b]	stoichiometric formula[c]	Cl (wt%)[d]	C (wt%)[e]
0.86	0.08	0.05	$Ca_{0.09}SiP_{0.06}O_{2.24}$	0.00	0.17

[a]Final composition analyzed by XRF and elemental chemical analysis. [b]Final composition analyzed by XRF where χ_E corresponds to the atomic fraction of the E element. [c]Stoichiometric formula normalized to Si from the composition analyzed by XRF. [d]Percentage of chlorine analyzed by XRF. [e]Percentage of carbon analyzed by elemental chemical analysis.

The gelation process occurred after 3 days, and the gels were aged for 7 days in the Petri dishes at 30 °C. Finally, the dried gels were removed as homogeneous and transparent membranes (several hundreds of micrometers thick) and calcined at 700 °C during 6 h to remove the surfactant, organics residue, and chloride ions. Table 1 displays the amount of each reactive as well as the final composition of MG-HA material determined by X-ray fluorescence (XRF) in a Philips PANalytical AXIOS spectrometer (Philips Electronics NV) where the X-rays were generated using an Rh Kα source at k = 0.614 Å and CHNS elemental chemical analysis in a Perkin-Elmer 2400CHNS thermo analyzer. The obtained results show a composition in very good agreement with the nominal composition and the total elimination of organic material and chlorides.

A deep physic-chemistry characterization of the synthesized material has been carried out by X-ray diffraction (XRD) and transmission electron microscopy (TEM), solid-state nuclear magnetic resonance (NMR), N_2 adsorption, and Fourier transform infrared spectroscopy (FTIR). Moreover, the *in vitro* response concerning bioactivity and in vitro biocompatibility in the presence of murine L929 fibroblasts or human Saos-2 osteoblasts of this synthesized material has been also performed. The details of such characterization are shown in Supporting Information.

3. RESULTS AND DISCUSSION

Figure 1A displays a small-angle XRD pattern corresponding to MG-HA material demonstrating the presence of mesoporous

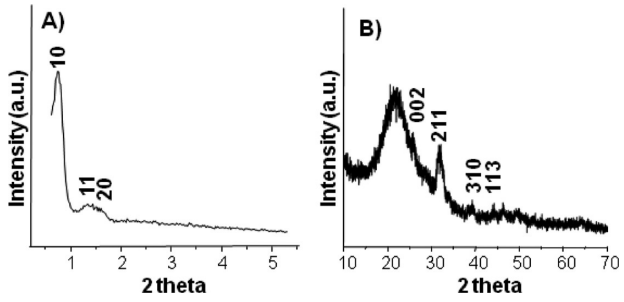

Figure 1. (A) Small-angle and (B) low-angle XRD patterns of calcined MG-HA material.

arrangement. XRD diffractogram shows a well-defined diffraction maximum at 2θ = 0.71 degree and wide maxima around 2θ = 1.36 and 1.56 degree, which can be indexed as 10, 11, and 20 reflections of a 2D-hexagonal structure,[31] according to TEM results. Wide angle XRD pattern (Figure 1B) reveals the presence of nanocrystalline apatite phase exhibiting very broad (002), (211), (310), and (113) reflections.[32,33] These data indicate that the inorganic framework may exhibit

dx.doi.org/10.1021/cm203416x | *Chem. Mater.* 2012, 24, 1100−1106

nanocrystalline apatite domains. However, on the basis of this evidence alone, the possibility that these nanocrystalline domains are associated with a phase separation cannot be strictly excluded. An important technique to resolve this question and with particular value for the characterization of mesoscopically ordered semicrystalline inorganic framework is TEM. Figure 2A shows a typical image of a 2D-hexagonal

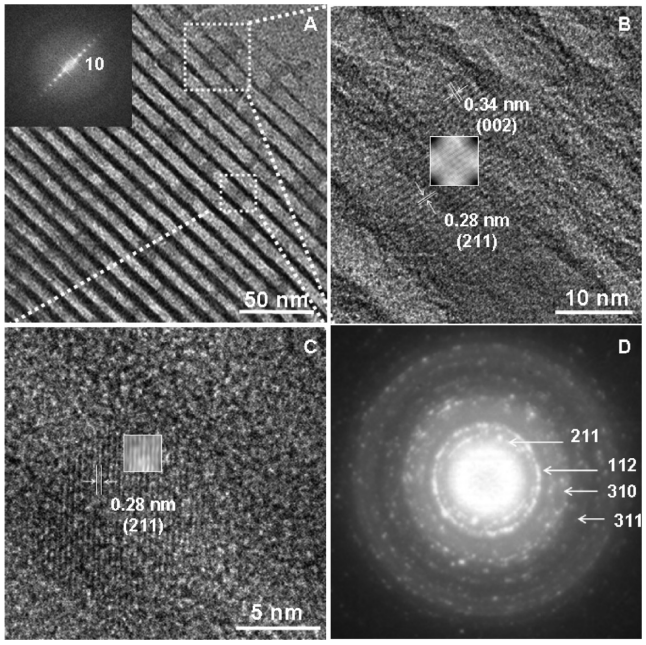

Figure 2. TEM study corresponding to MG-HA material. (A) Low magnification TEM image and its FT pattern with the electron beam perpendicular to the pore arrangement of a 2D hexagonal structure. (B, C) Higher resolution TEM images corresponding to the darker contrasts, showing lattice spacing at 0.28 and 0.34 nm apatite phase. (D) The selected area ED pattern of MG-HA material.

structure taken with the electron beam perpendicular to the channels, revealing the presence of dark contrast ovoid particles around 12 × 9 nm which are homogeneously distributed throughout the mesoporous wall. High resolution TEM images of two of these particles (Figure 2B,C) show lattice spacings at 0.34 and 0.28 nm, corresponding to the reflections (002) and (211) of apatite phase, according to the results by XRD (Figure 1B). Moreover, selected-area electron diffraction pattern (ED) recorded on MG-HA material, showing characteristic diffuse electron diffraction rings (Figure 2D), confirms that the wall of this material is made by nanocrystalline apatite particles uniformly embedded in a continuous amorphous glassy inorganic matrix.

In order to determine at the atomic level the chemical environment of the various constituents of the MG-HA sample, a study by NMR solid state has been carried out. Figure 3 shows the ^{31}P and ^{29}Si NMR spectra obtained by single pulse (SP) and cross-polarization (CP) under MAS conditions. Moreover, Table 2 shows the relative populations (expressed as percentages) of Q^n for ^{29}Si units, which have been obtained by deconvolution of the experimental spectra. Concerning ^{31}P NMR, SP spectrum shows an intense signal at 2.1 ppm, having a full width at half-maximum height (fwhm) around 4.02 ppm. This chemical shift could be assigned to q^0 enviromental of typical nanocrystalline apatite as it has been previously reported by Lin et al.[34] Although this assignment could have some

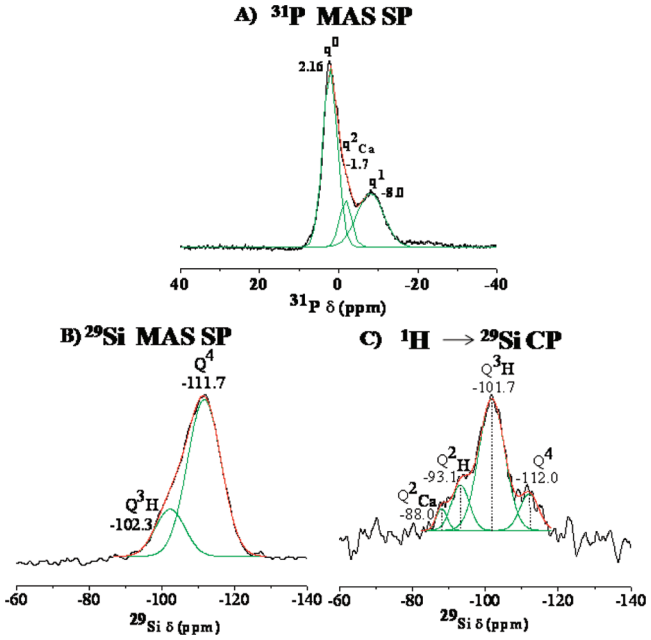

Figure 3. (A) Solid-state ^{31}P single pulse and (B, C) ^{29}Si single-pulse and cross-polarization MAS NMR spectra (with their q^n and Q^n phosphorus and silicon environments, respectively). The areas for the Q^n and q^n units were calculated by Gaussian line-shape deconvolutions.

controversy compared to Jäger et al., who attributed the same chemical shift with lower fwhm value (around 2.3 ppm) to nanocrystalline apatite,[35] XRD and TEM results reveal the nanocrystalline nature of these particles. Moreover, the small particle size of nanocrystalline apatite observed by TEM could explain that the signal found in MG-HA is broader than that observed by Jäger et al., where a nanocrystalline apatite with a particle size of 10 nm of diameter and 30−50 nm of length was studied.

Furthermore, a less intense second signal around −8 ppm was observed. This signal falls within the range typically found for ^{31}P in q^1 tetrahedral and may as such conform to either of the P−O−X (X = P, Si) scenarios.[36] Similar ^{31}P signals have been reported as P−O−Si in mesoporous bioactive glasses.[22,23,37] Moreover, the spectrum displays a very weak signal around −1.7 ppm, which could be assigned to dicalcium phosphate dehydrate.[38] The obtained results in the present study reveal that the joint presence of Ca^{2+} and PO_4^{3-} provokes the formation nanocrystalline apatite particles located at the mesopore wall as it has been evidenced by TEM and XRD techniques. In this case, 56% of phosphorus present in the sample is in the form of nanocrystalline apatite particles, while 32% remaining is making up the silica network as a P−O−Si bond. These results differ from the obtained in MBGs with the same silica content, since MBGs exhibited ACP clusters and no evidence of phosphorus incorporation into the silica network.[22,23] Such differences could be explained by the conditions used for MG-HA *nanocomposite* synthesis. For this material, the use of higher [HCl/TEOS + TEP] molar ratio provokes an acceleration of TEP hydrolysis,[39] increasing the phosphorus incorporation into the silica network and the crystallization rate of sol−gel apatite.[19−21]

Moreover, the use of F127 surfactant in the present study plays a decisive role in the mesostructure formation as well as in the homogeneous distribution of nanocrystalline apatite

dx.doi.org/10.1021/cm203416x | *Chem. Mater.* 2012, 24, 1100−1106

Table 2. Textural Properties Obtained by N_2 Adsorption of the Calcined MG-HA and Si100 Materials[a]

				^{29}Si SP		^{29}Si CP			
sample	S_{BET} (m^2/g)	V_p (cm^3/g)	D_p (nm)	Q^3_H (%)	Q^4 (%)	Q^2_{Ca} (%)	Q^2_H (%)	Q^3_H (%)	Q^4 (%)
MG-HA	235	0.4	8.0	20.9	79.1	4.6	15.8	66.2	13.4
Si100	120	0.2	8.5	17.9	82.1		12.4	54.6	33.0

[a]Relative populations, expressed as percentages, corresponding to the Q^n ^{29}Si units obtained by deconvolution of the experimental spectra NMR solid state obtained by single pulse and cross-polarization, respectively.

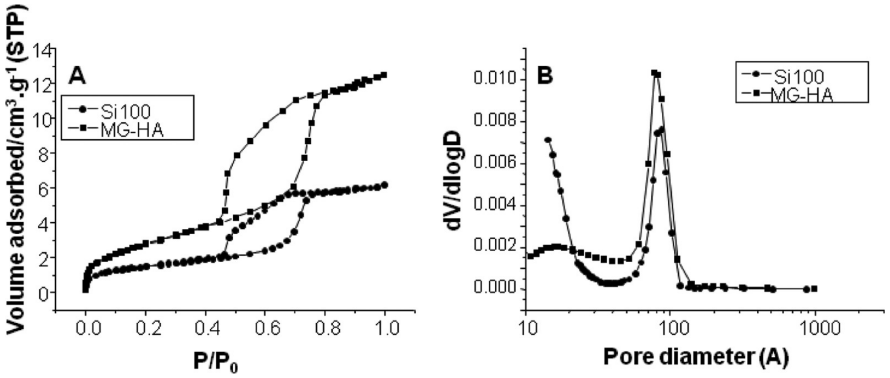

Figure 4. (A) Nitrogen sorption isotherms and (B) pore size distribution of calcined MG-HA and Si100 materials.

particles into amorphous matrixes.[24] In fact, when the MG-HA material was synthesized with Pluronic P123 instead of F127, the glass mesostructure formation was greatly disturbed due to the presence of agglomerates located outside of mesoporous arrangement (Supporting Information, S2).

^{29}Si NMR spectroscopy was used to evaluate the network connectivity of MG-HA material. Q^2, Q^3, and Q^4 represent the silicon atoms (denoted Si*) in $(NBO)_2$ Si*-$(OSi)_2$, (NBO)Si*-$(OSi)_3$, and Si*$(OSi)_4$ (NBO = nonbonding oxygen), respectively. In the case of the SP spectrum, two signals, centered at −112 and −102 ppm, are observed, corresponding to the Q^4 and Q^3_H environments of silicon, respectively. In contrast, in the spectrum obtained by CP, 4 signals centered at −112, −102, −93, and −88 ppm are observed, corresponding to the Q^4 environments, Q^3_H, Q^2_H, and Q^2_{Ca}, respectively. The presence of a signal in CP spectrum corresponding to Q^2_{Ca} environment reveals that a small amount of free CaO (not entrapped as apatite particles) is forming part of the glassy structure as network modifier. Moreover, the nonexistence of this signal in SP spectrum demonstrates that this specie is close to the protons sited at the material surface.[22] Therefore, from our results, we can consider the apatite crystallization restricts the amount of Ca ion available for silica matrix, obtaining a mesoporous glassy matrix poor in Ca and richer in Si and P cations. Moreover, MG-HA also shows a similar disruption silica network grade in the surface, in comparison to MBGs with the same silica content,[22,23] due to that the apatite nanoparticles have a similar effect on the silica network disruption that the ACP clusters in the MBGs.

Textural properties of MG-HA *nanocomposite* were quantitative studied by N_2 adsorption isotherms. Figure 4A shows type IV isotherm with H1-type hysteresis identified as cylindrical mesopores. This material exhibits a BET surface area value of 235 m^2/g and a pore volume value of 0.4 cm^3/g. It is also important to remark on the presence of micropores (<2 nm), with an area of 9.25 m^2/g, which could act to interconnect the mesoporous channels, as it has been demonstrated in other 2D-hexagonal mesoporous structures as SBA-15.[40] The study of pore size distribution reveals the existence of a large mesoporous size of 8 nm (Figure 4B). This *nanocomposite* also exhibits lower BET surface area and pore volume values in comparison with MBGs in the SiO_2−CaO−P_2O_5 system. This decrease could be attributed to the presence of larger mesopores sizes (8 nm instead of 4.4 nm). To determine if the existence of the nanocrystalline apatite particles into mesoporous wall affects the MG-HA textural properties, such material was compared with Si100 sample (Figure 4A, B). The results evidence higher BET surface area and pore volume (Table 2) in the MG-HA material, exhibiting similar pore size diameter (around 8 nm). These results could be directly related to the presence of micropores, which are not evidenced in Si100 sample (Figure 4). As it has been commented above, the disrupting effect of apatite nanoparticles on silica framework provokes (Q^4 unit of ^{29}Si CP NMR, Table 2) a notable increase in the microporosity, in a similar way that titania particles behave on silica framework in titania−silica mesoporous nanocomposites films.[24] To assess the functionality of the MG-HA *nanocomposite*, its *in vitro* bioactivity in simulated body fluid (SBF) and its biocompatibility on L929 fibroblasts and Saos-2 osteosblasts have been evaluated.

In order to compare the bioactive behavior of MG-HA with MBGs, the bioactivity has been analyzed in the similar conditions by keeping the same external surface/volume ratio.[9] In this case, FTIR spectroscopy cannot be used to determine the changes in the MG-HA surface after SBF exposure, because the starting material exhibits the characteristic doublet at 560 and 600 cm^{-1} corresponding to crystalline phosphate (see Supporting Information, S3).[41] Therefore, SEM-EDS and TEM-ED studies were carried out to determine the changes in the MG-HA surface as function of soaking time. Figure 5 displays SEM micrographs and their corresponding EDS spectra, showing a thin layer composed of needle-shaped crystallites after 8 h in SBF. The morphological evolution is more evident after 24 h, when MG-HA surface is fully covered by this new layer composed of hemispherical particles formed by needle-shaped crystallites, typical of biomimetic processes of

dx.doi.org/10.1021/cm203416x | Chem. Mater. 2012, 24, 1100−1106

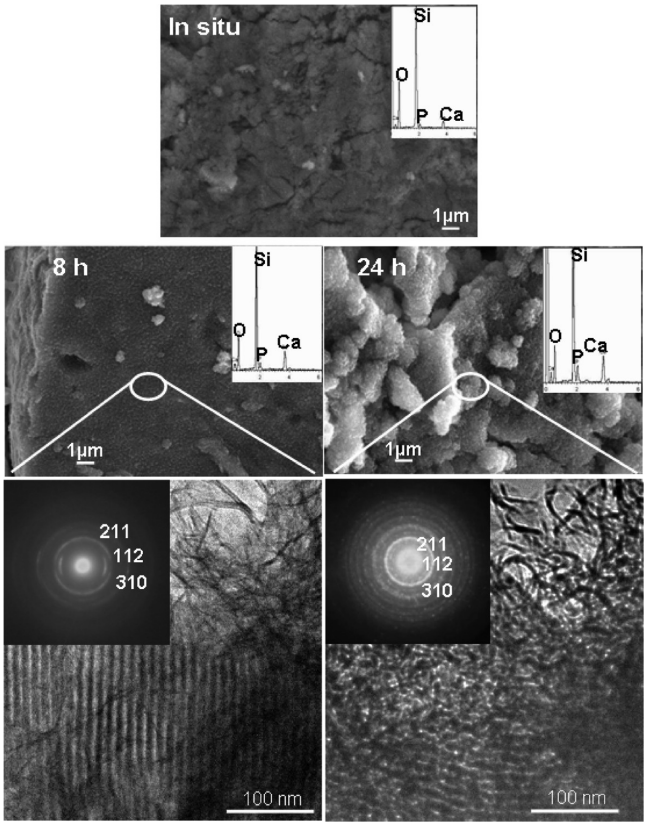

Figure 5. *In vitro* bioactivity in SBF: study of the *nanocomposite* MG-HA surface by SEM/EDS and TEM/ED before and after different times in SBF.

bioactive surfaces.[42] EDS analyses reveal a notable increase in phosphorus and calcium content in the MG-HA surface after 8 and 24 h of incubation. To confirm the new formed phase on the MG-HA material, TEM study has been performed. Results show that in the first 8 h the surface is plenty covered by needle-like particles, which correspond to apatite phase, as it has been evidenced by ED study. A higher number of these needle-like apatite particles are observed in TEM image after 24 h. Moreover, it is important to note that the mesoporous arrangement is kept after 8 and 24 h, as it can be evidenced in TEM images.

Figure 6 shows the calcium, pH, and silicon variations in the SBF over soaking time. In the first 8 h of incubation, calcium concentration displays a slight increase around 10 ppm, followed by a gradual decrease until 24 h. Finally, a sudden decrease until almost the total calcium depletion at 48 h is observed. Concerning the pH variation, this parameter follows the same initial trend of calcium variation values, being constant along the time of the experiment. In the case of silicon, a gradual lixiviation over time is observed.

The obtained results reveal the highly bioactive behavior of MG-HA material when it is soaked in SBF. The initial slight increase of Ca^{2+} content and pH evolution in SBF suggests that an ionic exchange between $Ca^{2+}$of MG-HA material (in this case, calcium of glass network as network modifier) and H^+ from SBF takes place. In agreement with Hench theory,[43] this process leads to silanol formation on its surface which is a mandatory step for the subsequently apatite precipitation. The obtained TEM/SEM results show that MG-HA and MBGs materials have similar bioactive behaviors.[9,44]

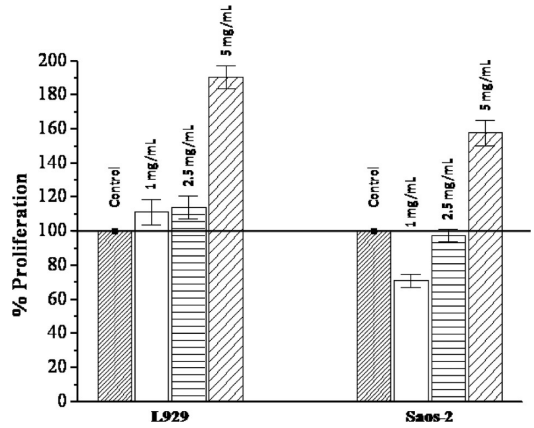

Figure 7. Effect of MG-HA bioceramic *nanocomposite* on proliferation of cultured murine L929 fibroblasts and human Saos-2 osteoblasts after 4 days of treatment. The cell number obtained in the presence of different MG-HA doses was referred as percentage in relation to the controls (100%) carried out in the absence of biomaterial.

With the purpose of evaluating the cell response to the MG-HA *nanocomposite*, *in vitro* biocompatibility studies were carried out with cultured murine L929 fibroblasts and human Saos-2 osteoblasts. Figure 7 shows the effect of MG-HA material on cell proliferation of both cell types after 4 days of treatment. The cell number obtained in the presence of different MG-HA doses was referred as percentage in relation to the controls (100%) carried out in the absence of biomaterial. As it can be observed in all cases, high proliferation values were obtained

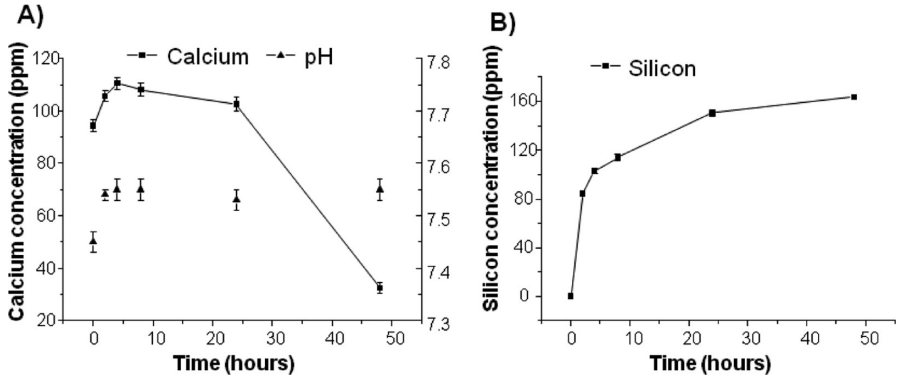

Figure 6. (A) Calcium, pH, and (B) silicon variations in the SBF solution over time.

dx.doi.org/10.1021/cm203416x | *Chem. Mater.* 2012, 24, 1100–1106

and no significant differences exist between MG-HA treated cells and controls ($p > 0.05$). Previous studies using MBGs with the same silica content also showed satisfactory results. However, a cytostatic effect was observed through the reduction of cell proliferation with MBGs.[45] The absence of this cytostatic effect when MG-HA was added to the cell cultures can be due to the presence of nanocrystalline apatite particles embedded into the mesoporous glass walls, which improves the biocompatibility of MG-HA with respect to MBGs with ACP clusters. It has been demonstrated that cells are sufficiently sensitive to alterations at the nanoscale level which can elicit diverse cell behaviors.[6] In this sense, previous studies have shown that the nanocrytalline apatites compared to ACP enhance notably the adhesion, proliferation, and differentiation of osteogenic cells.[46,47]

Figure 8 shows the cell morphology of murine L929 fibroblasts (A) and human Saos-2 osteoblasts (B) cultured for 4 days in the presence of 5 and 2.5 mg/mL of MG-HA *nanocomposite* respectively. This biomaterial does not produce morphological alterations in these cell types, which proliferate in the presence of MG-HA, showing their normal characteristics as it was observed by optical microscopy. No changes of cell size and complexity were detected by flow cytometry after MG-HA treatment (data not shown).

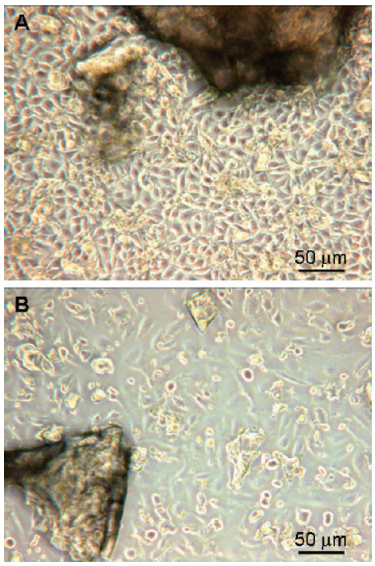

Figure 8. Cell morphology of murine L929 fibroblasts (A) and human Saos-2 osteoblasts (B) cultured for 4 days in the presence of 5 and 2.5 mg/mL of MG-HA *nanocomposite* respectively.

High values of cell viability (around 90%), evaluated by propidium iodide exclusion and flow cytometry, were obtained after 4 days of treatment of cultured murine L929 fibroblasts and human Saos-2 osteoblasts with different doses of MG-HA (Table 3). In order to know if this biomaterial induces apoptosis in these cell types, the cell percentage in each cell cycle phase was analyzed by flow cytometry and the $SubG_1$ fraction (cells with fragmented DNA) was used as an indication of apoptosis. Very low values of apoptosis (lower than 1%) in both murine L929 fibroblasts and human Saos-2 osteoblasts were obtained after 4 days of treatment with different doses of MG-HA (Table 3). All these results indicate the excellent biocompatibility of this novel MG-HA bioceramic *nanocomposite* where the nanocrystalline apatite nanoparticles improve the cell response.

Table 3. Effect of MG-HA *Nanocomposite* Different Doses on Cell Viability and Apoptosis of Cultured Murine L929 Fibroblasts and Human Saos-2 Osteoblasts after 4 Days of Treatment

MG-HA	concentration (mg/mL)	L929	Saos-2
viability		99.4 ± 0.1	93.8 ± 0.7
	1	95.6 ± 0.8	94.8 ± 0.2
	2.5	88.3 ± 0.1	89.4 ± 0.7
	5	75.4 ± 1.1	87.3 ± 0.5
apoptosis		0.2 ± 0.1	1.1 ± 0.1
	1	0.2 ± 0.1	0.5 ± 0.2
	2.5	0.6 ± 0.2	0.6 ± 0.1
	5	0.7 ± 0.2	0.6 ± 0.1

4. CONCLUSIONS

In this manuscript, the synthesis of a novel mesostructured *nanocomposite* formed by nanocrystalline apatite particles uniformly embedded into mesoporous $SiO_2-CaO-P_2O_5$ matrix is shown. This *nanocomposite* presents a mesoporous arrangement with a well-defined 2D-hexagonal structure exhibiting high surface area and pore volume values with large pore size of 8 nm.

The *in vitro* bioactivity assays have shown a fast apatite-like phase formation on the surface of this *nanocomposite* material. The fibroblast and osteoblast response to this material reveals a significant biocompatibility improvement compared with the mesoporous bioactive glasses which could be due to the presence of nanocrystalline apatite units distributed into mesoporous glass architecture. The obtained results indicate that this novel *nanocomposite* offers a synergy of its two constituents, enhancing its potential for bone tissue regeneration purposes.

■ ASSOCIATED CONTENT

Supporting Information

Detailed description of Material and Methods. Figure S1 showing the structural and textural characterization corresponding to Si100 material. Figure S2 displaying a TEM image corresponding to MG-HA material using P123 surfactant as structure directing agent instead of F127. Figure S3 showing FTIR spectrum corresponding to calcined MG-HA material (PDF). This material is available free of charge via the Internet at http://pubs.acs.org.

■ AUTHOR INFORMATION

Corresponding Author

*Fax: +34 394 1786. Tel.: +34 91 394 1861. E-mail: vallet@farm.ucm.es (M.V.-R.); ibarba@farm.ucm.es (I.I.-B.).

Notes

The authors declare no competing financial interest.

■ ACKNOWLEDGMENTS

In memoriam of Prof. Purificación Escribano López. We thank the following for funding this work: the Spanish CICYT through project MAT2008-00736, the Comunidad Autónoma de Madrid via the S2009MAT-1472 program grant, and the Ministerio de Ciencia e Innovación through project CS02010-11384-E. We also thank Fernando Conde (CAI X-ray

Diffraction), CAI Elemental analysis, CAI NMR, ICTS Centro Nacional de Microscopia Electrónica of Universidad Complutense de Madrid. M.C. is grateful to MICINN for the financial support through FPI fellowship.

REFERENCES

(1) Hench, L. L.; Polak, J. M. *Science* **2002**, *295*, 1014.
(2) Vallet-Regí, M. *J. Int. Med.* **2010**, *267*, 22.
(3) Willians, D. *Biomaterials* **2008**, *29*, 1737.
(4) Vallet-Regí, M; Ruiz-Hernández, E. *Adv. Mater.* **2011**, *23*, 5177.
(5) Thomas, V.; Dean, D. R.; Vohra, Y. K. *Curr. Nanosci.* **2006**, *2*, 155.
(6) Dorozhkin., S. V. *Acta Biomater.* **2010**, *6*, 715.
(7) Vallet-Regí, M; Gonzalez-Calbet, J. M. *Prog. Solid State Chem.* **2004**, *32*, 1.
(8) Yan, X.; Yu, C.; Zhou, X.; Tang, J.; Zhao, D. *Angew. Chem., Int. Ed.* **2004**, *43*, 5980.
(9) López-Noriega, A.; Arcos, D.; Izquierdo-Barba, I.; Sakamoto, Y.; Terasaki, O.; Vallet-Regí, M. *Chem. Mater.* **2006**, *18*, 3137−3144.
(10) Shi, Q.; Wang, J.; Zhang, J.; Fan, J.; Stucky, G. D. *Adv. Mater.* **2006**, *18*, 1038.
(11) Xia, W.; Chang, J. *J. Controlled Release* **2006**, *110*, 522.
(12) Arcos, D.; López-Noriega, A.; Ruiz-Hernández, E.; Terasaki, O.; Vallet-Regí, M. *Chem. Mater.* **2009**, *21*, 1000.
(13) López-Noriega, A.; Arcos, D.; Vallet-Regí, M. *Chem.−Eur. J.* **2010**, *16*, 10879.
(14) Lin, H.-M.; Wang, W.-K.; Hsiung, P.-A.; Shyu, S.-G. *Acta Biomater.* **2010**, *6*, 3256.
(15) Yang, P.; Zhao, D.; Margolesem, D. I.; Chemelka, B. F.; Stucky, G. D. *Nature* **1998**, *396*, 152.
(16) Pinna, N.; Niederberger, M. *Angew. Chem., Int. Ed.* **2008**, *47*, 5292.
(17) Andersson, J.; Areva, S.; Spliethoff, B.; Linden, M. *Biomaterials* **2005**, *26*, 6827.
(18) Sousa, A.; Souza, K. C.; Sousa, E. M. B. *Acta Biomater.* **2008**, *4*, 671.
(19) Diaz, A.; Lopez, T.; Manjarrez, J.; Basaldella, E.; Martínez-Blanes, J. M.; Odriozola, J. A. *Acta Biomater.* **2006**, *2*, 173.
(20) Borwoka, A.; Szczes, A. *Mater. Lett.* **2011**, *65*, 175.
(21) Jagadeesan, D.; Deepak, C.; Siva, K.; Inamdar, M. S.; Eswara-Moorthy, M. *J. Phys. Chem. C* **2008**, *112*, 7379.
(22) Leonova, E.; Izquierdo-Barba, I.; Arcos, D.; López-Noriega, A.; Heddin, N.; Vallet-Regí, M.; Edén, M. *J. Phys. Chem. C* **2008**, *112*, 5552.
(23) García, A.; Cicuéndez, M.; Izquierdo-Barba, I.; Arcos, D.; Vallet-Regí, M. *Chem. Mater.* **2009**, *21*, 5474.
(24) Fattakhova-Rohlfing, D.; Szeifert, J. M.; Yu, Q.; Kalousek, V.; Rathouský, J.; Bein, T. *Chem. Mater.* **2009**, *21*, 2410.
(25) Brinker, C. J.; Lu, Y. F.; Sellinger, A.; Fan, H. Y. *Adv. Mater.* **1999**, *11*, 579.
(26) Yu, B.; Poologasundarampillai, T.; Turdean-Ionescu, C.; Smith, M. E.; Jones, J. R. *Biocer. Develop. Apps.* **2011**, *1*, ID D110178.
(27) Westheimer, F. H.; Huang, S.; Coritz, F. *J. Am. Chem. Soc.* **1988**, *110*, 181.
(28) Chai, C. S.; Gross, K. A.; Ben Nissan, B. *Biomaterials* **1998**, *19*, 2291.
(29) Jillavenkatesa, A.; Condrate, R. A. *J. Mater. Sci.* **1998**, *33*, 4111.
(30) Liu, D. M.; Yang, Q.; Troczynski, T.; Tseng, W. J. *Biomaterials* **2002**, *23*, 1679.
(31) Zhao, D.; Feng, J. P.; Huo, Q.; Melosh, N.; Fredrickson, G. H.; Chmelka, B. F.; Stucky, G. D. *Science* **1998**, *279*, 548.
(32) Panda, R. N.; Hsieh, M. F.; Chung, R. J.; Chin, T. S. *J. Phys. Chem. Solids* **2003**, *64*, 193.
(33) Padilla, S.; Izquierdo-Barba, I.; Vallet-Regí, M. *Chem. Mater.* **2008**, *20*, 5942.
(34) Lin, K. S. K.; Tseng, Y. H.; Mou, Y.; Hsu, Y. C.; Yang, C. M.; Chan, J. C. C. *Chem. Mater.* **2005**, *17*, 4493.
(35) Jäger, C.; Welzel, T.; Meyer-Zaika, W.; Epple, M. *Magn. Reson. Chem.* **2006**, *44*, 573.
(36) Mankenzie, K. J. D.; Smith, M. E. *Multinuclear solid-state NMR of inorganic materials*; Pergamon Press: Amsterdam, 2002.
(37) Gunawidjaja, P. N.; Lo, A. Y. H.; Izquierdo-Barba, I.; García, A.; Arcos, D.; Stevensson, B.; Grins, J.; Vallet-Regí, M.; Edén, M. *J. Phys. Chem. C* **2010**, *114*, 19345.
(38) Zhongqi, H.; Wayne Honeycutt, C.; Baoshan, X.; McDowel, R. W.; Pellechia, P. J.; Tiequan, Z. *Soil Sci.* **2007**, *172*, 7.
(39) Tilocca, A.; Cormack, A. N. *J. Phys. Chem. B* **2007**, *111*, 14256.
(40) Liu, Z.; Terasaki, O.; Ohsuna, T.; Hiraga, K.; Shin, H. J.; Ryoo, R. *Chem. Phys Chem.* **2001**, *2*, 229.
(41) Vallet-Regí, M.; Romero, A. M.; Ragel, C. V.; LeGeros, R. Z. *J. Biomed. Mater. Res.* **1999**, *44*, 416.
(42) Vallet-Regi, M.; Ragel, C. V.; Salinas., A. J. *Eur. J. Inorg. Chem.* **2003**, 1029.
(43) Hench, L. L.; Andersson, O. In Hench, L.L.; Wilson, J., Eds.; *Bioactive Glasses. An Introduction to Bioceramics*; Elsevier Science: New York, 1995; p 477.
(44) Izquierdo-Barba, I.; Arcos, D.; Sakamoto, Y.; Terasaki, O.; Lopez-Noriega, A.; Vallet-Regí, M. *Chem. Mater.* **2008**, *20*, 3191.
(45) Alcaide, M.; Portolés, P.; López-Noriega, A.; Arcos, D.; Vallet-Regí, M.; Portolés, M. T. *Acta Biomater.* **2010**, *6*, 892.
(46) Ginebra, M. P.; Espanol, M.; Montufar, E. B.; Perez, R. A.; Mestres, G. *Acta Biomater.* **2010**, *6*, 2863.
(47) Hu, Q.; Tan, Z.; Liu, Y.; Tao, J.; Cai, Y.; Zhang, M.; Pan, H.; Xu, X.; Tang, R. *J. Mater. Chem.* **2007**, *17*, 4690.

Supporting information:

New nanocomposite system with nanocrystalline apatite embedded into mesoporous bioactive glass

Mónica Cicuéndez[a,b], María Teresa Portolés[c], Isabel Izquierdo-Barba[a,b]* and María Vallet-Regí[a,b]*

1. Material and Methods

1.1. Characterization physic-chemical of MG-HA nanocomposite

The structural characteristics of MG-HA material were investigated by X-ray diffraction (XRD) and transmission electron microscopy (TEM). The diffraction was performed on a Philips X'Pert diffractometer equipped with Cu Kα radiation source (wavelength 1.5406 Å). To determine the mesoporous ordering, XRD patterns were measured in a 2θ range between 0.6 and 8, with a step of 0.02° and an accumulation time of 0.5 s per step. To determine the structural order at the atomic level, XRD patterns were measured between 5 and 80° with a step of 0.02° and an accumulation time of 10 s per step. TEM was performed in a JEOL 3000 FEG electron microscope fitted with a double tilting goniometer stage (±45º) and with an Oxford LINK EDS analyzer. TEM images were recorded using a CCD camera (MultiScan model 794, Gatan, 1024 x 1024 pixels, size 24 μm x 24 μm) in the low-dose condition. Fourier transform (FT) patterns were conducted using Digital Micrograph (Gatan).

^{29}Si and ^{31}P CP (cross-polarization)/MAS (magic-angle-spinning) and single-pulse (SP) solid-state nuclear magnetic resonance (NMR) measurements were performed to evaluate the different silicon and phosphorus environments in the synthesized samples. The NMR spectra were recorded on a Bruker Model Avance 400 spectrometer. Samples were spun at 10 kHz for ^{29}Si and 6 kHz in the case of ^{31}P. Spectrometer frequencies

were set to 79.49 and 161.97 MHz for ^{29}Si and ^{31}P, respectively. Tetramethylsilane (TMS) and 85 % H_3PO_4 were used as the chemical shift standard for ^{29}Si and ^{31}P, respectively. All spectra were obtained using a proton enhanced CP method, using a contact time of 1 ms. The time period between successive accumulations was 5 and 4 s for ^{29}Si and ^{31}P, respectively, and the number of scans was 10,000 for all spectra.

The textural properties were obtained by N_2 adsorption/desorption analyses at -196 ºC on a Micromeritics ASAP 2020 instrument (Micromeritics Co., Norcross, USA). Before each measurement, 100 – 150 mg of the sample were degassed for 24 h at 200ºC under vacuum (<0.3 kPa). The surface area (SBET) was determined using the Brunauer–Emmett–Teller (BET) method [1]. The total pore volume (VT) was calculated from the amount of N_2 adsorbed at a relative pressure of 0.97. To assess the possible existence of micropores (pore diameter < 2 nm), the t-plot method was employed [2]. The average mesopore diameter was obtained from the adsorption branch of the isotherm by means of the Barrett–Joyner–Halenda (BJH) method [3].

Fourier transform infrared spectroscopy (FTIR) was carried out in a Thermo Nicolet Nexus spectrometer equipped with a GoldenGate attenuated total reflectance (ATR) device.

1.2. *In vitro* bioactivity assays

The assessment of *in vitro* bioactivity was performed in a Simulated Body Fluid (SBF) solution, proposed by Kokubo *et al* [4]. The SBF solution has a composition and concentration similar to the inorganic part of human plasma and it was prepared by dissolving NaCl, KCl, $NaHCO_3$, $K_2HPO_4.3H_2O$, $MgCl_2.6H_2O$, $CaCl_2$, and Na_2SO_4 into distilled water and buffering at pH 7.4 with tris(hydroxymethyl)aminomethane $NH_2C(CH_2OH)_3$ and HCl. The *in vitro* bioactivity test was carried out by soaking disks of 6 mm diameter of MG-HA material in a SBF solution. To obtain the disks, 50 mg of

powdered material were compacted by uniaxial and isostatic pressure as described [5]. The disks were incubated at 37 °C under orbital stirring (300 r.p.m.) for different times (8 h and 24 h) in an Ecotron HT. The bioactivity was evaluated by determining the evolution of the material surface by scanning electron microscopy (SEM), energy dispersive spectroscopy X-ray (EDS) and TEM. The SEM was performed in a field emission JEOL JSM 6335F microscope. Previously, the samples were carbon coated by evaporation. EDS analysis were carried out in an Oxford system attached to the microscope Pentafet 6335F. Finally, the content of Ca^{2+} and the evolution of pH in the SBF were measured in an ion analyzer Ilyte Na^{+} K^{+} Ca^{2+} pH. The released silicon into the medium was determined by colorimetric analysis using the USEPA370.1 [6]. This method involves the formation of a complex of yellow-green, with the addition of molybdenum, which is proportional to the amount of silicon present in the solution. The molybdenum complex is measured by spectroscopy at a $\lambda = 660$ nm in the range of 0.1 to 10 µL/mL. Measurements were carried out in a Smart-Chem Analyzer 140 (Alliance Instruments, AMS, France).

1.3. Cell culture for the *in vitro* biocompatibility studies

Either murine L929 fibroblasts or human Saos-2 osteoblasts were seeded on 6 well culture plates (CULTEK S.L.U., Madrid, Spain, reference 153516), at a density of 10^5 cells/ml in DMEM supplemented with 10% fetal bovine serum (FBS, Gibco, BRL), 1 mM L-glutamine (BioWhittaker Europe, Belgium), penicillin (200 µg/mL, BioWhittaker Europe, Belgium), and streptomycin (200 µg/mL, BioWhittaker Europe, Belgium), under a CO_2 (5%) atmosphere and at 37ºC for 24 h. To evaluate the effect of MG-HA material on both cell types, different doses (1, 2.5, and 5 mg/mL) of this material in powder form were added to the culture medium and cells were maintained in

the presence of this bioceramic for 4 days. After each treatment, the attached fibroblasts and osteoblasts were washed with Phosphate Buffer Saline (PBS) and harvested using 0.25% trypsin-EDTA solution for 15 min. The reaction was stopped with culture medium and cells were counted with a Neubauer hemocytometer for the analysis of cell proliferation, centrifuged at 310xg for 10 min and resuspended in fresh medium for the analysis of viability, cell cycle, apoptosis, cell size and complexity by flow cytometry. Controls with cultures of each cell type without treatment were always carried out.

1.4. Flow cytometry studies

As it has been indicated above, cells cultured for 4 days in the presence or the absence of MG-HA material were washed twice with PBS and incubated at 37ºC with trypsin-EDTA solution for cell detachment. After 15 min, the reaction was stopped with culture medium; cells were centrifuged at 310xg for 10 min and resuspended in fresh medium.

After incubation with the different probes, as it is described below, the conditions for the data acquisition and analysis were established using negative and positive controls with the CellQuest Program of Becton Dickinson and these conditions were maintaned during all the experiments. Each experiment was carried out three times and single representative experiments are displayed. For statistical significance, at least 10,000 cells were analyzed in each sample and the mean of the fluorescences emitted by these single cells was used.

1.4.1. Cell viability

Cell viability was determined by addition of propidium iodide (PI; 0.005% in PBS, Sigma-Aldrich Corporation, St. Louis, MO, USA) to stain the DNA of dead cells.

The IP fluorescence was excited at 488 nm and the emission was measured with a 670 LP in a FACScalibur Becton Dickinson flow cytometer.

1.4.2. Cell cycle analysis and apoptosis detection

Cell suspensions were incubated with Hoechst 33258 (PolySciences, Inc., Warrington, PA) (Hoechst 5μg/ml, ethanol 30%, and BSA 1% in PBS), used as a nucleic acid stain, for 30 min at room temperature in darkness. The fluorescence of Hoechst was excited at 350 nm and the emitted fluorescence was measured at 450 nm in a LSR Becton Dickinson flow cytometer. The cell percentage in each cycle phase: G_0/G_1, S and G_2/M was calculated with the CellQuest Program of Becton Dickinson and the $SubG_1$ fraction was used as indicative of apoptosis.

1.4.3. Cell size and complexity

The light scattering properties of cells seeded were examined by flow cytometry measuring forward angle (FSC) and side angle (SSC) light scatters as indicators of cell size and complexity, respectively.

1.5. Cell morphology studies by optical mycroscopy

Optical microscopy studies were carried out on both L929 fibroblasts and Saos-2 osteoblasts after different MG-HA biomaterial treatments. Cells were examined with a Leitz Labovert FS inverted microscope equipped with a Leica DC 300 Digital Camera.

1.6. Statistics

Data are expressed as means + standard deviations of a representative of three experiments carried out in triplicate. Statistical analysis was performed using the

Statistical Package for the Social Sciences (SPSS) version 11.5 software. Statistical comparisons were made by analysis of variance (ANOVA). Scheffé test was used for post hoc evaluations of differences among groups. In all of the statistical evaluations, $p < 0.05$ was considered as statistically significant.

2. Results

Figure S1: Structural and textural characterization corresponding to Si100 material. A) XRD/TEM showing a mesoporous arrangement in 2D-hexagonal structure. B) N_2 adsorption isotherm showing a type IV isotherm with H1-type hysteresis identified as cylindrical mesopores. This material exhibits a BET surface area value of 120 m^2/g and a pore volume value of 0.2 cm^3 /g. It is also important to remark the absence of microporous. (Inset) Pore diameter distribution showing a very sharp peak centred at 8.5 nm. C) ^{29}Si MAS by single pulse and D) ^{29}Si MAS by cross-polarization NMR solid state**,** with a slight increase in the connectivity of silica network due to the presence of calcium as modifier network in the MG-HA material.

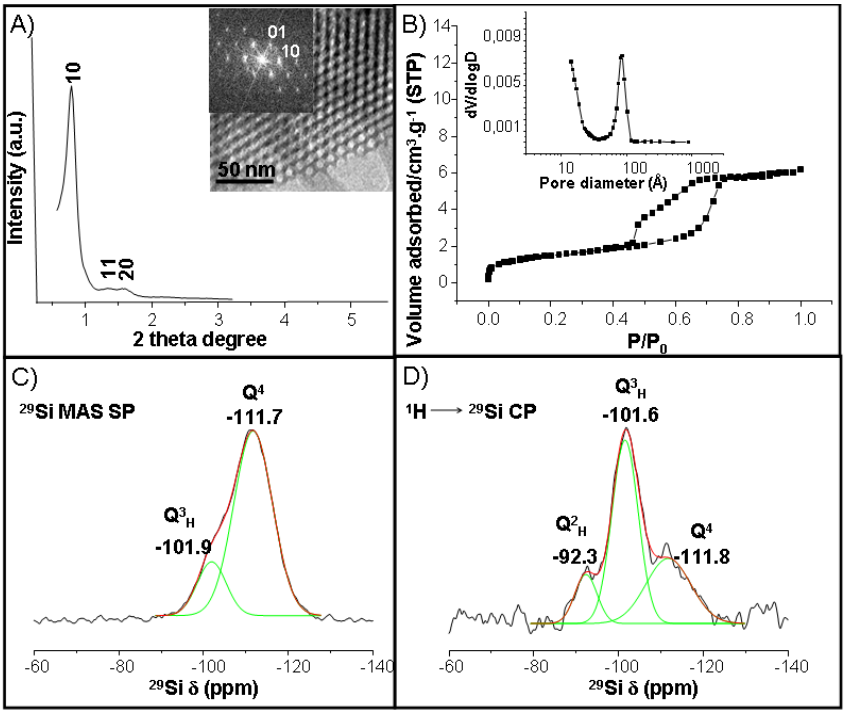

Figure S2: TEM image corresponding to MG-HA material synthetized with P123 as a structure directing agent instead of F127. In this case the ordering mesoporous was disrupted and agglomerates of apatite nanoparticles were formed. The obtained results evidence the important role of F127 in the incorporation of nanoparticles into mesoporous wall.

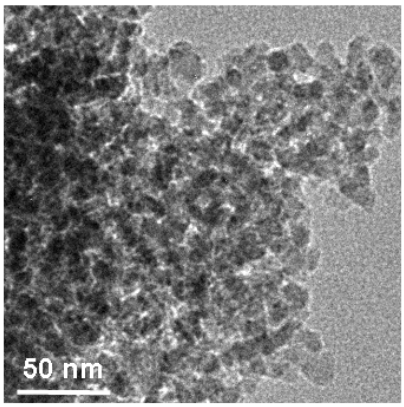

Figure S3: FTIR spectrum of *nanocomposite* MG-HA material as made.

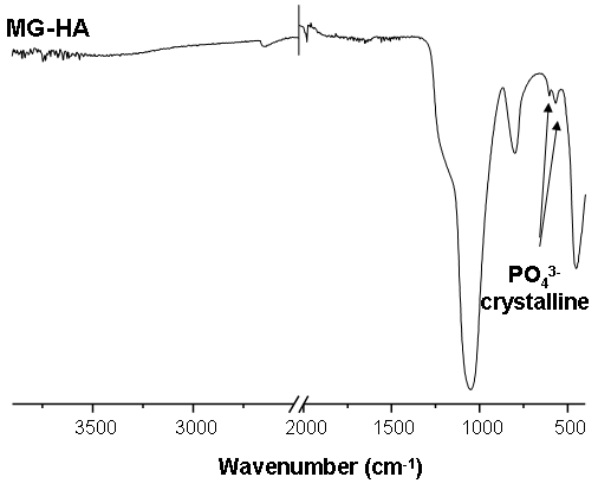

References:

[1] Brunauer, S.; Emmett, P.H.; Teller, E. *J. Am. Chem. Soc.* **1938**, *60*, 309.

[2] Gregg, S.J.; Sing, K.S.W. Adsorption, Surface Area and Porosity, 2nd ed.; Academic Press: New York, **1982**.

[3] Barrett, E.P.; Joyner, L.G.; Halenda, P.H. *J. Am. Chem. Soc.* **1951**, *73*, 373.

[4] Kokubo, T.; Kushitani, H.; Sakka, S.; Kitsugi, T.; Yamamuro, T. J. *J. Biomed. Mater. Res.* **1990**, *24*, 721.

[5] Vallet-Regí, M.; Izquierdo-Barba, I.; Salinas, A.J. *J. Biomed. Mater. Res.* **1999**, *46*, 560.

[6] Koch, O.G.; Koch-Dedic, G.A. Silicon molybdaleblan-Verfahren in Handbuch der Spurenanalyse, Springer-Verlag, Berlín. **1974**, p1105.

1.3. Bibliografía

[1] I. Izquierdo-Barba, M. Vallet-Regí. Fascinating properties of bioactive templated glasses: A new generation of nanostructured biocermamics. Solid State Sci. 2011, 13, 73-783.

[2] X. X. Yan, C. Z. Yu, X. F. Zhou, J. W. Tang, D. Y. Zhao. Highly Ordered Mesoporous Bioactive Glasses with Superior *In Vitro* Bone-Forming Bioactivities. Angew. Chem. Int. Ed. 2004, 43, 5980–5984.

[3] X. X. Yan, H. X. Deng, X. H. Huang, G. Q. Lu, S. Z. Qiao, D. Y. Zhao, C. Z. Yu. Non-Cryst Solids 2005, 351, 3209-3217.

[4] A. López-Noriega, D. Arcos, I. Izquierdo-Barba, Y. Sakamoto, O. Terasaki, M. Vallet-Regí. Chem. Mater. 2006, 18, 3137–3144.

[5] X. X. Yan, H. H. Huang, C. Z. Yu, H. X. Deng, Y. Wang, A. D. Zhang, S. Z. Quiao, G. D. Lu, D. Y. Zhao. Biomaterials 2006, 27, 3336-3403.

[6] X. Li, L. Zhang, X. Dong, J. Liang, J. Shi. Preparation of mesoporous calcium doped silica spheres with narrow size dispersion and their drug loading and degradation behavior. Micro Mesoporous Mater. 2007, 102, 151-158.

[7] D. Arcos, A. López-Noriega, E. Ruiz-Hernández, O. Terasaki, M. Vallet-Regí. Ordered Mesoporous Microspheres for Bone Grafting and Drug Delivery. Chem. Mater. 2009, 21, 1000-1009.

[8] G. Miao, X. Chen, H. Dong, L. Fang, C. Mao, Y. Li, Z. Li, Q. Hu. Investigation of emulsified, acid and acid-alkali catalyzed mesoporous bioactive glass microspheres for bone regeneration and drug delivery. Mater. Sci. Eng. C, 2013, 33, 4236-4243.

[9] Q. Hu, X. Chen, N. Zhao, Y. Li. Facile synthesis and *in vitro* bioactivity of monodispersed mesoporous bioactive glass sub-micron spheres. Mater. Letter. 2013, 106, 452-455.

[10] Q. H. Shi, J. F. Wang, J. P. Zhang, J. Fan, G. D. Stucky. Rapid-Setting, Mesoporous, Bioactive Glass Cements that Induce Accelerated *In□Vitro* Apatite Formation. Adv. Mater. 2006, 18, 1038-1042.

[11] H. Yun, S. Kim, Y. Hyeon. Design and preparation of bioactive glasses with hierarchical pore networks. Chem. Commun. 2007, 2139–2141.

[12] X. Li, J. Shi, X. Dong, L. Zhang, H. Zeng. A mesoporous bioactive glass/polycaprolactone composite scaffold and its bioactivity behavior. J. Biomed. Mater. Res. Part A. 2008, 84A, 84–91.

[13] Y. Zhu, C. Wu, Y. Ramaswamy, E. Kockrick, P. Simon, S. Kaskel, H. Zreiqat. Preparation, characterization and *in vitro* bioactivity of mesoporous bioactive glasses (MBGs) scaffolds for bone tissue engineering. Micro Mesoporous Mater. 2008, 112, 494-503.

[14] D. Arcos, M. Vila, A. López-Noriega, F. Rossignol, E. Champion, F.J. Oliveira, M. Vallet-Regí. Mesoporous bioactive glasses: Mechanical reinforcement by means of a biomimetic process. Acta Biomaterialia 2011, 7, 2952-2959.

[15] G. Wei, X. Yan, J. Yi, L. Zhao, L. Zhou, Y. Wang, C. Yu. Synthesis and *in vitro* bioactivity of mesoporous bioactive glasses with tunable macropores. Micro Mesoporous Mater. 2011, 143, 157-165.

[16] C. Wu, W. Fan, Y. Zhu, M. Gelinsky, J. Chang, G. Cuniberti, V. Albrecht, T. Friis, Y. Xiao. Multifunctional magnetic mesoporous bioactive glass scaffolds with a hierarchical pore structure. Acta Biomaterialia 2011, 7, 3563-3572.

[17] S. Shruti, A. J. Salinas, G. Lusvardi, G. Malavasi, L. Menabue, M. Vallet-Regí. Mesoporous bioactive scaffolds prepared with cerium-, gallium- and zinc-containing glasses. Acta Biomaterialia 2013, 9, 4836-4844.

[18] J. Sun, Y. S. Li, L. Li, W. Zhao, L. Li, J. H. Gao, M. L. Ruan, J. L. J. Shi. Non-Cryst. Solids 2008, 354, 3799–3805.

[19] A. López-Noriega, D. Arcos, M. Vallet-Regí. Functionalizing Mesoporous Bioglasses for Long-Term Anti-Osteoporotic Drug Delivery. Chemistry-A European Journal 2010, 16, 10879-10886.

[20] T. A. Ostomel, Q. Shi, C. K. Tsung, H. Liang, G. D. Stucky. Spherical Bioactive Glass with Enhanced Rates of Hydroxyapatite Deposition and Hemostatic Activity. Small 2006, 2, 1261–1265.

[21] W. Xia, J. Chang. Well-ordered mesoporous bioactive glasses (MBG): A promising bioactive drug delivery system. Journal of Controlled Release 2006, 110, 522–530.

[22] L. Zhao, X. Yan, X. Zhou, L. Zhou, H. Wang, J. Tang, C. Yu. Mesoporous bioactive glasses for controlled drug release. Micro Mesoporous Mater. 2008, 109, 210–215.

[23] W. Xia, J. Chang, J. Lin, J. Zhu. The pH-controlled dual-drug release from mesoporous bioactive glass/polypeptide graft copolymer nanomicelle composites. Eur. J. Pharm. Biopharm. 2008, 69, 546-552.

[24] Y. Zhu, S. Kaskel. Comparison of the *in vitro* bioactivity and drug release property of mesoporous bioactive glasses (MBGs) and bioactive glasses (BGs) scaffolds. Micro Mesoporous Mater. 2009, 118, 176-182.

[25] D. Arcos, M. Vallet-Regí. Bioceramics for drug delivery. Acta Materialia 2013, 61, 890-911.

[26] S. Shruti, A. J. Salinas, E. Ferrari, G. Malavasi, G. Lusvardi, A. L. Doadrio, L. Menabue, M. Vallet-Regí. Curcumin release from cerium, gallium and zinc containing mesoporous bioactive glasses. Micro Mesoporous Mater. 2013, 180, 92-101.

[27] M. Vallet-Regi. Nanoestructured Mesoporous Silica Matrices in Nanomedicine. J. Internal Medicine. 2010, 267, 22-43.

[28] I. Izquierdo-Barba, A. J. Salinas, M. Vallet-Regí. Bioactive Glasses: From Macro to Nano. International Journal of Applied Glass Science 2013, 4, 149-161.

[29] M. Vallet-Regí, C. V. Ragel, A. J. Salinas. Glasses with medical applications. European Journal of Inorganic Chemistry 2003, 1029-1042.

[30] C. T. Kresge, M. E. Leonowicz W. J. Roth, J. C. Vartuli, J. S. Beck. Ordered mesoporous molecular-sieves synthesized by a liquid-crystal template mechanism. Nature 1992, 359, 710-712.

[31] C. J. Brinker, Y. F. Lu, A. Sellinger, H. Y. Fan. Evaporation-induced self-assembly: Nanostructures made easy. Adv. Mater. 1999, 11, 579–585.

[32] Y. F. Zhao, S. C. J. Loo, Y. Z. Chen, F. Y. C. Boey, J. Ma. *In situ* SAXRD study of sol–gel induced well-ordered mesoporous bioglasses for drug delivery. J. Biomed. Mater. Res. 2008, 85A, 1032–1042.

[33] H-S. Yun, S. Kim, Y-T. Hyun. Preparation of 3D cubic ordered mesoporous bioactive glasses. Solid State Sci. 2008, 10, 1083–1092.

[34] H. Yun, S. Kim, Y. Hyeon. Highly ordered mesoporous bioactive glasses with *Im3m* symmetry. Mater. Lett. 2007, 61, 4569–4572.

[35] C.-C. Shih, C-S. Chien, J-K Kung, J-C Chen, S-S Chang, P-S Lu, C-J Shih. Effect of surfactant concentration on characteristics of mesoporous bioactive glass prepared by evaporation induced self-assembly process. Appl. Surface Sci. 2013, 264, 105-110.

[36] M. Kaneda, T. Tsubakiyama, A. Carlsson, Y. Sakamoto, T. Ohsuna, O. Terasali, S. H. Joo, R. Ryoo. Structural study of mesoporous MCM-48 and carbon networks synthesized in the spaces of MCM-48 by electron crystallography. Journal of Physical Chemistry B 2002, 106, 1256-1266.

[37] I. Izquierdo-Barba, D. Arcos, Y. Sakamoto, O. Terasaki, A. López- Noriega, M. Vallet-Regí. High-performance mesoporous bioceramics mimicking bone mineralization. Chem. Mater. 2008, 20, 3191–3198.

[38] D. Arcos, I. Izquierdo-Barba, M. Vallet-Regí. Promising trends of bioceramics in the biomaterials field. J. Mater Sci. Mater. Med. 2009, 20, 447–455.

[39] W. E. Brown, M. U. Nylen. Role of octacalcium phosphate in formation of hard tissues. J. Dent. Res. 1964, 43, 751-764.

[40] E. Leonova, I. Izquierdo-Barba, D. Arcos, A. López-Noriega, N. Hedin, M. Vallet-Regí, M. Eden. Multinuclear solid-state NMR studies of ordered mesoporous bioactive glasses. Journal of Physical Chemistry C 2008, 112, 5552-5562.

[41] P.N. Gunawidjaja, R. Mathew, A. Y. H. Lo, I. Izquierdo-Barba, A. García, D. Arcos, M. Vallet-Regí, M. Eden. Local structures of mesoporous bioactive glasses and their surface alterations *in vitro*: inferences from solid-state nuclear magnetic resonance. Philosophical Transactions of the Royal Society A-Mathematical Physical and Engineering Sciences 2012, 370, 1376-1399.

[42] R. Mathew, P. N. Gunawidjaja, I. Izquierdo-Barba, K. Jansson, A. García, D. Arcos, M. Vallet-Regí, M. Eden. Solid-State P-31 and H-1 NMR Investigations of Amorphous and Crystalline Calcium Phosphates Grown Biomimetically From a Mesoporous Bioactive Glass. Journal of Physical Chemistry C 2011, 115, 20572-20582.

[43] P. N. Gunawidjaja, Y. H. Lo, I. Izquierdo-Barba, A. García, D. Arcos, B. Stevensson, J. Grins, M. Vallet-Regí, M. Eden. Biomimetic Apatite Mineralization Mechanisms of Mesoporous Bioactive Glasses as Probed by Multinuclear P-31, Si-29, Na-23 and C-13 Solid-State NMR. Journal of Physical Chemistry C 2010, 114, 19345-19356.

[44] D. Li, H. Zhou, I. Honma. Design and synthesis of self-ordered mesoporous nanocomposite through controlled in situ crystallization. Nature Mater 2004, 3 65-72.

[45] Scott C. Warren, Lauren C. Messina, Liane S. Slaughter, Marleen Kamperman, Qin Zhou, Sol M. Gruner, Francis J. DiSalvo, Ulrich Wiesner. Ordered Mesoporous Materials from Metal Nanoparticle–Block Copolymer Self-Assembly. SCIENCE 320. 1748-1752 (2008)

[46] D. Wang, R. Kou, D. Choi, Z. Yang, Z. Nie, J. Li, L. V. Saraf, D. Hu, J. Zhang, G. L. Graff, J. Liu, M.A. Pope, and I. A. Aksay. Ternary Self-Assembly of Ordered Metal

Oxide Graphene Nanocomposites for Electrochemical Energy Storage. ACS nano 2010, 4, 1587-1595.

[47] D. Fattakhova-Rohlfing, J. M. Szeifert, Q. Yu, V. Kalousek, J. Rathousky, T. Bein. Low Temperature Synthesis of Mesoporous Titania-Silica films with pre-formed Anatasa nanocrystals. Chem Mater 2009, 21, 2410-2417.

[48] M. Vila, M. Cicuéndez, J. Sánchez-Marcos, V. Fal-Miyar, M. Manzano, C. Prieto, M. Vallet-Regí. Electrical stimuli to increase cell proliferation on carbon nanotubes/mesoporous silica composites for drug delivery. J. Biomed Mater Res A 2013, 101A 213-22.

[49] H. H. P. Yiu, H-J Niu, E. Biermans, G. van Tendeloo, and M.J. Rosseinsky Designed Multifunctional Nanocomposites for Biomedical Applications. Adv. Funct. Mater. 2010, 20, 1599–1609.

[50] E. Ruiz-Hernández, A. López-Noriega, D. Arcos, I. Izquierdo-Barba, O. Terasaki, M. Vallet-Regí. Aerosol-assisted synthesis of magnetic mesoporous silica spheres for drug targeting. Chem Mater 2007, 19, 3455-3463.

[51] T. Sen, A. Sebastianelli, I. J. Bruce. Mesoporous Silica-Magnetite Nanocomposite: Fabrication and Applications in Magnetic Bioseparations. J. Am. Chem. Soc. 2006, 128, 7130-7131.

[52] H. Yang, Y. Liu, Q. Shen, L. Chen, W. You, X. Wang, J. Sheng. Mesoporous silica microcapsule-supported Ag nanoparticles fabricated via nano-assembly and its antibacterial properties. J. Mater. Chem. 2012, 22, 24132-24138.

[53] A. Sousa, K.C. Souza, E.M.B. Sousa. Mesoporous silica/apatite nanocomposite: Special synthesis route to control local drug delivery. Acta Biomaterialia 2008, 4, 671–679.

[54] W. Luo, X. Hu, Y. Sun, Y. Huang. Controlled Synthesis of Mesoporous MnO/C Networks by microwave Irradiation and Their Enhanced Lithium-Storage Properties. ACS Appl. Mater. Interfaces 2013, 5, 1997−2003.

[55] J-M. Oh, A.S. Kumbhar, O. Geiculescu, S.E. Creager. Mesoporous Carbon/Zirconia Composites: A Potential Route to Chemically Functionalized Electrically-Conductive Mesoporous Materials. Langmuir 2012, 28, 3259−3270.

[56] J. Park, G.-P. Kim, I. Nam, S. Park, J. Yi. One-pot synthesis of silicon nanoparticles trapped in ordered mesoporous carbon for use as an anode material in lithium-ion batteries. Nanotechnology 2013, 24, 025602.

[57] C. J. Brinker, Y. Lu, A. Sellinger, H. Fan. Evaporation-Induced Self-Assembly: Nanostructures Made Easy. Adv. Mater. 1999, 11, 579–585.

[58] M. Vallet-Regí, J. M. Gonzalez-Calbet. Calcium phosphates as substitution of bone tissues. Prog. Solid State Chem. 2004, 32, 1.

[59] S. V. Dorozhkin. Nanosized and nanocrystalline calcium orthophosphates. Acta Biomaterialia 2010, 6, 715.

[60] H. Zhou, J. Lee. Nanoscale hydroxyapatite particles for bone tissue engineering. Acta Biomaterialia 2011, 7, 2769-2781.

[61] M. Sadat-Shojai, M.-T. Khorasani, E. Dinpanah-Khoshdargi, A. Jamshidi. Synthesis methods for nanosized hydroxyapatite with diverse structures. Acta Biomaterialia 2013, 9, 7591–7621.

[62] A. García, M. Cicuéndez, I. Izquierdo-Barba, D. Arcos, M. Vallet-Regí. Essential Role of Calcium Phosphate Heterogeneities in 2D-Hexagonal and 3D-Cubic SiO_2-CaO-P_2O_5 Mesoporous Bioactive Glasses. Chem. Mater. 2009, 21, 5474-5484.

[63] M. Alcaide, P. Portolés, A. López-Noriega, D. Arcos, M. Vallet-Regí, M. T. Portolés. Interaction of an ordered mesoporous bioactive glass with osteoblasts, fibroblasts and lymphocytes, demonstrating its biocompatibility as a potential bone graft material. Acta Biomaterialia 2010, 6, 892-899.

Capítulo 2

CAPÍTULO 2. INTERACCIÓN DE TIPOS CELULARES ESPECÍFICOS CON ANDAMIOS MACROPOROSOS TRIDIMENSIONALES BASADOS EN EL *NANOCOMPOSITE* MGHA

2.1. Andamios tridimensionales (3D) para regeneración tisular ósea

La utilización de andamios tridimensionales (3D) para regeneración tisular ósea tiene como objetivo mimetizar la arquitectura porosa y las funciones de la matriz extracelular natural del hueso, creando el microambiente adecuado para permitir el crecimiento de nuevo tejido óseo con las características estructurales y funcionales típicas de dicho tejido [1,2,3,4,5,6,7,8,9]. Estos soportes deben actuar como plantillas temporales y estructurales permitiendo a las células proliferar y diferenciarse, pero al mismo tiempo deben ser reabsorbidos, para que finalmente solo permanezca el nuevo tejido vivo formado.

Los andamios pueden ser implantados directamente en el organismo o ser previamente cultivados *in vitro* con células precursoras del tejido para su posterior implantación [1]. Asimismo, los andamios pueden combinarse con factores de crecimiento u otras biomoléculas que favorezcan la regeneración tisular *in situ* [1,10,11]. La **Figura 2.1.** ilustra el proceso seguido en la utilización de andamios 3D para regeneración tisular ósea, desde la fabricación de los andamios macroporosos a partir de datos de Resonancia Magnética de Imagen (RMI), pasando por su implantación en el defecto óseo hasta alcanzar la regeneración total del tejido.

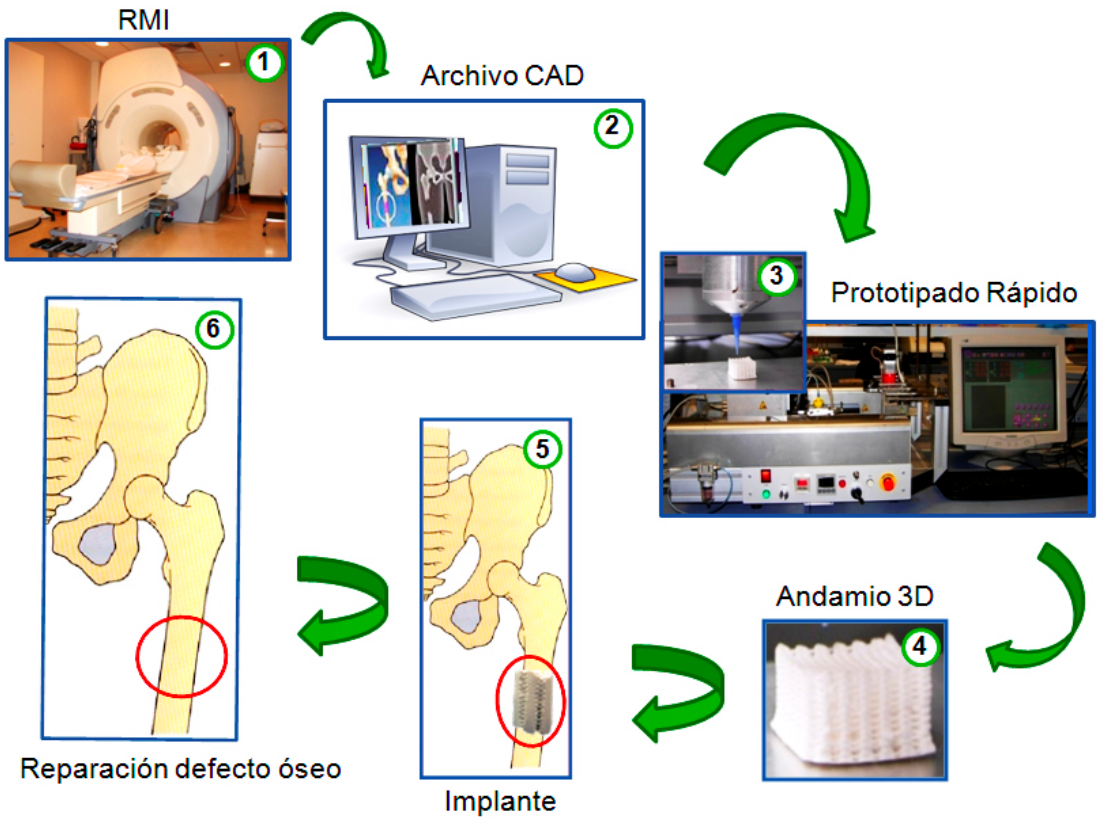

Figura 2.1. Pasos secuenciales del proceso de utilización de andamios 3D para regeneración tisular ósea.

Según Hutmacher y colaboradores, un implante óseo sintético, también llamado andamio, debe reunir una serie de requisitos: (i) ser biocompatible y bioreabsorbible, manteniendo un equilibrio entre el proceso de degradación controlable y el proceso de resorción, permitiendo el crecimiento del tejido, (ii) ser tridimensional y altamente poroso con una red porosa interconectada que permita el crecimiento y la colonización celular, la vascularización, el flujo de transporte de nutrientes y de residuos metabólicos, (iii) presentar unas características químicas de superficie adecuadas para garantizar los procesos de adhesión, proliferación y diferenciación celular, (iv) tener propiedades mecánicas similares a las del tejido en el que va a ser implantado, (v) ser sintetizado a través de un proceso de fabricación que permita su producción a gran escala y (vi) ser esterilizable y presentar los requerimientos necesarios para su uso clínico [12,13].

Desde que en la década de los noventa, R. Langer, J. Vacanti, L. Griffith y sus colaboradores del Massachusetts Institute of Technology (MIT) y la Harvard University definieran la ingeniería de tejidos como la aplicación de principios y métodos de la ingeniería y las ciencias biológicas para el desarrollo de sustitutos para restaurar tejidos utilizando células transplantadas en matrices sintéticas (andamios) [1], en las dos décadas posteriores ha existido un gran avance en el diseño de nuevos materiales y estructuras que sirvan como andamios para ingeniería tisular [14]. Sin embargo, el paso de estos materiales y estructuras desde los laboratorios a la clínica es tremendamente limitado, debido a la confluencia de varios factores: (i) conocimiento limitado tanto de los requerimientos necesarios en el diseño de los andamios, como de los diferentes materiales de partida a partir de los cuales se pueden fabricar andamios 3D; (ii) necesidad de un conocimiento más completo de los procesos de degradación *in vivo* del material; (iii) falta de desarrollo de métodos para la fabricación de biomateriales con estructuras 3D complejas; (iv) falta de una mejor integración de las técnicas de diseño computacional con los métodos de fabricación de andamios y con la terapia personalizada. En este sentido, la integración de todos estos factores es vital para alcanzar el reto "*desde el concepto a la clínica*" [15].

Teniendo en cuenta la normativa citada por la US Food and Drug Administration (FDA), en referencia a la aplicación clínica y al material del que está formado un andamio, se han establecido cuatro aspectos fundamentales que constituyen los pilares para el éxito de los andamios utilizados en ingeniería de tejidos. Éstos son: *Forma*, *Función*, *Formación* y *Fijación* [15]. **Forma**, viene definida por el defecto geométrico 3D obtenido, normalmente, por tomografía computacional (TC) o a través de imágenes de resonancia magnética (RM). Se refiere a que el andamio debe rellenar inicialmente todo el defecto 3D y con el paso del tiempo, el nuevo tejido formado debe alcanzar la anatomía 3D original. **Función**, hace referencia a que el andamio debe temporalmente soportar todas las demandas funcionales diarias, normalmente mecánicas, hasta que el nuevo tejido formado pueda hacerse cargo de ellas. Asimismo, la porosidad del andamio también estaría incluida en este punto, ya que como veremos posteriormente, está implicada en los procesos de osteogénesis. **Formación**, significa que el andamio debe mejorar la regeneración tisular mediante la liberación de moléculas biológicas apropiadas, proporcionando un microambiente adecuado para el transporte de masa. Por último, **Fijación** hace referencia a un compendio de los tres aspectos anteriores,

encaminados todos ellos a garantizar la adhesión e integración del andamio con los tejidos circundantes. En este sentido, las características químicas y estructurales de la superficie del andamio van a jugar un papel primordial. La **Figura 2.2.** esquematiza los cuatro requerimientos fundamentales (4F) que tiene que cumplir un andamio en relación con las diferentes propiedades a tener en cuenta en el diseño de andamios para ingeniería tisular ósea.

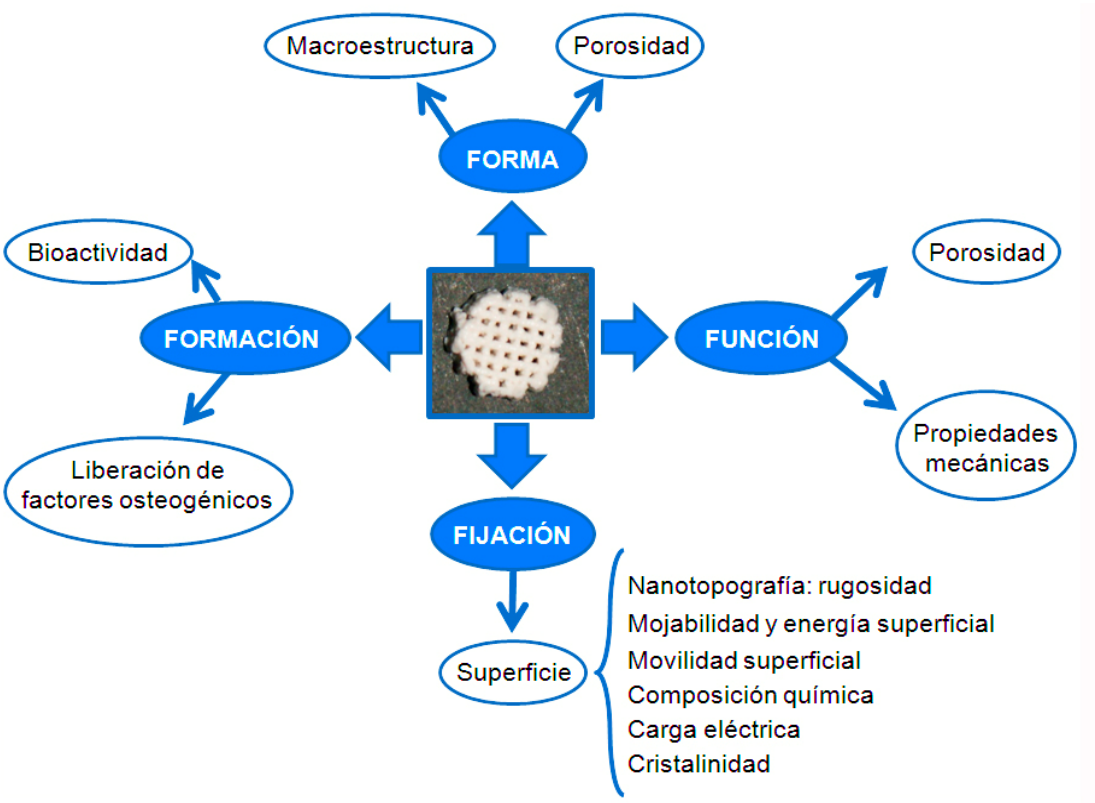

Figura 2.2. Requerimientos de los andamios para ingeniería tisular ósea.

Dado que el objetivo de la ingeniería tisular ósea es obtener nuevo tejido que mimetice al hueso natural [12], es importante conocer en detalle la estructura jerárquica ósea, que se pone de manifiesto a diferentes escalas de magnitud como se muestra en la **Figura 2.3.**, desde la macroestructura a la escala nanométrica. El hueso tiene una fuerte capa compacta externa calcificada, la cual presenta unidades estructurales cilíndricas denominadas osteonas o sistemas de Harvers (**Figura 2.3.A y 2.3.B**). Las células residentes en el tejido óseo presentan receptores de membrana celular a través de los cuales interaccionan con sitios de unión específicos de las fibras de colágeno (**Figura 2.3.C**). Además, el hueso natural muestra organización a nivel de escala nanométrica,

donde la matriz extracelular está principalmente constituida por fibras de colágeno que interaccionan con cristales de apatita nanocristalina (25-4 nm) (**Figura 2.3.D**) [16,17]. Esta complejidad estructural del tejido óseo es la base de sus excelentes propiedades mecánicas. Convencionalmente, los andamios han sido diseñados a nivel macroscópico con propiedades mecánicas similares a las del tejido óseo natural, sin prestar demasiada atención a los detalles a nivel de escala nanométrica observados en este tejido. Sin embargo, desde que es conocido que dichos detalles ejercen una gran influencia en la respuesta celular, la incorporación de los mismos a los andamios constituiría una mejora en sus propiedades finales [18,19,20].

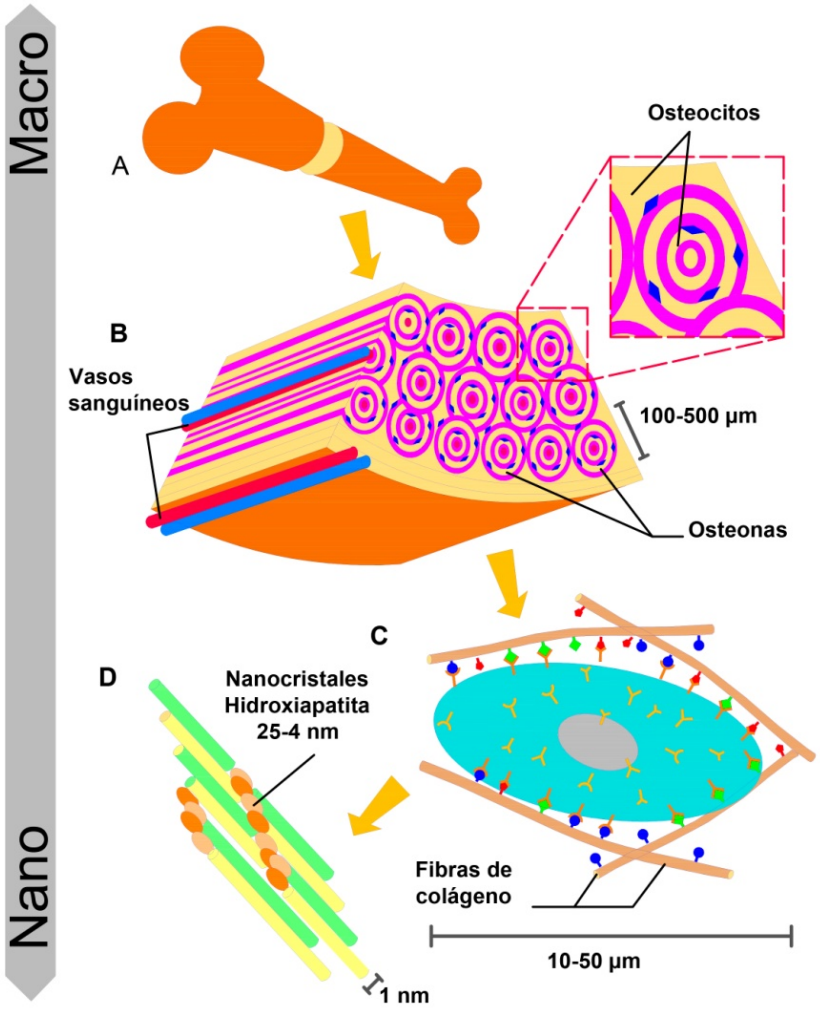

Figura 2.3. Organización jerarquizada del tejido óseo a diferentes escalas de magnitud. Adaptada de la referencia [17].

Los principales tipos celulares presentes en el tejido óseo son osteoblastos, osteocitos y osteoclastos, a partir de los cuales la estructura ósea es continuamente remodelada. Los osteoblastos son las células osteoformadoras que llevan a cabo la síntesis y deposición de proteínas de la matriz ósea [21]. También producen factores de crecimiento que provocan efectos autocrinos y paracrinos sobre el crecimiento óseo. Los osteoblastos totalmente diferenciados quedan embebidos en la matriz ósea mineralizada y se convierten en osteocitos, que residen en el interior de las lagunas de la sustancia intersticial calcificada pero también participan en el remodelado óseo a través de mecanismos de comunicación celular. Los osteoclastos son los responsables de la resorción ósea. Son células móviles de mayor tamaño ampliamente ramificadas, con citoplasma acidófilo, varios núcleos y numerosos lisosomas con enzimas proteolíticas que intervienen en la degradación de la matriz ósea [22].

Los principales rasgos a considerar en el diseño de andamios 3D para regeneración tisular ósea son:

(i) *Macroestructura*. Es importante definir el volumen final del andamio que dará forma al tejido en proceso de regeneración. Existen situaciones en las que la zona a reparar es muy compleja por lo que se necesitan técnicas más precisas que permitan una réplica exacta del defecto a reparar.

(ii) *Propiedades mecánicas*. Los andamios 3D deben presentar fuerza mecánica suficiente para poder actuar como plantillas temporales en los defectos mientras que el tejido se regenera. Utilizando las propiedades mecánicas del hueso nativo como referencia, los andamios deberían exhibir propiedades elásticas lineares con un módulo de cientos de MPa. Además, las propiedades del andamio irán disminuyendo conforme se vaya produciendo la degradación del mismo. Por lo tanto, aunque el andamio presente propiedades mecánicas suficientes en el momento de la implantación, la manera en que sus propiedades cambian durante el proceso de degradación también podría afectar a la función del mismo [23].

(iii) *Tamaño de poro, porosidad e interconectividad*. Mientras que el tamaño de poro es una variable importante para estimular el crecimiento óseo y la formación de nuevo hueso, la red porosa interconectada y la porosidad de un andamio son factores críticos para asegurar la distribución espacial uniforme de las células, la supervivencia celular, la proliferación y la migración celular [24]. Además, tanto la porosidad como el grado de interconectividad de un andamio 3D afectan

directamente a la difusión de los nutrientes fisiológicos y gases, así como a la eliminación de los productos de desecho metabólico. Tamai y colaboradores han determinado que interconexiones de poros < 10 micras no permiten la migración de células de poro a poro [25]. Teniendo en cuenta datos bibliográficos, la porosidad ideal necesaria para al crecimiento óseo se encuentra en el rango de 35-75% [3, 12]. Asimismo, se ha establecido que poros con tamaños inferiores a 1 μm, son apropiados para interaccionar con proteínas y son los principales responsables de inducir la formación de la capa de hidroxicarbonato apatita en contacto con los fluidos fisiológicos. Poros con tamaños en el rango de 1-20 μm son importantes en los procesos de adhesión celular, orientación y direccionalidad del crecimiento celular. Los poros entre 100 y 1000 μm juegan un importante papel en la funcionalidad del implante, siendo esenciales para garantizar los procesos de angiogénesis y permitir el aporte de nutrientes y la eliminación de los desechos celulares.

(iv) *Propiedades de superficie*. Las propiedades de superficie de un implante tales como rugosidad (nanotopografía), mojabilidad y energía superficial, movilidad superficial, composición, carga eléctrica y cristalinidad juegan un papel primordial en la adhesión de las células al mismo [26]. Diferentes estudios han puesto de manifiesto que los detalles a nivel de escala nanométrica presentes en los tejidos y órganos (**Figura 2.3.**) han de ser tenidos en cuenta en el diseño de implantes ya que influyen de forma importante en la respuesta celular y son vitales para garantizar su éxito [17,27,28,29,30].

Existe una gran variedad de metodologías para fabricar andamios porosos 3D con propósitos en reparación y regeneración ósea [3,14,31,32,33,34,35,36,37]. Cada una de ellas confiere al andamio final características estructurales diferentes, por lo que es muy importante elegir la técnica correcta según la aplicación final del andamio. Dichas metodologías incluyen desde métodos más convencionales caracterizados, en general, por un diseño no controlado, hasta tecnologías más sofisticadas como las técnicas de prototipado rápido, que permiten un control exacto tanto en la forma (macroestructura) como en la porosidad interna [38].

Los métodos convencionales, entre los que destacamos, *solvent casting* [39,40,41], disolución y colada con liberación de partículas, *gel-casting*/replica [42],

separación de fases inducida térmicamente [43], sinterización de microesferas [44], espumeo mediante generación de gas [45,46,47], electrohilado [48,49], hacen referencia a los procesos de fabricación de andamios con un diseño no controlado, de forma que estos métodos de fabricación no producen arquitecturas 3D con un diseño específico, tienen una reducida reproducibilidad y un bajo control sobre la geometría y porosidad interna del andamio. La principal ventaja de estos métodos es su bajo coste y su capacidad para crear andamios con elevada porosidad (40-90 %) y con macroporos entre 100-500 μm. Sin embargo la interconectividad obtenida es muy baja, reduciéndose a unas pocas micras [50].

Dentro de estos métodos convencionales, cabe destacar la técnica de espumeo por gas (*gas-foaming*), a partir de la cual se obtienen andamios 3D *tipo espumas*. Estos andamios se caracterizan por ser redes macroporosas que mimetizan la estructura del hueso esponjoso [51,52,53,54,55,56]. Presentan una estructura interconectada con una porosidad, generalmente superior al 60% y con un tamaño de poro en el rango de 200-700 μm. Sin embargo, debido a su elevado grado de porosidad las propiedades mecánicas son muy pobres, siendo inevitable el recubrimiento de dichos andamios con soluciones polímericas para aumentar tales propiedades [57,58,59,60]. La **Figura 2.4.** muestra andamios 3D tipo *espumas* de hidroxiapatita nanocristalina exhibiendo una red macroporosa interconectada y altamente jerarquizada en el rango de 1-400 μm, con un tamaño de cristal similar al de las apatitas biológicas. Tales *espumas* macroporosas han mostrado excelente internalización, proliferación y diferenciación de osteoblastos, con una adecuada colonización de toda la superficie útil de la *espuma* y una apropiada degradación sin ocasionar efectos citotóxicos [61]. Estos resultados se muestran en el artículo titulado: "***Biological performance of HA-biopolymer foams: in vitro cell response***", citado en el **anexo IV**. Además, los estudios *in vivo* han revelado excelentes índices de osteointegración con el tejido circundante [62].

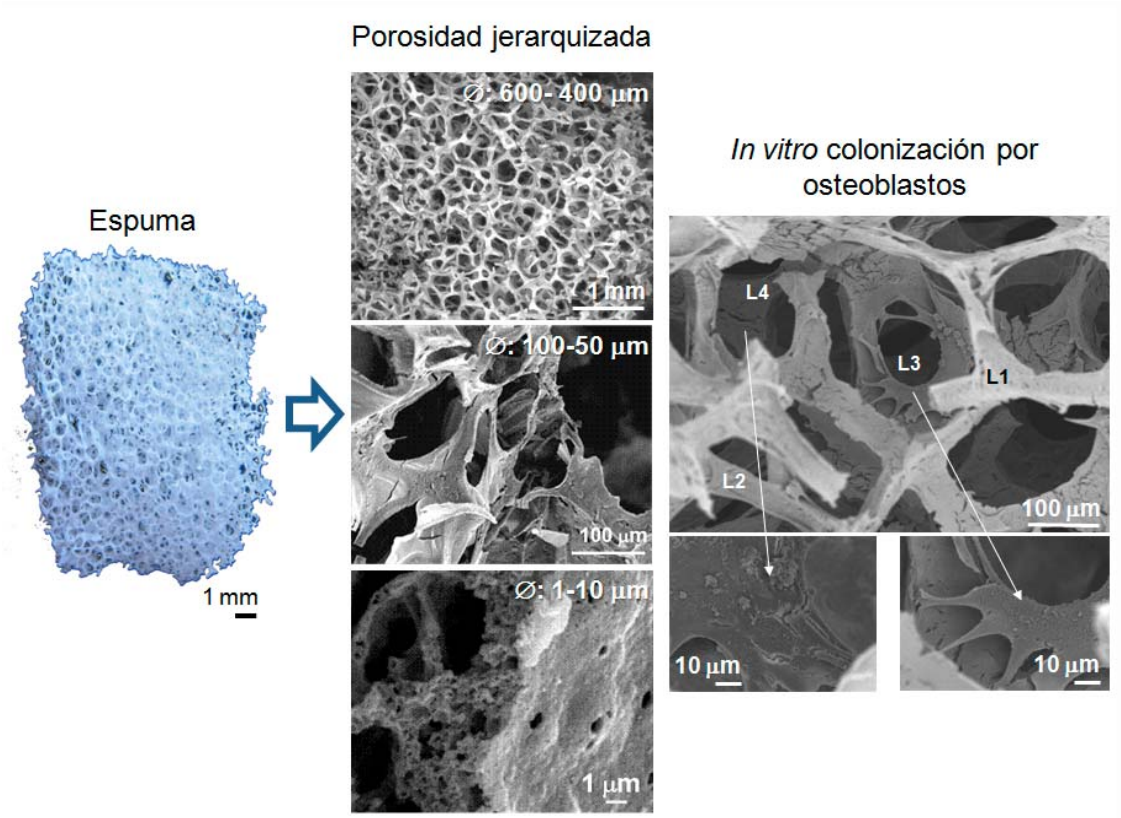

Figura 2.4. Espuma de hidroxiapatita pura obtenida mediante el proceso *gas foaming* en presencia de un surfactante mostrando diferentes rangos de porosidad. *In vitro* colonización de la *espuma* por osteoblastos. Adaptada de las referencias [60, 61].

Una alternativa a estos métodos convencionales es la técnica de prototipado rápido, también llamada fabricación libre de forma sólida (SFF) [63,64]. Este es el nombre dado al conjunto de tecnologías que implican la construcción 3D de objetos mediante una impresora 3D que va reproduciendo, capa por capa, un modelo de diseño asistido por ordenador (formato CAD). La ventaja adicional de estas técnicas es que para crear el archivo en formato CAD, se pueden utilizar los datos obtenidos a partir de tomografía computarizada (TC) o de resonancia magnética de imagen (RMI), produciendo andamios con un elevado control de su estructura porosa, comportamiento mecánico, permeabilidad y difusión al tejido dañado (**Figura 2.1.**). Asimismo, dichas técnicas son capaces de reproducir, de forma exacta, la geometría del tejido dañado a reparar. Por tanto, las tecnologías SFF son una alternativa para producir andamios de forma personalizada, predefinida y reproducible, reduciendo notablemente los tiempos de fabricación. Estos métodos permiten la construcción de estructuras macroporosas en las que los poros y sus interconexiones son similares en tamaño y forma a los del hueso

dañado. Por esta razón, para que las estructuras construidas por estas tecnologías tengan el mismo grado de funcionalidad que las obtenidas por los métodos convencionales no es necesario que presenten un elevado volumen de porosidad [65,66,67]. Además, los poros interconectados de forma regular proporcionan canales continuos para la vascularización, siendo necesarios para nutrir al hueso neoformado y eliminar los productos de desecho metabólico [68,69].

La **Tabla 2.1.** muestra los diferentes tipos de técnicas de SFF, detallando las ventajas y desventajas de cada una de ellas.

Tabla 2.1. Tipos de técnicas de fabricación libre de forma sólida (SFF). Adaptada de la referencia [67].

Método	Tamaño de poro/precisión	Ventajas	Desventajas
3DP 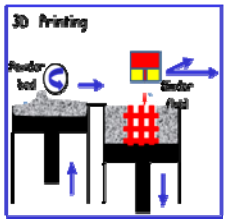	45-500µm/0.1	Aplicable a una amplia gama de materiales Ninguna estructura de apoyo necesario Coste eficiente	Baja resistencia Unión débil entre partículas Puede quedar atrapado polvo en el interior del cuerpo Requiere temperatura elevada
SLS 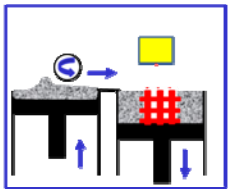	45-100µm/0.075	Elevadas propiedades mecánicas Ninguna estructura de apoyo necesaria	Puede quedar atrapado polvo en el interior del cuerpo
SLA 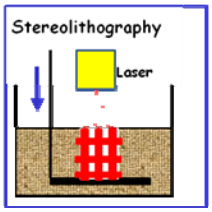	400-1 µm/0.05	Alta precisión	Limitaciones a materiales Bajas propiedades mecánicas Fotopolímero necesario Estructura de soporte necesaria
RC 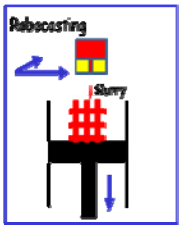	250-1000 µm/0.1	Alta precisión Ninguna estructura de apoyo necesaria Combinación de materiales con 2 boquillas	Elevado tiempo de conformación de la pieza Proceso caro
FDM 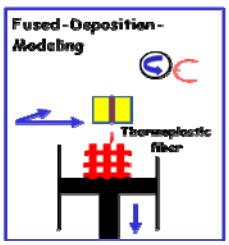	250-1000 µm/0.05	Ninguna estructura de apoyo necesario Sin polvo atrapado	Limitaciones a materiales Requiere temperatura elevada Polímeros termoplásticos requeridos Anisotropía mecánica

Dado que uno de los objetivos de esta Tesis Doctoral es la fabricación por *robocasting* de andamios 3D a partir del *nanocomposite* MGHA, en esta sección se describirá brevemente dicha técnica. *Robocasting*, también conocido como montaje de escritura directa o deposición microrobótica, permite construir andamios 3D a partir de pastas (generalmente poliméricas) con un alto grado de precisión y con un amplio rango de tamaño de poro, según las necesidades. Así, un andamio 3D se va construyendo capa por capa, a partir de la extrusión de la pasta a través de la boquilla de deposición (**Figura 2.5.**) siguiendo el patrón específico del archivo CAD previamente diseñado. La optimización de la pasta adecuada para esta técnica requiere de una cuidadosa adaptación de sus propiedades viscoelásticas a través de un control preciso de su composición [70,71].

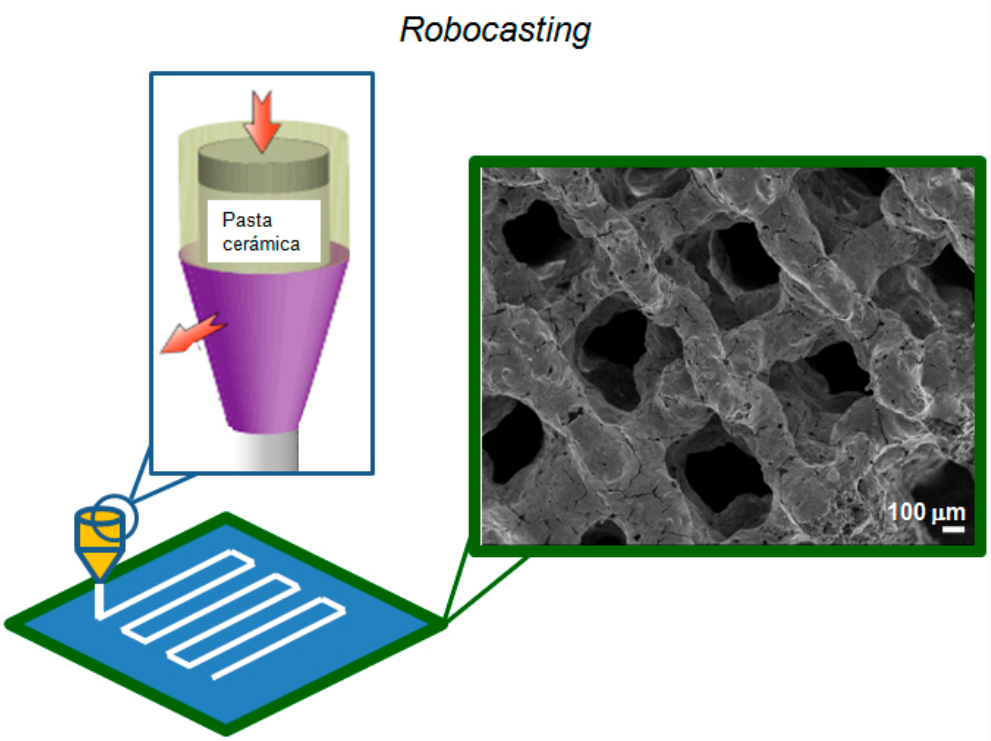

Figura 2.5. Ilustración esquemática del proceso de fabricación de un andamio 3D por *robocasting*. Micrografía de SEM de un andamio obtenido por esta técnica.

A pesar del gran potencial que tiene la técnica *robocasting* para aplicaciones en ingeniería tisular ósea, las pastas mayoritariamente utilizadas hasta el momento han sido de naturaleza polimérica, no habiéndose desarrollado hasta hace poco tiempo pastas a partir de polvos cerámicos de fosfatos de calcio. Las pastas formadas a partir de

cualquier polvo cerámico deben satisfacer dos criterios importantes [72]: (i) las propiedades viscoelásticas de la pasta deben permitir que ésta fluya a través del cartucho de inyección para que las diferentes capas se puedan ir depositando consecutivamente, (ii) la pasta debe tener un alto contenido en material cerámico para minimizar la contracción durante el secado del andamio, de manera que la red de partículas sea capaz de resistir la tensión capilar [73]. La fabricación de estas pastas es tediosa y para su adecuada extrusión se requiere la obtención previa del material cerámico en polvo y la posterior selección de un tamaño de partícula apropiado, mediante procesos de tamización. En general, a continuación, el polvo cerámico es disuelto en un solvente orgánico y posteriormente es mezclado con una disolución polimérica, obteniéndose así una pasta fácil de extruir [74]. Dependiendo del polímero utilizado, la temperatura de calcinación de los andamios conformados oscila entre los 300-1000ºC. Diferentes estudios han mostrado una relación directa entre la temperatura de calcinación y las propiedades mecánicas de los andamios obtenidos [75,76,77].

Otra manera de obtener una pasta óptima para la técnica *robocasting* es la posibilidad de combinar un componente cerámico con un componente polimérico biocompatible/biodegradable, sin la necesidad de calcinar posteriormente los andamios conformados. Esto permite obtener andamios *composites* (polímero-cerámico) con propiedades mecánicas optimizadas y mejores respuestas celulares [78,79,80,81]. En este caso, el componente cerámico es un polvo cerámico previamente calcinado y tamizado.

La tecnología *robocasting* también ha sido empleada para la conformación de andamios a partir de materiales nanoestructurados como son los vidrios bioactivos mesoporosos [82]. Dicho proceso es muy tedioso y requiere de dos calcinaciones, una previa, necesaria para la obtención del material nanoestructurado en polvo, y otra necesaria para la eliminación del componente polimérico tras el conformado del andamio. Esto provoca una brusca disminución en las propiedades texturales finales del andamio con respecto a las del material nanoestructurado de partida.

Recientemente, para la obtención de pastas cerámicas se ha descrito una metodología muy sencilla realizable en un único paso, basada en la incorporación de un polímero concreto, (hidroxi)metilcelulosa, en el sol-precursor de un vidrio mesoporoso

[83,84,85]. La incorporación de este polímero durante el proceso de síntesis del vidrio mesoporoso permite incrementar las propiedades reológicas del sol para poder ser extruido y la formación de macroporosidad en el andamio tras el proceso de calcinación (normalmente a 700ºC). Dicha metodología ha permitido la fabricación de andamios macroporosos preservando la mesoporosidad intrínseca del vidrio. Uno de los objetivos de la presente Tesis Doctoral ha sido el conformado por *robocasting* de andamios 3D con meso-macroporosidad jerarquizada a partir del sol precursor del *nanocomposite* MGHA y utilizando el polímero metilcelulosa para la formación de la pasta. Además, se ha realizado la evaluación biológica *in vitro* de los mismos analizando los efectos que ejercen sobre diferentes tipos celulares implicados en la respuesta inmune, tanto innata como adaptativa y sobre la adhesión, proliferación y diferenciación de preosteoblastos.

A día de hoy, uno de los principales retos en el campo de los biomateriales para ingeniería tisular ósea es garantizar el éxito del implante tras la intervención quirúrgica. La primera característica que ha de cumplir cualquier andamio para ingeniería tisular es que debe ser biocompatible, no produciendo citotoxicidad y permitiendo además los procesos de adhesión, proliferación y migración celular a través de él. Sin embargo, el éxito o el fracaso de un andamio después de ser implantado dependen invariablemente de la respuesta del tejido huésped a él. Por esta razón, el andamio no debe inducir reacción inmune, ya que se podría ralentizar el proceso de cicatrización, o incluso, se podría producir el rechazo por el organismo. Así, el estudio *in vitro* de los efectos del biomaterial sobre las células del sistema inmune es un aspecto esencial en la evaluación de la biocompatibilidad de cualquier andamio, previa a su implantación *in vivo* [86].

La respuesta inmune comprende mecanismos de defensa tanto innatos como adaptativos que activan coordinadamente a diferentes poblaciones celulares. La respuesta innata implica la acción de neutrófilos, primera población celular en llegar al tejido dañado, seguida de la acción de monocitos y macrófagos, que son células presentadoras de antígenos (APC) con función fagocitaria. Estas poblaciones celulares realizan varias funciones biológicas como la producción de especies reactivas de oxígeno y de mediadores inflamatorios [87]. Las células *natural killer* (NK) también juegan un importante papel en la respuesta innata, eliminando directamente células transformadas o infectadas por determinados virus, mediante secreción de moléculas citotóxicas o citoquinas [88]. Todas estas poblaciones celulares circulan por el

organismo monitorizando señales que puedan desencadenar su activación, diferenciación y expansión, activando así, a su vez a las poblaciones celulares que forman parte de la respuesta inmune adaptativa. La respuesta adaptativa está mediada por linfocitos antígeno-específicos, como las células T y las células B. Estas poblaciones celulares se activan tras entrar en contacto con los péptidos antigénicos procesados y presentados por las células APC a través de receptores específicos. La activación de linfocitos promueve su diferenciación a diferentes fenotipos de subpoblaciones efectoras y conduce a la expresión de citoquinas y anticuerpos específicos. La expresión y secreción de citoquinas constituye un mecanismo efector importante de células inmunes, ya que determina la subsecuente activación o supresión de otras subpoblaciones celulares. Considerando su importante implicación en la respuesta inmune y en los procesos de inflamación, algunas de las citoquinas más destacadas son la interleuquina-2 (IL-2), interleuquina-10 (IL-10), INFγ (Interferón de tipo II) y el TNFα (Factor de Necrosis Tumoral Alpha). La IL-2 juega un papel central en la activación, proliferación y diferenciación de linfocitos T. También modula la expresión del INFγ, estimula la proliferación y diferenciación de células B activadas y aumenta la actividad de las células NK. La IL-10 es una citoquina antiinflamatoria expresada por diferentes subpoblaciones de células T, por células B, además de por células de la inmunidad innata como macrófagos, NK, eosinófilos y neutrófilos. El INFγ es producido por células B, T y NK activadas. Este interferón actúa de modo sinérgico con otras citoquinas, incluida el TNFα, activando a monocitos, macrófagos, NK y neutrófilos. El TNFα es una citoquina que juega un papel tanto en la inmunidad innata como en la adquirida. Está relacionado con propiedades pro-inflamatorias induciendo la expresión de varias citoquinas tales como IL-1, IL-6, IL-8, entre otras, lo que conduce a un reclutamiento y activación de células en el lugar de la lesión. El TNFα es expresado tanto por macrófagos como por linfocitos activados, células NK y neutrófilos, entre otros tipos celulares. La **Figura 2.6.** representa a modo de esquema los mecanismos de defensa tanto innatos como adquiridos que forman parte de la respuesta inmune.

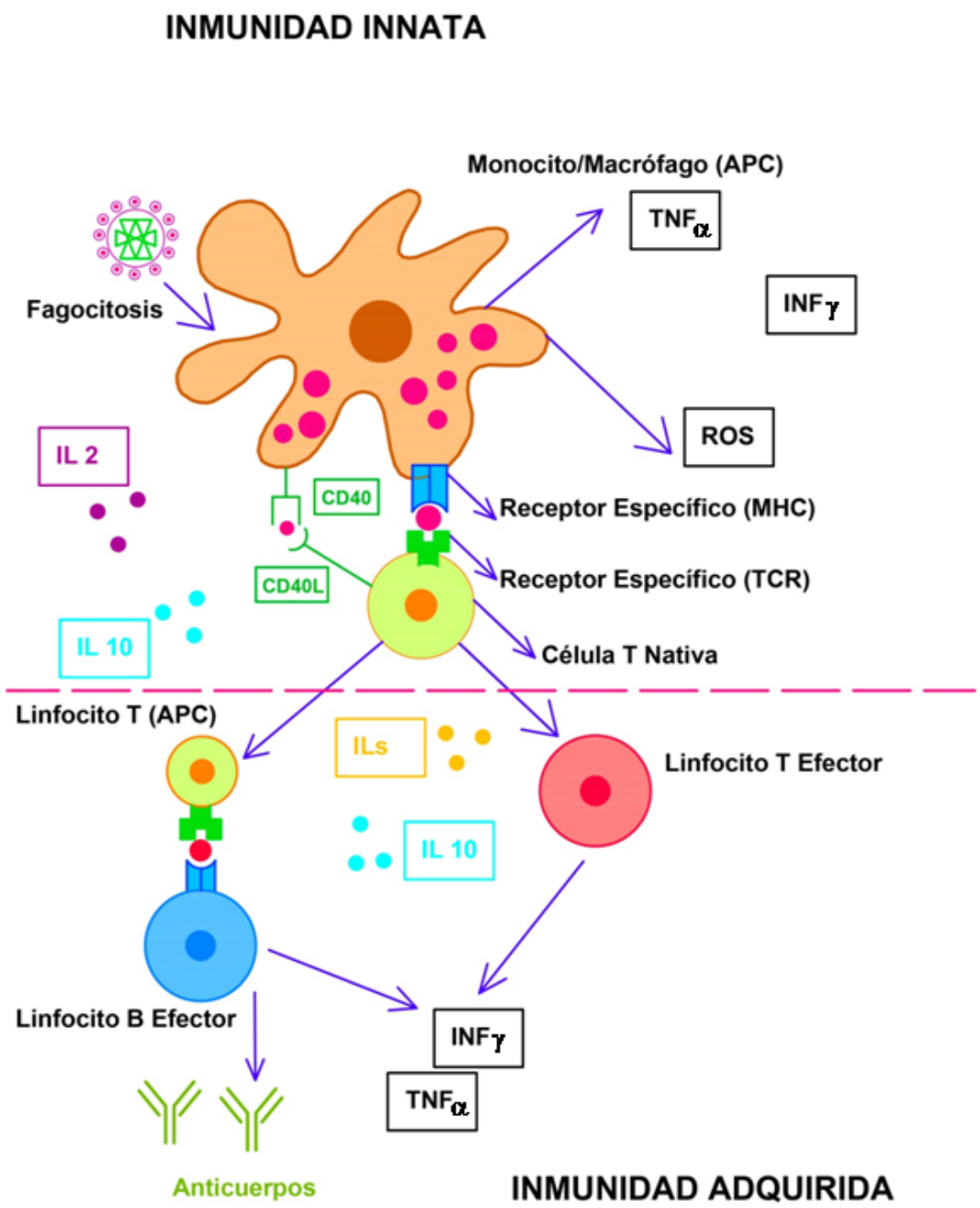

Figura 2.6. Mecanismos de defensa de la inmunidad innata y adquirida.

Normalmente, la interacción de todas estas células inmunes del huésped con los biomateriales tiene implicaciones negativas para la remodelación de tejidos. De hecho, durante décadas, la interacción de los macrófagos con la matriz extracelular recién depositada alrededor del implante, acompañada de una respuesta angiogénica, se ha interpretado como un paso precursor de la formación de tejido de granulación, la clásica reacción de cuerpo extraño, con consecuencias negativas en la aceptación del implante

por el organismo [89]. Sin embargo, recientemente se ha demostrado que los macrófagos pueden ser beneficiosos para mejorar la integración del implante debido a su notable plasticidad funcional. Así, los macrófagos pueden desempeñar tanto funciones positivas como negativas en los procesos de remodelación tisular. Estas células presentan dos fenotipos, proinflamatorio (M1) y reparador (M2) [90], cuyo balance determina la respuesta del huésped al biomaterial junto con la participación de diversas citoquinas específicas. En este sentido, las investigaciones más recientes proponen el diseño de biomateriales capaces de modular la función de las células del sistema inmune, para obtener respuestas apropiadas en los lugares de la implantación [91,92]. Uno de los objetivos de la presente Tesis Doctoral ha sido estudiar los efectos producidos por andamios 3D del material *nanocomposite* MGHA sobre la respuesta inmune mediante el estudio de su interacción con los diferentes tipos celulares implicados. Los resultados obtenidos, se muestran en el artículo titulado: **"*Effects of 3D nanocomposite bioceramic scaffolds on the immune response*"**, expuesto en el apartado **2.3.**

El primer acontecimiento que tiene lugar durante el reconocimiento biológico entre la superficie de un implante y las células adyacentes es el proceso de adhesión celular, el cual es vital ya que de él dependen las posteriores respuestas celulares como extensión, proliferación y diferenciación celular [93]. Este proceso se produce a través de interacciones no específicas e interacciones específicas, existiendo efectos cooperativos entre ambas [94], tal y como se muestra en la **Figura 2.7.** La *adhesión no específica* tiene lugar mediante interacciones físicas y químicas y es responsable de la denominada *etapa temprana de adhesión celular*. Esta etapa implica el contacto de la superficie del biomaterial, en la cual, previamente se han depositado proteínas del plasma sanguíneo que formarán parte de la matriz extracelular, con el espacio pericelular (PCC) que contiene ácido hialurónico, cargado negativamente en condiciones fisiológicas [95]. Subsecuentemente, se activan los *mecanismos de adhesión específicos* a través de la interacción de ligandos extracelulares con receptores de la membrana plasmática [96]. Estos receptores son proteínas transmembrana heterodiméricas denominadas integrinas, las cuales, interaccionan con secuencias peptídicas específicas de las proteínas de la matriz extracelular que se depositaron previamente [97].

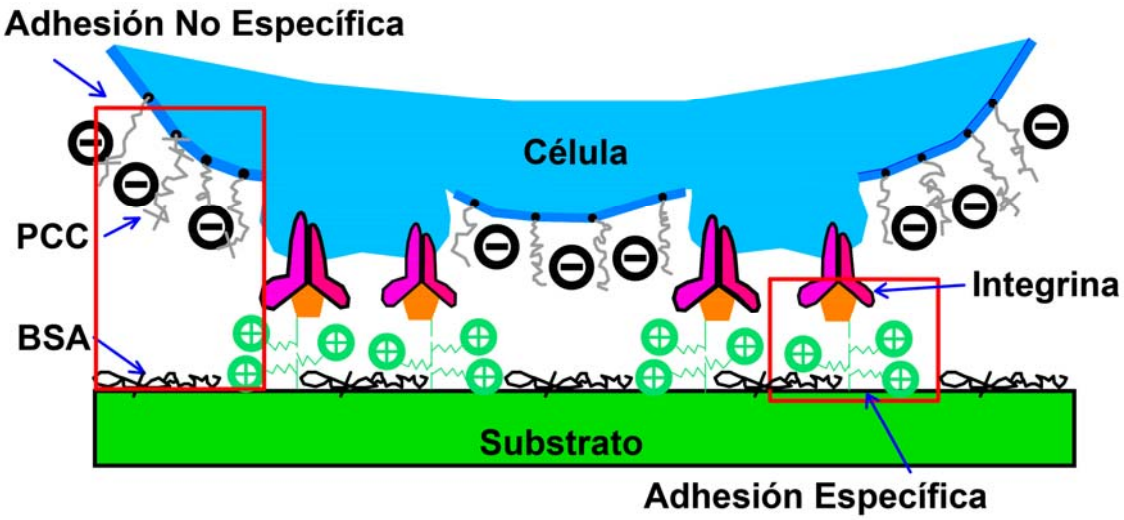

Figura 2.7. Esquema representativo de las interacciones específicas y no específicas de la membrana celular con la superficie de un substrato. Las siglas en inglés BSA hacen referencia a la proteína albúmina de suero bovino, utilizada como modelo de proteína sérica. Adaptada de la referencia [101].

Desgraciadamente, la mayoría de los implantes candidatos para ingeniería tisular carecen de las propiedades de superficie necesarias para que el reconocimiento biológico se produzca de forma satisfactoria, asegurando la adhesión celular adecuada [98]. Por este motivo, la mayoría de los esfuerzos realizados en este tema se han dirigido hacia la "*biodecoración*" de la superficie de dichos implantes con el fin de hacerla más atractiva a las células. Normalmente, dicho proceso consiste en anclar de forma covalente a la superficie del implante proteínas o cortas secuencias peptídicas presentes en las proteínas específicas de la matriz extracelular, como son las conocidas secuencias RGDs (arginina-glicocola-aspártico), entre otras [98,99,100,101,102]. Sin embargo, los resultados obtenidos hasta el momento no satisfacen los requerimientos necesarios para lograr una óptima adhesión celular y garantizar así una colonización completa del implante. De hecho, cuando se realizan estudios celulares *in vitro*, ninguno de los andamios estudiados logra superar en su superficie los niveles de adhesión conseguidos en las placas comercializadas para cultivo celular (TCP = Tissue Culture Plastic). Dicho soporte se caracteriza por poseer moléculas de polilisina en su superficie, las cuales proporcionan cargas positivas gracias al grupo amino presente en su cadena lateral. Debido a sus cargas positivas, el TCP presenta una buena adhesión celular por su capacidad de adsorción de las proteínas del medio de cultivo, mejorando

así la *adhesión celular no específica* fundamental en las primeras etapas del proceso [103,104].

Este hecho llevó a pensar que un método sencillo y con óptima relación coste/efectividad, como es el proceso de funcionalización directa de la superficie de los andamios con grupos aminopropilsilano, podría ser clave para mejorar el proceso de adhesión celular sobre los andamios. Por ello, uno de los objetivos de la presente Tesis Doctoral fue la funcionalización de la superficie de andamios 3D del material MGHA con grupos aminopropilsilano y el posterior estudio de los efectos producidos por dicha funcionalización sobre la adhesión y diferenciación de preosteoblastos. Los resultados obtenidos, se muestran en el artículo titulado: **"*Tailoring hierarchical meso-macroporous 3D scaffolds: from nano to macro*"**, expuesto en el apartado **2.4.**

2.2. Conformado de andamios meso-macroporosos basados en el *nanocomposite* MGHA mediante prototipado rápido

Durante esta Tesis Doctoral, se han conformado andamios jerarquizados meso-macroporosos mediante la técnica de prototipado rápido utilizando un 3D Bioplotter™ EnvisionTEC GmbH Prefactory® (Gladbeck, Germany). Para ello se ha preparado una pasta cerámica utilizando como material de partida el sol precursor del *nanocomposite* MGHA al que posteriormente se le añadirá el polímero metilcelulosa.

En una síntesis típica, 19.5 g de surfactante *Pluronic F127* se disuelven en 168.6 mL de etanol absoluto (99.5%) con 12.8 mL de una solución HCl 1.0 M y 19.4 mL de agua MiliQ. A continuación, las cantidades apropiadas de tetraetilortosilicato (TEOS, 98%), trietilfosfato (TEP, 99.8%) y cloruro de calcio ($CaCl_2$•$4H_2O$, 99%) fueron añadidas como fuentes de SiO_2, P_2O_5 y CaO, respectivamente, en intervalos de 1 h en condiciones de agitación durante un total de 4 h a 40ºC. A continuación, el sol precursor se mantuvo en condiciones estáticas a la misma temperatura durante toda la noche, tras lo cual se envejeció mediante el método EISA durante 4-5 días, a 30ºC hasta alcanzar una reducción de volumen del 30%, aproximadamente. En ese momento, 5.55 g del polímero (hidroxipropil) metilcelulosa (MC) fueron incorporados al sol envejecido bajo condiciones de agitación en una relación molar *F127*/MC = 6, obteniendo así una pasta con la consistencia adecuada para su extrusión por el equipo de prototipado rápido. Los andamios fueron conformados mediante una deposición directa capa por capa, a temperatura ambiente. Cada capa fue previamente prediseñada en formato CAD con una rotación de 90º con respecto a la capa depositada con anterioridad. Tanto la velocidad de dispensación de la pasta como la presión a la que fue extruida fueron con el paso del tiempo modificadas ligeramente de los parámetros iniciales, con el fin de obtener resultados óptimos. El proceso de secado del andamio se produjo por evaporación del solvente (EISA) a 30ºC, tras lo cual fueron calcinados a 700ºC durante 6 h, dando lugar a los andamios denominados MGHA. La **Figura 2.8.** esquematiza el proceso de síntesis, obtención de la pasta adecuada para su extrusión y conformado de los andamios MGHA, así como la caracterización macro- y mesoestructural de los mismos.

Los andamios MGHA fueron exhaustivamente caracterizados por diferentes técnicas. Los resultados obtenidos forman parte del artículo titulado: **"*Tailoring***

hierarchical meso-macroporous 3D scaffolds: from nano to macro", expuesto en el apartado **2.4.** La macroporosidad de los andamios fue caracterizada por SEM y por porosimetría de intrusión de mercurio. Las micrografías de SEM muestran andamios MGHA con una simetría tetragonal de acuerdo con el diseño asistido por ordenador del prototipado rápido, donde veinte capas de pasta fueron extruidas hasta obtener andamios con un espesor total de 2 mm y un diámetro de 6,6 mm. Estos andamios presentan una red porosa jerarquizada con macroporos de 500 μm, conectados por canales de 250-300 μm de diámetro (**Figura 2.8.A**), características de porosidad requeridas para el crecimiento de nuevo tejido y el proceso de vascularización [3,6]. La micrografía de SEM a mayor magnificación (**Figura 2.8.B**) correspondiente a una sección transversal del andamio muestra notables diferencias entre el interior y el exterior del mismo. Mientras que la superficie externa muestra una topografía relativamente lisa con poros en el intervalo entre 1-10 μm, la superficie interna presenta numerosos poros en el intervalo de 30 a 80 μm, resultado del proceso de calcinación del polímero metilcelulosa [83,84]. Los datos obtenidos por porosimetría de intrusión de mercurio indican que los andamios presentan un sistema macroporoso perfectamente conectado, donde el porcentaje de porosidad total es del 60%, principalmente en el rango de 1-10 μm y 100-300 μm, acorde con los datos obtenidos por SEM. El difractograma de Rayos-X a bajos ángulos muestra tres máximos de difracción a 0.86, 1.43 y 1.67º (2θ), que pueden indexarse como las reflexiones (10), (11) y (20), respectivamente, de una estructura 2D hexagonal con grupo planar *P6mm*, en base a los resultados obtenidos por TEM. Las isotermas de adsorción/desorción de nitrógeno demuestran la presencia en los andamios MGHA de mesoporos de 10 nm, con valores de superficie de área y volumen de poro de 123 m^2/g y 0.2 cm^3/g, respectivamente. Al comparar estos resultados con los obtenidos en el *nanocomposite* MGHA pulverizado, se aprecia un notable incremento en el tamaño de poro desde 8.0 nm en el material en polvo, hasta 10 nm en el andamio MGHA, acompañado de una disminución tanto en los valores de superficie de área como en los de volumen de poro. Esta variación en los parámetros texturales (incremento en el tamaño de poro) probablemente sea debida a la incorporación durante el proceso de síntesis y posterior calcinación del polímero metilcelulosa.

Con el fin de confirmar la presencia de apatita nanocristalina en los andamios MGHA, se han realizado exhaustivos estudios de XRD y TEM. En el difractograma de

Rayos-X a altos ángulos se aprecian las reflexiones (002), (211) y (310), las cuales podrían corresponder a la presencia de una fase apatita. Además, las imágenes obtenidas por TEM (**Figura 2.8.C**) muestran zonas oscuras de mayor contraste distribuidas homogéneamente por toda la estructura mesoporosa. Estas zonas corresponden a partículas de una fase apatita nanocristalina. Al realizar la difracción de electrones a una de esas partículas (**Inset Figura 2.8.C**), aparecen halos de difracción difusos con espaciados d a 0.28, 0.27 y 0.34 nm, lo que corresponde a una fase apatita. Estos resultados confirman la estructura *nanocomposite* de los andamios MGHA, indicando que la incorporación del polímero metilcelulosa, necesario para el conformado de los mismos, no altera la estructura bifásica del material MGHA.

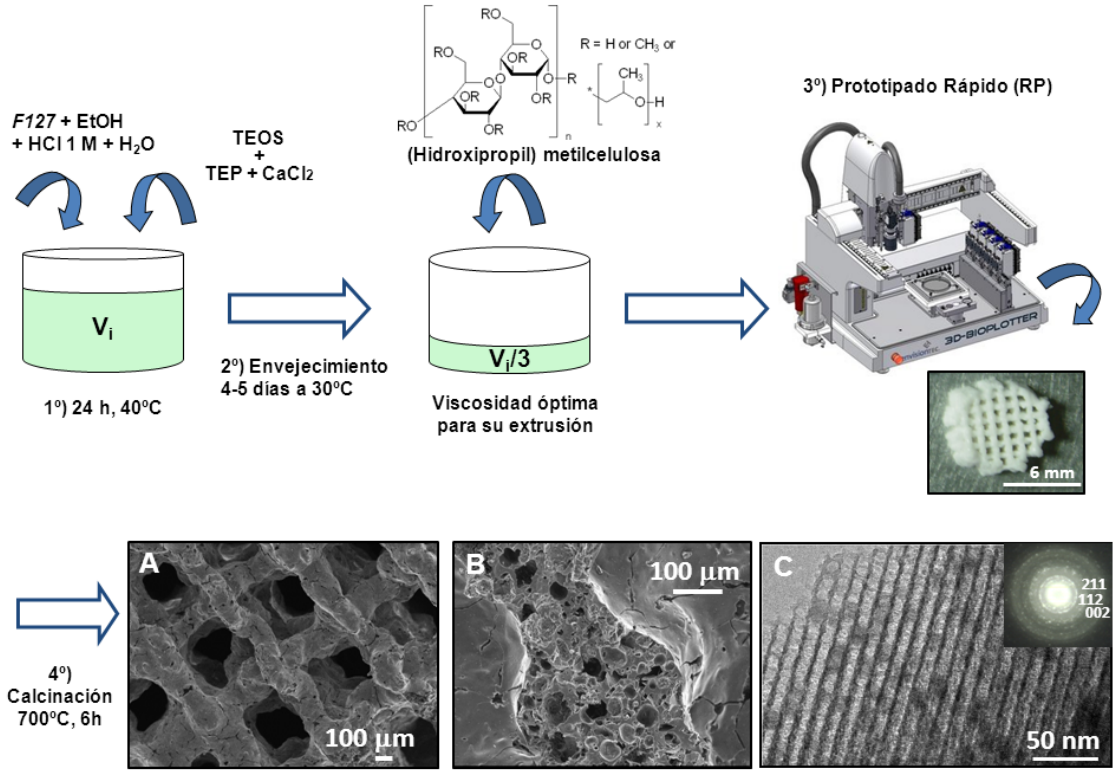

Figura 2.8. Pasos secuenciales del proceso de síntesis y conformado de andamios 3D MGHA (pasos 1º, 2º y 3º). Fotografía digital de uno de los andamios. Caracterización macro- y mesoestructural de andamios MGHA jerarquizados e interconectados: **(A)** Superficie y **(B)** sección transversal, obtenidas por SEM. **(C)** Imagen de TEM en la que se muestra la distribución homogénea de las partículas de apatita nanocristalina en una estructura mesoporosa 2D-hexagonal.

Por tanto, el proceso de síntesis sol-gel en presencia de un surfactante (*F127*) como agente director de la mesoestructura y un polímero biomacromolecular (metilcelulosa) como plantilla macroestructural, seguido de la técnica de prototipado rápido (*robocasting*, concretamente), permite la formación de andamios *nanocomposite* MGHA interconectados y jerarquizados, con diferentes escalas de porosidad: (i) mesoporos ordenados con diámetros de poro de 10 nm; (ii) macroporos con diámetros en el rango de 30-80 μm, con interconexiones de 1-10 μm y (iii) macroporos de 500 μm. Aparte de estas propiedades, el hecho de que uno de los componentes del andamio MGHA sea apatita nanocristalina, lo que constituye un elemento más común con la estructura ósea, hace pensar en las potenciales ventajas de estos andamios encaminadas a la regeneración tisular ósea.

2.3. Efectos de los andamios MGHA sobre la respuesta inmune

Mónica Cicuéndez, Pilar Portolés, María Montes-Casado, Isabel Izquierdo-Barba, María Vallet-Regí and María Teresa Portolés. ***Effects of 3D nanocomposite bioceramic scaffolds on the immune response. Journal of Materials Chemistry B. Enviado TB-ART-01-2014-000106.***

El éxito o el fracaso de un andamio tras ser implantado dependen de la respuesta del tejido en el que es colocado y sobre el que no debería inducir reacción inmune, ya que de lo contrario, se podría ralentizar el proceso de cicatrización, o incluso, se podría producir el rechazo por el organismo. Considerando este hecho y, como aspecto esencial en la evaluación de la biocompatibilidad de los andamios *nanocomposite* MGHA, el objetivo de este trabajo de investigación ha consistido en estudiar *in vitro* los efectos ocasionados por dichos andamios en diferentes poblaciones celulares implicadas tanto en la inmunidad innata como en la adquirida. Puesto que las células del sistema inmune pueden verse afectadas tanto por la superficie de un andamio como por los productos iónicos de su degradación, se han evaluado los posibles efectos citotóxicos producidos por los andamios *nanocomposite* MGHA y por sus extractos.

Paralelamente y con el fin de conocer el proceso de la degradación *in vitro* de dichos andamios, se han analizado los cambios producidos en su superficie así como la evolución de su estructura macroporosa a diferentes tiempos. Los resultados referentes a los cambios producidos en la superficie de dichos andamios ponen de manifiesto el elevado carácter reactivo de la misma en las primeras 24h, el cual queda reflejado por una gradual deposición de partículas aciculares de apatita propia del comportamiento bioactivo del material MGHA. Tras 7 días de ensayo, se observaron importantes cambios en la arquitectura macroporosa de los andamios, mostrando una notable degradación de su superficie. Con respecto a las variaciones iónicas del medio (DMEM), los resultados indican un elevado incremento en las concentraciones de calcio y fósforo en las primeras 24h de ensayo, seguido de un aumento más sostenido en tales concentraciones hasta los 7 días de ensayo. El perfil referente al silicio muestra un aumento progresivo de su concentración a lo largo del tiempo. Teniendo en cuenta la elevada reactividad de la superficie de los andamios MGHA en las primeras 24h y el proceso de degradación sufrido por el andamio a los 7 días de ensayo, los extractos

escogidos para estudiar su posible efecto sobre la respuesta inmune han sido los extractos obtenidos a 24h y 7 días.

En los estudios realizados con macrófagos RAW 264.7 como modelo experimental no se observaron alteraciones ni en la proliferación ni en la viabilidad de dichos macrófagos tras su cultivo sobre andamios MGHA. Estos andamios tampoco indujeron apoptosis en esta línea celular. Sin embargo, se detectó tanto una disminución del tamaño celular como un aumento del contenido de calcio intracelular después del contacto de los macrófagos RAW 264.7 con la superficie de andamios MGHA o con sus extractos. En relación con el aumento observado en el contenido de calcio intracelular, se detectaron variaciones en el contenido de especies reactivas de oxígeno (ROS), las cuales a su vez justifican los cambios observados en los porcentajes de poblaciones de macrófagos proinflamatorios (M1) y reparativos (M2), poniendo de manifiesto la plasticidad funcional de este tipo celular. Concretamente, tras cultivar macrófagos RAW 264.7 con los extractos de 7 días, los porcentajes de ambas poblaciones celulares se mantuvieron en equilibrio. Sin embargo, cuando dicho tipo celular se cultivó en contacto directo con los andamios durante 24h o en presencia de los extractos de 24h, se detectaron cambios en los porcentajes de las poblaciones M1 y M2 que pueden estar relacionados con la elevada reactividad/bioactividad de los andamios *nanocomposite* MGHA a tiempos iniciales. No obstante, cuando los ensayos se realizaron con células primarias de bazo de ratón, como un modelo experimental más próximo a las condiciones *in vivo*, no se detectaron alteraciones significativas en la activación de diferentes subpoblaciones de células del sistema inmune en presencia de extractos del material MGHA obtenidos en las primeras 24h del ensayo de degradación. Además, también se observó que los andamios MGHA no inducen apoptosis espontánea ni alteran la expresión intracelular de las citoquinas IL-2, IL-10, IFNγ ni TNFα en las diferentes subpoblaciones estudiadas. La **Figura 2.9.** muestra un resumen representativo de los resultados obtenidos.

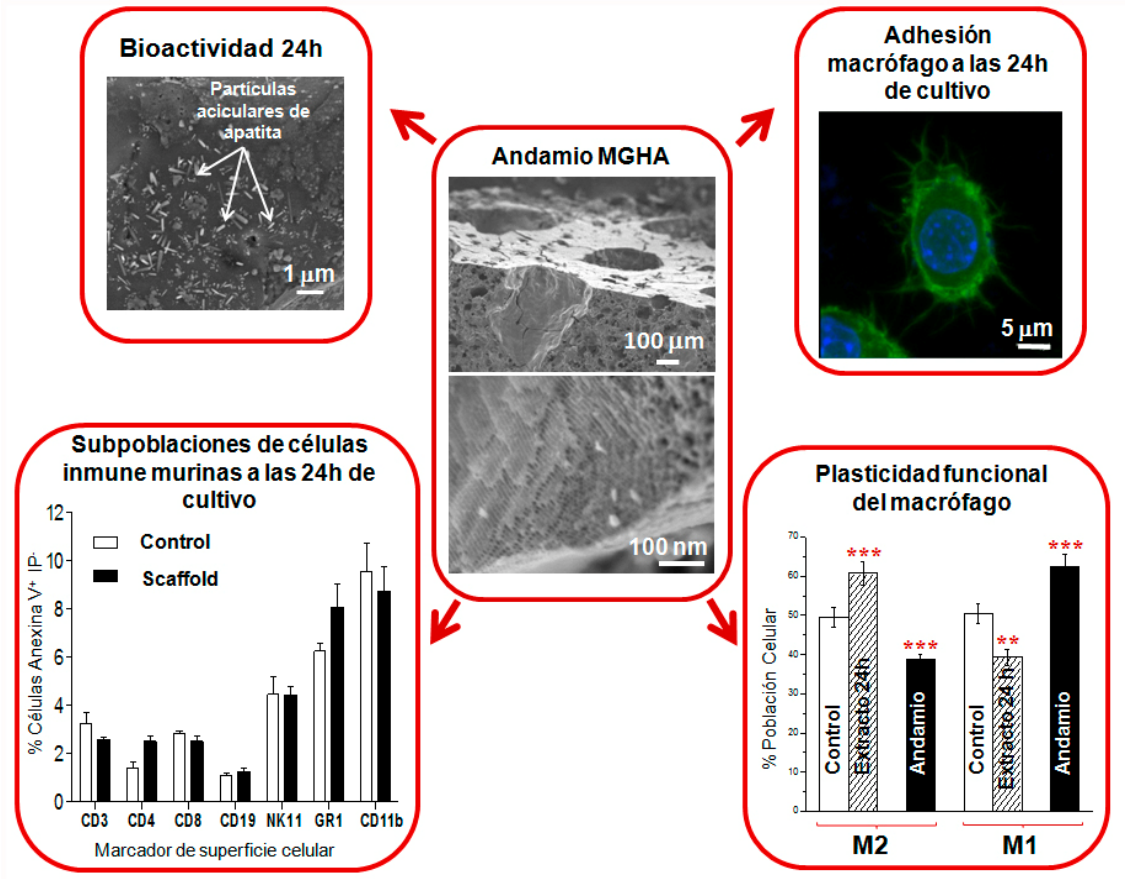

Figura 2.9. Cambios producidos en la superficie de los andamios *nanocomposite* MGHA en las primeras 24h del ensayo de degradación *in vitro*. Efectos ocasionados por dichos andamios sobre la respuesta inmune.

En conclusión, los andamios *nanocomposite* MGHA y sus extractos de 24h inducen modificaciones en los porcentajes de las poblaciones de macrófagos RAW 264.7, las cuales pueden estar relacionadas con la elevada reactividad/bioactividad mostrada por este material *nanocomposite* a 24 h. Sin embargo, estos mismos andamios no producen alteraciones significativas en la activación *in vitro* de macrófagos, linfocitos B, linfocitos T ni células *natural killer* cuando se utilizaron diferentes subpoblaciones de células primarias de ratón como modelo experimental. Por tanto, el presente estudio pone de manifiesto la elevada biocompatibilidad de los andamios *nanocomposite* MGHA y sugiere una adecuada respuesta de los tejidos adyacentes después de su implantación *in vivo*.

Journal of Materials Chemistry B RSCPublishing

ARTICLE

Effects of 3D *nanocomposite* bioceramic scaffolds on the immune response

Cite this: DOI:

Received
Accepted

DOI:

www.rsc.org/

Mónica Cicuéndez[a,b], Pilar Portolés[c,d], María Montes-Casado[d], Isabel Izquierdo-Barba[a,b], María Vallet-Regí[a,b]*and María Teresa Portolés[e]*

The interaction of new *nanocomposite* mesoporous glass/hydroxyapatite (MGHA) scaffolds with immune cells involved in both innate and acquired immunity has been studied *in vitro* as an essential aspect of their biocompatibility assessment. Since the immune response can be affected by the degradation products of bioresorbable scaffolds and scaffold surface changes, both processes have been evaluated. No alterations in RAW-264.7 macrophage proliferation and viability were detected after culture on MGHA scaffolds which did not induce cell apoptosis. However, a slight cell size decrease and intracellular calcium content increase were observed after contact of this cell line with MGHA scaffolds and their extracts. Although no changes in proinflammatory (M1) and reparative (M2) macrophage populations are observed by treatment with 7d extracts, this study has revealed modifications of these percentages after direct contact with scaffolds and by treatment with 24h extracts, related to the high reactivity/bioactivity of this MGHA *nanocomposite* at initial times. Furthermore, when normal fresh murine spleen cells were used as an experimental model closer to physiological conditions, no significant alterations in the activation of different immune cell subpopulations were detected in the presence of 24h MGHA extract. MGHA scaffolds did not affect the spontaneous apoptosis or intracellular cytokine expression (IL-2, IL-10, IFN-γ, TNF-α) either after 24h treatment. The results obtained in the present study with murine immune cell subpopulations (macrophages, lymphocytes B, lymphocytes T and natural killer cells) reveal the high biocompatibility of MGHA scaffolds suggesting an adequate host tissue response after implantation.

1. Introduction

Tissue engineering, due to its highly multidisciplinary nature, needs the combination of clinical medicine, mechanical engineering, materials science, genetics, and related disciplines from both engineering and life sciences.[1] This field relies on the use of porous 3D scaffolds to provide the appropriate environment for the regeneration of tissues and organs.[2] These scaffolds essentially act as a template for tissue formation and are seeded with cells and occasionally growth factors. The combination of cells, biomolecules and scaffolds constitute the tissue engineering triad.[3]

The composition, macroporous architecture, microporosity, surface topography and chemistry, as well as the mechanical properties of scaffolds used for tissue engineering play a crucial role in the success rates of implants.[3] Fundamental aspects in the manufacturing process of 3D scaffolds are the starting material and the methodology which must be used for configuring the 3D structure. Different biomaterials are employed in the fabrication of scaffolds for tissue engineering, with specific advantages and disadvantages. Recently, the use of composite scaffolds allows improving their properties due to the synergy of the features of their components. For this reason, composite scaffolds are widely used for different applications.[4-8] In this sense, our research group have recently synthesized a novel *nanocomposite* material formed by nanocrystalline apatite uniformly embedded into a mesostructured SiO_2–CaO–P_2O_5 glass wall (MGHA material).[9] The response of L929 fibroblasts and Saos-2 osteoblasts to this powdered *nanocomposite* has been previously studied, demonstrating a significant improved biocompatibility in comparison with conventional mesoporous glasses.[9,10] Furthermore, recently 3D scaffolds based on this *nanocomposite* material have been exhibited a good preosteoblast cell adhesion, colonization, proliferation and differentiation, suggesting their great potential application in bone tissue engineering.[11]

The first characteristic of any scaffold for tissue engineering is that it must be biocompatible, allowing the cell adhesion, proliferation and migration through it.[12,13] However, the ultimate functional success or failure of the scaffolds after implantation, depends invariably on the host tissue response and therefore, the scaffold must not induce immune reaction which might reduce healing or produce rejection by the body.

Thus, the *in vitro* evaluation of the biomaterial effects on immune system is an essential aspect of biocompatibility assessment.[14] The immune response comprises both innate and adaptive defence mechanisms which activate different cell populations co-ordinately. The innate response involves the action of neutrophils, monocytes and macrophages which carry out phagocytosis and produce reactive oxygen species, antimicrobial peptides, and inflammatory mediators.[15] Natural killer (NK) cells also play a role in the innate response by directly killing virus-infected or transformed cells without prior priming by secretion of cytotoxic molecules and cytokines.[16] The adaptive response is mediated by antigen-specific lymphocytes (T and B cells) which produce inflammatory cytokines and antibodies.[15] Largely, the interaction of these host immune cells with biomaterials has negative implications for tissue remodelling. For decades, the interaction of macrophages with newly deposited extracellular matrix, accompanied by an angiogenic response, has been interpreted as a precursor of granulation tissue formation, the classic foreign body reaction, with negative implications for outcomes.[17] However, it has been recently shown that macrophages may be beneficial for biomaterial integration improving implant performance due to a remarkable functional plasticity. Thus, macrophages can play both positive and negative roles in disease processes and tissue remodeling. These cells are classified in two phenotypes: proinflammatory (M1) and reparative (M2),[17,18] whose balance determine the host response to biomaterials, with participation of diverse specific cytokines. In this sense, the design of biomaterials capable of modulating immune cell function has been suggested in order to obtain appropriate immune responses at implantation sites.[16-20]

Given the excellent biocompatibility and bioactivity shown by the MGHA *nanocomposite* and taking into account its potential application in bone tissue engineering,[9,11] the present study is focused on the *in vitro* interaction of 3D MGHA scaffolds with immune cells involved in both innate and acquired immunity. Furthermore, since the immune response can be additionally affected by the degradation products of bioresorbable scaffolds, the possible cytotoxic effects caused by MGHA extracts obtained at different times have been also studied.

2. Materials and Methods

2.1. Preparation of MGHA 3D scaffolds

MGHA 3D scaffolds based on highly mesostructured *nanocomposite* material were prepared by rapid prototyping (RP) using methylcellulose (MC), as previously reported.[11] Once fabricated, these MGHA scaffolds were sterilized under UV light for 30 min and then submerged in Dulbecco´s Modified Eagle´s Medium (DMEM) supplemented with penicillin (800 μg/mL), streptomycin (800 μg/mL), under a CO_2 (5%) atmosphere at 37ºC for 24 h to stabilize before cell culture.

2.2. Characterization of MGHA 3D scaffolds

X-ray diffraction (XRD) experiments were performed on a Philips X'Pert diffractometer (Eindhoven, The Netherlands), equipped with Cu Kα (40 kV, 20 mA). Transmission electron microscopy (TEM) was performed on a JEOL 3010 electron microscope (Jeol Ltd., Japan) operating at 300 kV (Cs; 0.6 mm, resolution 1.7 Å). All TEM images were recorded employing a CCD camera (MultiScan model 794, Gatan Inc., UK) under low-dose conditions. Fourier transform (FT) patterns were extracted from the images of thin crystal regions using a Digital Micrograph (Gatan Inc., UK). Scanning electron microscopy (SEM) was performed using a field emission JEOL JSM-6335F microscope (Tokyo, Japan) at an acceleration voltage of 10 kV. The textural properties of samples were determined by N_2 adsorption porosimetry using a Micromeritics ASAP2020 analyzer (Norcross, USA). The surface area was determined using the multipoint Brunauer–Emmett–Teller method included in the software. The porosity of 3D scaffolds was measured by mercury intrusion porosimetry in a MicromeriticsAutopore IV 9500 device (Micromeritics Instrument Corporation, Norcross, GA, USA). Elemental analyses (C, H, N) were carried out on a LECO CHNS-932 microanalyzer (Saint Joseph, Michigan USA). Fourier transform Infrared (FTIR) spectroscopy was performed in a Thermo Nicolet Nexus spectrometer (Thermo Scientific, USA) from 4000 to 400 cm^{-1}, using the KBr pellet method and operating in transmittance mode.

2.3. *In vitro* degradation of MGHA 3D scaffolds and preparation of MGHA extracts

MGHA scaffolds of ca. 23-25 mg, were immersed at different time periods during 30 days in a total volume of 100 mL of DMEM supplemented with 10% fetal bovine serum (FBS) and antibiotics (100 U ml^{-1} penicillin, 100 mg ml^{-1} streptomycin), in a Ecotron at 37ºC and 150 r.p.m. The supernatants obtained after 24h and 7d, named E 24h and E 7d, were selected for immune response studies. These extracts were filtered and added to RAW-264.7 macrophages to evaluate any potential cytotoxic effect. Determination of Si (IV), Ca (II) and P(V) variations in these extracts were carried out after different time intervals by inductively coupled plasma/optical emission spectrometry (ICP/OES) in a Perkin Elmer OPTIMA 3300 DV device. The scaffold surface was evaluated by scanning electron microcopy (SEM) after different times.

2.4. Culture and treatment of RAW-264.7 macrophages

Murine RAW-264.7 macrophages were seeded at a density of 10^5 cells/mL in culture medium supplemented with 10% FBS, 1 mM L-glutamine, penicillin, streptomycin, under a 5% CO_2 atmosphere, at 37ºC for 24h. Extract 24h and 7d have been also added to RAW cells to know the effects of the released products during the degradation process. Then, the attached cells were harvested with PBS/1mM EDTA at 4ºC and counted with a Neubauer hemocytometer. Cell suspensions were centrifuged at 310xg for 10 min and resuspended in fresh medium for the analysis of different parameters by Flow Cytometry as described below (*sections 2.5-2.8*). Controls without treatment were carried out in parallel.

2.5. Cell cycle analysis and apoptosis detection

After detachment of RAW-264.7 macrophages, cell suspensions were incubated with Hoechst 33258 (5 μg/ml, ethanol 30%, and BSA 1% in PBS), used as nucleic acid dye, for 30 min at room temperature in darkness. The fluorescence of Hoechst was excited at 350 nm and the emitted fluorescence was measured at 450 nm in a LSR Becton Dickinson Flow Cytometer. The cell percentage in each cycle phase (G_0/G_1, S and G_2/M) was calculated with the CellQuest Program of Becton Dickinson and the $SubG_1$ fraction (cells with fragmented DNA) was used as indicative of apoptosis.

2.6. Cell size and complexity
After detachment of RAW-264.7 macrophages, forward angle (FSC) and side angle (SSC) scatters were evaluated as indicative of cell size and complexity respectively using a FACScalibur Becton Dickinson flow cytometer.

2.7. Intracellular reactive oxygen species (ROS) content and cell viability
After detachment of RAW-264.7 macrophages, cell suspensions were incubated with 100μM 2´,7´-dichlorofluorescein diacetate (DCFH/DA) at 37°C for 30 min. DCF fluorescence was excited at 488 nm and measured with a 530/30 nm band pass filter in a FACScalibur Becton Dickinson flow cytometer. Cell viability was determined by addition of propidium iodide (PI; 0.005% in PBS).

2.8. Intracellular calcium content
After detachment of RAW-264.7 macrophages, cell suspensions were incubated with the probe Indo-1 AM at a concentration of 10 μM for 30 min at room temperature, darkness, and shaking. The fluorescence of Indo-1 was excited at 325 nm and the emitted fluorescence was measured with 380 nm long pass (FL1) and 424/44 nm band pass (FL2) filters in a LSR Becton Dickinson flow cytometer. After all the measurements, 10 μM A-23187 ionophore (Enzo Life Sciences) was added in order to prove the sensitivity of the assay.

2.9. Morphological studies by Confocal Microscopy
For Confocal Microscopy studies, RAW-264.7 cells were cultured for 24 h on MGHA disks (10 mm diameter and 4 mm high) prepared by uniaxial and isostatic pressure of powder. After fixation with 3.7% paraformaldehyde in PBS for 10 min, samples were washed with PBS and permeabilized with 0.1% Triton X-100 for 3 to 5 min. The samples were then washed with PBS and preincubated with PBS containing 1% BSA for 20 to 30 min. Then cells were incubated for 20 min with FITC phalloidin which stains F-actin filaments. Samples were then washed with PBS and the cell nuclei were stained with DAPI (4′-6-diamidino-2′-phenylindole, 3 μM in PBS). After staining and washing with PBS, cells were examined by a LEICA SP2 Confocal Laser Scanning Microscope. The fluorescence of FITC was excited at 488 nm and the emitted fluorescence was measured at 491-586 nm. The fluorescence of DAPI was excited at 405 nm and measured at 420-480 nm.

2.10. Mice
Mice from C57BL/6 strain were bred under specific pathogen-free conditions in the animal care facility of the Centro Nacional de Microbiología (Instituto de Salud Carlos III, Majadahonda, Madrid, Spain), from stock purchased from Charles River. Sex-matched, 10–12 weeks old mice were used throughout the experiments. All procedures were approved by Institutional Animal Care and Use Committees.

2.11. Culture and activation of murine spleen cells
Cell suspensions from C57Bl/6 spleens in Click´s culture medium supplemented with 10% FBS were obtained, and the erythrocytes were lysed by hypotonic shock. Cell suspensions were filtered through 30 microns mesh and washed. *In vitro* primary stimulation was performed by culturing $5x10^5$ cells in 200 μl of Click´s medium supplemented with 10% FBS and 10mM HEPES, in the presence of Y-CD3-1 (anti-CD3 monoclonal antibody, 5 μg/ml)[21] or Lipopolysaccharide (LPS, *E.coli* 055:B5, 25 μg/ml) as stimuli and in the presence or absence of filtered MGHA extracts. After 3d culture at 37ºC and 5% CO_2, viability measured as mitochondrial activity was assessed by a colorimetric assay using 3-(4,5-dimethylthiazol-2-yl)-2,5-diphenyltetrazolium bromide (MTT) as a substrate for mitochondrial dehydrogenases in living cells as previously described by Mosmann.[22]

2.12. Detection of murine lymphocyte spontaneous apoptosis
To assess the effect of MGHA scaffolds on murine lymphocyte spontaneous apoptosis, spleen cells were prepared as above but cells were cultured in flat-bottom P-48 culture plates containing previously stabilized scaffolds. 5 x 10^6 cells were seeded onto the scaffold in a final volume of 0.5 ml culture medium. After 24h culture at 37ºC and 5% CO_2, cells were collected and spontaneous apoptosis was determined by Flow Cytometry in cells stained with AnnexinV-FITC and propidium iodide using the Human Annexin V-FITC kit (eBioscience) according to the manufacturer's instructions and analyzed in a FacsCanto (B-D Biosciences) flow cytometer with DIVA software.

2.13. Analysis of intracellular cytokine expression
To analyze the effect of MGHA scaffolds on cytokine expression, suspensions of murine spleen cells were prepared as above. 10^6 cells were seeded onto scaffolds in P-48 culture plates and cultured 3d in the presence of Y-CD3-1 (anti-CD3 antibody, 5 μg/mL) or LPS (50 μg/ml) or culture medium, in 1 ml final volume. After this time, cells were collected and processed for intracellular cytokine detection by Fluorescence-activated cell sorting (FACS). Intracellular cytokine staining was performed essentially as described by Rojo et al.[23] Cells were washed and re-suspended at 2 x 10^6 /ml in culture medium and stimulated with 20ng/ml phorboldibutyrate (PDB; Sigma-Aldrich) plus 1 μM ionomycin (Calbiochem) for 1.5h. Brefeldin A (10 μg/ml; Sigma-Aldrich) was added, and the cells were incubated for further 3.5h, washed and surface labeled with desired antibodies by incubation for 30 min on ice with fluorocrome-coupled antibodies diluted in cold staining buffer (PBS containing 2% FCS and 0.1% sodium azide). Then, the cells were washed two times and fixed for 5 min at room temperature with 4% paraformaldehyde in PBS. After stopping the fixation with ice-cold 0.1% BSA in PBS/0.1% azide, the cells were washed with 0.1% saponin (Sigma-Aldrich) in PBS/0.1% BSA/10mM HEPES/azide (PBS/saponin) and blocked at 4ºC for 30 min with 5% non-fat milk in PBS/saponin. Then, the cells were stained with PE-, Alexa Fluor 647-, DyLight 649 (Pierce)- or FITC-coupled antibodies in 5% non-fat milkin PBS/saponin for 30 min in the cold. After washing three times with PBS/saponin, the cells were analyzed in a FACSCanto (B-D Biosciences) flow cytometer. The antibodies for cytokine intracellular detection were from eBioscience:PE-coupled anti-IL-2 (JES6-5H4), and anti-IL-10 (JES5-16E3); FITC-coupled anti-IFNγ (XMG 1.2) and anti-TNFα. As negative controls, PE- or FITC-conjugated isotype control mAb were used.

2.14. Statistics
Data are expressed as means ± standard deviations of a representative of three experiments carried out in triplicate. Statistical analysis was performed using the Statistical Package for the Social Sciences (SPSS) version 19 software. Statistical comparisons were made by analysis of variance (ANOVA). Scheffé test was used for post hoc evaluations of differences

among groups. In all of the statistical evaluations, $p < 0.05$ was considered as statistically significant.

3. Results and discussion

3.1. MGHA 3D scaffolds

The new mesoporous glass/hydroxyapatite *nanocomposite* MGHA has been used as starting material for the manufacturing of the 3D scaffolds by RP technique, as previously has been reported.[11] Previous results demonstrate its high biocompatibility and bioactivity[9,11] and drug loading capability,[24] characteristics which make to MGHA a potential biomaterial for bone tissue engineering. In the present study, hierarchical 3D MGHA scaffolds and their degradation products (extracts) have been prepared to evaluate their effects on immune cells, involving macrophages and lymphocytes.

As it can be observed in **Fig. 1**, MGHA 3D scaffolds present a hierarchical porous macro-mesoarchitecture which improves cell adhesion, proliferation differentiation and colonization.[11]

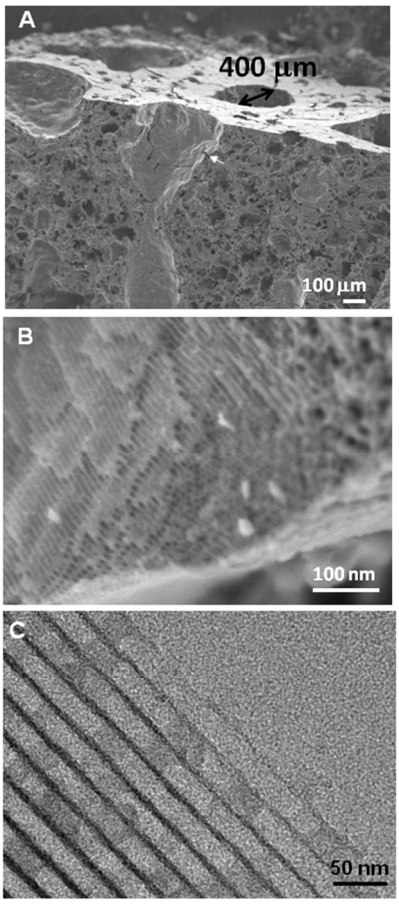

Fig. 1 SEM and TEM studies of the macro and mesostructure of MGHA 3D scaffolds. (A) Cross section of a 3D scaffold showing the hierarchical pore structure of MGHA scaffolds. The small arrow shows the interconnections of large channels of 400 µm with the interior. **(B)** SEM micrograph taken with a JEOL JSM7600F of 3D scaffold surface, showing mesoporous channels typical of a 2D hexagonal structure. **(C)** TEM image showing a mesoporous arrangement, where the darker zones homogeneously distributed into the mesoporous channels correspond to apatite nanocrystalline phase.

Moreover, these porosity properties can lead to mineralization, vascularisation and nutrient diffusion which are critical for the osteogenesis.[25-27] Furthermore, the mesoporous arrangement could lead an added value as controlled delivery systems of biologically active molecules.[28,29]

With the aim of evaluating the *in vitro* degradation of MGHA 3D scaffolds, the surface changes and the evolution of their macroporous structure after different incubation times in culture medium have been studied by SEM (**Fig. 2**). In the first 24h, the SEM micrographs (**Fig. 2D, 2E** and **2F**) show an early gradual degradation of the surface with small deposits of particles.

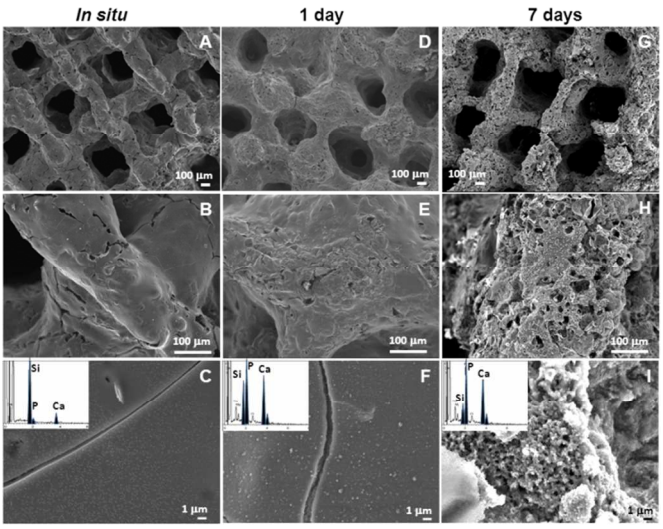

Fig. 2 In vitro degradation test. SEM micrographs at different magnifications and EDS analyses (inset) before **(A**, **B** and **C)** and after 1 **(D**, **E** and **F)** and 7 days **(G**, **H** and **I)** soaking in DMEM.

Fig. 3 shows in details this gradual deposition which is formed by needled-like particles typical of apatite formation on bioactive surfaces.[27] On the other hand, after 7d, there are substantial changes in the surface and the macroporous architecture of the scaffold (**Fig. 2G and 2H**), showing a notable degradation from a smooth surface (*in situ*) to a highly degraded surface which exhibits macroporous in the range of 100-25µm. Moreover, SEM higher magnification (**Fig. 2I**) shows the existence in this surface of acicular particles with a majority composition of Ca and P (Ca/P =1.67), corresponding to apatite phase, in agreement with other studies.[30] EDS analyses (inset **Fig. 2C, 2F and 2I**) confirm both notable increase of the amount Ca and P together with a decrease of Si amount in the scaffold surface after 1 and 7d of incubation in DMEM, respectively **(Fig. 4)**. These results evidence the excellent bioactive behaviour, according to previous results in simulated body fluid.[9]

Fig. 4 shows a gradual degradation of 3D scaffolds, exhibiting an initial rapid increase of calcium and phosphorus concentration in the soaking medium in the first 24h of incubation. Then, the ionic concentrations slightly increase until 7d and remain without variation until 30d. Concerning the silicon variation, the plot shows constant gradual silicon leaching during all period time. Thus, the obtained results reveal a gradual degradation of these 3D MGHA scaffolds over time.

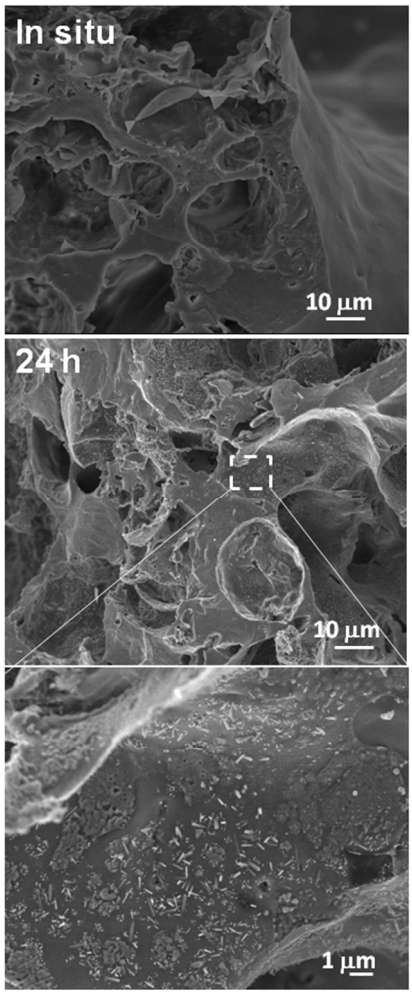

Fig. 3 SEM study of MGHA scaffolds before and after 24 hours of incubation in DMEM. The micrographs show clearly the formation of needled-like aggregated of apatite phase on the scaffolds surface after 24h.

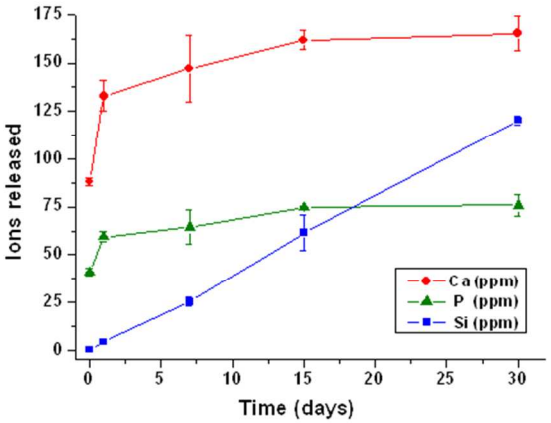

Fig. 4 Variation of the Calcium, Phosphorous and Silicon concentration in DMEM overtime.

FTIR spectroscopy was carried out to evaluate the changes in the MGHA *nanocomposite* scaffold surface as a function of soaking time in DMEM (**Fig. 5**). Before soaking, the spectrum shows characteristic absorption bands of Si-O bonds at 1040, 800, and 470 cm^{-1}. After 24 hours of soaking in DMEM, an increase of the doublet at 560 and 600 cm^{-1}, corresponding to a crystalline phosphate is observed, confirming the formation of a new crystalline phosphate onto the scaffold surface in agreement to SEM-EDS results. Moreover, after 7d, the spectrum analysis shows clearly the proteins adsorption derived of completed DMEM onto the MGHA surface formed onto newly apatite layer.

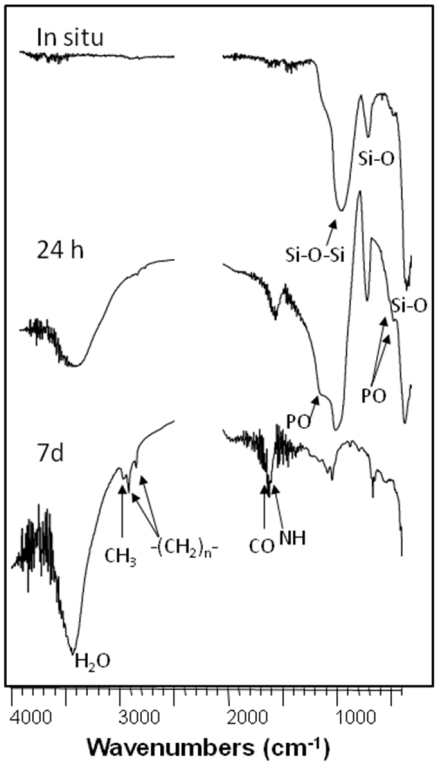

Fig. 5 FTIR spectra corresponding to MGHA scaffolds before and after 24h and 7d in DMEM.

To evaluate *in vitro* the response of immune cells to MGHA scaffolds, RAW-264.7 macrophages and murine spleen cells have been cultured in contact with these samples or their extracts (obtained after 24h and 7d as described above in *section 2.3*). These incubation times have been chosen taking into account the higher reactivity of MGHA material at 24h and the scaffold degradation/bioactivity observed after 7d.

3.2. Effects of MGHA biomaterial on RAW-264.7 macrophages

RAW-264.7 cells are functional macrophages with the ability of autophagy and phagocytosis as immune cells and retain many of the characteristics of macrophages *in vivo,* for these reasons this cell line is usually used for *in vitro* biocompatibility studies.[31] **Table I** shows that no significant changes of cell viability (up 75 %) were detected by propidium iodide exclusion test after 24h culture of RAW-264.7 macrophages with MGHA extracts (obtained at 24h and 7d; E 24h and E 7d, respectively) or MGHA scaffolds (SC).

Table I. Effect of MGHA extracts (obtained at 24h and 7d) and MGHA scaffolds (SC) on RAW-264.7 macrophage viability after 24h treatment. Cells without treatment were cultured in parallel (Control).

Sample	Viability (%)
Control	79.3 ± 2.2
E 24h	78.8 ± 2.8
E 7d	82.1 ± 3.4
SC	75.8 ± 2.1

When RAW-264.7 macrophage proliferation on MGHA scaffolds were evaluated, no alterations were detected in comparison with control samples (**Table II**). The cell cycle was studied by flow cytometry after culture of these cells on MGHA scaffolds and the $SubG_1$fraction, attributed to cells with fragmented DNA, was used as indicative of apoptosis.[32] Viable cell number count was used to assess proliferation. As it can be observed in **Table II**, MGHA samples did not produce changes in $SubG_1$ phase of RAW-264.7 macrophages, thus indicating that MGHA scaffolds did not induce apoptosis in this cell type which presented apoptosis levels lower than 3 %.

Table II. Effect of MGHA scaffolds (SC) on RAW-264.7 macrophage proliferation and apoptosis.

Sample	Proliferation (Cell number x 10^{-3})	Apoptosis (%)
Control	32.2 ± 6.2	2.81 ± 0.14
SC	30.5 ± 4.4	2.57 ± 0.13

When Confocal Microscopy techniques were carried out to evaluate the RAW-264.7 morphology in contact with MGHA disks, the typical characteristics of these macrophages were observed. **Fig. 6** shows that no morphological alterations induced by MGHA material were detected in RAW-264.7 macrophages which showed intact cytoplasmic filaments of F-actin (**Fig. 6**, FITC phalloidin labeling in green). DAPI is a DNA dye widely used to visualize the changes of the chromatin in apoptotic cells. This probe stains the cell nuclei and allows detecting the presence of apoptotic bodies produced by the chromatin condensation/fragmentation as a late marker of apoptosis. No apoptotic nuclei were detected in RAW-264.7 macrophages cultured on MGHA disks in agreement with the low levels of apoptosis detected by flow cytometry (**Table II**).

The effects of 24h and 7d MGHA extracts and scaffolds on the cell size and complexity of RAW-264.7 macrophages were also evaluated by Flow Cytometry through FSC and 90º SSC light scatter as indicators of cell size and complexity, respectively. These properties are determined in part by cell size, plasma membrane, cytoplasm, mitochondria, pinocytic vesicles, and lysosomes.[33] As it can be observed in **Fig. 7**, the contact of RAW-264.7 macrophages with MGHA scaffolds and their extracts produce a decrease of cell size (**Fig. 7A**) with a slight increase of macrophage complexity (**Fig. 7B**).

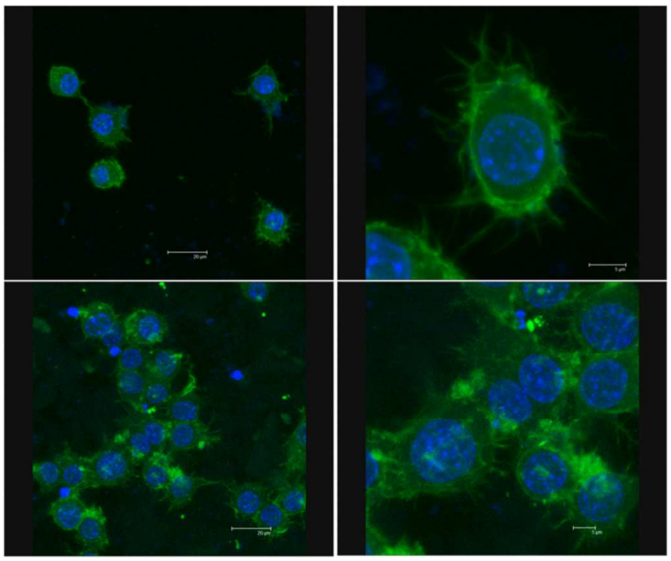

Fig. 6 Morphological evaluation of RAW-264.7 macrophages on MGHA disks. Cells were stained with DAPI for the visualization of the cell nuclei in blue and with FITC phalloidin for the visualization of cytoplasmic F-actin filaments in green.

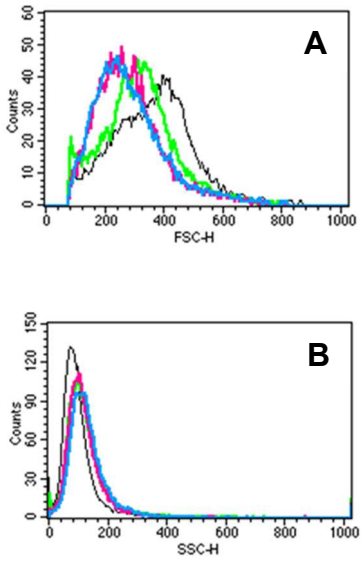

Fig. 7 Effect of MGHA extracts and MGHA scaffolds on light scattering properties of RAW-264.7 macrophages. (A) Forward angle scatter (FSC, cell size) versus number of cells after treatment with MGHA scaffolds (green), 24 h extract (pink), and 7 d extract (blue). **(B)** 90 side angle light scatter (SSC, internal complexity) versus number of cells after treatment with MGHA scaffolds (green), 24 h extract (pink), and 7 d extract (blue).Control cells without treatment (black).

Macrophages are one of the most versatile type of immune cells, carrying out a large number of important functions, essential to both innate and acquired immune responses. These functions include: phagocytosis of apoptotic cells, bacteria, and viruses; production of reactive nitrogen and oxygen species; antigen processing and presentation; and cytokine and chemokine production.[15] Since reactive oxygen species (ROS) and Ca^{2+} constitute the most important intracellular signaling molecules for the regulation and integration of diverse cellular functions, the effects of MGHA extracts (obtained at 24h and 7d) and MGHA scaffolds (SC) on intracellular ROS content

and cytosolic calcium of RAW-264.7 macrophages after 24h treatment were evaluated by flow cytometry with the probes DCFH and Indo-1 respectively. Significant ROS increases ($p< 0.005$) were produced by 7d MGHA extracts and scaffolds (**Table III**, a.u. = arbitrary units of fluorescence). Concerning intracellular calcium measurements, the probe Indo-1shifts their spectral characteristics upon calcium binding, from FL1 to FL2;[34] ratio FL1/FL2 can be used as an indicator of intracellular Ca^{2+} content. As it can be observed in **Table III**, fluorescence ratio of RAW-264.7 macrophages significantly increased ($p<0.001$) after culture with 24h and 7d MGHA extracts and scaffolds, thus indicating the MGHA extracts and scaffolds induced a significant cytosolic calcium increase of these cells. Several studies have demonstrated that some materials increase $[Ca^{2+}]_i$ possibly through the entry of extracellular Ca^{2+} via Ca^{2+} channels in the plasma membrane, and activate the generation of ROS.[35]

Table III. Effect of MGHA extracts and MGHA scaffolds on intracellular ROS content and intracellular calcium of RAW-264.7 macrophages.

Sample	ROS (a.u.)	Ca_i (FL_1/FL_2)
Control	476 ± 23.8	1.70 ± 0.09
E 24h	471 ± 23.6	2.47 ± 0.12
E 7d	606 ± 30.3	2.36 ± 0.12
SC	611 ± 30.6	2.45 ± 0.12

Macrophages have capability of playing both positive and negative roles in disease processes and tissue remodelling after injury and these cells can be classified in proinflammatory macrophages (M1) and reparative macrophages (M2). It has been recently proposed that the *in vivo* response to biomaterials depends on the balance between the M1 and M2 phenotypes, with participation of diverse specific cytokines.[17-20] In the present study, the effects of MGHA extracts and MGHA scaffolds on RAW-264.7 macrophage subpopulations have been evaluated through intracellular ROS measurement by Flow Cytometry. **Fig. 8** shows the profiles of cell number (counts) versus DCF fluorescence (FL1) used as indicative of intracellular ROS. Macrophages in contact with MGHA scaffolds (**Fig. 8B**) and control macrophages (**Fig. 8A**) showed different intracellular ROS profiles. Since several studies have demonstrated that M1 macrophages produce and secrete higher ROS levels than M2 cells,[17,36] the effect of MGHA extracts and scaffolds on the percentage of high (M1) or low (M2) ROS subpopulations was evaluated with RAW macrophages.[36] **Fig. 9** shows that in the presence of 24h extracts, M2 population is significantly higher than M1 percentage, in agreement with the results presented in **Table III** which indicates no high intracellular ROS levels when RAW cells are cultured with these extracts. This effect can be related to the rapid release of ions (calcium, phosphorous and silicon) to the medium in the early steps of the reactivity/bioactivity process (**Fig. 4**). On the other hand, 7d MGHA extract does not induce changes of M1 and M2 percentages probably due to the stabilization of this release which is slower at this time (**Fig. 4**). The direct contact of RAW-264.7 cells with the MGHA scaffolds during 24h increases both the intracellular ROS content (**Table III**) and subsequently the M1 population in comparison with control, thus indicating the high reactivity/bioactivity of the surface-level of MGHA scaffolds previously observed in **Fig. 3** and **Fig. 4**.

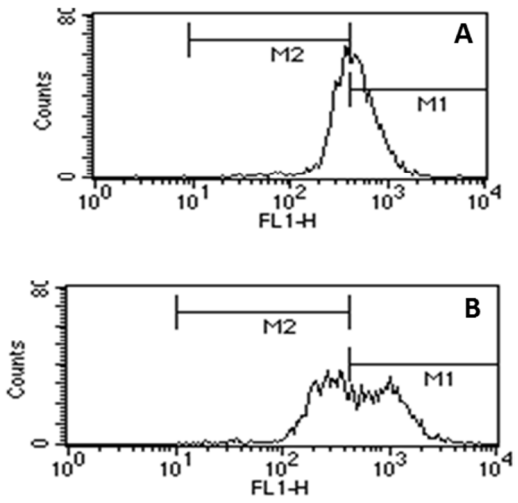

Fig. 8 Effect of MGHA scaffolds on RAW-264.7 macrophage populations evaluated through intracellular ROS (Flow Cytometry profiles). Intracellular ROS (FL1, a.u.) versus number of cells after treatment with MGHA scaffolds **(B)**. Control untreated cells **(A)**.

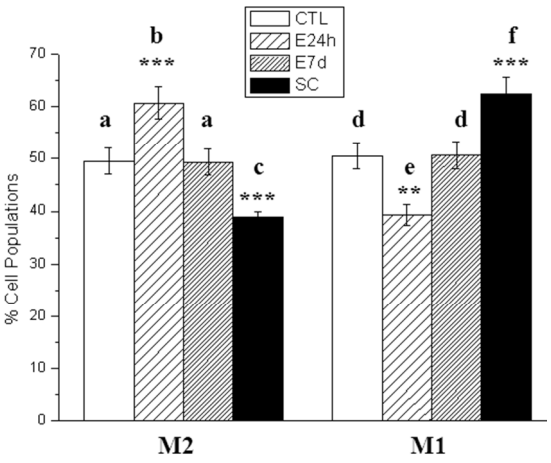

Fig. 9 Effect of MGHA extracts and MGHA scaffolds on the percentage of M2 and M1 populations of RAW-264.7 macrophages evaluated through intracellular ROS. CTL = Control untreated cells. Columns with different letters are statistically different. Statistical significance ** $\rho < 0.01$; *** $\rho < 0.005$.

3.3. Effects of MGHA biomaterial on murine spleen cell suspensions

Immune response plays a determinant role in the tolerance, survival and functioning of biomaterials. Immune system is composed of many different subpopulations which mutually interact and cross-talk determining the final outcome of the immune response. To assess the potential effect of MGHA on immune cells, we chose to analyze its effect on murine spleen cell suspensions, an *in vitro* system in which different untransformed normal cell subpopulations interact in among them, better resembling the *in vivo* ambient. The spleen is a

lymphoid organ which contains different types of immune cells, mainly including T- and B-lymphocytes (about 80% in the mouse spleen), macrophages and other antigen-presenting (APC) (about 10%) and natural killer (NK) cells. These cells circulate through the body monitoring for signals which trigger an innate response or detecting non-self antigens, thus becoming activated, differentiated and expanded, mounting an acquired immune response. The contact of body fluids and blood cells with biomaterials may trigger the activation of granulocytes, monocytes and macrophages, driving to an acute and lately chronic inflammatory response. Although the biomaterial composition does not allow T cell activation via antigen presentation, it has been suggested that synthetic biomaterials present functional groups on their surfaces acting as mitogens which can trigger lymphocytes by cross-linking of glycoproteins on the cell surface.[15] We assessed this possibility studying the effect of MGHA extracts and scaffolds on murine normal and activated immune cells.

3.3.1. MGHA biomaterial does not alter murine lymphocyte activation or spontaneous apoptosis. To evaluate the biocompatibility of MGHA on murine spleen immune cells, we firstly assayed the *in vitro* effect of 24h biomaterial extracts, analysing any potential cytotoxic or immunomodulatory effect of the biomaterial components released to the medium. The MGHA extracts were added to cell suspensions of murine spleen cells in an *in vitro* activation assay in the absence or the presence of anti-CD3 antibody (5 μg/ml) or LPS (25 μg/ml) as mitogens. Cell activation was measured 72h later as mitochondrial activity (**Fig. 10**). Cell subpopulations became activated and proliferated in the presence of these stimuli, while cells in the control cultures (CTL) did not, even when MGHA extracts had been added to the cultures, indicating that no mitogen activity for immune cells is present in this biomaterial extract. No significant modification of cell activation was detected in control or mitogen-treated cultures in the presence of MGHA extracts. This assay also shows that the viability in the cultures was not modified in the presence of different proportions of MGHA extracts. We further analyzed the effect of MHGA-lymphoid cell contact by studying apoptosis of different lymphoid subpopulations in the presence of MGHA scaffolds. Spleen cells were seeded onto scaffolds and incubated during 24h before analyzing spontaneous apoptosis.

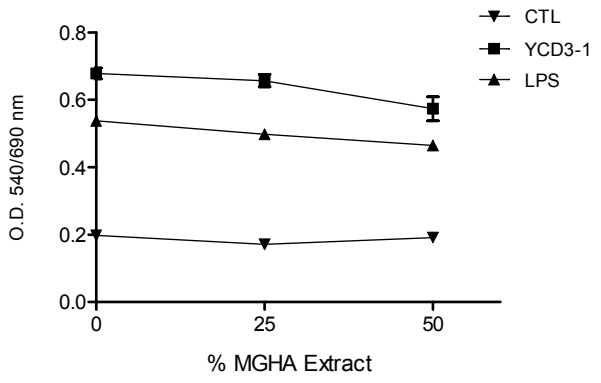

Fig. 10 Effect of MGHA extracts on murine spleen cell activation. The effect of two different concentrations of MGHA extract was evaluated in an activation assay in the presence of anti-CD3 antibody (YCD3-1, T-cell mitogen, squares), LPS (B-cell mitogen, triangles) or medium (control, CTL, inverted triangle). Mitochondrial activity was measured after 72 hours culture and represented as O.D.

Fig. 11 shows that no significant modification of spontaneous apoptosis was induced by MGHA scaffolds in T ($CD3^+$, $CD4^+$, $CD8^+$) or B ($CD19^+$) lymphocytes, natural killer ($NK1.1^+$, $GR1^+$, $CD11b^+$) or monocytes-macrophages ($CD11b^+$) subpopulations in the spleen cell cultures. GR1 is also a marker for the low proportion of peripheral granulocytes found in the spleen which did not result affected by MGHA in this assay.

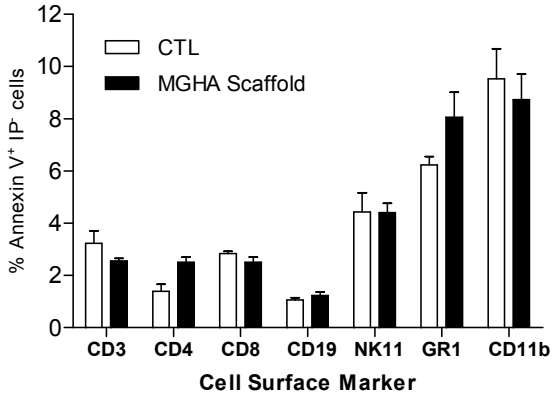

Fig. 11 MGHA scaffolds do not affect spontaneous apoptosis of different spleen cell subpopulations. Apoptosis was measured as percent of $AnnexinV^+Propidium\ Iodide^-$ cells by FACS in murine spleen cells which were seeded onto MGHA scaffolds (filled bars) or directly in the culture wells (CTL, empty bars) and cultured overnight.

3.3.2. MGHA biomaterial does not affect the subpopulations balance or cytokine expression in activated murine immune cells. Activation of normal resting lymphocytes promotes their differentiation to different phenotypes of effector subpopulations and expression of specific cytokines. In T lymphocytes and macrophages co-culture it has been found that T cells are attached predominantly to macrophages and not to the biomaterial surface, promoting macrophage adhesion and fusion via paracrine effects mediated by different cytokines.[37] To further study the potential effect of the biomaterial in these processes we analyzed the effect of MGHA scaffolds in the balance of lymphoid subpopulations (measured by specific surface markers) and cytokine secretion (measured as intracellular interleukin expression). **Fig. 12A** shows that the frequency of different T cells subpopulations was not significantly altered by the presence of MGHA scaffold during the activation process mediated by T cell stimulus (anti-CD3 antibody) on spleen cells cultures. The frequency of total T cells ($CD3^+$), helper ($CD4^+$) or cytotoxic ($CD8^+$) was evaluated. T activated cells were identified by CD25 and/or ICOS markers, in total T or in among $CD4^+$ or $CD8^+$ subpopulations showing no significant alteration of these subpopulations mediated by MGHA scaffolds. The use of a higher concentration of YCD3-1 (10 μg/ml) or LPS (50 μg/ml) for activation did not yield a different effect of the biomaterial extracts (data not shown). Natural $CD4^+CD25^+Foxp3^+$ T regulatory cells play a very important role in controlling activation and effector functions of different lymphoid cells, and a disbalance in this subpopulation may cause lymphoproliferative and inflammatory disorders. Thus, we also analyzed the potential effect of MGHA scaffolds on T regulatory cells, but the frequency of natural Treg inactivated cultures was not changed in the presence of MGHA scaffolds (**Fig. 12A**). The potential effect of MGHA scaffolds was also assessed in LPS-stimulated spleen cells. Again, the frequency

of B lymphocytes ($CD19^+$), macrophages ($CD11b^+$) or ICOS-ligand expressing cells remained unaltered in the presence of MGHA as shown in **Fig. 12B**.

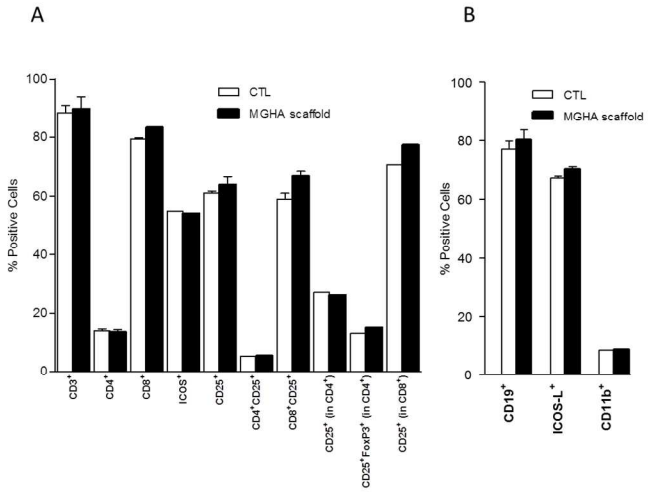

Fig. 12. **MGHA scaffolds do not affect the subpopulations in a murine spleen cell activation assay. (A)** Percentage of different spleen cell subpopulations (indicated in the X axis) was evaluated by FACS analysis after 72 hours culture under T- (anti-CD3 antibody) or **(B)** B-cell stimulus (LPS) in the presence (filled bars) or absence (CTL, empty bars) of MGHA scaffolds.

Cytokine expression and secretion constitute an important effector mechanism of immune cells, determining subsequent activation or suppression of other subpopulations. In among them, we chose to analyse IL-2, IL-10, IFNγ and TNFα because of their important implication in the immune response and inflammation. IL-2 is a Th1 cytokine that plays a central role in the activation, proliferation and differentiation of Ag-primed T lymphocytes.[38,39] It also modulates the expression of IFNγ and MHC antigens, stimulates proliferation and differentiation of activated B cells and augments NK cell activity. IL-10 is an anti-inflammatory Th2 cytokine that has a critical role in limiting the immune response to prevent host damage.[40] It is expressed by Th2, Th17, T regulatory and B cells, as well as innate immune cells as dendritic cells, macrophages, mast cells, NK, eosinophils and neutrophils. As IL-10 is produced in several T helper populations, it is proposed that it provides a feedback loop to limit the effector function of macrophages and dendritic cells. IFN-γ (Type-II Interferon) is produced by activated T, B and NK cells. During infection is produced by cytotoxic $CD8^+$ T cells and Th1, inhibiting the proliferation of Th2 phenotype subpopulation. IFNγ acts in synergy with other cytokines including TNFα to inhibit the proliferation of normal or transformed cells but also activates monocytes, macrophages, NK and neutrophils. IFNγ is a marker for a number of different pathological situations including infections, autoimmune diseases, transplant rejection and diabetes.[41,42] TNF-α (Tumor Necrosis Factor alpha) is a pleiotropic cytokine that plays a role in innate and adaptive immunity.[43] Though it is widely implicated in numerous immune responses and regulations, it is most often associated with regulation of cell survival and pro-inflammatories properties which lead to the recruitment and activation of inflammatory cells to the site of injury where it is known to induce various cytokines, including IL-1, IL-6, IL-8, MCP-1 and RANTES. TNF-α is primarily expressed by macrophages, but also by activated lymphocytes, NK cells and neutrophils in among others. It is associated with numerous inflammatory illnesses and autoimmunity. To analyze the potential secondary effect of MGHA on immune cells we studied the intracellular expression of IL-2, IL-10, IFN-γ or TNF-α in spleen cell cultures which were activated by mitogens during 72h. No significant effect of MGHA scaffolds on the intracellular cytokine expression was detected in spleen cells cultured under T- (**Fig. 13A**) or APC-activating conditions (**Fig. 13B**). The absence of significant changes in IL-2 and IFNγ expression in the presence of the scaffolds indicates the lack of MGHA effects on T cells (**Fig. 13A**). In parallel the absence of changes in TNF-α or IL-10 expression indicates that pro- or anti-inflammatory loops are not significantly modified by MGHA scaffolds in T- or APC-stimuli conditions (**Fig. 13A and B**). $CD4^+$, $CD19^+$ or $CD11b^+$ subpopulations producing the former cytokines were also analyzed separately, but no statistically significant differences were found when comparing the cytokine expression in the presence or absence of MGHA scaffolds (data not shown).

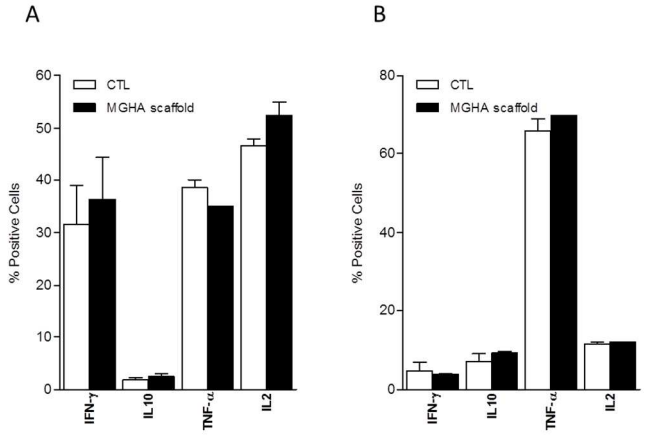

Fig. 13. MGHA biomaterial does not affect the cytokine expression in activated murine immune cells. (A) Percent of cytokine positive spleen cell (indicated in the X axis) was evaluated by FACS analysis after 72 hours culture under T- (anti-CD3 antibody) or **(B)** B-cell stimulus (LPS) in the presence (filled bars) or absence (CTL, empty bars) of MGHA scaffolds.

4. Conclusions

Some modifications are induced by MGHA *nanocomposite* on RAW macrophages after contact with the scaffold surface and with 24h extracts, which can be related to the high reactivity/bioactivity of this *nanocomposite*. However, MGHA material does not produce significant *in vitro* alterations in the activation of macrophages, B- or T-lymphocytes and natural killer cells when an immune response stimulation model was carried out using murine primary immune cell subpopulations. The present study reveals the high biocompatibility of MGHA material and suggests an adequate host tissue response to their scaffolds *in vivo* after implantation.

Acknowledgements

This study was supported by research grants from Comunidad de Madrid (S2009/MAT-1472), and Ministerio de Economía y Competitividad (MINECO) (research grants MAT2012-35556,

CS2010-11384-E and FIS PI10/0648). Mónica Cicuéndez is grateful to MICINN for the financial support through FPI fellowship. The authors wish to thank also to the staff of the ICTS Centro Nacional de Microscopia Electrónica (Spain) and Centro de Citometría y Microscopia de Fluorescencia. The authors thank to Dr. Shunsuke Asahina (SMBU, JEOL, Akishima, Tokyo 196-8558, Japan) and Prof. Osamu Terasaki (Graduate School of EEWS, WCU, KAIST, Daejeon, Republic of Korea) for their help in the tuning of JEOL JSM7600F microscope in the ICTS (http://www.cnme.es) and capture of the micrographs.

Notes and references

[a] Departamento de Química Inorgánica y Bioinorgánica. Facultad de Farmacia. Universidad Complutense de Madrid. Plaza Ramón y Cajal s/n. 28040 Madrid. Spain.

[b] Networking Research Center on Bioengineering, Biomaterials and Nanomedicine (CIBER-BBN), Madrid, Spain.

[c] Consejo Superior de Investigaciones Científicas, CSIC, Spain

[d] Centro Nacional de Microbiología, Instituto de Salud Carlos III, Majadahonda, 28220-Madrid, Spain

[e] Departamento de Bioquímica and Biología Molecular I, Facultad de Ciencias Químicas, Universidad Complutense de Madrid, Ciudad Universitaria s/n, 28040-Madrid, Spain.

[*] Corresponding author: E-mail address: portoles@quim.ucm.es, vallet@ucm.es.

1 R. Langer, J.P. Vacanti. *Science* 1993, **260**, 920–926.
2 T.G. Kim, H. Shin, D.W. Lim. *Adv Funct Mater* 2012, **22**, 2446–2468.
3 F.J. O'Brien. *Materials Today* 2011, **14**, 88–95.
4 S.K. Misra, T.I. Ansari, S.P. Valappil, D. Mohn, S.E. Philip, W.J. Stark, I. Roy, J.C. Knowles, V. Salih, A.R. Boccaccini. *Biomaterials* 2010, **31**, 2806–2815.
5 X. Wang, G. Song, T. Lou. Med. Eng. Phys. 2010, **32**, 391–397.
6 M.T. Arafat, C.X.F. Lam, A.K. Ekaputra, S.Y. Wong, X. Li, I. Gibson. *Acta Biomater.* 2011, **7**, 809–820.
7 M. Ebrahimian-Hosseinabadi, F. Ashrafizadeh, M. Etemadifar, S.S. Venkatraman. *Polym. Deg. Stab.* 2011, **96**, 1940–1946.
8 X.Y. Lu, T. Qiu, X.F. Wang, M. Zhang, X.L. Gao, R.X. Li, X. Lu, J. Weng. *Appl. Surf. Sci.* 2012, **262**, 227–230.
9 M. Cicuéndez, M.T. Portolés, I. Izquierdo-Barba, M. Vallet-Regí. Chem Mater 2012, **24**, 1100–1106.
10 M. Alcaide M, M.T. Portolés, A. López-Noriega, D. Arcos, M. Vallet-Regí. *Acta Biomater.* 2010, **6**, 892–899.
11 M. Cicuéndez, M. Malmsten, J.C. Doadrio, M.T. Portolés, I. Izquierdo-Barba, M. Vallet-Regí. J. Mater. Chem. B. 2014, **2**, 49–58.
12 S. Hollister. *Adv Mater* 2009, **21**, 3330–3342.
13 D.W. Hutmacher. *Biomaterials* 2000, **21**, 2529–2543.
14 A. Remes, D.F. Williams. *Biomaterials* 1992, **13**, 731–743.
15 S. Franz, S. Rammelt, D. Scharnweber, J.C. Simon. *Biomaterials* 2011, **32**, 6692–6709.
16 M.J. Smith, K.L. White, D.C. Smith, G.L. Bowlin. *Biomaterials* 2009, **30**, 149–159.
17 B.N. Brown, B.D. Ratner, S.D. Goodman, S. Amar, S.F. Badylak. *Biomaterials* 2012, **33**, 3792–3802.
18 B.N. Brown, R. Londono, S. Tottey, L. Zhang, K.A. Kukla, M.T. Wolf, K.A. Daly, J.E. Reing, S.F. Badylak. *Acta Biomater.* 2012, **8**, 978–987.
19 K. Garg, N.A. Pullen, C.A. Oskeritzian, J.J. Ryan, G.L. Bowlin. *Biomaterials* 2013, **34**, 4439–4451.
20 R.M. Boehler, J.G. Graham, L.D. Shea. *BioTech.* 2011, **51**, 239-254.
21 P. Portolés, J.M. Rojo, A. Golby, M. Bonneville, S. Gromkowski, L. Greenbaum, C.A. Janeway, D.B. Murphy. *J. Immunol* 1989, **142**, 4169–4175.
22 T. Mosmann. *J. Immunol. Methods* 1983, 65, 55–63.
23 J.M. Rojo, E. Pini, G. Ojeda, R. Bello, C. Dong, R.A. Flavell, U. Dianzani, P. Portolés. *Int. Immunol.* 2008, **20**, 577–589.
24 M. Cicuéndez, I. Izquierdo-Barba, M.T. Portolés, M. Vallet-Regí. *Eur. J. Pharm. Biopharm.* 2013, **84**, 115–124.
25 M. Vallet-Regí, J.M. González-Calbet. *Prog. Solid State Sci* 2004, **3,** 1–31.
26 J.R. Jones. *Acta Biomater.* 2013, **9**, 4457-4486.
27 M. Vallet-Regí, M. Colilla, I. Izquierdo-Barba *J. Biomed. Nanotech* 2008, **4**, 1–15.
28 M. Vallet-Regí. *ISRN Mater Sci* 2012. Article ID 608548, 20 pages.
29 M. Vallet-Regí. *J. Intern. Med.* 2010, **267**, 22–43.
30 M. Vallet-Regí, C.V. Ragel, A.J. Salinas. *Eur. J. Inorg. Chem.* 2003, 1029–1042.
31 H. Kim, B. Cheon, Y.H. Kim, S.Y. Kim, H.P. Kim. *Biochem. Pharm.* 1999, **58**, 759–765.
32 M. Alcaide, M.C. Serrano, R. Pagani, S. Sánchez-Salcedo, M. Vallet-Regí, M.T. Portolés. *Biomaterials* 2009, **30**, 45–51.
33 J.M. Udall, R.A. Moscicki, F.I. Preffer, P.D. Ariniello, E.A. Carter, A.K. Bhan, K.J. Bloch. *Adv. Exp. Med. Biol.* 1987, **216**, 821–827.
34 G. Grynkiewicz, M. Poenie, R.Y. Tsien. *J. Biol. Chem.* 1985, **260**, 3440–50.
35 F. Tian, T. Zhu, Y. Shang. *Toxicol. App. Pharm.* 2010, **242**, 173–181.
36 S. Franz, F. Allenstein, J. Kajahn, I. Forstreuter, V. Hintze, S. Möller. *Acta Biomater.* 2013, **9**, 5621–5629.
37 W.G. Brodbeck, M. Macewan, E. Colton, H. Meyerson H, J.M. Anderson. *J. Biomed. Mater. Res. A* 2005, **74**, 222–229.
38 S.L. Gaffen, K.D. Liu. *Cytokine* 2004, **28**, 109–23.
39 J. Banchereau, V. Pascual, A. O'Garra A. *Nat. Immunol.* 2012, 925-31.
40 M. Saraiva, A. O´Garra. *Nat. Rev. Immunol.* 2010, **10**, 170–181.
41 K. Schroder, P.J. Hertzog, T. Ravasi, D.A. Hume. J. Leukoc. *Biol.* 2004, **75**, 163–189.
42 L.C. Platanias. *Nat. Rev. Immunol.* 2005, **5**, 375–386.
43 M. Croft M. *Nat. Rev. Immunol.* 2009, **9**, 271–285.

2.4. Efectos de la funcionalización de la superficie de andamios MGHA sobre la adhesión y diferenciación celular

Tailoring hierarchical meso-macroporous 3D scaffolds: from nano to macro. **Mónica Cicuéndez**, Martin Malmsten, Juan C. Doadrio, María Teresa Portolés, Isabel Izquierdo-Barba y María Vallet-Regí. ***Journal of Materials Chemistry B, 2014, 2, 49-58. Front Cover.***

Teniendo en cuenta que cualquier andamio diseñado para ingeniería tisular ósea debe permitir los procesos de adhesión, proliferación y diferenciación de células óseas sobre su superficie, el objetivo de este trabajo ha sido evaluar la respuesta de preosteoblastos MC3T3 cultivados sobre andamios MGHA y andamios MGHA-NH_2, analizando su adhesión, proliferación y diferenciación a osteoblastos, así como la colonización celular del interior de dichos andamios.

Los resultados obtenidos evidencian la presencia de células perfectamente ancladas a la superficie del andamio MGHA a través de prolongaciones citoplasmáticas, exhibiendo la morfología típica de este tipo celular tras 2 días de cultivo. Sin embargo, se observó una disminución en el número de células presentes en los niveles más profundos de los mismos, por lo que, aunque las características químicas y estructurales de estos andamios permiten una adecuada adhesión celular, es necesaria una mejora de su superficie que garantice una completa colonización. Con el fin de favorecer el proceso de reconocimiento celular, se realizó una modificación de la superficie de los andamios MGHA a través de un método directo y fácilmente aplicable como es la funcionalización con grupos aminopropilsilano, lo cual proporciona carga positiva a la superficie. La **Figura 2.10.** muestra tanto las características químicas (referidas a la composición) como las características estructurales (con respecto a los distintos rangos de magnitud) presentes en los andamios *nanocomposite* MGHA junto con la mejorada adhesión celular de preosteoblastos a los mismos tras la amino funcionalización de su superficie.

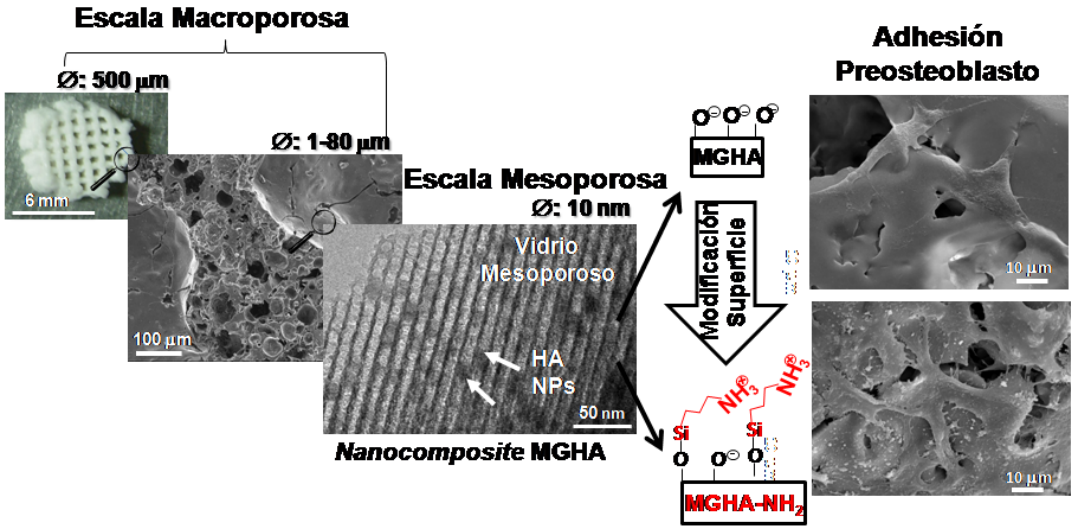

Figura 2.10. Representación de las diferentes escalas de porosidad presentes en los andamios *nanocomposite* MGHA, así como de la mejora observada en el proceso de adhesión celular tras la modificación de la superficie de los mismos con grupos aminopropilsilano.

El notable incremento observado en el proceso de adhesión celular tras la amino funcionalización podría ser debido tanto a la atracción electrostática entre las superficies catiónicas y las membranas celulares cargadas negativamente, como a la incrementada adsorción de proteínas del medio de cultivo, implicadas en la etapa temprana de adhesión celular no específica. Con el fin de determinar el papel de los grupos amino de superficie en la adsorción proteica, se realizaron estudios de adsorción de fibrinógeno (proteína modelo) mediante la técnica de elipsometría, en colaboración con la Universidad de Uppsala bajo la tutela del Prof. Martin Malmsten. Los estudios de elipsometría realizados con ambas superficies, MGHA y MGHA-NH_2, mostraron que las muestras amino funcionalizadas presentaban mayores cantidades de proteína adsorbida en comparación con las superficies no funcionalizadas.

Tras la modificación química de la superficie de los andamios MGHA, no sólo se mejoraron significativamente los resultados *in vitro* de adhesión celular de preosteoblastos, sino que los resultados obtenidos referentes a la colonización celular también mostraron un notable incremento del número de preosteoblastos en los niveles más profundos de los andamios funcionalizados, denominados MGHA-NH_2. Estos resultados se muestran en la **Figura 2.11.**

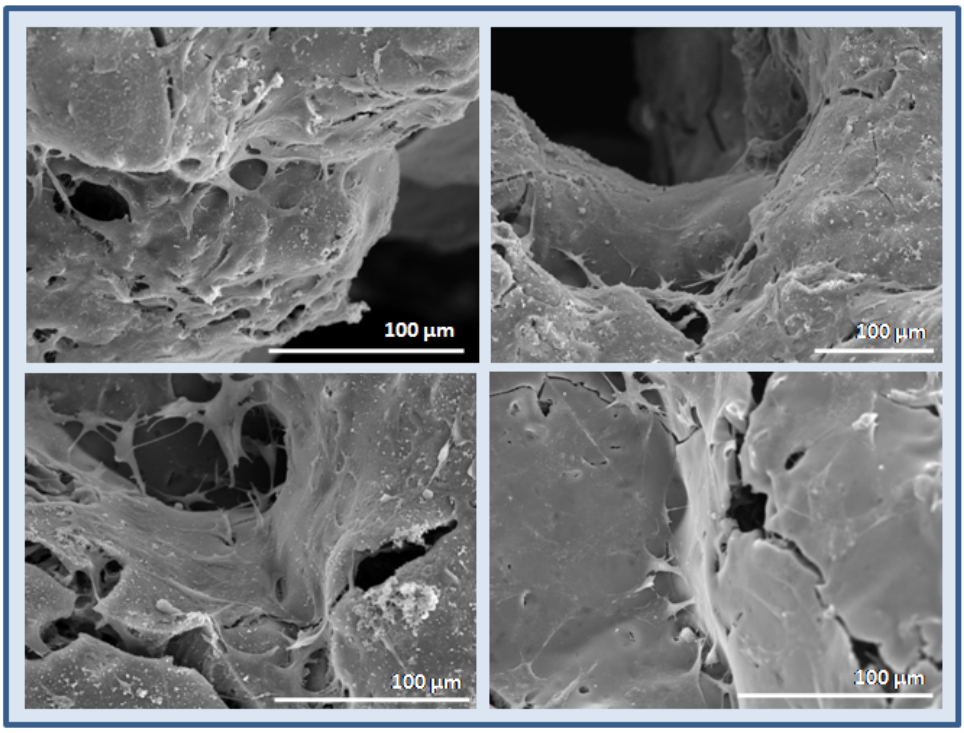

Figura 2.11. Colonización a las 48h del interior del andamio MGHA-NH_2 por preosteoblastos. Todas las imágenes de SEM corresponden a macroporos de 400-500 µm.

El análisis de la actividad mitocondrial de los preosteoblastos sobre los andamios MGHA y MGHA-NH_2, evidencia un aumento significativo 2.3 veces superior en los andamios amino funcionalizados, de acuerdo con el mayor número de células adheridas a los mismos (**Figura 2.11.**). Para los estudios de diferenciación de preosteoblastos MC3T3 en osteoblastos se eligió la determinación de la actividad enzimática fosfatasa alcalina (ALP) como marcador. El análisis de la diferenciación celular mediante este parámetro tras 7 días de cultivo sobre andamios MGHA-NH_2, mostró un incremento significativo de la actividad ALP referida al contenido de proteína total, 4.8 veces superior al valor obtenido en los andamios MGHA. Asimismo se observaron cambios morfológicos característicos, como consecuencia de la diferenciación de preosteoblastos en osteoblastos (**Figura 2.12.**).

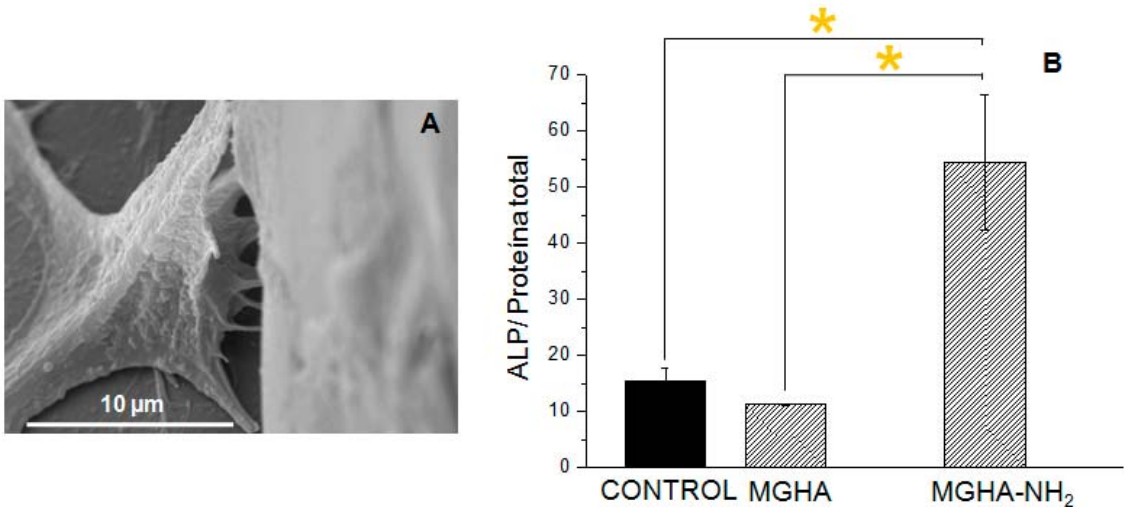

Figura 2.12. Diferenciación celular tras 7 días de cultivo sobre andamios MGHA-NH_2. (A) Morfología de un osteoblasto anclado al andamio. **(B)** Actividad fosfatasa alcalina (ALP) referida al contenido total de proteínas.

Estos resultados sugieren que la composición y estructura jerarquizada meso-macroporosa de los andamios MGHA junto con la modificación química de su superficie, mejoran significativamente la biocompatibilidad de los andamios *nanocomposite* MGHA, poniendo de manifiesto el elevado potencial de este material para regeneración tisular ósea.

Volume 2 | Number 1 | 7 January 2014 | Pages 1–140

Journal of Materials Chemistry B

Materials for biology and medicine

www.rsc.org/MaterialsB

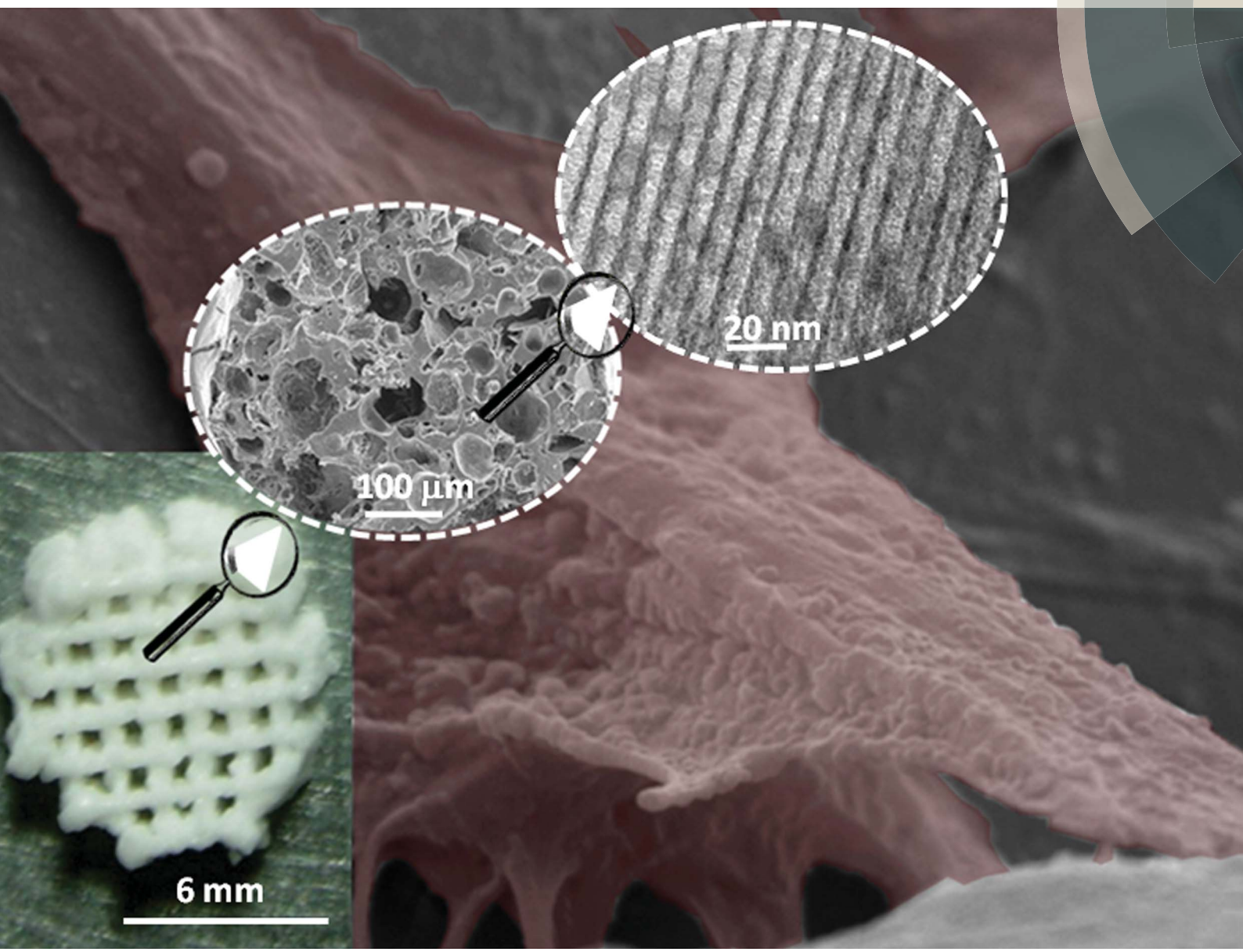

ISSN 2050-750X

ROYAL SOCIETY OF CHEMISTRY

PAPER

Isabel Izquierdo-Barba, María Vallet-Regí *et al.*

Tailoring hierarchical meso–macroporous 3D scaffolds: from nano to macro

Journal of Materials Chemistry B

PAPER

View Article Online
View Journal | View Issue

Tailoring hierarchical meso–macroporous 3D scaffolds: from nano to macro

Cite this: *J. Mater. Chem. B*, 2014, **2**, 49

Mónica Cicuéndez,[ab] Martin Malmsten,[c] Juan Carlos Doadrio,[a] María Teresa Portolés,[d] Isabel Izquierdo-Barba*[ab] and María Vallet-Regí*[ab]

Received 20th September 2013
Accepted 21st October 2013

DOI: 10.1039/c3tb21307b

www.rsc.org/MaterialsB

Bone tissue regeneration requires the use of 3D scaffolds which mimic the architecture of the natural extracellular matrix, creating an adequate microenvironment for bone cell growth. Such 3D scaffolds need surface properties suitable for biological recognition in the early stage of cell adhesion, necessary to ensure complete cell colonization, retained cell functionality, and subsequently bone regeneration. Herein, hierarchical 3D scaffolds based on new hydroxyapatite/mesoporous glass nanocomposite bioceramic (MGHA) exhibiting different scales of porosity have been synthesized. These 3D scaffolds possess: (i) highly ordered mesopores with diameters of 10 nm; (ii) macropores with diameters in the 30–80 μm range with interconnections of 1–10 μm; and (iii) large macropores of *ca.* 500 μm. To improve their surface properties, 3D scaffolds were modified through direct functionalization with amine propyl groups, which notably improve preosteoblast adhesion, proliferation (2.3 fold), differentiation (4.8 fold) and further cell colonization of these scaffolds. The observed enhancement can be related to these amine groups which favour early adhesion, *e.g.*, based on nonspecific protein adsorption as was demonstrated by ellipsometry. These results suggest that the combination of hierarchical structure design and amine surface modification of hydroxyapatite/mesoporous nanocomposite scaffolds yields a double increase in cell proliferation, as well as a quadruple increase in cell differentiation, demonstrating the potential of these nanocomposite materials for bone tissue regeneration purposes.

1. Introduction

Bone tissue engineering requires the use of tridimensional (3D) scaffolds which act as temporary templates for migration, proliferation, and differentiation of cells to guide bone repair, stimulating natural mechanisms of bone regeneration.[1–3] These processes are affected by both pore structure at different length scales and the chemical surface composition of these implants, which constitute fundamental pillars in the design and manufacture of these scaffolds.[1] The macroporous architecture of the scaffold should maintain the mechanical integrity of the material during bio-resorption, and also sustain both cell proliferation and new extracellular matrix deposition. *In vivo* studies have shown that interconnected macropores in the range of 150–500 μm and porosity over 50% led directly to bone mineralization.[4–6] Moreover, pore interconnection is directly related to vascularisation and nutrient diffusion, both critical for osteogenesis.[5] Furthermore, it has been established that the nanoscale in the scaffold surface has important implication in the control of cell behaviour. In fact, natural bone has nanoscale dimensions, where the extracellular matrix (ECM) is mainly constituted by the collagen-fiber framework (10–300 nm) with interconnected nanopores, and hydroxyapatite nanocrystals (25–4 nm).[7,8] Thus, several studies have shown that nanostructured porous surfaces significantly enhance cell attachment, cell viability, alkaline phosphatase (ALP) activity, and gene expression of osteoblasts on hydroxyapatite scaffolds.[9]

However, most synthetic 3D scaffolds lack chemical surface properties involved in the biological recognition processes and in the early stage of cell adhesion, necessary to ensure the complete cell colonization for subsequent bone regeneration.[6,10] Cell adhesion is the first event in the recognition between the 3D scaffold surface and cells, playing a primary role in posterior cellular responses.[11,12] This process depends on both non-specific and specific cell/biomaterial surface interactions with cooperative effects.[11] Non-specific cell adhesion through physical/chemical interactions is responsible for the early stage cell adhesion, which involves the contact of the biomaterial surface with the pericellular coat (PCC) containing hyaluronan, highly negatively charged under the physiological conditions.[13,14] Subsequently, specific adhesion mechanisms are triggered by

[a]*Departamento de Química Inorgánica y Bioinorgánica, Facultad de Farmacia, Universidad Complutense de Madrid, Plaza Ramón y Cajal s/n, 28040 Madrid, Spain. E-mail: vallet@ucm.es; ibarba@ucm.es*

[b]*Networking Research Center on Bioengineering, Biomaterials and Nanomedicine (CIBER-BBN), Madrid, Spain*

[c]*Department of Pharmacy, Uppsala University, SE-75123 Uppsala, Sweden*

[d]*Departamento de Bioquímica and Biología Molecular I, Facultad de Ciencias Químicas, Universidad Complutense de Madrid, Ciudad Universitaria s/n, 28040-Madrid, Spain*

conjugation of extracellular ligands to receptors in the cell membrane.[12] These receptors are heterodimeric transmembrane proteins called integrins, which, in a natural environment, interact with adhesion peptide sequences of extracellular matrix proteins.[15]

Numerous studies have focused on the anchoring of specific adhesion peptides, *e.g.*, RGD, a peptide to enhance both processes.[1,16–18] These approaches are, however, expensive and require high control of peptide location and final conformation on the scaffold surface. In fact, cell adhesion on these modified supports is often not significantly better than on commercialized tissue-culture plastic (TCP), based on a simple functionalization with lysine moieties on the plate surface.[19] In this sense, TCP exhibits good cell adhesion due to its ability to enable absorption of proteins in culture medium and then enhances non-specific adhesion of cells. Based on this strategy, there is considerable interest in using simple chemistry to improve cell responses, addressing the incorporation of positively charged amino moieties in the biomaterial surface which significantly favour cell adhesion and further differentiation.[20,21]

Recently, a nanocomposite bioceramic (MGHA), formed by particles of nanocrystalline apatite embedded into amorphous mesoporous bioactive glass in the SiO_2–P_2O_5–CaO system, has been reported.[22] Due to the synergy of the features of its two components, including (i) ordered mesoporous arrangement with pores of 8 nm, (ii) high surface area and pore volume, (iii) high bioactivity, (iv) presence of nanocrystalline apatite particles homogeneously distributed, and (v) improved *in vitro* biocompatibility, this nanocomposite material is an excellent candidate for bone tissue engineering. However, with this objective, it is necessary to obtain 3D macroporous scaffolds based on this nanostructured material with the porosity ranges required for proper cell colonization, preserving the intrinsic characteristics of both components during the scaffold manufacturing process. The aim of the present study was therefore to prepare hierarchical meso–macroporous 3D MGHA scaffolds in a one-pot process by the combination of different meso- and macro-structural directing agents through the rapid prototyping (RP) technique. Moreover, to improve the cell adhesion and the scaffold colonization, a simple surface functionalization with aminopropyl groups directly on the scaffolds was also carried out. MC3T3 preosteoblast proliferation and differentiation on these 3D MGHA scaffolds were analysed to confirm the performance of the scaffold design, while ellipsometry was employed for investigating the potential role of protein adsorption in cell adhesion.

2. Materials and methods

2.1. 3D MGHA scaffold preparation

3D scaffolds based on a mesoporous glass/hydroxyapatite nanocomposite (MGHA) were prepared by rapid prototyping (RP) *via* direct-write assembly of precursor slurry using an EnvisionTEC GmbH Prefactory® 3D Bioplotter™ (Gladbeck, Germany). This RP technique constitutes an excellent alternative for the manufacture of scaffolds suitable for different clinical applications and individuals.[23] The slurry is derived from a sol precursor of MGHA nanocomposite previously synthesized in powder,[22] to which was added methylcellulose (MC) to produce a slurry with a suitable consistency to be extruded during the RP process.[24,25] In a typical synthesis, 19.5 g of F127 was dissolved in 168.6 mL of absolute ethanol (99.5%, Panreac) with 12.8 mL of 1.0 M HCl (prepared from 37% HCl, Panreac) solution and 19.4 mL of Milli-Q water. Afterwards, the appropriate amounts of tetraethyl orthosilicate (TEOS, 98%, Sigma-Aldrich), triethyl phosphate (TEP, 99.8%, Sigma-Aldrich), and calcium chloride ($CaCl_2 \cdot 4H_2O$, 99%, Sigma-Aldrich) as SiO_2, P_2O_5, and CaO sources, respectively, were added in 1 h intervals under continuous stirring for 4 h at 40 °C and subsequently maintained under static conditions at the same temperature overnight. Subsequently, the MGHA sol precursor was aged for 4–5 days until reaching a final volume reduction of ≈30% through evaporation-induced self-assembly (EISA). Then, MC was added under vigorous stirring in a F127/MC molar ratio of 6 obtaining a suitable consistency to be extruded in the RP process. Cylindrical 50 × 133 × 38 mm scaffolds were designed and fabricated layer-by-layer by direct ink deposition over a plate at room temperature. Each layer was pre-designed showing a 90° rotation with respect to the previous. To obtain the best results, the dispensing speed and pressure were slightly modified from the initial machine parameters during the dispensing process for each scaffold. The scaffold hardening process occurred by solvent evaporation and the pieces were left to dry at 30 °C. Finally, the pieces were calcined at 700 °C for 6 h.

2.2. Amine functionalization of 3D MGHA scaffolds

Nanocomposite 3D MGHA scaffolds were functionalized directly post-synthesis with amine groups using 3-aminopropyltriethoxysilane ($C_9H_{23}NO_3Si$, APTES, ≥98% wt, Sigma-Aldrich). In doing so, two scaffold pieces (25 mg of weight per piece) were degassed overnight at 100 °C, followed by the addition of 12.5 mL of dried toluene (98%, Aldrich). Subsequently, 0.5 mL of APTES reactant was incorporated and kept for 12 h in reflux under a nitrogen atmosphere at 80 °C. Then, the scaffolds were removed and washed in aqueous medium under continuous stirring for 24 h. The resulting amine functionalized scaffolds are denoted as MGHA-NH_2.

2.3. Characterization

X-ray diffraction (XRD) experiments were performed on a Philips X'Pert diffractometer (Eindhoven, The Netherlands), equipped with Cu Kα (40 kV, 20 mA). Transmission electron microscopy (TEM) was performed on a JEOL 3010 electron microscope (Jeol Ltd., Japan), operating at 300 kV (Cs; 0.6 mm, resolution 1.7 Å). All TEM images were recorded employing a CCD camera (MultiScan model 794, Gatan Inc., UK) under low-dose conditions. Fourier transform (FT) patterns were extracted from the images of thin crystal regions using a Digital Micrograph (Gatan Inc., UK). Scanning electron microscopy (SEM) was performed using a field emission JEOL JSM-6335F microscope (Tokyo, Japan) at an acceleration voltage of 10 kV. Textural properties were determined by N_2 adsorption porosimetry using a Micromeritics ASAP2020 analyzer (Norcross, USA). Prior to these measurements,

both MGHA and MGHA-NH_2 scaffolds were degassed at 60 °C for 24 hours under vacuum (<0.3 kPa). The surface area was determined using the multipoint Brunauer–Emmett–Teller method included in the software. The porosity of 3D scaffolds was measured by mercury intrusion porosimetry using a Micromeritics Autopore IV 9500 device (Micromeritics Instrument Corporation, Norcross, GA, USA). Elemental analyses (C, H, N) were carried out on a LECO CHNS-932 microanalyzer (Saint Joseph, Michigan USA). Fourier transform infrared (FTIR) spectroscopy was performed in a Thermo Nicolet Nexus spectrometer (Thermo Scientific, USA) from 4000 to 400 cm^{-1}, using the KBr pellet method and operating in transmittance mode. ^{29}Si, ^{31}P and ^{13}C single pulse (SP) and cross-polarization (CP)/MAS (magic angle spinning) solid-state nuclear magnetic resonance (NMR) measurements were performed to evaluate the different silicon, phosphorus, and carbon environments in synthesized scaffolds. NMR spectra were recorded on a Bruker Avance 400 WB spectrometer (Karlsruhe, Germany). Samples were spun at 10, 6, and 12 kHz for ^{29}Si, ^{31}P and ^{13}C, respectively. These spinning speeds were sufficient to make the spinning sidebands of low intensity and outside the region of interest. Spectrometer frequencies were set to 79.49, 161.97, and 75.45 MHz for ^{29}Si, ^{31}P, and ^{13}C, respectively. Chemical shift values were referenced to 3-trimethylsilyl-1-propanesulfonic acid sodium salt (DDS), 85% phosphoric acid (H_3PO_4) and glycine for ^{29}Si, ^{31}P, and ^{13}C, respectively. Time periods between successive accumulations were 5, 4, and 3 ms for ^{29}Si, ^{31}P, and ^{13}C, respectively, and the number of scans was *ca.* 13 000 for all spectra. Zeta-potential (ζ) measurements were performed on a Malvern Zetasizer Nano Series instrument (Malvern Instruments Ltd., UK). For this purpose, 10 mg of each powdered sample was added to 20 mL of KCl solution (20 mM) and the mixture was vigorously stirred to reach a homogenous suspension. The measurements were carried out at in the pH range of 2–10 by the addition of HCl solution (0.01 M) and NaOH (0.01 M). Six ζ-potential runs were recorded for each sample at 37 °C, with a minimum of 30 sub runs per measurement, whereafter average values and standard deviations were calculated ($n = 6$).

2.4. Protein adsorption

Hydrophilic and negatively charged silica surfaces were prepared from polished silicon slides (p-type, boron doped). The surfaces were cleaned in a mixture of 25% NH_4OH, 30% H_2O_2, and H_2O (1 : 1: 5, by volume) at 80 °C for 5 min, followed by cleaning in a mixture of 32% HCl, 30% H_2O_2, and H_2O (1 : 1 : 5, by volume) at 80 °C for 5 min. The slides were then rinsed twice with water and ethanol. This procedure rendered the surfaces hydrophilic, with a water–air contact angle of less than 10°. MGHA was deposited on these silica slides through a dip-coating method using the MGHA precursor sol aged for 24 hours at room temperature, with a withdrawal rate of 2500 mm s^{-1}. The coatings were dried at 100 °C (1 h) and annealed in air at 700 °C for 1 hour to remove the surfactant and to produce the MGHA nanocomposite phase. Finally, the coatings were washed with ethanol in an ultrasonic bath for 2 min. Homogeneous MGHA coatings obtained were confirmed by SEM and EDS studies. Subsequently, these coatings were amine functionalized by the same procedure, this time using APTES moieties as the functionalizing agent. The effectiveness of the amine functionalization process was confirmed by FTIR and XRD analyses. Fibrinogen adsorption to such MGHA deposited on silica surfaces was studied *in situ* by null ellipsometry, using an Optrel Multiskop (Optrel, Kleinmachnow, Germany) equipped with a 100 mW argon laser. All measurements were carried out at 532 nm and an angle of incidence of 67.66° in a 5 mL cuvette under stirring (300 rpm). Both the principles of null ellipsometry and the procedures used have been described extensively before.[26] In brief, by monitoring the changes in the state of polarization of light reflected at a surface in the absence and presence of an adsorbed layer, the mean refractive index (n) and layer thickness (d) of the adsorbed layer can be obtained. From the thickness and refractive index the adsorbed amount (Γ) was calculated according to:

$$\Gamma = \frac{(n - n_0)}{\mathrm{d}n/\mathrm{d}c} d \quad (1)$$

where n_0 is the refractive index of the bulk solution, and $\mathrm{d}n/\mathrm{d}c$ the refractive index increment (0.154 $cm^3\ g^{-1}$). Corrections were routinely done for changes in the bulk refractive index caused by changes in temperature and excess electrolyte concentration.

2.5. Cell adhesion, morphology, mitochondrial activity and cell differentiation

2.5.1. Cell culture. MGHA and MGHA-NH_2 scaffolds were sterilized under UV light for 15 min and then submerged in Dulbecco's Modified Eagle's Medium (DMEM, Sigma Chemical Company, St. Louis, MO, USA) supplemented with penicillin (800 μg mL^{-1}, BioWhittaker Europe, Belgium), streptomycin (800 μg mL^{-1}, BioWhittaker Europe, Belgium), β-glycerolphosphate (50 μg mL^{-1}, Sigma Chemical Company, St. Louis, MO, USA) and L-ascorbic acid (10 mM, Sigma Chemical Company, St. Louis, MO, USA), under a CO_2 (5%) atmosphere at 37 °C for 24 h to stabilize before cell culture. Subsequently, murine MC3T3-E1 preosteoblasts (as undifferentiated osteoblast-like cells) were seeded at a density of 10^5 cells per mL in DMEM with 10% fetal bovine serum (FBS, Gibco, BRL), 1 mM L-glutamine (BioWhittaker Europe, Belgium), penicillin (200 μg mL^{-1}, BioWhittaker Europe, Belgium), and streptomycin (200 μg mL^{-1}, BioWhittaker Europe, Belgium), under a CO_2 (5%) atmosphere at 37 °C for 48 h.

2.5.2. Morphological studies by scanning electron microscopy. For SEM studies, cells attached to the 3D scaffolds were fixed with glutaraldehyde (2.5% in Phosphate Buffer Saline, PBS) for 45 min. Sample dehydration was performed by slow water replacement, using a series of ethanol solutions (30%, 50%, 70%, 90%) for 30 min with a final dehydration in absolute ethanol for 60 min, allowing samples to dry at room temperature and under vacuum. Afterwards, the pieces were mounted on stubs and coated in a vacuum with gold–palladium. Cells were examined with a JEOL JSM-6400 scanning electron microscope.

2.5.3. Mitochondrial activity. To evaluate the cell mitochondrial activity of living cells on MGHA and MGHA-NH_2 3D

scaffolds, as well as around them (in the bottoms of the cell culture wells) after 48 h of incubation, an MTT method was employed, based on the reduction of yellow 3[4,5-dimethylthiazol-2yl]-2,5-diphenyltetrazolium bromide to blue formazan.[27] For this, the culture media were replaced with 1 mL of DMEM and 125 μL of 0.012 g L^{-1} MTT solution in PBS. Samples were incubated for 4 h at 37 °C and 5% CO_2 under dark conditions. Then, the medium was removed and 500 μL of 0.4 N isopropanol–HCl were added. Finally, the absorbance was measured at 570 nm using a Helios Zeta UV-VIS spectrophotometer.

2.5.4. Alkaline phosphatase activity. The alkaline phosphatase (ALP) activity of cells growing on the both MGHA and MGHA-NH_2 scaffolds was used as the key differentiation marker in assessing expression of the osteoblast phenotype. ALP activity was measured using the Reddi and Huggins method based on the hydrolysis of *p*-nitrophenylphosphate to *p*-nitrophenol.[28] For this, MC3T3 cells (5×10^4 cells per mL) were seeded directly onto scaffolds in 24-well plates and incubated under standard culture conditions using supplemented medium with β-glycerolphosphate (50 μg mL^{-1}, Sigma Chemical Company, St. Louis, MO, USA) and L-ascorbic acid (10 mM, Sigma Chemical Company, St. Louis, MO, USA). In order to evaluate ALP activity both in and around the scaffolds after 7 days of incubation, each scaffold was transferred to a new well. Moreover, the total protein value after 7 days was determined by a colorimetric method at 540 nm (Bio-Analítica, S.L.), using a Helios Zeta UV-VIS spectrophotometer.

2.6. Statistics

Data are expressed as means ± standard deviations of three experiments. Statistical analysis was performed using the Statistical Package for the Social Sciences (SPSS) version 11.5 software. Statistical comparisons were made by analysis of variance (ANOVA). The Scheffé test was used for *post hoc* evaluations of differences among groups. In all statistical evaluations, $p < 0.05$ was considered as statistically significant.

3. Results and discussion

3.1. 3D MGHA scaffolds and cell colonization

The macroporosity of the 3D MGHA scaffolds obtained by the RP technique was characterized by SEM and Hg intrusion porosimetry. The digital photograph (inset Fig. 1A) displays the image of a cylindrical piece of MGHA scaffold. The SEM micrograph (Fig. 1A) shows that MGHA scaffolds consist of a lattice of rods stacked with simple tetragonal symmetry according to the RP computer-aided design, where twenty layers of mesh were stacked to a total thickness of *ca.* 2 mm, with a diameter of ≈6.6 mm. These scaffolds present a hierarchical pore network with macropores around 500 μm connected by rods of 250–300 μm diameter, corresponding to the porosity required for tissue growth and vascularization in the human body.[29,30] The higher magnification SEM micrograph, corresponding to a scaffold cross-section (Fig. 1B), shows notable differences between the interior and exterior scaffold surface. While the external surface exhibits cylinders with relatively smooth topography and a small fraction

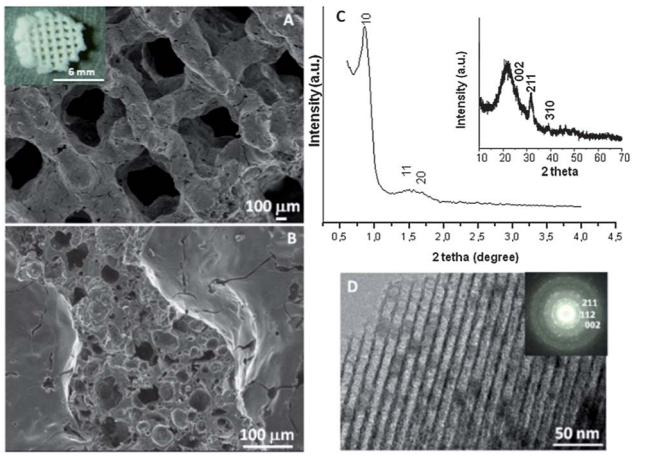

Fig. 1 Macro- and mesostructural characterization of the hierarchical interconnected MGHA nanocomposite 3D scaffold. Surface (A) and cross-transversal section (B) obtained by SEM. (Inset) Digital photograph of a MGHA scaffold. (C) XRD pattern at low scattering angles showing the ordered mesoporous arrangement. (Inset) XRD pattern at wide scattering angles demonstrates the presence of the apatite phase. (D) TEM image showing the homogeneous distribution of the nanocrystalline apatite particles in the 2D hexagonal mesoporous structure. (Inset) ED pattern.

of pores in the range between 1 and 10 μm, the interior surface exhibits numerous pores in the range of 30 to 80 μm, resulting from the MC calcination process.[24,25] Moreover, Hg intrusion porosimetry shows that the internal larger pores are accessible to the liquid probe, indicating well-connected macroporous systems (data not shown). Total percentage porosity is 60%, mainly in the 1–10 μm and 100–300 μm range according to SEM images. Low angle XRD patterns of these scaffolds (Fig. 1C) show three diffraction maxima at 0.86, 1.43, and 1.67° (2θ), which can be indexed to (10), (11), and (20) reflections of a 2D hexagonal structure (*P6mm* plane group) based on TEM results (Fig. 1D). N_2 isotherms (Table 1) demonstrate the presence of a very narrow distribution of large mesopores centred at 10 nm, with a surface area and pore volume of 123 $m^2\ g^{-1}$ and 0.2 $cm^3\ g^{-1}$, respectively. Compared to the powder MGHA nanocomposite, the results obtained for the 3D MGHA scaffolds reveal a notable increase in pore size, from 8.0 nm for the powder nanocomposite[22] to 10 nm for the scaffold, accompanied by a decrease both in the surface area and pore volume. This increase in pore size can be attributed to MC incorporation during the synthesis process.[31]

To confirm the presence of nanocrystalline apatite in the 3D MGHA scaffolds, XRD and TEM studies were carried out. Wide-angle XRD patterns (inset, Fig. 1C) show very broad (002), (211) and (310) reflections, which could be attributed to apatite occurrence.[32] Furthermore, TEM studies (Fig. 1D) showed a small darker zone homogeneously distributed in the mesoporous structure corresponding to nanocrystalline apatite phase particles. The electron diffraction (inset) of the dark zone displayed diffuse halos, showing *d*-spacing at 0.28, 0.27, and 0.34 nm, corresponding to the apatite phase. This confirms the nanocomposite structure of scaffolds, indicating that the incorporation of the MC polymer in the synthesis for the scaffolding process did not affect the biphasic structure of MGHA.

Table 1 Textural parameters corresponding to MGHA scaffolds before and after amine functionalization. The amount of aminopropyl moieties covalently bound to the scaffolds was determined by CHN elemental analyses and ζ-potential under physiological pH conditions

Sample	S_{BET} ($m^2\ g^{-1}$)	V_p ($cm^3\ g^{-1}$)	D_p (nm)	mmol APTES m^{-2}	ζ (mV)
Powder MGHA[a]	235	0.4	8.0	—	−25 ± 5
MGHA scaffold	123	0.2	10.0	—	−35 ± 6
MGHA-NH_2 scaffold	101	0.2	8.6	0.02	+8 ± 3

[a] Corresponds to the powder MGHA nanocomposite previously reported in ref. 22.

Therefore, the single-step sol–gel route synthesis in the presence of a surfactant (F127) as the mesostructure directing agent and a biomacromolecular polymer (methylcellulose) as the macrostructure template, followed by the RP technique, allows the formation of the hierarchical interconnected 3D scaffolds exhibiting different scales of porosity: (i) highly ordered mesopores with diameters of *ca.*10 nm that may act as local controlled delivery systems of biologically active molecules, and allow better nutrient diffusion;[33–35] (ii) interconnected macropores with diameters in the 1–80 μm, and (iii) ultra-large macropores of *ca.* 500 μm, that may provide the opportunities for cell colonization.[29] Furthermore, the presence of nanocrystalline apatite particles homogeneously distributed along the composite constitutes one more common element with the bone structure and may influence and control protein interactions through its surface properties, guiding cellular responses as they occur in the natural bone.[36] Thus, this combination of the macroporous architecture, the nanoscale structure of the surface, and the presence of apatite particles may provide real benefits for MGHA nanocomposite scaffolds in bone tissue regeneration.

To investigate whether the MGHA scaffold architecture and composition would permit good bone integration, cell morphology, spreading degree, and internalization of MC3T3 preosteoblasts were studied after 2 days culture at different levels (depth) inside the macroporous structure. L1 label indicates the outer level, while L2 and L3 correspond to inner levels of macropores. Fig. 2A shows a low magnification SEM micrograph evidencing the presence of cells anchored through filopodia projections (inset) on the surface of L1, L2, and L3 zones, demonstrating that the MGHA scaffolds are colonized over the entire visible surface. Fig. 2B–D provide details of the three levels in which cells exhibit a typical morphology of this cell type.[37]

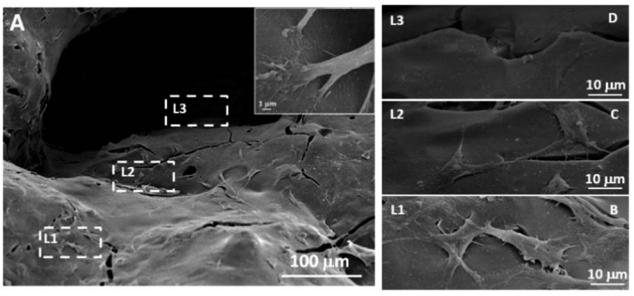

Fig. 2 SEM studies of 3D MGHA scaffold colonization by MC3T3 preosteoblasts. (A) Low magnification micrograph of cell adhesion and colonization at different macroporous levels (L1, L2, and L3) of the scaffold. (Inset) cell anchoring in detail. (B)–(D) Higher magnifications micrographs showing the details of spreading MC3T3 cells at these macroporous levels. All micrographs are representative of the study.

The obtained results revealed adequate cell colonization over the MGHA scaffold surface. A commonly used approach for making the scaffold surface more conductive to cell adhesion is its preconditioning with cell adhesive peptides or proteins.[16,17] In the present study, without any such preconditioning, the chemical and structural characteristics of these MGHA scaffolds are proved to be excellent in terms of biocompatibility. However, the cell number at the inner levels of these scaffolds could be improved by a suitable surface treatment to enhance cell colonization.

3.2. Amine functionalization of the 3D scaffold surface and its influence on cell adhesion, mitochondrial activity and cell differentiation

Since it has been demonstrated that the surface chemistry of a material exerts an important influence on cell response,[7] amine functionalization of the 3D MGHA scaffold surface was carried out. Fig. 3 displays FTIR spectra before and after amine functionalization, both spectra exhibiting bands corresponding to the MGHA nanocomposite material. Thus, the bands of Si–O bonds at 1040, 800, and 470 cm^{-1} correspond to the amorphous silica mesoporous glass, while the doublet at 560 and 600 cm^{-1} is characteristic of crystalline phosphate.[38] After amine functionalization, the FTIR spectrum of the MGHA-NH_2 scaffold shows the appearance of new bands at 3344 and *ca.* 1500 cm^{-1}, corresponding to NH stretching and deformation frequencies, respectively, whereas bands at 3030 and ≈1590 cm^{-1} are attributed to $-NH_3^+$ stretching and deformation frequencies, respectively.[39,40] Moreover, the band at 2980 cm^{-1} corresponds to $-CH_2-$ groups, the band at 1260 cm^{-1} to the Si–C bond, and the small band at 1300 cm^{-1} to the C–N bond, confirming also the presence of organosilane (APTES).[40]

To quantify the number of amine groups present on the surface of the MGHA-NH_2 scaffold, a CHNS elemental chemical analysis was carried out. The experimental data indicated 0.02 mmol of APTES per square meter surface. Textural properties after the functionalization process revealed a slight decrease in the surface area, and pore diameter values (Table 1), indicating the incorporation of amino propyl silane moieties, maintaining the pore volume. Moreover, concerning meso–macroporosity, XRD, TEM, SEM, and Hg intrusion studies demonstrated that the

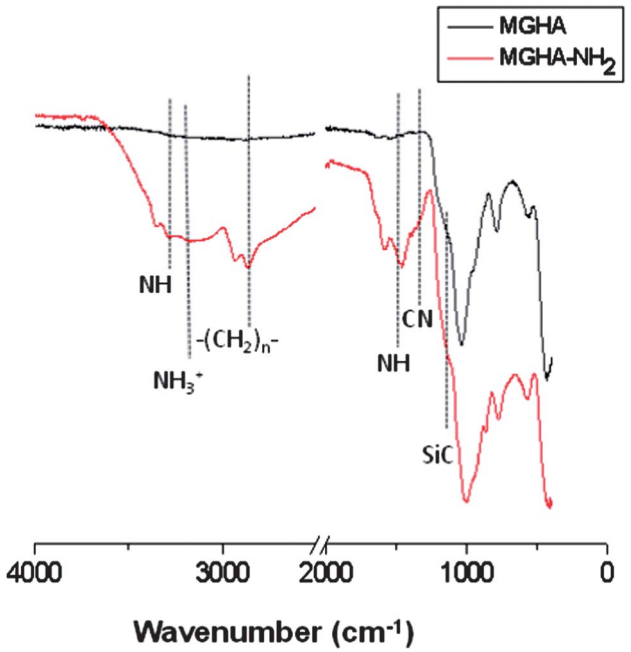

Fig. 3 FTIR spectra corresponding to the 3D MGHA scaffold before and after amine functionalization.

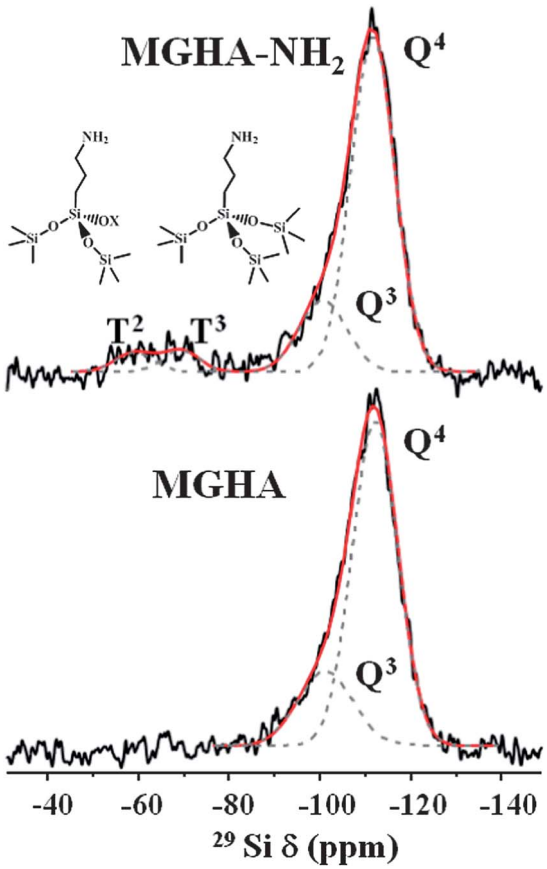

Fig. 4 Solid-state ^{29}Si single-pulse MAS NMR spectra (with their Q^n and T^n silicon environments) corresponding to the 3D MGHA scaffold before and after amine functionalization. The areas for the Q^n and T^n units were calculated by Gaussian line-shape deconvolutions.

both meso–macrostructural parameters were not altered after functionalization (data not shown).

^{29}Si and ^{31}P solid state SP and CP/MAS NMR measurements were carried out to further investigate the grafting of aminopropyl moieties to the MGHA scaffold surface as well as their condensation degree. Fig. 4 displays ^{29}Si MAS NMR spectra recorded from MGHA and MGHA-NH_2 3D scaffolds using single-pulse excitation, together with their component lines obtained from spectral deconvolutions. Both spectra show resonances at *ca.* −102 and −112 ppm, corresponding to Q^3[Si(OSi)^3(OX)], and Q^4[Si(OSi)$_4$] silicon sites, respectively (X = H, C). No significant changes are observed in Q^3/Q^4 relative populations after the functionalization process. The presence of signals attributable to T^n units [R–Si(OSi)$_n$–(OX)$_{3-n}$] (X = H, C) are indicative of the organosilane groups, only evidenced in the MGHA-NH_2 3D scaffold. The presence of T^3 and T^2 signals demonstrates the existence of covalent linkages between the silica surface and the organic groups.[41] Table 2 confirms that no significant changes occur in the $Q^2/Q^3/Q^4$ and $q^2/q^1/q^0$ relative populations for ^{29}Si and ^{31}P environments after the functionalization process.

Solid state ^{13}C CP/MAS NMR spectra were collected to confirm the surface functionalization of MGHA scaffolds and to get information concerning the ionization state of amine (Table 3). As expected, no signals are observed in the ^{13}C NMR spectrum of the unmodified MGHA scaffold (data not shown). In contrast, well-defined signals at 11, 24, and 45 ppm are observed after amine functionalization, which can be assigned to carbon atoms from APTES in three different environments (Table 3). Note that there is no resonance at *ca.* 28 and 85 ppm which would be attributed to the central carbon of the 3-aminopropyl chain of APTES with the –NH_2 group as the nonprotonated form. The resonance appearing in the region of stronger fields, at 24 ppm, assignable to the central carbon of APTES, evidences the protonation of 3-aminopropyl groups, as it has also been confirmed by FTIR data.[42,43]

With the chemical nature of scaffolds clarified, their charge in aqueous media was investigated by ζ-potential measurements. Fig. 5A displays the ζ-potential of MGHA and MGHA-NH_2 scaffolds as a function of pH, and reveals notable differences before and after amine functionalization. Thus, at physiological pH 7.4, the ζ-potential was ≈−35 mV for the unmodified MGHA scaffold. This negative surface charge is due to the presence of deprotonated species, *i.e.*, Si–O$^-$ (pK_a = 4.5) from mesoporous glass and P–O$^-$ species (pK_a = 6.5) from apatite clusters. For MGHA-NH_2 scaffolds, on the other hand, the ζ-potential at pH 7.4 was +8 mV due to the presence of NH_3^+species (pK_a = 10.0). To confirm the pK_a values corresponding to all functional groups present in the MGHA-NH_2 scaffold, a titration curve was carried out between pH values from 10 to 4. Fig. 5B demonstrates that, in agreement with expected bibliographic data, pK_a (NH_3^+) is 10.0; pK_a (POH) is 6.3, and pK_a (SiOH) is 4.5. These results demonstrate that at physiological pH (7.4), the majority species present in the surface scaffold could correspond to NH_3^+, PO$^-$, and SiO$^-$ moieties.

Table 2 Population percent of ^{29}Si and ^{31}P environments resulting in deconvolution of the experimental NMR spectra recorded by cross-polarization (CP) corresponding to unmodified and functionalized scaffolds

	^{29}Si CP					^{31}P CP		
Sample	T^2 (%)	T^3 (%)	Q_H^{2a} (%)	Q_H^3 (%)	Q^4 (%)	q^0 (%)	q^1 (%)	q^2 (%)
MGHA	—	—	19.7	57.2	23.1	65.7	32.2	2.1
MGHA-NH_2	45	55	16.8	46.8	36.4	55.5	35.7	8.8

[a] This NMR signal may comprise minor contributions from Q_{Ca}^2 tetrahedral.[22]

Table 3 Data of solid state ^{13}C CP/MAS NMR corresponding to the MGHA-NH_2 3D scaffold

MGHA-NH_2	
δ (ppm)	Assignment
11	Si–*C*H_2–CH_2–CH_2–NH_2
24	Si–CH_2–*C*H_2–CH_2–NH_3^+
45	Si–CH_2–CH_2–*C*H_2–NH_2

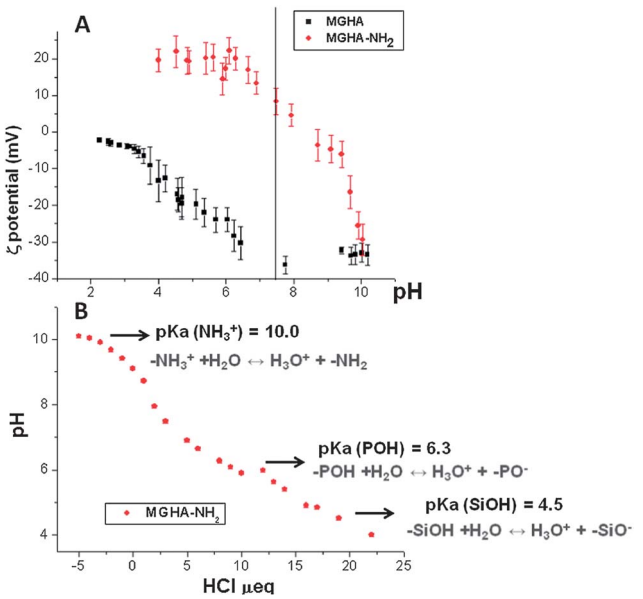

Fig. 5 (A) ζ-potential curves as a function of pH before and after amine functionalisation of MGHA nanocomposite 3D scaffolds. (B) Titration curve with HCl corresponding to MGHA-NH_2.

When cell adhesion on MGHA-NH_2 scaffolds was analyzed by SEM after 2 days culture, a multilayer of MC3T3 cells anchored through filopodia projections (inset in Fig. 6) was observed throughout the surface of these scaffolds (Fig. 6A). Compared to MGHA scaffolds (Fig. 2), a larger number of cells are observed colonizing at all studied levels (L1, L2, and L3; Fig. 6B–D, respectively) of the MGHA-NH_2 scaffold. In all cases there is multilayer cell growth, also at the inner level (L3). This multilayer growth at all levels demonstrates intercellular communication which constitutes a fundamental pillar for total scaffold colonization, ensuring new bone in-growth.[44]

This notable enhancement of cell colonization on MGHA-NH_2 with respect to unmodified MGHA scaffolds could be explained by the different surface chemistry of these samples. At physiological pH (7.4), the MGHA scaffold surface is negatively charged (−35 mV) due to the presence of SiO^- and PO^- groups, whereas after amine functionalization (MGHA-NH_2), the scaffold surface attains a positive surface charge (+8 mV) because of the presence of NH_3^+ groups. Thus, there is an increased direct electrostatic attractive interaction between cationic surfaces and negatively charged membrane cells.[45] In addition, the positive charge promotes adsorption of culture medium proteins, which are involved in the non-specific early stage of cell adhesion.[18] To confirm the role of the surface amine groups in protein adsorption, ellipsometry studies with both surfaces, MGHA and MGHA-NH_2, were carried out. In analogy to the increased cell adhesion, the amine functionalized surfaces display increased adsorption of serum proteins, exemplified for fibrinogen in Fig. 7. As can be seen, adsorption of this important serum protein is much higher for the cationic MGHA-NH_2 compared to unmodified and negatively charged MGHA. This is a reflection of the net negative charge of fibrinogen under these conditions (IEP ≈ 5.5),[46] promoting its adsorption to the oppositely charged MGHA-NH_2 surface. This is in agreement with similar findings obtained for surfaces rendered cationic also by other approaches.[47] Particularly, for serum proteins stimulating cell adhesion, such as fibrinogen and fibronectin, the mechanism for promoting increased cell adhesion and spreading of the MGHA-NH_2 scaffold is likely facilitated by the formation of a conditioning protein layer.

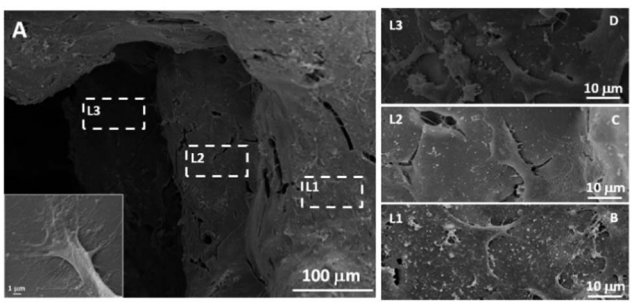

Fig. 6 (A) SEM studies of MGHA-NH_2 scaffold colonization by MC3T3 preosteoblasts showing internalization and cell spreading of pre-osteoblast MC3T3 cells cultured for 2 days on the amine functionalized 3D-MGHA scaffold at different macropore levels (L1, L2, and L3). Inset: detail of the filopodia projections. (B–D) Higher magnification SEM micrographs of spreading MC3T3 cells at the different macropore levels. All micrographs are representative of the study.

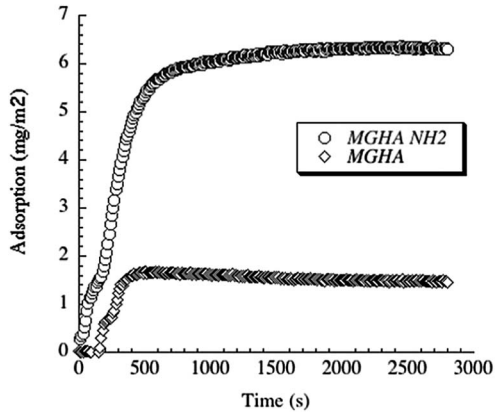

Fig. 7 Fibrinogen adsorption to MGHA and MGHA-NH_2 surfaces detected by ellipsometry.

Moreover, in order to investigate the broader potential of these 3D scaffolds, other cell parameters as mitochondrial activity and cell differentiation were evaluated. The results show a significant increase of mitochondrial activity (2.3 folds, $p \leq 0.05$) when the scaffold surface is previously amine functionalized (Fig. 8A) which is due to the higher number of cells on these scaffolds. Concerning MC3T3 preosteoblast differentiation, evaluated after 7 days culture by ALP activity per total protein, the results reveal a significant increase (4.8 folds, $p < 0.05$) of this cell differentiation parameter on MGHA-NH_2 scaffolds with respect to MGHA scaffolds and TCP control (Fig. 8B). Non-significant differences between the MGHA scaffold and TCP control were observed ($p > 0.05$).

Taken together, these results thus demonstrate that both the structure design of the 3D MGHA scaffold at different length scales (macro and nanoscale) and the use of basic chemistry to incorporate simple amine functional groups to their surface

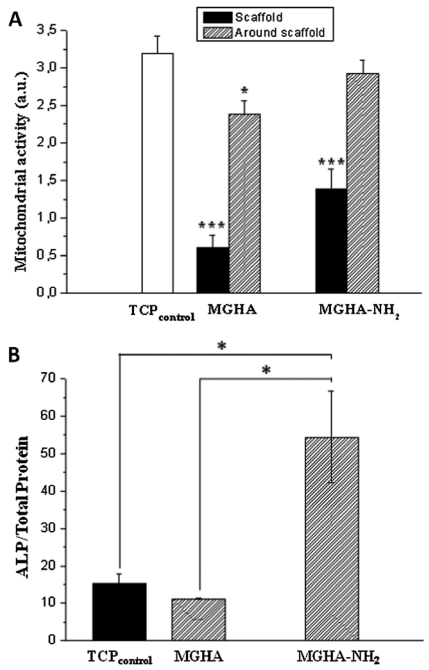

Fig. 8 (A) Mitochondrial activity of preosteoblast MC3T3 cells on the surface scaffold and around the scaffold of unmodified and amine modified ones after 2 days of incubation. (B) ALP per total protein of preosteoblast MC3T3 cells on the surface scaffold of unmodified (MGHA) and amine modified (MGHA-NH_2) ones after 7 days of incubation. Statistical significance: *$p < 0.05$, ***$p < 0.005$.

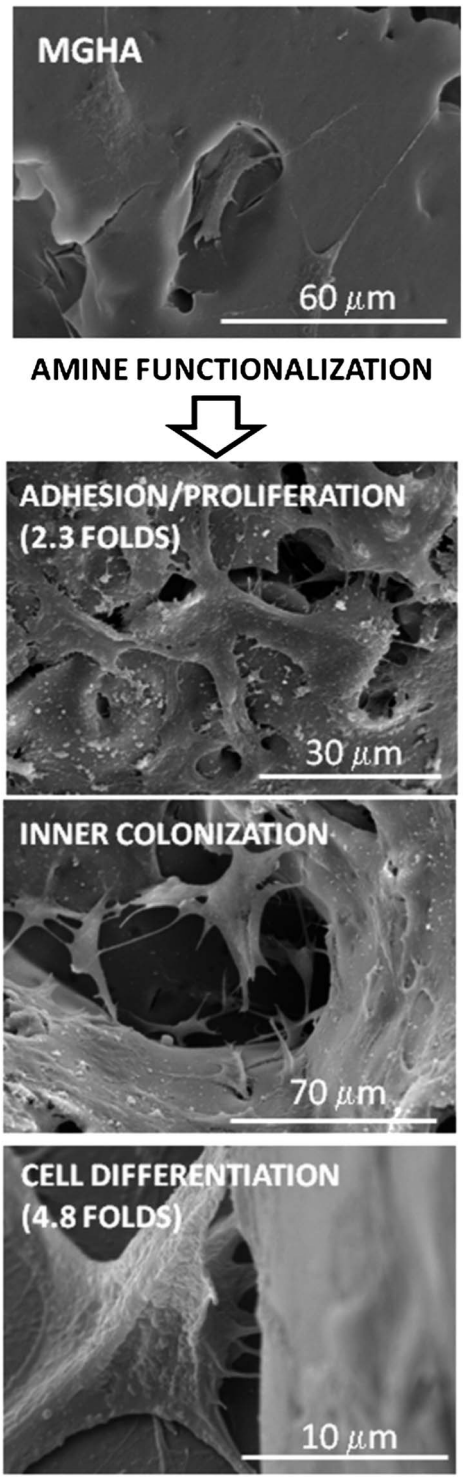

Fig. 9 Summary of effects produced by amine functionalisation of MGHA nanocomposite 3D scaffolds.

enhance notably the cell adhesion, scaffold colonization and preosteoblast differentiation (Fig. 9).

Conclusions

3D scaffolds based on a new nanocomposite (MGHA) composed of hydroxyapatite nanocrystals embedded into mesoporous glass have been fabricated through a rapid prototyping technique. The 3D MGHA scaffolds exhibit three scales of porosity: ordered mesopores (10 nm), interconnected macropores (1–80 μm), and ultra-large macropores (500 μm). This hierarchical meso–macroporous system is obtained by using a sol precursor containing different scale-length polymers (Pluronic F127 and methylcellulose as meso and macrostructure directing agents, respectively) together with a robocasting process. The surface properties of these MGHA scaffolds, concerning cell recognition have been enhanced through a direct functionalization with aminopropyl moieties. This simple and cost-effective amine modification causes noticeable improvements in the preosteoblast adhesion, as well as a double increase in cell proliferation and a quadruple increase in cell differentiation. Moreover, ellipsometry studies demonstrated that the protonated amino propyl moieties favour the early step in the adhesion process by an increase in the nonspecific protein adsorption. Therefore, these studies reveal that both the structure design of hierarchical meso–macroporous 3D MGHA scaffolds and the amine chemical modification of their surface significantly improve the biocompatibility of these nanocomposite scaffolds.

Acknowledgements

This study was supported by research grants from Comunidad de Madrid (S2009/MAT-1472) and Ministerio de Ciencia e Innovacion (MICINN) through the projects MAT2012-35556 and CS2010-11384 E. M. Cicuéndez is grateful to MICINN for the financial support through the FPI fellowship. The authors wish to thank also the staff of the ICTS Centro Nacional de Microscopia Electrónica (Spain) and Centro de Citometría y Microscopia de Fluorescencia, Centro de Difracción de Rayos X, Centro de Microanálisis Elemental and Centro de Resonancia Magnética Nuclear of the Universidad Complutense de Madrid (Spain).

Notes and references

1 S. J. Hollister, *Adv. Mater.*, 2009, **21**, 330–3342.
2 R. Langer and J. P. Vacanti, *Science*, 1993, **260**, 920–926.
3 T. G. Kim, H. Sim and D. W. Lin, *Adv. Funct. Mater.*, 2012, **22**, 2446–2468.
4 X. Yu, Z. Xia, L. Wang, F. Peng, X. Jiang, J. Huang, D. Rowed and M. Wei, *J. Mater. Chem.*, 2012, **22**, 9721–9730.
5 V. Karageorgiou and D. Kaplan, *Biomaterials*, 2005, **26**, 5474–5491.
6 M. Vallet-Regí, *Chem.–Eur. J.*, 2006, **12**, 5934–5943.
7 M. M. Stevens and J. H. George, *Science*, 2005, **310**, 1135–1138.
8 M. Vallet-Regi and J. M. Gonzalez-Calbet, *Prog. Solid State Chem.*, 2004, **32**, 1–31.
9 L. Xia, K. Lin, X. Jiang, Y. Xu, M. Zhang, J. Chang and Z. Zhang, *J. Mater. Chem. B*, 2013, **1**, 5403–5416.
10 M. Vallet-Regí, M. Colilla and I. Izquierdo-Barba, *J. Biomed. Nanotechnol.*, 2008, **4**, 1–15.
11 K. Anselme, *Biomaterials*, 2000, **21**, 667–681.
12 B. Geiger, J. P. Spatz and A. D. Bershadsky, *Nat. Rev. Mol. Cell Biol.*, 2009, **10**, 21–33.
13 M. Cohen, D. Joester, I. Sabanay, L. Addadi and B. Geiger, *Soft Matter*, 2007, **3**, 327–332.
14 S. P. Evanko, M. I. Tammi, R. H. Tammi and T. N. Wight, *Adv. Drug Delivery Rev.*, 2007, **59**, 1351–1365.
15 J. P. Xiong, T. Stehle, R. G. Zhang, A. Joachimiak, M. Frech, S. L. Goodman and M. A. Arnaout, *Science*, 2002, **296**, 151–155.
16 M. D. Pierschbacher and E. Ruoslahti, *Nature*, 1984, **308**, 30–33.
17 U. Hersel, C. Dahmen and H. Kessler, *Biomaterials*, 2003, **24**, 4385–4415.
18 Y. Lai, C. Xie, Z. Zhang, W. Lu and J. Ding, *Biomaterials*, 2010, **31**, 4809–4817.
19 M. Cohen, D. Joester, B. Geiger and L. Addadi, *ChemBioChem*, 2004, **5**, 1393–1399.
20 J. M. Curran, R. Chen and J. A. Hunt, *Biomaterials*, 2010, **31**, 1463–1464.
21 D. Trimbach, B. Keller, R. Bhat, S. Zankovych, R. Pohlmann, S. Schroter, J. Bosert and K. D. Jandt, *Adv. Funct. Mater.*, 2008, **18**, 1723–1731.
22 M. Cicuéndez, M. T. Portolés, I. Izquierdo-Barba and M. Vallet-Regí, *Chem. Mater.*, 2012, **24**, 1100–1106.
23 A. Butscher, M. Bohner, S. Hofmann, L. Gauckler and R. Muller, *Acta Biomater.*, 2011, **7**, 907–920.
24 A. García, I. Izquierdo-Barba, M. Colilla, C. López de Laorden and M. Vallet-Regí, *Acta Biomater.*, 2011, **7**, 1265–1273.
25 H. S. Yun, S. E. Kim and Y. T. Hyeon, *Chem. Commun.*, 2007, 2139–2141.
26 M. Malmsten, *J. Colloid Interface Sci.*, 1994, **166**, 333–342.
27 M. Cicuéndez, I. Izquierdo-Barba, S. Sánchez-Salcedo, M. Vila and M. Vallet-Regí, *Acta Biomater.*, 2012, **8**, 802–810.
28 A. H. Reddi and C. B. Huggins, *Proc. Soc. Exp. Biol. Med.*, 1972, **140**, 807–810.
29 S. J. Hollister, *Nat. Mater.*, 2005, **4**, 518–524.
30 J. R. Jones, L. M. Ehrenfried and L. L. Hench, *Biomaterials*, 2006, **27**, 964–973.
31 I. Medved and R. Cerny, *Microporous Mesoporous Mater.*, 2011, **142**, 405–422.
32 S. Padilla, I. Izquierdo-Barba and M. Vallet-Regí, *Chem. Mater.*, 2008, **20**, 5942–5944.
33 M. Vallet-Regí, *J. Intern. Med.*, 2010, **267**, 22–43.
34 M. Vallet-Regi, *ISRN Mater. Sci.*, 2012, 20.
35 M. Cicuéndez, I. Izquierdo-Barba, M. Portolés and M. Vallet-Regí, *Eur. J. Pharm. Biopharm.*, 2013, **84**, 115–124.
36 T. J. Webster, C. Ergun, R. H. Doremus, R. W. Siegel and R. Bizios, *J. Biomed. Mater. Res., Part A*, 2000, **51**, 475–483.

37 S. F. Lamolle, M. Monjo, M. Rubert, H. J. Haugen, S. P. Lyngstadaas and J. E. Ellingsen, *Biomaterials*, 2009, **30**, 736–742.
38 R. Z. Legeros, *Clin. Orthop. Relat. Res.*, 2002, **395**, 81–98.
39 F. Zhang and M. P. Srinivasan, *Langmuir*, 2004, **20**, 2309–2314.
40 M. Colilla, I. Izquierdo-Barba, S. Sanchez-Salcedo, J. L. G. Fierro, J. L. Hueso and M. Vallet-Regi, *Chem. Mater.*, 2010, **22**, 6459–6466.
41 M. P. J. Peeters, W. J. J. Wakelkamp and A. P. M. Kentgens, *J. Non-Cryst. Solids*, 1995, **189**, 77–84.
42 P. Innocenzi, Y. L. Zub and V. G. Kessler, *Sol–gel methods for materials processing*, Springer Science, Netherlands, 2008.
43 S. Sánchez-Salcedo, M. Colilla, I. Izquierdo-Barba and M. Vallet-Regí, *J. Mater. Chem. B*, 2013, **1**, 1595–1606.
44 L. G. Griffith and G. Naughton, *Science*, 2002, **295**, 1009–1014.
45 N. G. Maroudas, *J. Theor. Biol.*, 1975, **49**, 417–424.
46 H. A. Scheraga and J. R. Laskowski, *Adv. Protein Chem.*, 1957, **12**, 2–5.
47 B. Lassen and M. Malmsten, *J. Colloid Interface Sci.*, 1997, **186**, 9–16.

2.5. Bibliografía

[1] R. Langer, J. P. Vacanti. Tissue Engineering. Science 1993, 260, 920-926.

[2] S. J. Hollister, R. D. Maddox, J. M. Taboas. Optimal design and fabrication of scaffolds to mimic tissue properties and satisfy biological constraints. Biomaterials 2002, 23, 4095-4103.

[3] S. J. Hollister. Porous scaffold design for tissue engineering. Nat. Mater. 2005, 4, 518-524.

[4] S. Yang, K. F. Leong, Z. Du, C. K. Dua. The design of scaffolds for use in tissue engineering. Part I. Traditional factors. Tissue Eng. Part A 2001, 7, 679-689.

[5] A. J. Salgado, O. P. Coutinho, R. L. Reis. Bone tissue engineering: State of the art and future trends. Macromol Biosci. 2004, 4, 743-765.

[6] J. R. Jones. Review of bioactive glass: From Hench to hybrids. Acta Biomaterialia 2013, 9, 4457-4486.

[7] M. A. Woodruff, C. Lange, J. Reichert, A. Berner, F. Chen, P. Fratzl, J-T. Schantz, D. W. Hutmacher. Bone tissue engineering: from bench to bedside. Mater Today 2012, 15, 430-435.

[8] M. Manzano, M. Vallet-Regí. Revisiting bioceramics: Bone regenerative and local drug delivery systems. Prog. Solid State Chem. 2012, 40, 17-30.

[9] M. M. Stevens. Biomaterials for bone tissue engineering. Mater Today 2008, 11, 18-25.

[10] D. Lozano, C. G. Trejo, E. Gómez-Barrena, M. Manzano, J. C. Doadrio, A. J. Salinas, M. Vallet-Regí, N. García-Honduvilla, P. Esbrit, J. Bujan. Osteostatin-loaded onto mesoporous ceramics improves the early phase of bone regeneration in a rabbit osteopenia model. Acta Biomater. 2012, 8, 2317-2323.

[11] X. Sun, Y. Kang, J. Bao, Y. Zhang, Y. Yang, X. Zhou. Modeling vascularized bone regeneration within a porous biodegradable CaP scaffold loaded with growth factors. Biomaterials 2013, 34, 4971-4981.

[12] D. W. Hutmacher. Scaffolds in Tissue engineering bone and cartilage. Biomaterials 2000, 21, 2529-2543.

[13] D. W. Hutmacher, J. T. Schantz, C. X. F. Lam, K. C. Tan, T. C. Lim. State of the art and future directions of scaffold-based bone engineering from a biomaterials perspective. J. Tissue Eng. Regenerative Med. 2007, 1, 245-260.

[14] J. R. Jones, P. D. Lee, L. L. Hench. Hierarchical porous materials for tissue engineering. Phil. Trans. R. Soc. A. 2006, 364, 263-281.

[15] S. J. Hollister. Scaffold Design and manufacturing from concept to clinic. Adv. Mater. 2009, 21, 3330-3342.

[16] M. Vallet-Regí, J. M. Gonzalez-Calbet. Calcium phosphates as substitution of bone tissues. Prog. Solid State Sci. 2004, 32, 1-31.

[17] M. M. Stevens, J. H. George. Exploring and Engineering the Cell Surface Interface. Science 2005, 310.

[18] M. Goldberg, R. Langer, X. Jia. Nanostructured materials for applications in drug delivery and tissue engineering. J. Biomater. Sci. Polymer Ed. 2007, 18, 241-268.

[19] L. Zhang, T. J. Webster. Nanotechnology and nanomaterials: Promises for improved tissue regeneration. Nano Today 2009, 4, 66-80.

[20] M. Vallet-Regí, E. Ruiz-Hernández. Bioceramics: From Bone Regeneration to Cancer Nanomedicine. Adv. Mater. 2011, 23, 5177-5218.

[21] S. Harada, G. A. Rodan. Control of osteoblasts function and regulation of bone mass. Nature 2003, 423, 349-355.

[22] W. J. Boyle, W. S. Simonet, D. L. Lacey. Osteoclast differentiation and activation. Nature 2003, 423, 337-342.

[23] J. Vivanco, A. Aiyangar, A. Araneda, H-L. Ploeg. Mechanical characterization of injection-molded macro porous bioceramic bone scaffolds. J. Mechanical Behavior Biomed Mater 2012, 9, 137-152.

[24] V. Karageorgiou, D. Kaplan. Porosity of 3D biornaterial scaffolds and osteogenesis. Biomaterials 2005, 26, 5474-5491.

[25] N. Tamai, A. Myoui, T. Tomita, T. Nakase, J. Tanaka, T. Ochi, H. Yoshikawa. Novel hydroxyapatite ceramics with an interconnective porous structure exhibit superior osteoconduction *in vivo*. J. Biomed. Mater. Res. 2002, 59, 110-117.

[26] D. G. Castner, B. D. Ratner. Biomedical surface science: Foundations to frontiers. Surface Sci. 2002, 500, 28-60.

[27] L. Xia, K. Lin, X. Jiang, Y. Xu, M. Zhang, J. Chang, Z. Zhang. Enhanced osteogenesis through nano-structured surface design of macroporous hydroxyapatite bioceramic scaffolds via activation of ERK and p38 MAPK signaling pathways. J. Mater. Chem. B 2013, DOI: 10.1039/c3tb20945h.

[28] M. J. Dalby, N. Gadegaard, R. Tare, A. Andar, M. O. Riehle, P. Herzyk, C. D. W. Wilkinson, R. O. C. Oreffo. The control of human mesenchymal cell differentiation using nanoscale symmetry and disorder. Nature Mater. 2007, 6, 997-1003.

[29] E. S. Place, N. D. Evans, M. M. Stevens. Complexity in biomaterials for tissue engineering. Nature Mater 2009, 8, 457-470.

[30] T. J. Sill, H. A. Von Recum. Electrospinning: applications in drug delivery and tissue engineering. Biomaterials 2008, 29, 1989-2006.

[31] S. V. Dorozhkin. Bioceramics of calcium orthophosphates. Biomaterials 2010, 31, 1465-1485.

[32] K. A. Al Ruhaimi. Bone graft substitutes: a comparative qualitative histologic review of current osteoconductive grafting materials. Int. J. Oral Maxillof. Implants 2001, 16, 105–114.

[33] T. D. Roy, J. L. Simon, J. L. Ricci, E. D. Rekow, V. P. Thopson, J. R. Parsons. Performance of degradable composite bone repair products made via three-dimensional fabrication techniques. J. Biomed. Mater. Res. A 2003, 66, 283-91.

[34] W. Y. Yeong, C. K. Chua, K. F. Leong, M. Chandrasekaran. Rapid prototyping in tissue engineering: challenges and potential. Trends Biotech 2004, 22, 643-652.

[35] R. A. Martin, S. Yue, J. V. Hanna, P. D. Lee, R. J. Newport, M. E. Smith, J. R. Jones. Characterizing the hierarchical structures of bioactive sol-gel silicate glass and scaffolds for bone regeneration. Phil. Trans. R. Soc. A 2012, 370, 1422-1443.

[36] B. Holmes, N. J. Castro, L. G. Zhang, E. Zussman. Electrospun Fibrous Scaffolds for Bone and Cartilage Tissue Generation: Recent Progress and Future Developments. Tissue Eng. Part B-Reviews 2012, 18, 478-486.

[37] O. Mohony, O. Tsigkou, C. Ionescu, C. Minelli, L. Ling, R. Hanly, M. E. Smith, M. M. Stevens, J. R. Jones. Silica-gelatin hybrids with tailorable degradation and mechanical properties for tissue regeneration. Adv. Funct. Mater 2010, 20, 3835-3845.

[38] K. F. Leong, C. M. Cheah, C. K. Chua. Solid free form fabrication of three-dimensional scaffolds for engineering replacement tissue and organs. Biomaterials 2003, 24, 2363-2378.

[39] H. R. Ramay, M. Q. Zhang. Preparation of porous hydroxyapatite scaffolds by combination of the gel-casting and polymer sponge methods. Biomaterials 2003, 24, 2293-2303.

[40] S. Sánchez-Salcedo, A. Nieto, M. Vallet-Regí. Hydroxyapatite/beta tricalcium phosphate/agarose macroporous scaffolds for bone tissue engineering. Chem. Eng J. 2008, 137, 62-71.

[41] A. Almirall, G. Larrecq, J. A. Delgado, S. Martinez, J. A. Planell, M. P. Ginebra. Fabrication of low temperature macroporous hydroxyapatite scaffolds by foaming and hydrolysis of an alpha-TCP paste. Biomaterial 2004, 25, 3671-3680.

[42] S. Padilla, S. Sánchez-Salcedo, M. Vallet-Regí. Bioactive glass as precursor of designed –architecture scaffolds for tissue engineering. J. Biomed. Mater. Res. 81A 2007, 224-232.

[43] S. Deville, E. Saiz, R. K. Nalla, A. P. Tomsia. Freezing as a path to build complex composites. Science 2006, 311, 515-518.

[44] H. H. Lu, S. F. El-Amin, K. D. Scott, C. T. Laurencin. Three dimensional, bioactive, biodegradable, polymer-bioactive glass composite scaffolds with improved mechanical properties support collagen synthesisand mineralization of human osteoblast-like cells *in vitro.* J. Biomed. Mater. Res. Part A, 2003, 64A, 465-474.

[45] R. P. del Real, J. G. C. Wolke, M. Vallet-Regí, J. A. Jansen. A new method to produce macropores in calcium phosphate cements. Biomaterials 2002, 23, 3673–3680.

[46] M. P. Ginebra, M. Espanol, E. B. Montufar, R. A. Pérez, G. Mestres. New processing approaches in calcium phosphate cements and their applications in regenerative medicine. Acta Biomaterialia 2010, 6, 2863-2873.

[47] S. Padilla, J. Roman, M. Vallet-Regí. Synthesis of porous hydroxyapatites by combination of gelcasting and foams burn out methods. J. Mater. Sci. Mat Med 2002, 13, 1193-1197.

[48] Q. P. Pham, U. Sharma, A. G. Mikos. Electrospinning of polymeric nanofibers for tissue engineering applications: A review. Tissue Eng 2006, 12, 1197-1211.

[49] S. Pramanik, B. Pingguan-Murphy, N. A. Abu Osman. Progress of key strategies in development of electrospun scaffolds: bone tissue. Sci. Techn. Adv. Mater. 2012, 13 Article Number: 043002.

[50] H. Kim, D. Shin, W. Lim. Biomimetic scaffolds for tissue engineering. Adv. Funct. Mater. 2012, 22, 2446-2468.

[51] J. J. Yoon, J. H. Kim, T. G. Park. Dexamethasone-releasing biodegradable polymer scaffolds fabricated by a gas-foaming/salt-leaching method. Biomaterials 2003, 24, 2323-2329.

[52] J. Chen, J. Xu, A. Wang, M. Zheng. Scaffolds for tendon and ligament repair: review of the efficacy of commercial products. Expert Rev. Med. Devices 2009, 6, 61 - 73.

[53] P. Sepulveda, J. G. P. Binner. Evaluation of the *in situ* polyerization kinetics for the gel casting of ceramic foams. Chem. Mater. 2001, 13, 3882-3887.

[54] Z. Y. Wu, R. G. Hill, S. Yue, D. Nightingale, P. D. Lee, J. R. Jones. Melt-derived glass scaffolds by a gel cast foaming technique. Acta Biomaterialia 2011, 7, 1807-1816.

[55] J. R. Jones, L. M. Ehrenfried, L. L. Hench. Optimizing bioactive glass scaffolds for bone tissue engineering. Biomaterials 2006, 27, 964-73.

[56] E. B. Montufar, C. Gil, T. Traykova, M. P. Ginebra, J. A. Planell. Foamed surfactant solution as a template for self-setting injectable hydroxyapatite scaffolds for bone regeneration. Acta Biomaterialia. 2010, 6, 876-885.

[57] Q. Z. Chen, A. R. Boccaccini. Poly(D,L-Lactic) coated 45S5 Bioglass ® -based scaffolds: Processing and characterization. J. Biomed. Mater. Res. A. 2006, 77A, 445-457.

[58] O. Bretcanu, Q. Z. Chen, S. K. Misra, I. Roy, E. Verne, C. V. Brovarone, A. R. Boccaccini. Biodegradable, polymer coated 45S5 bioglass-derived glass-ceramic scaffolds for bone tissue enginnering. Eur. J. Glass Sci. Tech A 2007, 48, 227-234.

[59] S. Sánchez-Salcedo, M. Vila, I. Izquierdo-Barba, M. Cicuéndez, M. Vallet-Regí. Biopolymer-coated hydroxyapatite foams: a new antidote for heavy metal intoxication J. Mater Chem 2010, 20, 6956-6961.

[60] M. Vila, S. Sánchez-Salcedo, M. Cicuéndez, I. Izquierdo-Barba, M. Vallet-Regí. Novel biopolymers-coated hydroxyapatite foams for removing heavy metals from polluted water. J Hazard Mater 2011, 192, 71–77.

[61] M. Cicuéndez, I. Izquierdo-Barba, S. Sánchez-Salcedo, M. Vila, M. Vallet-Regí. Biological performance of hydroxyapatite−biopolymer foams: *In vitro* cell response. Acta Biomaterialia 2012, 8, 802–810.

[62] J. Gil-Albarova, M. Vila, J. Badiola-Vargas, S. Sánchez-Salcedo, A. Herrera, M. Vallet-Regí. *In vivo* osteointegration of three-dimensional crosslinked gelatin-coated hydroxyapatite foams. Acta Biomaterialia 2012, 8, 3777–3783.

[63] J. Cesarano, P. Carlvet. Free forming objects with low binder slurry. US Patent 2000, 6, 027, 326.

[64] A. Butscher, M. Bohner, C. Roth, A. Ernstberger, R. Heuberger, N. Doebelin, P. R. von Rohr, R. Müller. Printability of calcium phosphate powder for three-dimensional printing of tissue engineering scaffolds. Acta Biomaterialia 2012, 8, 373-385.

[65] D. W. Hutmacher, M. Sittinger, M. V. Risbud. Scaffold-based tissue engineering: rationale for computer-aided design and solid free-form fabrication systems. Trends Biotechn. 2004, 22, 354-362.

[66] A. Butscher, M. Bohner, S. Hofmann, L. Gauckler, R. Muller. Structural and material approaches to bone tissue engineering in powder-based three-dimensional printing . Acta Biomaterialia 2011, 7, 907-920.

[67] W. Sun, A. Darling, B. Starly, J. Nam. Computer-aided tissue engineering: overview, scope and challenges. Biotechn. Appl. Biochem. 2004, 39, 29-47.

[68] F. R. Rose, L. A. Cyster, D. M. Grant, C. A. Scotchford, S. M. Howdle, K. M. Shakesheff. *In vitro* assessment of cell penetration into porous hydroxyapatite scaffolds with a central aligned channel, Biomaterials 2004, 25, 5507-5514.

[69] K. A. Hing, B. Annaz, S. Saeed, P. A. Revell, T. Buckland. Microporosity enhances bioactivity of synthetic bone graft substitutes. J. Mater. Sci. Mater. Med. 2005, 16, 467-475.

[70] J. N. Stuecker, J. Cesarano, D. A. Hirschfeld. Control of the viscous behavior of highly concentrated mullite suspensions for robocasting. J. Mater. Process. Technol. 2003, 142, 318-325.

[71] J. Cesarano III, J. R. Segalman, P. Calvert. Robocasting provides mold less fabrication from slurry deposition. Ceram Ind 2008, 148, 94-102.

[72] P. Miranda, E. Saiz, K. Gryn, A. P. Tomsia. Sintering and robocasting of beta-tricalcium phosphate scaffolds for orthopaedic applications. Acta Biomaterialia 2006, 2 457-466.

[73] S. Michna, W. Wu, J. A. Lewis. Concentrated hydroxyapatite inks for direct-write assembly of 3-D periodic scaffolds. Biomaterials 2005, 26, 5632-5639.

[74] A. Baeza, I. Izquierdo-Barba, M. Vallet-Regí. Biotinylation of silicon-doped hydroxyapatite: A new approach to protein fixation for bone tissue regeneration. Acta Biomaterialia 2010, 6743-6749.

[75] P. Miranda, A. Pajares, E. Saiz, A. P. Tomsia, F. Guiberteau. Mechanical properties of calcium phosphate scaffolds fabricated by robocasting. J. Biomed Mater Res A 2008, 85, 218–227.

[76] P. Miranda, E. Saiz, K. Gryn, A. P. Tomsia. Sintering and robocasting of betatricalcium phosphate scaffolds for orthopedic applications. Acta Biomaterialia 2006, 2, 457–466.

[77] F. H. Perera, F. J. Martínez-Vazquez, P. Miranda, A. L. Ortiz, A. Pajares. Clarifying the effect of sintering conditions on the microstructure and mechanical properties of beta-tricalcium phosphate. Ceram. Int. 2010, 36, 1929-1935.

[78] K. S. Jack, S. Velayudhan, P. Luckman, M. Trau, L. Grøndahl, J. Cooper-White. The fabrication and characterization of biodegradable HA/PHBV nanoparticle–polymer composite scaffolds. Acta Biomaterialia 2009, 5, 2657–2667.

[79] L. Zhao, E. F. Burguera, H.H.K. Xu, N. Amin, H. Ryou, D. D. Arola. Fatigue and human umbilical cord stem cell seeding characteristics of calcium phosphate–chitosan–biodegradable fiber scaffolds. Biomaterials 2010, 31, 840–847.

[80] T. Billiet, M. Vandenhaute, J. Schelfhout, S. Van Vlierberghe, P. Dubruel. A review of trends and limitations in hydrogel-rapid prototyping for tissue Engineering. Biomaterials 2010, 33, 6020-6041.

[81] T. G. Kim, S. H. Park, H. J. Chung, D. Y. Yang, T. G. Park. Microstructure scaffolds coated with hydroxyapatite/collagen nanocomposite multilayer for enhance osteogenic induction of human mesenchymal stem cells. J. Mater. Chem. 2010, 20, 8927- 8933.

[82] S. Shruti, A. J. Salinas, G. Lusvardi, G. Malavasi, L. Menabue, M. Vallet-Regí. Mesoporous bioactive scaffolds prepared with cerium-, gallium- and zinc-containing glasses. Acta Biomaterialia 2013, 9, 4836-4844.

[83] H. S. Yun, S. E. Kim, Y. T. Hyeon. Design and preparation of bioactive glasses with hierarchical pore networks. Chem Comm 2007, 2139-2141.

[84] A. García, I. Izquierdo-Barba, M. Colilla, C. Laorden, M. Vallet-Regí. Preparation of 3-D scaffolds in the SiO_2–P_2O_5 system with tailored hierarchical meso-macroporosity. Acta Biomaterialia 2011, 7, 1265-1273.

[85] C. Wu, Y. Luo, G. Cuniberti, Y. Xiao, M. Gelinky. Three-dimensional printing of hierarchical and tough mesoporous bioactive glass scaffolds with a controllable pore architecture, excellent mechanical strength and mineralization ability. Acta Biomaterialia 2011, 7, 2644-2650.

[86] A. Remes, D. F. Williams. Immune response in biocompatibility. Biomaterials 1992, 13, 731-743.

[87] S. Franz, S. Rammelt, D. Scharnweber, J. C. Simon. Immune responses to implants. A review of the implications for the design of immunomodulatory biomaterials. Biomaterials 2011, 32, 6692-6709.

[88] M. J. Smith, K. L. Jr White, D. C. Smith, G. L. Bowlin. *In vitro* evaluations of innate and acquired immune responses to electrospun polydioxanone-elastic blends. Biomaterials 2009, 30, 149-159.

[89] B. N. Brown, B. D. Ratner, S. D. Goodman, S. Amar, S. F. Badylak. Macrophage polarization: An opportunity for improved outcomes in biomaterials and regenerative medicine. Biomaterials 2012, 33, 3792-3802.

[90] B. N. Brown, R. Londono, S. Tottey, L. Zhang, K. A. Kukla, M. T. Wolf, K. A. Daly, J. E. Reing, S. F. Badylak. Macrophage phenotype as a predictor of constructive remodeling following the implantation of biologically derived surgical mesh materials. Acta Biomaterialia 2012, 8, 978-987.

[91] K. Garg, N. A. Pullen, C. A. Oskeritzian, J. J. Ryan, G. L. Bowlin. Macrophage functional polarization (M1/M2) in response to varying fiber and pore dimensions of electrospun scaffolds. Biomaterials 2013, 34, 4439-4451.

[92] R. M. Boehler, J. G. Graham, L. D. Shea. Tissue engineering tools for modulation of the immune response. Bio Techniques 2011, 51, 239-254.

[93] K. Anselme. Osteoblast adhesion on biomaterials. Biomaterials 2000, 21, 667–681.

[94] B. Geiger, J. P. Spatz, A. D. Bershadsky. Environmental sensing through focal adhesions. Nat Rev Mol Cell Biol 2009, 10, 21–33.

[95] M. Cohen, D. Joester, I. Sabanay, L. Addadi, B. Geiger. Hyaluronan in the pericellular coat: an additional layer of complexity in early cell adhesion events. Soft Matter 2007, 3, 327–332.

[96] S. P. Evanko, M. I. Tammi, R. H. Tammi, T. N. Wight. Hyaluronan-dependent pericellular matrix. Adv Drug Deliv Rev 2007, 59, 1351–1365.

[97] J. P. Xiong, T. Stehle, R. G. Zhang, A. Joachimiak, M. Frech, S. L. Goodman, M. A. Arnaout. Crystal structure of the extracellular segment of integrin alpha V beta 3 in complex with an Arg-Gly-Asp ligand. Science 2002, 296, 151–155.

[98] M. Vallet-Regí, M. Colilla, B. González. Medical applications of organic-inorganic hybrid materials within the field of silica-based bioceramics. Chem Soc Rev 2011, 40, 596–607.

[99] M. D. Pierschbacher, E. Ruoslahti. Cell attachment activity of fibronectin can be duplicated by small fragments of the molecule. Nature 1984, 308, 30–33.

[100] U. Hersel, C. Dahmen, H. Kessler. RGD modified polymers: biomaterials for stimulated cell adhesion and beyond. Biomaterials 2003, 24, 4385–4415.

[101] Y. Lai, C. Xie, Z. Zhang, W. Lu, J. Ding. Design and synthesis of a potent peptide containing both specific and non-specific cell-adhesion motifs. Biomaterials 2010, 31, 4809–4817.

[102] C. G. Trejo, D. Lozano, M. Manzano, J. C. Doadrio, A. J. Salinas, S. Dapia, E. Gómez-Barrena, M. Vallet-Regí, N. García-Honduvilla, J. Buján, P. Esbrit. The osteoinductive properties of mesoporous silicate coated with osteostatin in a rabbit femur cavity defect model. Biomaterials 2010, 31, 8564–8573.

[103] M. Cohen, D. Joester, B. Geiger, L. Addadi. Spatial and temporal sequence of events in cell adhesion: from molecular recognition to focal adhesion assembly. Chem Bio Chem 2004, 5, 1393–1399.

[104] J. M. Curran, R. Chen, J. A. Hunt. Material induced mesenchymal stem cell differentiation. Biomaterials 2010, 31, 1463–1464.

Capítulo 3

CAPITULO 3. *NANOCOMPOSITE* MGHA PARA PREVENCIÓN Y TRATAMIENTO DE LA INFECCIÓN ÓSEA

3.1. Matrices nanoestructuradas para prevención y tratamiento de la infección

En el capítulo anterior se ha demostrado la potencial aplicabilidad del nuevo *nanocomposite* MGHA para regeneración tisular ósea. En este capítulo se analiza su capacidad para la prevención y el tratamiento de una infección ósea, lo que proporciona un valor añadido a este nuevo *nanocomposite*. Con este objetivo se han analizado los procesos de carga y liberación de levofloxacino utilizando MGHA como matriz y se ha evaluado la actividad antimicrobiana de este sistema de liberación así como sus efectos sobre células óseas. La **Figura 3.1.** esquematiza las interacciones entre biomaterial/tejido/bacteria propias de un sistema de liberación controlada de fármacos.

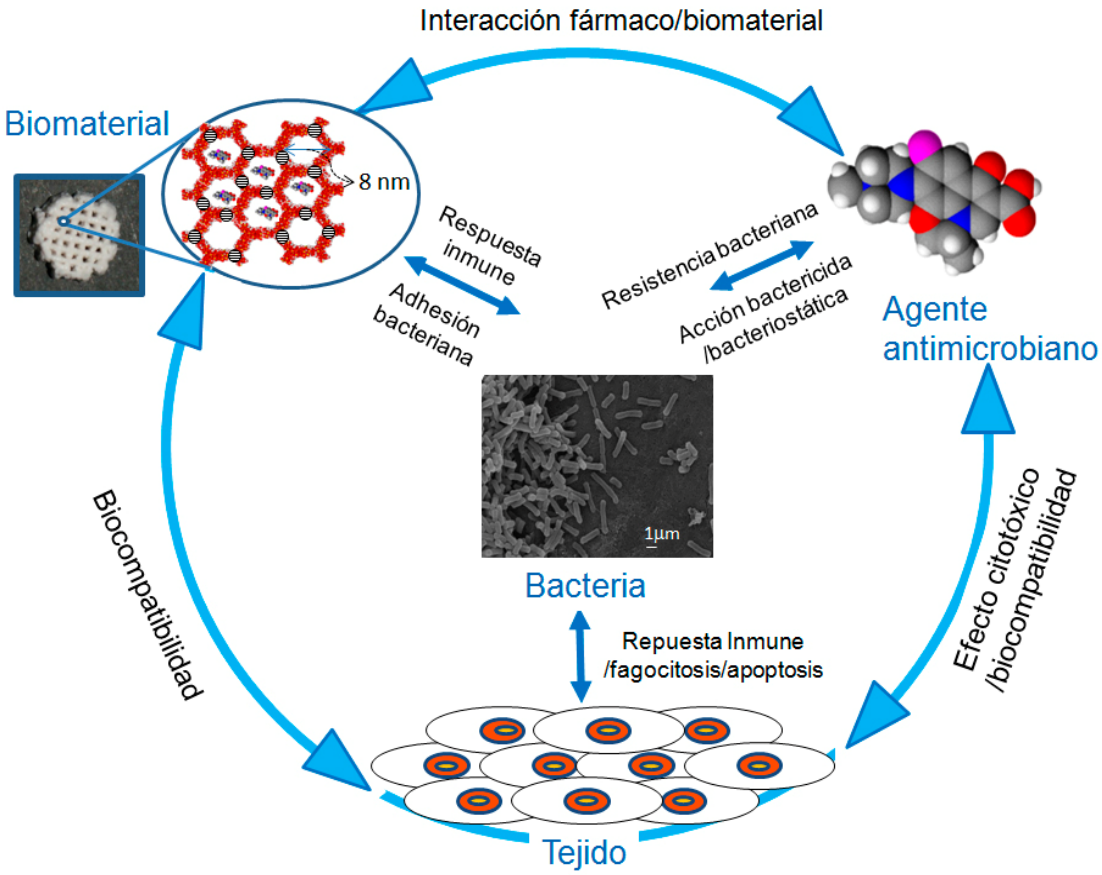

Figura 3.1. Interacciones entre biomaterial/tejido/bacteria propias de un sistema de liberación controlada de fármacos.

La infección es actualmente la complicación más grave asociada a la implantación de biomateriales en un organismo [1,2]. Aunque la incidencia de infecciones se ha reducido gracias a las técnicas quirúrgicas asépticas y al correcto tratamiento profiláctico perioperatorio con antibióticos sistémicos, los importantes impactos sociales, clínicos y económicos que produce, unidos al creciente número de intervenciones que se practican anualmente, están promoviendo el desarrollo de nuevas estrategias para evitar al máximo la aparición de estos procesos infecciosos [3,4,5].

Las infecciones asociadas a implantes se clasifican en tres grupos: (i) infecciones superficiales inmediatas causadas por bacterias que normalmente habitan en la piel y comienzan a colonizar el dispositivo médico; (ii) infecciones profundas inmediatas que se hacen evidentes poco después de cirugías invasivas y pueden deberse a la inadvertida reubicación de las bacterias de la piel en el cuerpo como consecuencia de prácticas de implantación sin la debida asepsia; (iii) infecciones profundas tardías que aparecen meses o años después de la cirugía y pueden ser debidas tanto a una contaminación durante la cirugía como a bacterias que migraron desde otro sitio anatómico [6].

La susceptibilidad a la infección en la superficie del implante depende del estado inmunológico del paciente así como de la virulencia de los microorganismos implicados [4,6]. A raíz de cualquier colonización microbiana inicial puede desarrollarse el *biofilm* bacteriano (**Figura 3.2.**), que se establece en las superficies contaminadas comprometiendo gravemente la funcionalidad y el rendimiento del propio implante. La formación del *biofilm* induce el reclutamiento de células inflamatorias en la zona, afectando a la integración del implante en los tejidos circundantes y representando un gran riesgo para el paciente que puede desarrollar septicemia o incluso, en los casos más graves, la muerte [7,8,9,10]. Una vez que el *biofilm* bacteriano maduro se ha establecido, las terapias médicas convencionales basadas en una administración sistémica de antibióticos no son eficaces y la extracción del implante representa la única solución para erradicar la infección. En cirugía ortopédica las consecuencias pueden ser incluso en ocasiones la amputación de miembros [11]. Estudios epidemiológicos recientes realizados en entornos hospitalarios, ponen de manifiesto además que las recaídas de la infección ocasionadas por patógenos como *S. aureus* resistente a la meticilina (MRSA) u otras cepas multirresistentes a los antibióticos son especialmente comunes [12].

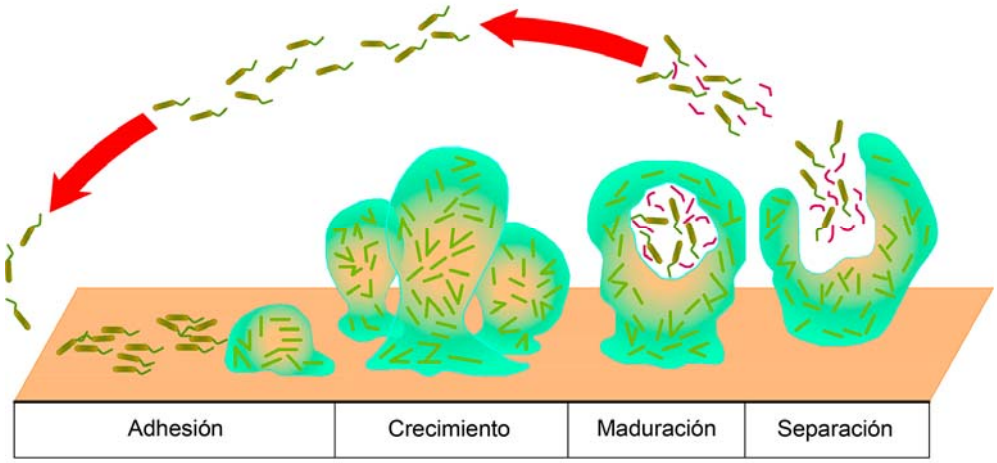

Figura 3.2. Etapas de formación del *biofilm* bacteriano.

Teniendo en cuenta todos estos factores, las infecciones asociadas a la implantación de biomateriales son ciertamente complicaciones difíciles de manejar que implican en algunos casos una importante morbilidad de los pacientes y conllevan grandes costes. Para tratar o prevenir eficazmente dichas infecciones, se ha de desarrollar una estrategia compleja que tenga en cuenta diferentes acciones combinadas que engloban desde el tratamiento perioperatorio y una técnica aséptica en la intervención quirúrgica, hasta el desarrollo de nuevos biomateriales con propiedades antiinfectivas [2]. Con la actual expansión del uso de dispositivos médicos, se ha incrementado notablemente el interés en investigación por desarrollar biomateriales con capacidad antimicrobiana, que sean menos susceptibles o incluso resistentes a las infecciones bacterianas [3]. Tales biomateriales incluyen, entre otros, materiales con superficies capaces de inhibir la adhesión bacteriana y biomateriales capaces de liberar localmente concentraciones activas de agentes antimicrobianos (incluyendo aquí agentes bactericidas, bacteriostáticos y/o combinaciones de ambos) para erradicar infecciones pre-existentes o prevenirlas [3,13,14,15].

Con el objetivo de desarrollar materiales eficaces en la prevención y/o tratamiento de la infección, y gracias a los recientes avances en el campo de la nanotecnología, los investigadores han aunado esfuerzos en el diseño de materiales nanoestructurados por su potencial uso como sistemas de liberación controlada de fármacos [16,17,18]. En este sentido, los materiales mesoestructurados de base de sílice, descritos por Kuroda y colaboradores [19] y por los investigadores de la Mobil

Company [20], están recibiendo una gran atención ya que han proporcionado nuevas posibles aplicaciones como prometedores sistemas de liberación [21,22,23,24,25,26,27,28,29,30]. Las características que definen a estas matrices mesoporosas, sintetizadas por autoensamblaje supramolecular utilizando un surfactante como plantilla, las hacen excelentes candidatas como reservorios ideales para el almacenamiento de fármacos y otras moléculas biológicamente activas con valor terapéutico [31,32]:

a) Su alto volumen de poro que permite la carga de una gran cantidad de la molécula seleccionada.
b) Su elevada superficie de área que conlleva un alto potencial para la adsorción del fármaco.
c) Su distribución porosa altamente ordenada que favorece la homogeneidad y reproducibilidad de la adsorción del fármaco y las cinéticas de liberación.
d) Su alta densidad de grupos silanol en la superficie que permite la funcionalización para un mejor control en los procesos de carga y liberación del fármaco.

Además de las características del material de partida, el diseño de un sistema de liberación ideal debe tener en cuenta otros factores que interactúen conjuntamente cuando el material cargado con el fármaco sea colocado en el organismo, asegurando el éxito del implante. Estos factores son: la localización anatómica del tejido que va a recibir el biomaterial, la capacidad del material para actuar como reservorio idóneo para liberar el agente terapéutico almacenado y su potencial para combatir una invasión bacteriana [33].

Respecto al proceso de carga de agentes terapéuticos en los materiales mesoporosos, se han desarrollado diferentes estrategias. En la mayoría de los casos, las moléculas de fármaco se cargan por el método de impregnación (IP) tras la eliminación de la plantilla del surfactante bien por el proceso de calcinación o por extracción [21,26,32]. La metodología IP se caracteriza por la inmersión de los materiales mesoporosos en una solución acuosa y/u orgánica saturada de fármaco y el posterior secado a una temperatura entre 25ºC y 30ºC [34,35]. Por este método, las moléculas del agente terapéutico quedan adsorbidas en el interior de los poros de la matriz mesoporosa a través de interacciones fisicoquímicas [36]. Esta metodología ofrece numerosas

ventajas debido a su simplicidad y eficiencia. Sin embargo, el proceso de carga IP presenta limitaciones debido a la distribución heterogénea del fármaco y a la posible agregación del mismo fuera del material, lo que conduciría a una carga parcial de la molécula en la matriz mesoporosa [26].

Otra estrategia para carga de matrices desarrollada recientemente consiste en utilizar la plantilla del surfactante como adyuvante durante la incorporación del agente terapéutico, generalmente de naturaleza hidrofóbica, para incrementar la cantidad de moléculas cargadas y su estabilidad. Este método se denomina carga asistida por surfactante u "One Pot method" (OP) [37], ya que las moléculas del fármaco se incorporan durante la síntesis del material mesoporoso, quedando atrapadas dentro de las micelas del surfactante, las cuales gobiernan los perfiles de liberación. Aunque el procedimiento OP parece ofrecer numerosas ventajas, pocos estudios referentes a este método se encuentran en la literatura, debido a la controversia existente con respecto a la biocompatibilidad de los sistemas OP.

Sea cual fuere la estrategia de carga elegida, el conocimiento de la biocompatibilidad del sistema preparado debe ser evaluado con los tipos celulares con los que va a entrar en contacto, analizando los efectos producidos sobre los mismos debidos a las características del material, a las propiedades y a la concentración del agente cargado, así como a las cinéticas de liberación que tienen lugar.

La elección del fármaco vendrá determinada por los microorganismos que puedan infectar el tejido donde va a ser colocado el material, eligiendo para una primera implantación antibióticos de amplio espectro eficaces para la mayoría de las especies patógenas. Asimismo, la molécula seleccionada deberá presentar compatibilidad física y química con la naturaleza del sistema de liberación elegido [33].

El levofloxacino es una fluoroquinolona de amplio espectro, ligeramente soluble en agua, con actividad frente a bacterias Gram negativas y Gram positivas, recientemente utilizada para el tratamiento sistémico de la osteomielitis y otras infecciones óseas [38]. Este fármaco presenta dos grupos ionizables (6-carboxílico y N4 de piperazina) con valores de pKa de 6.05 y 8.22 respectivamente, siendo su punto isoeléctrico de 7.14 (**Figura 3.3.**). Estas características químicas permiten al fármaco

establecer una fuerte interacción a pH fisiológico con los grupos silanol presentes en las matrices mesoporosas [39, 40].

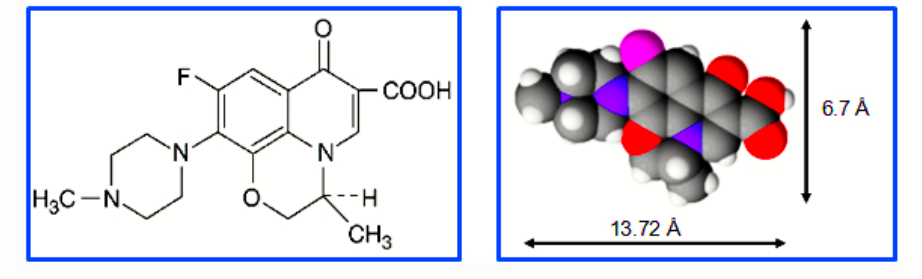

Figura 3.3. Representaciones de la molécula de levofloxacino.

Los sistemas de liberación local de antibióticos poseen un elevado potencial para prevenir la infección, presentando una baja toxicidad sistémica [33]. Sin embargo, con frecuencia estos sistemas no presentan la cinética de liberación requerida, siendo fundamental que la matriz permita la liberación controlada del agente terapeútico. Para asegurar la concentración de fármaco adecuada en el tejido, es necesaria una liberación sostenida del mismo, que ha de ser varias veces superior a la concentración mínima inhibitoria (CMI) obtenida *in vitro* [33]. Sin embargo, habrá que tener en cuenta que uno de los riesgos de la liberación sostenida a partir de estos sistemas es la aparición de cepas bacterianas resistentes al antibiótico utilizado [33].

Una de las estrategias desarrolladas para optimizar la liberación local del fármaco en caso de infección del implante, es la preparación de sistemas sensibles a pH, temperatura o campo eléctrico [41,42,43]. Entre estas posibilidades, los sistemas sensibles a pH presentan la ventaja de poder activar su liberación al producirse la acidificación local característica que tiene lugar durante la infección de un tejido. La disminución del pH en el lugar de la infección se debe a varios fenómenos. Algunas bacterias como *S. epidermidis* o *S. aureus* crean un ambiente ácido durante su proliferación debido a la producción de metabolitos como el ácido láctico [41]. Por otra parte, el sistema inmune desencadena respuestas inflamatorias que conllevan la secreción de proteína C reactiva [44] y citoquinas [45], que conducen a la infiltración de neutrófilos y macrófagos en el lugar de la infección [46]. Todas estas condiciones provocan una disminución local del pH desde el pH fisiológico (7.4) hasta un valor comprendido entre 5.5-7.0 [47]. Los sistemas de liberación de fármacos pH-

dependientes se basan en la unión del fármaco a la matriz a través de enlaces sensibles a cambios de pH [48] permitiendo una liberación del fármaco más acusada y rápida. Estos sistemas minimizan el riesgo de aparición de cepas resistentes a los antibióticos [48].

Uno de los objetivos de este capítulo ha sido el estudio de las dos diferentes estrategias de carga y liberación, IP y OP, de levofloxacino a partir de matrices mesoporosas analizando sus cinéticas de liberación, su biocompatibilidad y su actividad antimicrobiana. Los resultados obtenidos, se muestran en el artículo titulado: **"*Biocompatibility and levofloxacin delivery of mesoporous materials*"**, expuesto en el apartado **3.2.**

Por último, el objetivo final ha sido el estudio de la influencia del pH en la cinética de liberación de levofloxacino desde andamios tridimensionales del *nanocomposite* MGHA, evaluando sus efectos antimicrobianos frente a *E. coli* y *S. aureus* y comprobando la ausencia de efectos nocivos de las muestras sobre osteoblastos.

3.2. Estrategias de carga y liberación de matrices nanoestructuradas con agentes antimicrobianos. Evaluación biológica

Biocompatibility and levofloxacin delivery of mesoporous materials. **M. Cicuéndez**, I. Izquierdo-Barba, Mª T. Portolés, M. Vallet-Regí. ***European Journal of Pharmaceutics and Biopharmaceutics 2013, 84, 115-124.***

El objetivo de este trabajo de investigación ha sido realizar un estudio comparativo de los aspectos fundamentales que definen a dos metodologías de carga de fármacos, ampliamente utilizadas: impregnación (IP) y carga de fármaco asistido por un surfactante (One-Pot, OP). Concretamente, dicho estudio compara las características fisicoquímicas de ambas matrices (IP y OP), la respuesta celular a ambos sistemas y sus perfiles de liberación de levofloxacino. Para ello, se han utilizado distintos sistemas basados en sílice mesoporosa: sistemas libres de surfactante (materiales mesoporosos calcinados) y sistemas con la plantilla de surfactante presente (materiales mesoporosos sin calcinar), como matrices de partida de ambas metodologías, IP y OP, respectivamente.

El estudio de la biocompatibilidad *in vitro* de estas matrices ha demostrado que cambios a nivel atómico de las mismas pueden afectar de distinta manera al comportamiento de diferentes tipos celulares frente a estos sistemas. Así, ninguna de las matrices, tanto las calcinadas (IP) como las no calcinadas (OP), ejerce un efecto citotóxico sobre osteoblastos Saos-2. Sin embargo, las matrices no calcinadas inducen sobre fibroblastos L929 un significativo retraso de su proliferación, acompañado de alteraciones morfológicas y de un incremento dosis-dependiente del tamaño, de la complejidad interna y del contenido intracelular de calcio, sin ocasionar lisis celular ni apoptosis. Todos estos cambios observados en los fibroblastos pueden justificarse por la presencia de etanol residual y debido a los grupos silanol localizados en la superficie de las matrices no calcinadas (OP).

Los perfiles de liberación y la actividad antimicrobiana de ambas matrices mesoporosas (IP y OP) han sido estudiados mediante la incorporación de una fluoroquinolona de amplio espectro, como es el levofloxacino. Este agente antimicrobiano ha sido escogido para este estudio por su potencial actividad

antibacteriana en el tratamiento de osteomielitis y por su fuerte interacción con los grupos silanol a pH fisiológico, la cual, puede influir en sus cinéticas de liberación. Los resultados obtenidos muestran que ambas matrices, IP y OP, exhiben perfiles similares de liberación de levofloxacino, caracterizados por una rápida liberación inicial seguida de una más sostenida a lo largo del tiempo. Los resultados obtenidos se presentan de forma resumida en la **Figura 3.4.**

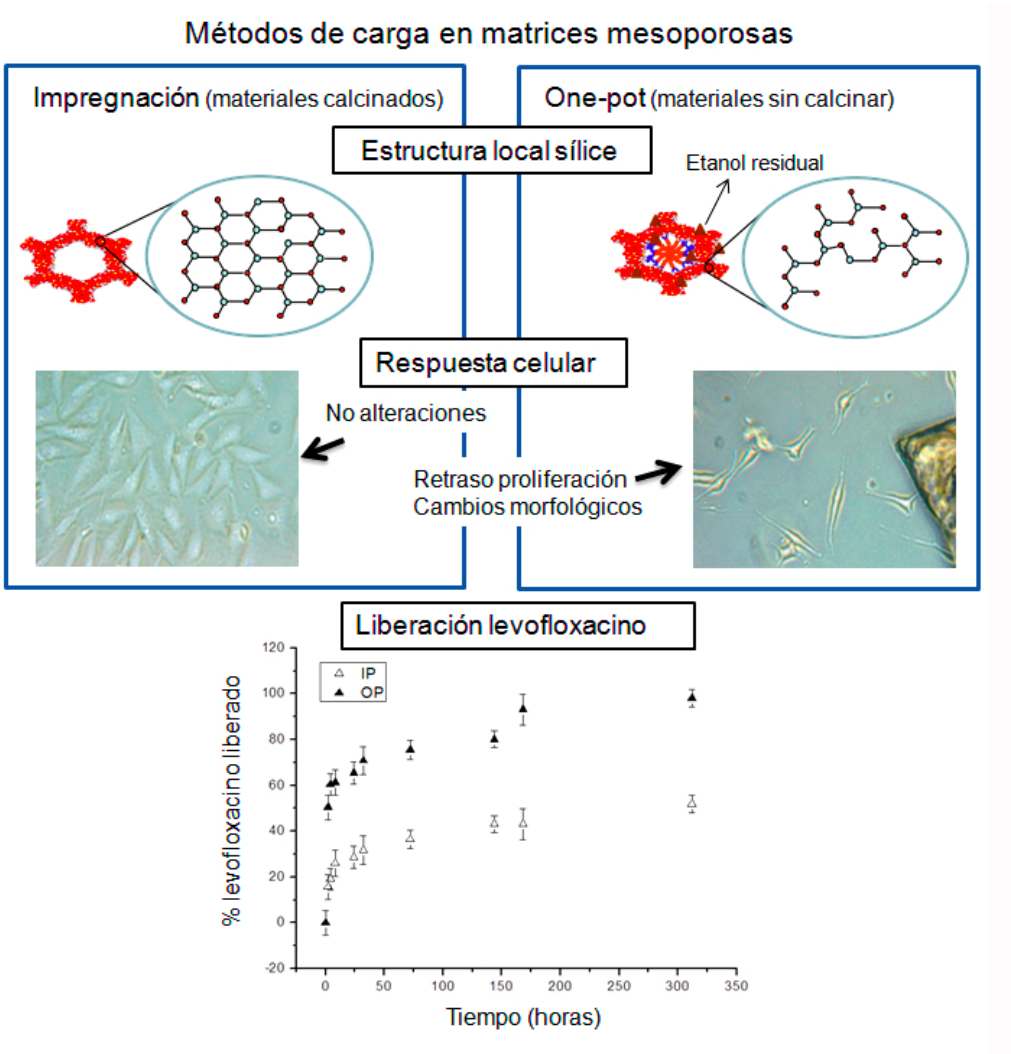

Figura 3.4. Figura resumen mostrando los resultados obtenidos.

El conjunto de resultados permite concluir que el proceso de calcinación de un material mesoporoso juega un papel crítico en su biocompatibilidad, ya que no sólo implica la eliminación del surfactante y de los reactivos utilizados durante la síntesis, sino que también produce cambios en la estructura local de la sílice a nivel atómico. De hecho, el presente estudio de biocompatibilidad revela diferentes respuestas celulares a

ambas matrices (IP y OP) en función del tipo celular. Estos resultados indican la importancia del método de preparación de matrices mesoporosas en el comportamiento de las células que van a entrar en contacto con el material atendiendo a su aplicación biomédica. Finalmente, los perfiles de liberación y los resultados de efectividad antimicrobiana obtenidos en función del tiempo, permiten sugerir el uso de estas matrices, IP y OP, como sistemas de liberación local en procesos de osteomielitis.

European Journal of Pharmaceutics and Biopharmaceutics 84 (2013) 115–124

Contents lists available at SciVerse ScienceDirect

European Journal of Pharmaceutics and Biopharmaceutics

journal homepage: www.elsevier.com/locate/ejpb

Research paper

Biocompatibility and levofloxacin delivery of mesoporous materials

Mónica Cicuéndez [a,b], Isabel Izquierdo-Barba [a,b], María Teresa Portolés [c,*], María Vallet-Regí [a,b,*]

[a] Departamento de Química Inorgánica y Bioinorgánica, Universidad Complutense de Madrid, Madrid, Spain
[b] Centro de Investigación Biomédica en Red Bioingeniería, Biomateriales y Nanomedicina (CIBER-BBN), Madrid, Spain
[c] Departamento de Bioquímica y Biología Molecular I, Universidad Complutense de Madrid, Madrid, Spain

ARTICLE INFO

Article history:
Received 30 July 2012
Accepted in revised form 26 November 2012
Available online 27 December 2012

Keywords:
Mesoporous
Drug delivery
Biocompatibility
Fibroblast
Osteoblast
Levofloxacin

ABSTRACT

A comparative study of mesoporous matrices designed for both drug-loading methods, impregnation (IP) and surfactant-assisted drug loading (also denoted as one-pot, OP), has been carried out evaluating their physicochemical characteristics, cell response, drug delivery profiles, and antibacterial activity. Surfactant-free (*calcined*) and surfactant-templated (*non-calcined*) mesoporous silica have been used as IP and OP starting matrices, respectively. Both non-calcined and calcined matrices do not exert any cytotoxic effect on osteoblasts. However, non-calcined matrices induce on fibroblasts a significant proliferation delay with morphological alterations and dose-dependent increases in fibroblast size, internal complexity, and intracellular calcium content but without cell lysis and apoptosis. Residual ethanol and the surface silanol groups in these non-calcined matrices are involved in the observed fibroblast changes. Finally, both IP and OP matrices have been loaded with levofloxacin to compare them as drug delivery systems. Both IP and OP matrices exhibit similar *in vitro* levofloxacin release profiles, showing an initial fast delivery followed by a sustained release during long time periods. These profiles and the antimicrobial activity results suggest the use of these IP and OP matrices as local drug delivery systems in the osteomyelitis and other bone infection treatments.

1. Introduction

Novel nanotechnology-based systems are currently being developed for controlled delivery of biologically active molecules [1–4]. Silica-based mesoporous materials, synthesized via supramolecular surfactant templating method, are nanostructured materials that have attracted a great attention due to their potential use as controlled delivery systems of therapeutics molecules [2–12]. Their unique ordered porosity at the nanoscale is translated into high surface area and pore volume able to load large amount of active molecules and subsequently to delivery them in controlled way. Moreover, their controllable surface chemistry by functionalization process lead to exert an exhaustive control of loading and pharmacokinetic profiles.

Different strategies have been used to encapsulate therapeutic agents into the mesoporous materials. In general, the drug molecules are loaded by the impregnation method (IP) after removal of the surfactant template by calcination or extraction processes [5,8,13]. The IP methodology involves soaking the surfactant-free mesoporous materials in a highly concentrated drug solution and subsequently drying [9,10]. This methodology offers numerous advantages regarding to its simplicity and efficiency; however, it presents limitations due to equilibrium distributions and the possible drug aggregation outside the material, yielding only a partial drug loading in the silica mesoporous matrix [5,8,9].

Recently, an interesting approach is to take advantage of the surfactant template as an adjuvant incorporating the drug molecules, in general of hydrophobic nature, to increase their loading amount, and to improve their kinetic profile and their stability [14,15]. In this sense, the drug molecules are incorporated during the mesoporous synthesis, being entrapped inside of surfactant micelles, which govern the delivery profiles as has been reported previously [16–21]. Although this surfactant-assisted loading methodology, denoted as one-pot methods (OP), *a priori* offers numerous advantages, only a few reports about OP systems were found in the literature, due mainly to controversies regarding to their biocompatibility. On the other hand, both IP and OP methodologies have not been compared in terms of drug loading and release to date.

In the present study, levofloxacin, a fluoroquinolone with a broad range of activity against both Gram-negative and Gram-positive bacteria, has been chosen to carry out a comparative study with IP and OP matrices as drug delivery systems. This antimicrobial agent has been chosen by its potential bactericidal activity in the

* Corresponding authors. Departamento de Bioquímica y Biología Molecular I, Facultad de Ciencias Químicas, Universidad Complutense, Ciudad Universitaria s/n, 28040 Madrid, Spain (M.T. Portolés), Departamento de Química Inorgánica y Bioinorgánica, Facultad de Farmacia, Universidad Complutense de Madrid, Plaza Ramón y Cajal s/n, 28040 Madrid, Spain. Tel.: +34 1 394 4666 (M. Vallet-Regí).
E-mail addresses: portoles@quim.ucm.es (M.T. Portolés), vallet@farm.ucm.es (M. Vallet-Regí).

0939-6411/$ - see front matter © 2012 Elsevier B.V. All rights reserved.
http://dx.doi.org/10.1016/j.ejpb.2012.11.029

osteomyelitis treatment [22] and by its strong interaction with silanol groups of silica nanoparticles at physiological pH. This fact is widely well-exploited in capillary electrophoresis applications [23].

In order to deep in the knowledge of fundamental aspects of both IP and OP loading methodologies, the present study compares the physicochemical characteristics of IP and OP matrices, the cell response to both systems, and their drug delivery profiles using different surfactant-free (*calcined*) and surfactant-templated (*non-calcined*) mesoporous silica. Thus, calcined and non-calcined 100%SiO_2 (Si), 90%SiO_2–10%CaO (SiCa), and 85%SiO_2–5%P_2O_5–10%CaO (SiCaP) systems have been used as starting mesoporous matrices for IP and OP methods, respectively. An exhaustive study of their *in vitro* biocompatibility has been performed, determining how changes at atomic level of these matrices can affect the cellular response to these systems. Finally, the kinetic release profiles and the antimicrobial activity of both IP and OP mesoporous matrices have been determined by the incorporation of an antimicrobial agent as levofloxacin.

2. Materials and methods

2.1. Synthesis of IP and OP matrices

The synthesis of both matrices has been carried out by using a biocompatible non-ionic surfactant, Pluronic® F127 (BASF), as structure directing agent through evaporation induced self-assembly (EISA) method [24]. Three different compositions in both IP and OP matrices, 100%SiO_2 (Si), 90%SiO_2–10%CaO (SiCa) and 85%SiO_2–5%P_2O_5–10%CaO (SiCaP) systems (% in mol), have been studied. Tetraethyl orthosilicate (TEOS), triethyl phosphate (TEP), and calcium chloride ($CaCl_2$) were used as SiO_2, P_2O_5, and CaO sources, respectively.

Briefly, 19.5 g of F127 was dissolved in 168.6 mL of absolute ethanol at 40 °C with 12.8 mL of 1.0 M HCl solution and 19.4 mL of MilliQ water. Afterward, the appropriate amounts of TEOS, TEP, and $CaCl_2$ were added in 1 h intervals, depending on the composition of each sample, under continuous stirring during 4 h at 40 °C and subsequently static conditions overnight. In all samples, the molar surfactant/network formed (TEOS + TEP) ratio was always keeping constant. The resulting sols were cast in Petri dishes (9 cm diameter) to undergo EISA process at 30 °C. The gelation process occurred after 3 days, and the gels were aged for 7 days in the Petri dish at 30 °C. Finally, the dried gels were removed as homogeneous and transparent membranes resulting in the Si, SiCa, and SiCaP non-calcined materials denoted with a subscript *nonCal*, for OP matrices. To obtain the Si, SiCa, and SiCaP materials for IP drug loading, a posterior treatment at 700 °C during 6 h was also carried out, resulting in the calcined matrices denoted with subscript *Cal*.

2.2. Characterization of IP and OP matrices

Powder X-ray diffraction (XRD) was carried out by using a Philips X'Pert diffractometer equipped with a Cu Kα radiation source (wavelength 1.5406 Å). XRD patterns were collected in the 2θ range between 0.6° and 8°, with a step size of 0.02° and a counting time of 0.5 s per step. Transmission electron microscopy (TEM) study was carried out with a JEOL 3000 FEG electron microscope fitted with a double tilting goniometer stage (±45°) and with an Oxford LINK EDS analyzer. TEM images were recorded using a CCD camera (MultiScan model 794, Gatan, 1024 × 1024 pixels, size 24 μm × 24 μm) in the low-dose condition. Fourier transform (FT) patterns were conducted using Digital Micrograph (Gatan).

The textural properties of the calcined samples were obtained by nitrogen adsorption/desorption analyses at −196 °C on a Micromeritics ASAP 2020 instrument (Micromeritics Co., Norcross, USA). Before each measurement, 100–150 mg of each sample was degassed under vacuum (<0.3 kPa) at 200 °C during 24 h. The surface area (S_{BET}) was determined using the Brunauer–Emmett–Teller (BET) method [25]. The total pore volume (V_T) was calculated from the amount of N_2 adsorbed at a relative pressure of 0.97 [26]. To assess the possible existence of micropores (pore diameter <2 nm) in our samples, the *t-plot* method was employed. The average mesopore diameter was obtained from the adsorption branch of the isotherm by means of the Barrett–Joyner–Halenda (BJH) method [27].

^{29}Si nuclear magnetic resonance (NMR) analyses were performed in a Bruker AV-400-WB spectrometer operating at 79.49 MHz for ^{29}Si. The ^{29}Si was recorded by magic angle spinning (MAS) at 12 kHz. Solid samples were analyzed in a 4-mm zirconia rotor. Chemical shifts (δ) of ^{29}Si were externally referred to 3-trimethylsilyl-1-propanesulfonic acid sodium salt (DDS) at δ = 0.0 ppm. The ^{29}Si NMR spectra were recorded with a 4.5-μs wide pulse, a contact time of 3.5 ms, and a recycle delay of 5 s. Typically, 15,000 scans were collected. The population of silanol groups per mol of silica has been calculated from the relative population of silanol and geminal species, divided by the weight per mol of silica materials (Eq. (1)), as previously reported [28]. The weight is derived from the relative populations and effective molecular weights (EMW) of the silanol, geminal, and siloxane species. The effective molecular weight of each species (EMW_Q) is defined as the sum of the molecular weight of the atoms contributing to each species, with the oxygen atoms in the siloxane bridges (Si–O–Si) that connect the species counted by half. The equation is:

$$[\mathrm{SiOH}] = \frac{(2 \times \%Q^2) + \%Q^3}{\sum(\%Q^i \times \mathrm{EMW_Q})} \quad (1)$$

where [SiOH] is the silanol group concentration in mol/g and $\%Q^i$ is the relative population of species Q^n (Q^2, Q^3, and Q^4).

The chemical composition was determined by X-ray fluorescence (XRF) in Philips PANalytical AXIOS spectrometer (Philips Electronics NV), which uses a Rh Kα source at k = 0.614 Å. CHNS elemental chemical analysis was carried out in a Perkin–Elmer 2400CHNS thermo analyzer. Thermogravimetric analysis (TG) was performed in dynamic air atmosphere between 30 and 1000 °C (flow rate 100 mL/min, heating rate 10 °C/min) using a Perkin–Elmer Diamond analyzer.

2.3. Cell culture for the in vitro biocompatibility studies

Either murine L929 fibroblasts or human Saos-2 osteoblasts (purchased from American Type Culture Collection, ATCC). were seeded on six well culture plates (CULTEK), at a density of 10^5 - cells/mL in DMEM supplemented with 10% fetal bovine serum (FBS, Gibco), 1 mM L-glutamine (BioWhittaker), penicillin (200 μg/mL, BioWhittaker), and streptomycin (200 μg/mL, BioWhittaker), under a CO_2 (5%) atmosphere and at 37 °C for 24 h. Different doses (1, 2.5, and 5 mg/mL) of calcined and non-calcined mesoporous materials in the three systems (Si, SiCa, and SiCaP) were added to the culture medium and incubated for 4 days. Then, cells were washed with Phosphate Buffer Saline (PBS), harvested using 0.25% trypsin–EDTA solution, and counted with a Neubauer hemocytometer for the analysis of cell proliferation. Cells were then centrifuged at 310*g* for 10 min and resuspended in fresh medium for the analysis of viability, cell cycle, apoptosis, intracellular calcium content, cell size, and complexity by flow cytometry. Controls without materials were always carried out.

2.4. Cell morphology studies by optical microscopy

Optical microscopy studies were carried out on both murine L929 fibroblasts and human Saos-2 osteoblasts after 4 days culture

in the presence of different doses of each pulverized samples with a Leitz Labovert FS inverted microscope equipped with a Leica DC 300 Digital Camera.

2.5. Flow cytometry studies

After the incubation with the different probes, as it is described below, the conditions for the data acquisition and analysis were established using negative and positive controls with the CellQuest Program of Becton Dickinson. For statistical significance, at least 10,000 cells were analyzed in each sample.

2.5.1. Cell viability

Cell viability was determined by addition of propidium iodide (PI; 0.005% in PBS, Sigma–Aldrich) to stain the DNA of dead cells. The fluorescence of PI was excited at 488 nm, and the emission was measured with a 670 nm LP in a FACScalibur Becton Dickinson flow cytometer.

2.5.2. Cell size and complexity

The light scattering properties were examined by flow cytometry measuring forward angle (FSC) and side angle (SSC) light scatters as indicators of cell size and complexity, respectively.

2.5.3. Intracellular calcium content

Cell suspensions were incubated with 10 μM Indo-1 AM (Enzo) for 30 min at room temperature, darkness, and shaking. The fluorescence of Indo-1 was excited at 325 nm, and the emitted fluorescence was measured at 380 nm in a LSR Becton Dickinson flow cytometer. After all the measurements, 10 μM A-23187 ionophore (Enzo) was added to prove the assay sensitivity.

2.5.4. Cell cycle analysis and apoptosis detection

Cell suspensions were incubated with Hoechst 33258 (Poly-Sciences, Hoechst 5 μg/mL, ethanol 30%, and BSA 1% in PBS), used as a nucleic acid stain, for 30 min at room temperature in darkness. The Hoechst fluorescence was excited at 350 nm, and the emission was measured at 450 nm in a LSR Becton Dickinson flow cytometer. The cell percentage in each cycle phase: G_0/G_1, S, and G_2/M were calculated with the CellQuest Program of Becton Dickinson, and the $SubG_1$ fraction was used as indicative of apoptosis.

2.6. Lactate dehydrogenase (LDH) measurement

To evaluate the plasma membrane integrity, lactate dehydrogenase activity was measured in the culture medium by an enzymatic method at 340 nm (Bio-Analítica) using a Beckman DU 640 UV–Visible spectrophotometer.

2.7. Loading of levofloxacin in IP and OP matrices

To simplify the study, only the SiO_2 composition in both systems was loading with levofloxacin. For the IP process, 700 mg of the Si calcined sample was immersed in an ethanolic solution containing 5.7 mg/mL of levofloxacin and was incubated during 24 h in dark and orbital stirring conditions. Then, the samples were filtered, gently washed with absolute ethanol, and denoted as $IPSi_{Levo}$ samples**.** To prepare the OP matrices, two different Levo/F127M ratios (1 and 2) were used and the drug incorporation was carried out in the first step of the synthesis process, during the surfactant dissolution into ethanol-aqueous solution. The resulting samples were denoted as $OPSi_{Levo\text{-}1}$ and $OPSi_{Levo\text{-}2}$, corresponding to the Levo/F127M ratio 1 and 2, respectively.

All samples containing levofloxacin were characterized by XRD to check that the mesoporous arrangement was maintained after drug incorporation. Moreover, N_2 adsorption studies were performed after levofloxacin loading. To confirm the presence of levofloxacin into samples, FTIR spectroscopy was carried out. The amount of loaded levofloxacin was determined by CHNS elemental chemical and TG analyses.

2.8. In vitro levofloxacin release from IP and OP matrices

In vitro levofloxacin release from the $IPSi_{Levo}$ and $OPSi_{Levo}$ samples was investigated by soaking 50 mg of each material in 12.5 mL of a Simulated Body Fluid (SBF, pH 7.5), proposed by Kokubo et al. [29], in dark conditions at 37 °C with continuous orbital stirring at 100 rpm. The amount of levofloxacin released to the SBF was determined by fluorescence spectroscopy with excitation and emission wavelengths of 292 and 494 nm, respectively, in a BioTek spectrofluorimeter.

2.9. In vitro stability studies of IP and OP matrices

In vitro stability tests of both IP and OP matrices have been carried out by soaking 50 mg of each sample in 12.5 mL of TRIS-buffer. The TRIS-soaking was performed at 37 °C, under continuous orbital stirring (100 rpm) in an Ecotron HT incubator in sterile conditions. The amount of SiO_2 leached to the different delivery media *versus* time was determined through colorimetrical analysis by using an equivalent method to US EPA 370.1 based in a molybdate complex formation which is measured at 660 nm [30]. To carry out this measurement, a SmartChem140 automatic discrete analyzer (Alliance Instruments, AMS France) was employed. Four samples were used for each measurement, and the results are shown as mean ± standard deviation.

2.10. Antibacterial activity of IP and OP matrices

Escherichia coli ATCC 25922 bacteria were grown to mid-logarithmic phase in Todd–Hewitt Broth (THB) medium (Sigma–Aldrich). For the antibacterial activity measurements, $IPSi_{Levo}$ and $OPSi_{Levo}$ samples (10 mg) were incubated into bacteria suspensions (2 mL, 2×10^6 cfu/mL) at 37 °C for different times in THB medium, inoculating daily such bacterial suspension on the antimicrobial system. To quantify bactericidal activity over time, 100 μL of the incubation mixtures were daily plated on TH agar, followed by incubation at 37 °C overnight. The presence of colony-forming units (cfu) was used as indirect measurement of antibacterial activity [17]. Controls with mesoporous matrices without levofloxacin were always carried out.

2.11. Statistics

Data are expressed as means + standard deviations of a representative of three experiments carried out in triplicate. Statistical analysis was performed using the Statistical Package for the Social Sciences (SPSS) version 19 software. Statistical comparisons were made by analysis of variance (ANOVA). Scheffé test was used for *post hoc* evaluations of differences among groups. In all of the statistical evaluations, $p < 0.05$ was considered as statistically significant.

3. Results and discussion

3.1. Physicochemical characterization of IP and OP matrices

The starting mesoporous matrices for both IP and OP loading methodologies (calcined and non-calcined materials, respectively) have been characterized to determine their structural and chemical differences and their effects on cell response and drug delivery

kinetics. TG studies have been carried out to evaluate the consequences of calcinations process (Fig. 1). Concerning non-calcined samples, the TG profiles show clearly three steps. A first step (30–180 °C) related to the elimination of adsorbed water and non-evaporated residual ethanol, a second step (180–380 °C) related to the total elimination of Pluronic F127 and finally a third step (380–700 °C) related to the condensation of silanol groups [19]. Concerning calcined samples, no weight variations are observed which confirms the absence of surfactant and other reagents thus revealing the efficacy of the calcination process.

Basically, the stoichiometric formula normalized to Si element from the composition analyzed by XRF for both IP and OP matrices is SiO_2, $Ca_{0.08}SiO_{2.08}$ and $Ca_{0.09}SiP_{0.06}O_{2.24}$, for Si, SiCa and SiCaP samples, respectively, revealing a good agreement to nominal ones. Moreover, CHNS elemental analysis shows the presence of carbon related to surfactant and/or residual ethanol in non-calcined samples (OP matrices) and the total absence of carbon in calcined samples (IP matrices). Furthermore, a complete elimination of chloride in the calcium-containing calcined samples is observed.

The mesostructural characterization of calcined and non-calcined materials has been carried out by TEM and small-angle XRD (data not shown). The results obtained reveal that the different compositions (Si, SiCa, and SiCaP) exhibit the same mesoporous arrangement in the 2D-hexagonal system before and after the calcination process (Fig. 2). However, a slight shrinking in the cell parameter (a_0), from around 20 nm values for non-calcined samples to around 14 nm values after calcination process (Table 1), has been observed. This shrinking has been attributed to an increase in the silica cross-linking degree into the pore wall by condensation of silanol groups, based on TG results as it has been previously described [19].

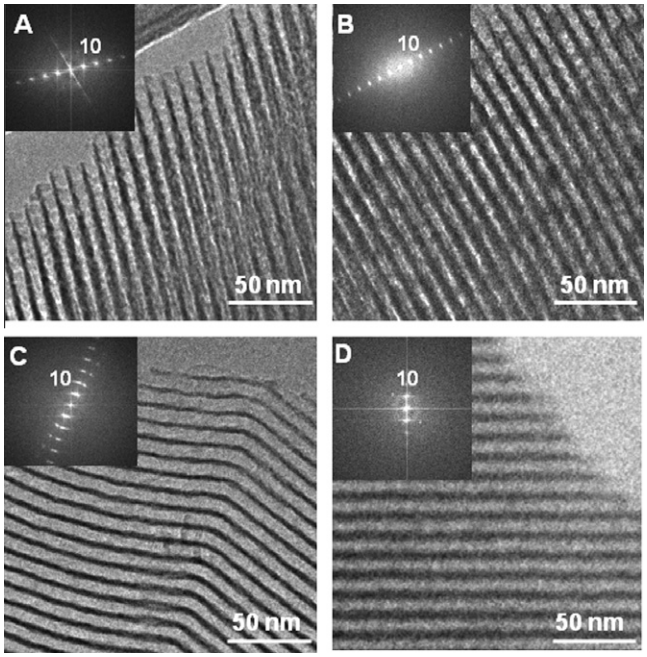

Fig. 2. TEM images and their FT difractograms of Si, SiCa, and SiCaP mesoporous matrices: (A) Si calcined, (B) SiCaP calcined, (C) SiCa calcined, and (D) SiCaP non-calcined. All images have been taken with the electron bean perpendicular to the mesoporous channels of a 2D-hexagonal structure with P6 mm plane group.

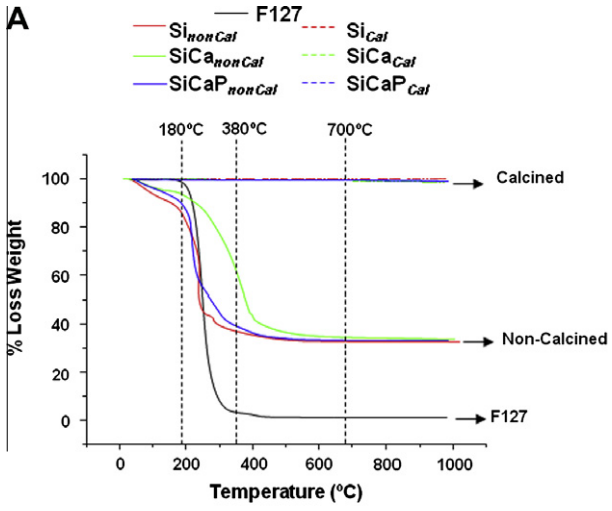

B

Sample/ΔT(°C)	30-180°C	180-380°C	380-700°C
F127	1.0	96.6	1.2
Si_{nonCal}	15.8	48.6	3.0
$SiCa_{nonCal}$	7.0	45.3	6.0
$SiCaP_{nonCal}$	10.4	51.3	4.8
Si_{Cal}	0.1	0.0	0.0
$SiCa_{Cal}$	0.4	0.3	0.4
$SiCaP_{Cal}$	0.4	0.3	0.3

Fig. 1. Thermogravimetric analysis of Si, SiCa, and SiCaP mesoporous matrices: (A) TG curves of non-calcined, calcined samples, and *F127* surfactant. (B) Percentages of loss weight. (For interpretation of the references to color in this figure legend, the reader is referred to the web version of this article.)

Table 1
Structural and textural properties corresponding to calcined samples.

Sample	Structure	a_0 (nm)	S_{BET} (m^2/g)	V_p (cm^3/g)	D_p (nm)	t_{wall} (nm)
Si_{cal}	*P6mm*	12.6	120	0.2	8.5	4.1
$SiCa_{cal}$	*P6mm*	13.1	130	0.2	8.4	4.7
$SiCaP_{cal}$	*P6mm*	14.4	235	0.4	8.1	6.3

a_0 is the unit cell parameter calculated by XRD being $a_0 = 2/\sqrt{3}d_{10}$ for hexagonal *P6mm* structure. S_{BET} is the surface area determined by using the BET method. V_p is the total pore volume obtained at P/P_0 0.98. D_p is the pore diameter calculated by means of the BJH method from the adsorption branch of the isotherm. t_{wall} corresponds to wall thickness calculated using the equation $t_{wall} = a_0 - D_p$ for hexagonal *P6mm* structure.

The adsorption/desorption analyses (data not shown) reveal type IV isotherms with H1-type hysteresis identified as cylindrical mesopores with high values of surface areas and pore volume (Table 1). The study of pore size distribution reveals the existence of large mesoporous size around 8 nm in all calcined samples.

For further establishing the chemical nature of silica network in both IP and OP matrices, the ^{29}Si SP/CP MAS NMR spectra were recorded before and after calcination process. Non-calcined samples show both ^{29}Si SP and CP MAS NMR spectra notably different to calcined ones, evidencing a higher opened silica framework with higher relative population for Q^3_H and Q^2_H species of non-calcined materials (Table 2). Moreover, the molar fraction of silanol groups measured by NMR data is also reported in Table 2 for all samples, showing a considerable silanol group population in the non-calcined samples (OP matrices).

3.2. In vitro biocompatibility of IP and OP matrices

In general, the development of mesoporous materials for biomedical applications requires close attention to safety issues. In

Table 2
Relative populations corresponding to Q^n ^{29}Si units obtained by deconvolution of the experimental single-pulse (SP) and cross polarization (CP) spectra. Amount of silanol groups in the surface of each material.

	^{29}Si SP								^{29}Si CP						
	Non-calcined				Calcined				Non-Calcined			Calcined			
	Q^4 (%)	Q^3_H (%)	Q^2_H (%)	SiOH (mmol/g)	Q^4 (%)	Q^3_H (%)	Q^2_H (%)	SiOH (mmol/g)	Q^4 (%)	Q^3_H (%)	Q^2_H (%)	Q^4 (%)	Q^3_H (%)	Q^2_H (%)	Q^2_{Ca} (%)
Si	24.9	66.1	9.0	12.3	82.1	17.9	–	2.8	14.0	76.3	8.7	33.0	54.6	1.4	–
SiCa	26.9	64.3	8.8	12.0	73.9	26.1	–	4.1	16.0	73.2	10.8	11.3	67.3	10.6	10.8
SiCaP	43.4	53.8	2.8	9.0	79.1	20.9	–	3.3	17.2	73.4	8.8	13.3	66.2	15.8	4.6

fact, the same properties which make them so promising for technological and biomedical perspectives, such as their high porosity, could also make them harmful to human health due to their reactivity rate derived of these properties [31–34].

To evaluate the *in vitro* biocompatibility of both IP and OP matrices, murine L929 fibroblasts and human Saos-2 osteoblasts have been cultured in the presence of different doses of these calcined and non-calcined mesoporous materials. The immortalized cell line L929 mouse fibroblasts is recommended as reference cell line for the cytotoxicity testing of biomaterials. On the other hand, Saos-2 is a human osteosarcoma cell line usually used as experimental model in this kind of *in vitro* studies due to its osteoblastic properties as production of mineralized matrix, high alkaline phosphatase levels, PTH receptors, and osteonectin presence.

As it can be observed in Fig. 3, the three non-calcined compositions produce a significant delay in fibroblast proliferation with respect to the control (cells cultured without material). This effect is dose-dependent and much more pronounced with Si matrix. However, no significant differences exist with respect to control when fibroblasts are cultured in the presence of calcined matrices (Fig. 3B) and cells reach confluence in all cases. When Saos-2 osteoblasts were cultured for 4 days in the presence of non-calcined and calcined Si, SiCa, and SiCaP materials, proliferation values were always similar to those obtained with control osteoblasts cultured in the absence of material (data not shown). These results reveal a higher sensitivity of fibroblasts in comparison with osteoblasts to non-calcined matrices, which could be due to the differences in the physiological function of each cell type [32].

The delay produced by non-calcined matrices in fibroblast proliferation (Fig. 3A) is accompanied by morphological changes in this cell type (Fig. 4B) with respect to control cells (Fig. 4A). No morphological alterations are observed in osteoblasts after treatment with non-calcined matrices (Fig. 4C and 4D), in agreement with the results of cell proliferation. The calcined matrices do not produce changes on the typical morphology of either fibroblasts or osteoblasts as it is observed by optical microscopy (data not shown).

The cell viability was up 85% in both fibroblasts and osteoblasts after treatment with both non-calcined and calcined matrices. However, since the proliferation results and the morphology evaluation reveal a possible fibroblast alteration produced by non-calcined matrices, the effects of all these matrices on the cell size and complexity of L929 fibroblasts and Saos-2 osteoblasts were also evaluated through FSC and 90° SSC light scatter as indicators of cell size and complexity, respectively. These properties are determined in part by cell size, plasma membrane, cytoplasm, mitochondria, pinocytic vesicles, and lysosomes [35]. Non-calcined matrices produce a dose-dependent increase in fibroblast size and internal complexity (Fig. 5), according to the morphological alterations observed by optical microscopy in the present study (Fig. 4). No changes of these parameters were found in fibroblasts treated with

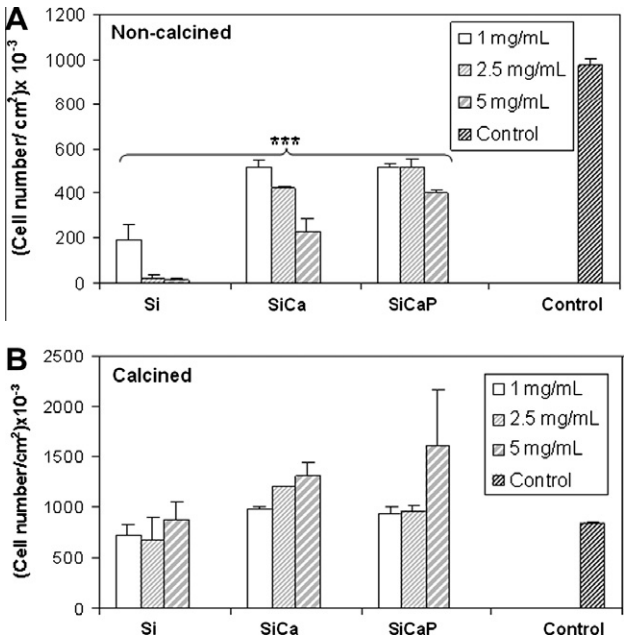

Fig. 3. Proliferation assays of L929 fibroblasts cultured for 4 days in the presence of 1, 2.5, and 5 mg/mL of Si, SiCa, and SiCaP mesoporous matrices: (A) non-calcined materials. Statistical significance: $^{***}p < 0.005$, (B) calcined materials. No significant differences were observed with respect to the control (cells cultured without materials).

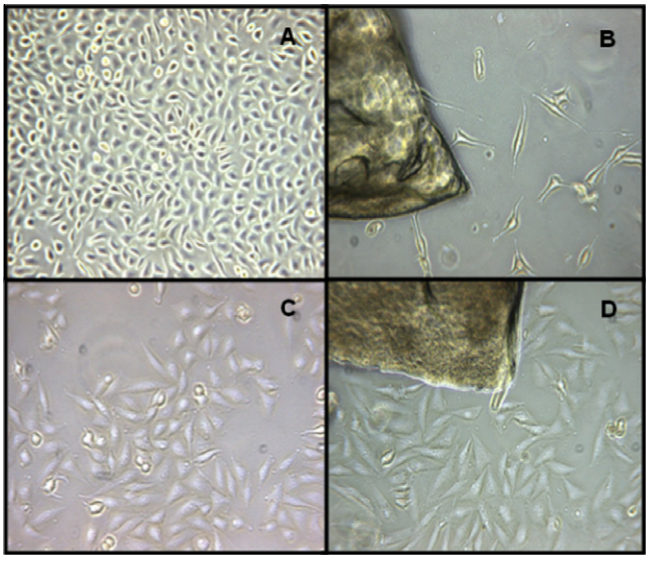

Fig. 4. Morphology evaluation of L929 fibroblasts and Saos-2 osteoblasts cultured for 4 days in the presence of 5 mg/mL of non-calcined SiCa and SiCaP materials: (A) control L929 fibroblasts, (B) L929 fibroblasts with non-calcined SiCa material, (C) Control Saos-2 osteoblasts, (D) Saos-2 osteoblasts with non-calcined SiCaP material. (For interpretation of the references to color in this figure legend, the reader is referred to the web version of this article.)

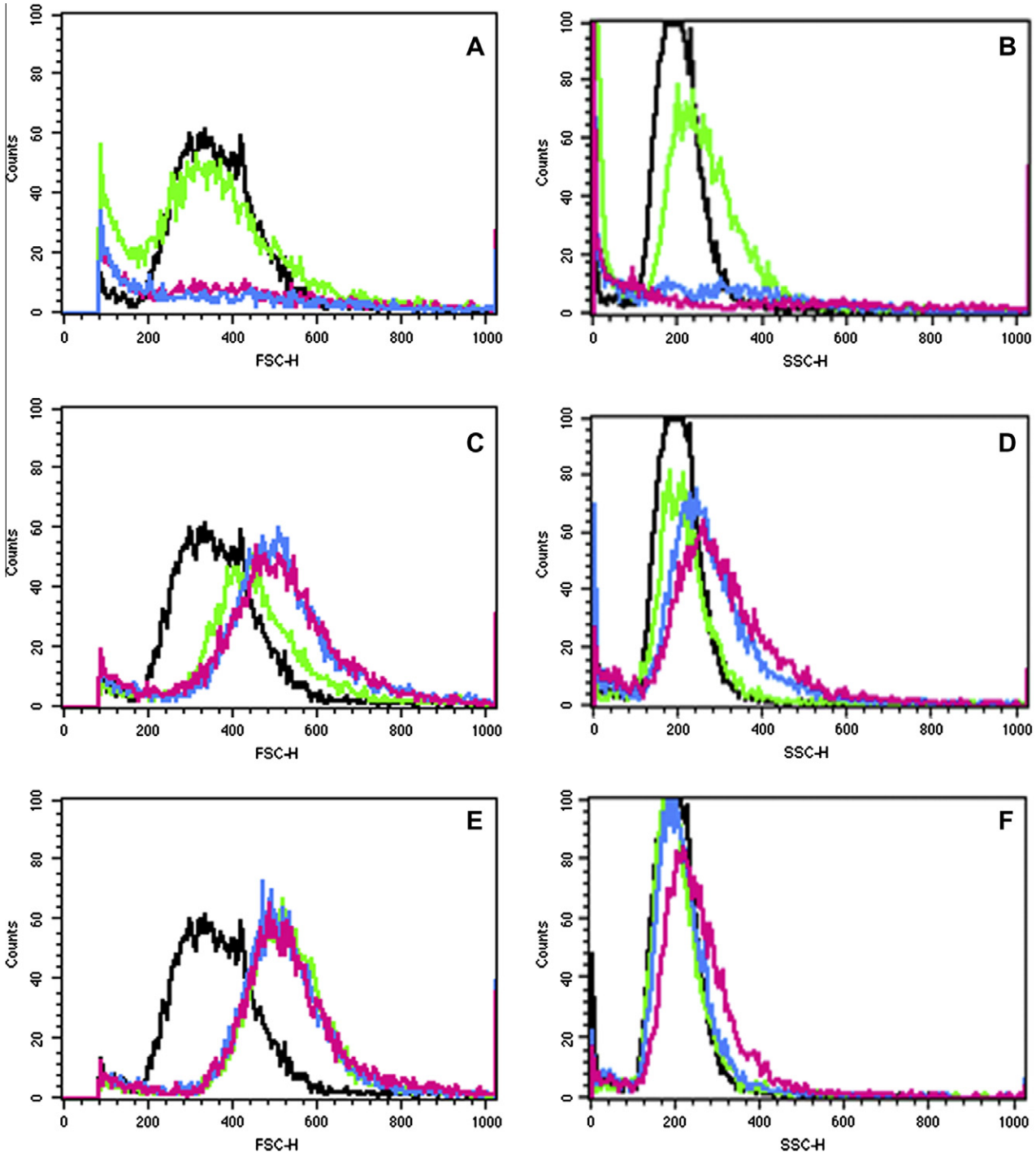

Fig. 5. Light scattering properties of L929 fibroblasts cultured in the presence of non-calcined matrices: (A, C and E) Forward angle scatter (FSC, cell size) *versus* number of cells after treatment with 1 (green), 2.5 (blue), and 5 mg/mL (pink) of non-calcined Si (A), SiCa (C), and SiCaP (E) matrices. (B, D, and F) 90° side angle light scatter (SSC, internal complexity) *versus* number of cells after treatment with 1 (green), 2.5 (blue) and 5 mg/mL (pink) of non-calcined Si (B), SiCa (D) and SiCaP (F) matrices. Controls with cultures without materials (black). (For interpretation of the references to color in this figure legend, the reader is referred to the web version of this article.)

calcined matrices. Osteoblasts do not show alterations after treatment with calcined and non-calcined matrices (data not shown).

It is known that many cell types have developed mechanisms which regulate their volume to protect themselves against lysis and apoptosis and to maintain an optimal concentration of intracellular enzymes and metabolites [36]. Thus, upon exposure to hypotonic or hypertonic conditions, cells readjust their volume producing regulatory volume changes through a complex system which include sensors of cell volume, intracellular signaling systems coupled to these sensors and membrane ion transporters. Since Ca^{2+} ions play an important role in cell volume regulation [37], the effects of different doses of non-calcined materials on intracellular calcium content of L929 fibroblasts and Saos-2 osteoblasts were analyzed. As it can be observed in Fig. 6, a dose-dependent increase in cytosolic Ca^{2+} is produced by non-calcined materials in L929 fibroblasts with respect to control cells. This effect is lower in Saos-2 osteoblasts showing similar calcium values with or without material probably due to the cytosolic Ca^{2+}

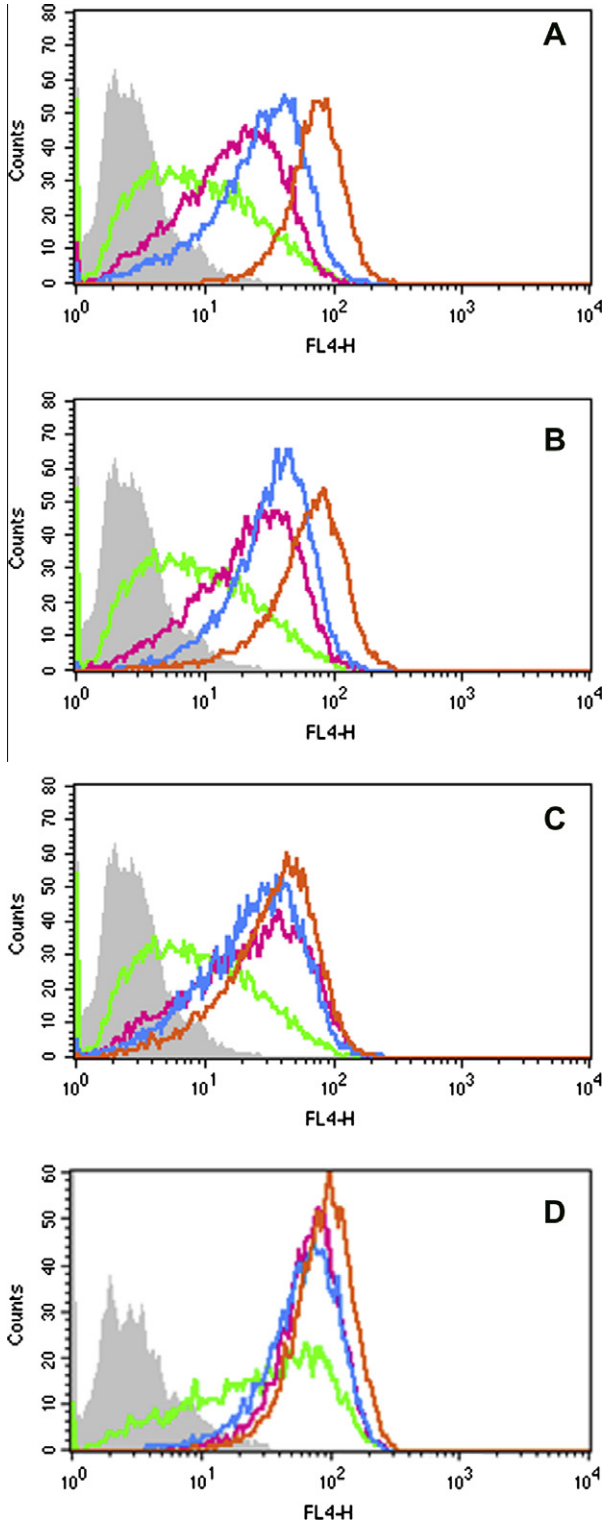

Fig. 6. Intracellular calcium content of L929 fibroblasts and Saos-2 osteoblasts cultured in the presence of non-calcined matrices: (A–C) Intracellular Indo-1 fluorescence *versus* number of cells after treatment of fibroblasts with 1 (pink), 2.5 (blue), and 5 mg/mL (orange) of non-calcined Si (A), SiCa (B), and SiCaP (C) matrices. D) Intracellular Indo-1 fluorescence *versus* number of cells after treatment of osteoblasts with 5 mg/mL of non-calcined Si (pink), SiCa (blue), and SiCaP (orange) matrices. Controls with cultures without materials (green). Cells without Indo-1 (gray). (For interpretation of the references to color in this figure legend, the reader is referred to the web version of this article.)

concentration of control osteoblasts which is higher than in control fibroblasts.

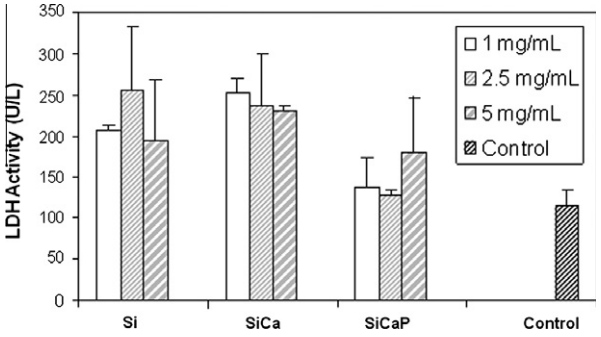

Fig. 7. Lactate dehydrogenase release (LDH) in the medium of L929 fibroblasts cultured in the presence of 1, 2.5, and 5 mg/mL of non-calcined Si, SiCa, and SiCaP materials. Controls with cultures without materials were always carried out.

To examine if the changes produced by non-calcined matrices in fibroblast size and complexity are accompanied by plasma membrane damaged, the LDH release to the culture medium was analyzed. No significant differences were found between LDH levels of controls and L929 cells treated with these matrices (Fig. 7), revealing that the morphology alterations observed in fibroblasts do not involve cellular lysis in agreement with the high viability values observed.

On the other hand, Table 2 shows the apoptosis values detected by $SubG_1$ fraction of fibroblasts cultured in the presence of non-calcined matrices. Low percentages of apoptosis (0.1–1.1%) were obtained after culture with these matrices except with 5 mg/mL of non-calcined Si sample which produces a slight but significant increase in this parameter ($p < 0.05$). Thus, although non-calcined matrices alter the fibroblast morphology and delay their proliferation, they do not induce fibroblast apoptosis.

In order to determine the influence of different physico-chemical characteristics of non-calcined matrices as surfactant, residual ethanol and the silica network connectivity grade on the cell response, specific studies have been carried out.

To clarify the role of F127 surfactant, the different doses (0.57 mg/mL, 1.45 mg/mL and 2.85 mg/mL) on cell size, complexity and cytosolic Ca^{2+} concentration of L929 fibroblasts were evaluated. Note that these surfactant doses are the amounts of surfactant present in the different doses of non-calcined material (1, 2.5, 5 mg/mL, respectively), determined by TG analyses. Fig. 8 shows that F127 does not alter these cell parameters demonstrating that this surfactant is not responsible for the alterations produced by non-calcined materials in this cell type.

Concerning the residual ethanol present in non-calcined materials, it can induce cell expansion probably due to increased intracellular osmotic pressure caused by its rapid permeation through the plasma membrane as it has been demonstrated elsewhere [38]. To assess the ethanol presence consequences, non-calcined Si materials with and without ethanol were compared. Thus, ethanol-free non-calcined samples were prepared eliminating residual ethanol by two different processes: (i) washing by soaking 50 mg of each sample in 20 mL of MilliQ water during 24 h at room temperature and posterior dried in vacuum conditions at 30 °C and (ii) drying at 150 °C during 6 h. The obtained samples were denoted as *washed* and *dried*, respectively. TG analyses of these samples reveal the total elimination of residual ethanol in the samples. The cell complexity has been chosen as a parameter to evaluate the residual ethanol effects of these Si samples on fibroblasts (Fig. 9). As it can be observed in Fig. 9A, dried (blue) and washed (orange) Si samples, which are ethanol-free-non-calcined materials, produce an improvement of this parameter with respect to non-calcined samples, exhibiting only a slight increase in fibroblast complexity with respect to control. The obtained results reveal that the residual ethanol present in

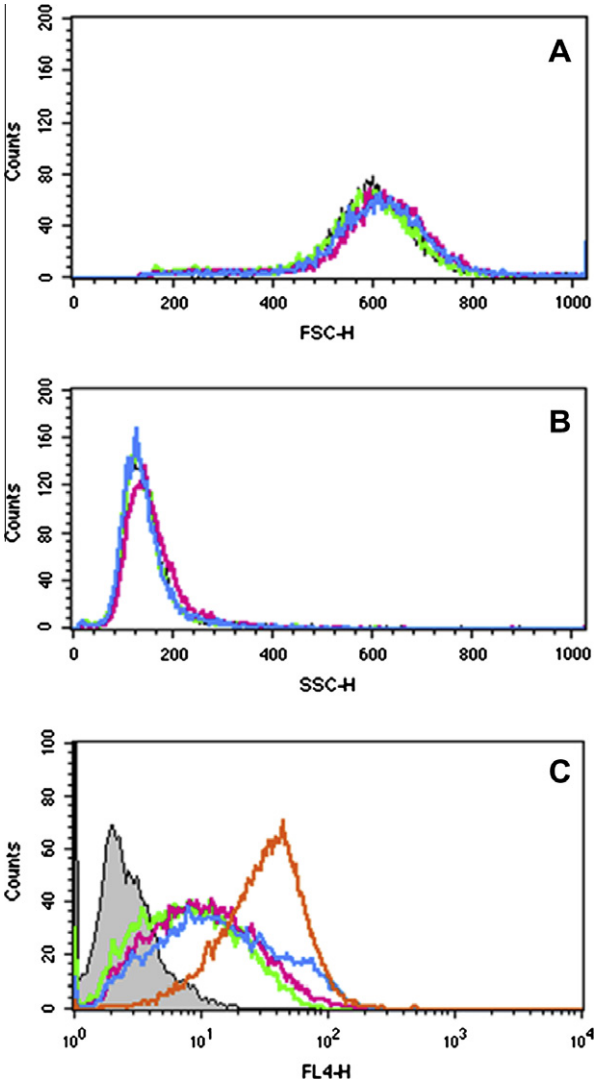

Fig. 8. Light scattering properties and intracellular calcium content of L929 fibroblasts cultured in the presence of F127 surfactant: (A) Forward angle scatter (FSC, cell size) *versus* number of cells after treatment with 0.57 (green), 1.45 (blue), and 2.82 mg/mL (pink) of F127 surfactant. (B) 90° side angle light scatter (SSC, internal complexity) *versus* number of cells after treatment with 0.57 (green), 1.45 (blue), and 2.82 mg/mL (pink) of F127 surfactant. Controls with cultures without materials (black). (C) Intracellular Indo-1 fluorescence *versus* number of cells after treatment with 0.57 mg/mL of F127 surfactant (pink) and 2.82 mg/mL of F127 surfactant (blue), and 10 μM A-23187 ionophore (orange). Controls with cultures without treatment (green). Cells without Indo-1 (gray). (For interpretation of the references to color in this figure legend, the reader is referred to the web version of this article.)

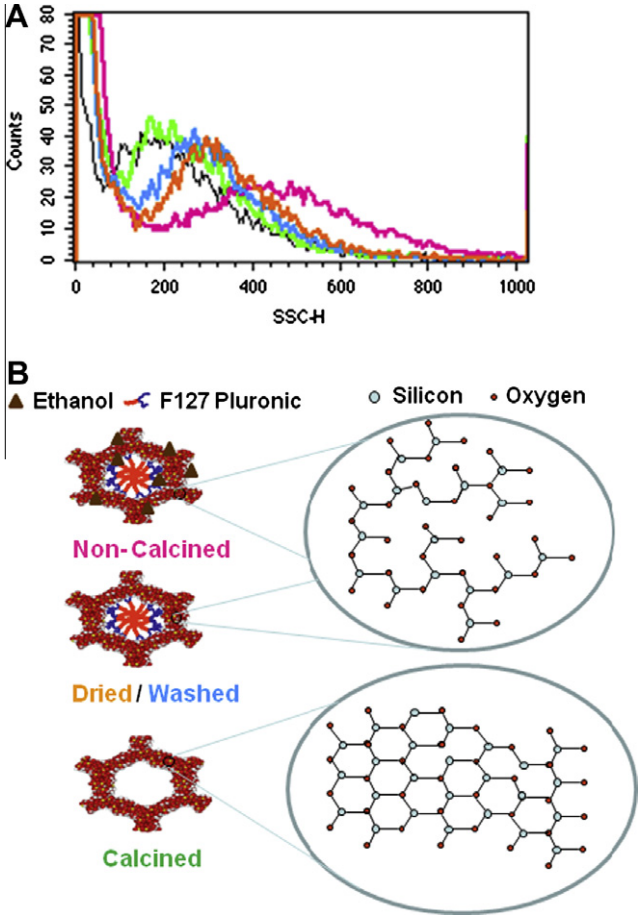

Fig. 9. (A) Light scattering properties of L929 fibroblasts cultured in the presence of 5 mg/mL of calcined, non-calcined, dried, and washed Si matrices: 90° side angle light scatter (SSC, internal complexity) *versus* number of cells after treatment with calcined (green), dried (blue), washed (orange), and non-calcined (pink) Si matrices. Controls with cultures without materials (black). (B) Local silica structure derived from NMR results corresponding to non-calcined, dried, washed, and calcined Si matrices. Inset represents the silica cross-linking degree related to amount of silanol groups on the surface of each sample. (For interpretation of the references to color in this figure legend, the reader is referred to the web version of this article.)

non-calcined matrices (10 mM) could be in part responsible for the increase observed in fibroblast complexity but it does not induce cell damage, demonstrating the existence of volume regulation mechanisms which protect these cells against lysis and apoptosis in these experimental conditions.

Other intrinsic parameter which could be also involved in this fibroblast alteration is the cross-linking degree related to the silanol group amount on the matrix surface. Note that all non-calcined matrices (ethanol-free and as made) exhibit similar silica cross-linking degree on the surface, as it has been schematized in Fig. 9B. Several authors have demonstrated that both distribution and abundance of surface silanol groups determine the cytoxicity degree of a nanostructured material [39]. In this sense, it has been demonstrated that silanol groups are directly involved in cellular permeability alterations of different cell types, inducing oxidative stress, reactive oxygen species (ROS) increase, lipid peroxidation, and perturbation of intracellular calcium homeostasis [40,41]. However, in the present study, although the abundance of silanol groups present in non-calcined materials could be responsible for fibroblast complexity alterations, this silica cross-linking degree is not enough to provoke cell lysis and apoptosis.

3.3. In vitro levofloxacin release and antimicrobial activity of IP and OP matrices

Finally, since both IP and OP matrices do not alter the osteoblast response, we suggest their use as local drug delivery systems for bone infection treatment. Therefore, levofloxacin has been loaded in both IP and OP matrices evaluating the loading process, kinetics profiles, and antimicrobial activity against *E. coli*. The obtained results revealed that $IPSi_{Levo}$ matrices loaded 0.095 mmol per gram of material and OP matrices loaded 0.043 mmol and 0.095 mmol per gram for the $OPSi_{Levo\text{-}1}$ and $OPSi_{Levo\text{-}2}$, respectively. However, only in $OPSi_{Levo\text{-}2}$ matrix, the mesoporous arrangement was destroyed (data not shown) and therefore this sample was not used in the *in vitro* release assay or in the antimicrobial activity study.

Another issue to taking into account is the yielding of loading process. While the IP matrices loaded the 4.3% respect to the total

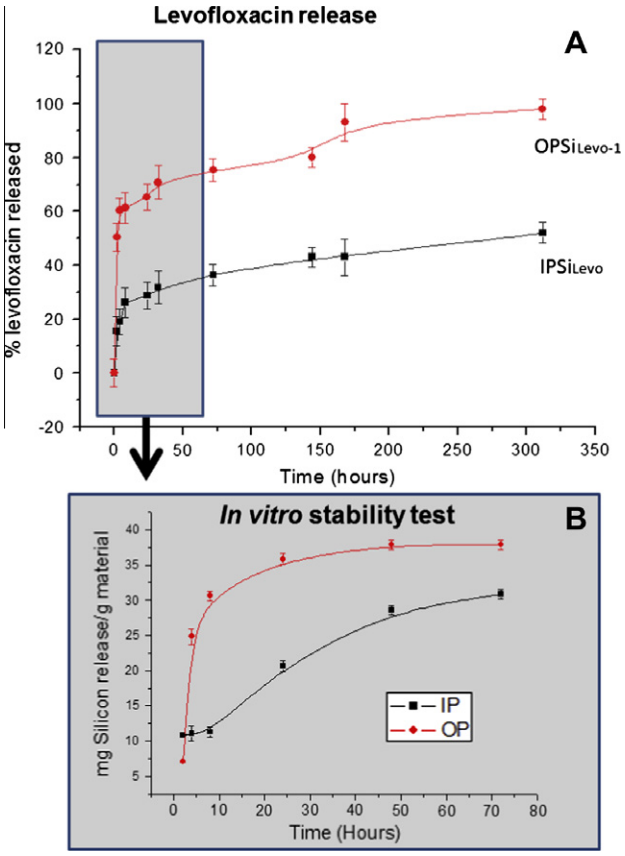

Fig. 10. (A) *In vitro* experimentally determined levofloxacin release profiles in SBF from $IPSi_{levo}$ and $OPSi_{levo-1}$ Si matrices. (B) *In vitro* stability test in TRIS-buffer of IP and OP Si matrices. (For interpretation of the references to color in this figure legend, the reader is referred to the web version of this article.)

drug amount used in the impregnation process, OP matrices loaded 100% of the used drug in the synthesis process. This is an important aspect when expensive biologically active molecules are used.

The textural properties revealed a significant decrease in both specific surface area and total pore volume after drug loading in $IPSi_{Levo}$ matrices, from values of 196 m^2/g and 0.21 cm^3/g to 96 m^2/g and 0.17 cm^3/g before and after drug loading, respectively. No significant variation in pore diameter was observed, exhibiting pore diameter values *c.a.* 8.5 nm. On the other hand, the $OPSi_{Levo-1}$ matrices exhibit fully mesoporous channels occupied by the joint presence of levofloxacin and surfactant. Moreover, powder small-angle XRD patterns confirmed the 2D-hexagonal pore arrangement in both IP and OP matrices after loading process. Furthermore, XRD patterns at $2\theta > 10^\circ$ exhibit no peaks which suggest that the majority of levofloxacin is accommodated inside the pore in non-crystalline state in both matrices (data no shown) [42].

Fig. 10A illustrates the levofloxacin release profiles of both matrices. The obtained results evidence a fast release on the first 24 h, reaching a 60% and 30% of the loaded levofloxacin amount for $OPSi_{Levo-1}$ and $IPSi_{Levo}$ matrices, respectively, followed by a slow and sustained release over the next hours in both cases. Both release profiles suggest a diffusion-controlled mechanism according to Higuchi model [43] in which the quantity released per gram is proportional to square root of time following the equation (inset):

$$M = K \cdot t_{1/2}$$

M is the cumulative percentage drug release at time t and k is the release rate constant that incorporates structural and geometric nature of the matrix. Thus, the release kinetic constants are 1.8 and 2.6 $h^{-1/2}$ for $IPSi_{Levo}$ and $OPSi_{Levo-1}$ matrices, respectively. These values are very low if they are compared with the kinetic constants of similar unmodified silica mesoporous matrices SBA-15-type [44], revealing a strong interaction between the levofloxacin molecules and silica network in both systems, in agreement with capillary electrophoresis studies in which there is a strong interaction between quinolones with silanol groups of silica nanoparticles [23]. The obtained release profiles could be fitted with a model for the bacterial infection treatment, characterized by an initial shock treatment followed by a prophylactic sustained dose during long time periods.

To explain the different initial release in both matrices, an *in vitro* stability test has been performed, since it has been demonstrated that the silica leaching from the mesoporous matrices is also a determining factor in drug release [45]. The SiO_2 leaching from both matrices is notably different (Fig. 10B). In OP matrices, the curves show a fast release in the first incubation hours (10 h) followed by a plateau in which the SiO_2 leached remains constant until the end of the *in vitro* assay, reaching the maximum level of saturation (around 40 mg SiO_2/g). However, IP matrices exhibit a *lag time* during the first 10 h, followed by gradual SiO_2 release, according to the higher silica cross-linking degree in these matrices (see Table 2). The results of SiO_2 leaching for both IP and OP matrices could explain the different initial levofloxacin release observed in the first 24 h.

The antimicrobial activity of both systems has been performed against *E. coli* and the results evidence bactericidal effectiveness during 14 days for IP matrices and 5 days for OP matrices (data not shown). These results are in agreement with the levofloxacin load and release studies as $IPSi_{Levo}$ samples loaded higher levofloxacin amount (0.095 mmol per gram) that $OPSi_{Levo-1}$ matrices (0.043 mmol per gram). This long time bactericidal activity of both systems suggests their applicability for local administration in osteomyelitis and other bone infections.

4. Conclusions

The comparative study of mesoporous matrices designed for both drug-loading methods, impregnation (IP) and one-pot (OP), reveals the critical role of the calcination process in mesoporous material biocompatibility and drug delivery because this step not only involves both surfactant and reactant eliminations but also changes in the local silica structure at atomic level.

The present biocompatibility studies reveal different cell responses to IP and OP matrices depending on the cell type evidencing that cells could detect both small changes in the local silica environment and the presence of residual ethanol. Therefore, we propose an exhaustive control in the design of these kinds of matrices as controlled drug delivery systems depending on their biomedical applications.

Both IP and OP matrices exhibit similar *in vitro* levofloxacin delivery profiles, showing an initial fast release followed of sustained release and antibacterial effectiveness during long time periods suggesting their use as local drug delivery in osteomyelitis and other bone infections.

Acknowledgments

This study was supported by research grants from Comunidad de Madrid (S2009/MAT-1472) and Ministerio de Ciencia e Innovación (MICINN) through the projects MAT2008-00736 and CS2010-11384-E. M. Cicuéndez is grateful to MICINN for the financial support through FPI fellowship. The authors wish to thank also to the staff of the ICTS Centro Nacional de Microscopia Electrónica (Spain) and Centro de Citometría y Microscopia de Fluorescencia, Centro

de Difracción de Rayos X, Centro de Microanálisis Elemental and Centro de Resonancia Magnética Nuclear of the Universidad Complutense de Madrid (Spain).

References

[1] O.C. Farokhzad, R. Langer, Impact of nanotechnology on drug delivery, ACS Nano 3 (2009) 51–59.
[2] J.M. Rosenholm, C. Sahlgren, M. Linden, Towards multifunctional, targeted drug delivery systems using mesoporous silica nanoparticles – opportunities & challenges, Nanoscale 2 (2010) (2010) 1870–1883.
[3] M. Vallet-Regí, E. Ruiz-Hernández, Bioceramics: from bone regeneration to cancer nanomedicine, Adv. Mater. 23 (2011) 5177–5218.
[4] M. Vallet-Regi, Mesoporous silica nanoparticles: their projection in nanomedicine, ISRN Mater. Sci. (2012), Article ID 608548 (20 pages).
[5] M. Vallet-Regí, F. Balas, D. Arcos, Mesoporous materials for drug delivery, Angew. Chem. Int. Ed. 46 (2007) 7548–7558.
[6] Y. Piao, A. Burns, J. Kim, U. Wisner, T. Hyeon, Designed fabrication of silica-based nanostructured particle systems for nanomedicine applications, Adv. Funct. Mater. 18 (2008) 3745–3758.
[7] M. Vallet-Regí, Nanostructured mesoporous silica matrices in nanomedicine, J. Int. Med. 267 (2009) 22–43.
[8] M. Manzano, M. Vallet-Regi, New developments in ordered mesoporous materials for drug delivery, J. Mater. Chem. 20 (2010) 5593–5604.
[9] M. Vallet-Regi, M. Colilla, B. Gonzalez, Medical applications of organic–inorganic hybrid materials within the field of silica-based bioceramics, Chem. Soc. Rev. 40 (2011) 596–607.
[10] S.H. Wu, Y. Hung, C.Y. Mou, Mesoporous silica nanoparticles as nanocarriers, Chem. Commun. 47 (2011) 9972–9985.
[11] I.I. Slowing, J.L. Vivero-Escoto, B.G. Trewyn, V.S.Y. Lin, Mesoporous silica nanoparticles: structural design and applications, J. Mater. Chem. 20 (2012) 7924–7937.
[12] Z.X. Li, J.C. Barnes, A. Bosoy, J.F. Stoddart, J.I. Zink, Mesoporous silica nanoparticles in biomedical applications, Chem. Soc. Rev. 41 (2012) (2012) 2590–2605.
[13] M. Vallet-Regí, A. Rámila, R.P. del Real, J. Pérez-Pariente, A new property of MCM 41: drug delivery system, Chem. Mater. 13 (2001) 308–311.
[14] H. Tan, Y. Zhang, M. Wang, Z. Zhang, X. Zhang, A.M. Yong, S.Y. Wong, A.Y. Chang, Z.K. Chen, X. Li, M. Choolani, J. Wang, Silica-shell cross-linked micelles encapsulating fluorescent conjugated polymers for targeted cellular imaging, Biomaterials 33 (2012) 237–246.
[15] K.M. Tyner, S.R. Schiffman, E.P. Giannelis, Nanobiohybrids as delivery vehicles for camptothecin, J. Control. Release 95 (2004) 501–514.
[16] N.W. Clifford, K.S. Iyer, C.L. Raston, Encapsulation and controlled release of nutraceuticals using mesoporous silica capsules, J. Mater. Chem. 18 (2008) 162–165.
[17] I. Izquierdo-Barba, M. Vallet-Regí, N. Kupferschmidt, O. Terasaki, A. Schmidtchen, M. Malmsten, Incorporation of antimicrobial compounds in mesoporous silica film monolith, Biomaterials 30 (2009) 5729–5736.
[18] C. Gao, I. Izquierdo-Barba, I. Nakase, S. Futaki, J. Ruan, K. Sakamoto, Y. Sakamoto, K. Kuroda, O. Terasaki, S. Che, Mesostructured silica based delivery system for a drug with a peptide as a cell-penetrating vector, Micropor. Mesopor. Mater. 122 (2009) 201–207.
[19] Q. He, J. Shi, F. Chen, M. Zhu, L. Zhang, An anticancer drug delivery system based on surfactant-templated mesoporous silica nanoparticles, Biomaterials 31 (2010) 3335–3346.
[20] C.-H. Tsai, J.L. Vivero-Escoto, I.I. Slowing, I.-J. Fang, B.G. Trewyn, V.S.Y. Lin, Surfactant-assisted controlled release of hydrophobic drugs using anionic surfactant template mesoporous silica nanoparticles, Biomaterials 32 (2011) 6234–6244.
[21] J. Tang, Z. Bian, J. Hu, S. Xu, H. Liu, The effect of a P123 template in mesopores of mesocellular foam on the controlled-release of venlafaxine, Int. J. Pharmaceut. 424 (2012) 89–97.
[22] R. Greenberg, M.T. Newman, S. Shariaty, R.W. Pector, Ciplofloaxin, lomefloxacin or levofloxacin as treatment for cronic osteomyelitis, Antimicrob. Agents Chemother. 44 (2000) 164–166.
[23] Y. Wang, W.R.G. Baeyens, C. Huang, G. Fei, L. He, J. Ouyang, Enhanced separation of seven quinolones by capillary electrophoresis with silica nanoparticles as additive, Talanta 77 (2009) 1667–1674.
[24] C.J. Brinker, Y.F. Lu, A. Sellinger, H.Y. Fan, Evaporation-induced self-assembly: nanostructures made easy, Adv. Mater. 11 (1999) 579–585.
[25] S. Brunauer, P.H. Emmett, E. Teller, Adsorption of gases in multimolecular layers, J. Am. Chem. Soc. 60 (1938) 309–319.
[26] S.J. Gregg, K.S.W. Sing, Adsorption, Surface Area and Porosity, second ed., Academic Press, New York, 1982.
[27] E.P. Barrett, L.G. Joyner, P.H. Halenda, The determination of pore volume and area distributions in porous substances. I. Computations from nitrogen isotherms, J. Am. Chem. Soc. 73 (1951) 373–380.
[28] B.H. Wouters, T. Chen, M. Dewilde, P.J. Grobet, Reactivity of the surface hydroxyl groups of MCM-41 towards silylation with trimethylchlorosilane, Micropor. Mesopor. Mater. 44 (2001) 453–457.
[29] T. Kokubo, H. Kushitani, S. Sakka, T. Kitsugi, T. Yamamuro, Solutions able to reproduce in vivo surface-structure changes in bioactive glass–ceramic A-W, J. Biomed. Mater. Res. 24 (1990) 721–724.
[30] O.G. Koch, G.A. Koch-Dedic, Siliconmolybdänblau-Verfahren, in: Handbuch der Spurenanalyse, Springer-Verlag, Berlin, 1974, p. 1105.
[31] A.E. García-Bennet, Synthesis, toxicology and potential of ordered mesoporous materials in nanomedicine, Nanomedicine 6 (2011) 867–877.
[32] T. Yu, A. Malugin, H. Ghadehari, Impact of silica nanoparticles design on cellular toxicity and hemolytic activity, ACS Nano 5 (2011) 5717–5728.
[33] J. Lu, M. Liong, Z.X. Li, J.I. Zink, F. Tamanoi, Biocompatibility, biodistribution, and drug-delivery efficiency of mesoporous silica nanoparticles for cancer therapy in animals, Small 6 (2010) 1794–1805.
[34] T. Heikkilä, H.A. Santos, N. Kumar, D.Y. Murzin, J. Salonen, T. Laaksonen, L. Peltonen, J. Hirvonen, V.-P. Lehto, Cytotoxicity study of ordered mesoporous silica MCM-41 and SBA-15 microparticles on Caco-2 cells, Eur. J. Pharm. Biopharm. 74 (2010) 483–494.
[35] J.M. Udall, R.A. Moscicki, F.I. Preffer, P.D. Ariniello, E.A. Carter, A.K. Bhan, K.J. Bloch, Flow cytometry: a new approach to the isolation and characterization of Kupffer cells, Adv. Exp. Med. Biol. 216 (1987) 821–827.
[36] A.A. Mongin, S.N. Orlov, Mechanisms of cell volume regulation and possible nature of the cell volume sensor, Pathophysiology 8 (2001) 77–88.
[37] R. Liu, A.E. Persson, Simultaneous changes of cell volume and cytosolic calcium concentration in macula densa cells caused by alterations of luminal NaCl concentration, J. Physiol. 563 (2005) 895–901.
[38] K. Sato, N. Sato, M. Mori, Isotonic ethanol inhibits the generation of superoxide anion in neutrophils by inducing cell expansion, Life Sci. 63 (1998) 1329–1337.
[39] S. Lee, H.-S. Yun, S.-H. Kim, The comparative effect of mesoporous silica nanoparticles and colloidal silica on inflammation and apoptosis, Biomaterials 32 (2011) 9434–9443.
[40] Z. Elias, O. Poirot, M.C. Danieve, F. Terzetti, A.M. Marande, S. Dzwigaj, H. Pezerat, I. Fenoglio, B. Fubini, Cytotoxic and transforming effects of silica particles with different surface properties in Syrian hamster embryo (She) cells, Toxicol. In Vitro 14 (2000) 409–422.
[41] V. Murashow, M. Harper, E. Dmchuz, Impact of silanol surface density on the toxicity haemolysis, J. Occup. Environ. Hyg. 3 (2006) 718–723.
[42] Y. Zhang, Z. Zhi, T. Jiant, Z. Wang, S. Wang, Spherical mesoporous silica nanoparticles for loading and release of poorly water-soluble drug telmisartan, J. Control. Release 145 (2010) 257–263.
[43] T. Higuchi, Mechanism of sustained-action medication, J. Pharm. Sci. 52 (1963) 1145–1147.
[44] J.C. Doadrio, E.M.B. Sousa, I. Izquierdo-Barba, A.L. Doadrio, J. Perez-Pariente, M. Vallet-Regi, Functionalization of mesoporous materials with long alkyl chains as a strategy for controlling drug delivery pattern, J. Mater. Chem. 16 (2006) 462–466.
[45] A.S. Alkady, M. Garber, M.M. Hussein, E.-Z. Ebeid, Nanostructure-loaded mesoporous silica for controlled release of coumarin derivatives: a novel testing of hyperthermia effect, Eur. J. Pharm. Biopharm. 77 (2011) 66–74.

3.3. Actividad antibacteriana y biocompatibilidad de los andamios MGHA cargados con levofloxacino

El objetivo de este apartado ha sido la incorporación de un agente antimicrobiano dentro de la estructura mesoporosa de los andamios MGHA como sistema modelo para el tratamiento y prevención local de una infección ósea. Para estos propósitos se incorporó levofloxacino (Levo) en los andamios mediante el método de impregnación y se realizó una profunda caracterización de las muestras. Con el fin de determinar la influencia del pH en la cinética de liberación del fármaco, se estudiaron los perfiles de liberación a diferentes pH (5.5; 6.7 y 7.4). Para determinar la efectividad antimicrobiana de estos sistemas se realizaron ensayos antimicrobianos frente a *S. aureus* and *E. coli* durante diferentes periodos de tiempo. Finalmente y dada la importancia de la biocompatibilidad de los implantes potenciales conteniendo levofloxacino, se comprobó la ausencia de posibles efectos citotóxicos producidos por los extractos procedentes de dichos andamios sobre osteoblastos humanos Saos-2 a diferentes tiempos de incubación (3 y 24 h).

Carga y liberación de levofloxacino en andamios 3D MGHA

La incorporación de levofloxacino a la estructura mesoporosa del andamio se ha realizado mediante el método de impregnación introduciendo individualmente cada andamio (con una masa de 23±2 mg) en 3 mL de una disolución etanólica de levofloxacino de 37 μg/mL a temperatura ambiente. Este procedimiento ha sido descrito en el **apartado 3.2.** para la impregnación del material MGHA en forma pulverizada. Transcurridas 24 horas de incubación y en agitación orbital de 200 r.p.m., los andamios se extrajeron de la solución de impregnación y se lavaron vigorosamente con etanol dejándose secar a temperatura ambiente. La manipulación de esta droga se ha realizado en condiciones de oscuridad por su sensibilidad a la luz. La cantidad de levofloxacino incorporado en cada andamio fue determinada por análisis químico elemental previa molturación del andamio y recogida del polvo para la medida. Dicha medida de carga se ha realizado por cuadruplicado, y se representa el porcentaje (%) de levofloxacino presente en cada andamio (**Tabla 3.1.**).

La **Tabla 3.1.** muestra la variación de las propiedades texturales del andamio MGHA tras su impregnación con levofloxacino valoradas por adsorción de N_2, observándose una disminución de los parámetros, superficie específica, volumen de poro y diámetros de mesoporo, lo cual confirma la incorporación del levofloxacino en la estructura mesoporosa del andamio [36]. Asimismo, un estudio por intrusión de Hg y SEM del andamio después de su impregnación ha confirmado que dicho proceso no afecta a las propiedades macroestructurales del andamio, mostrando la misma macroporosidad antes y después de ser cargado con levofloxacino.

Tabla 3.1. Cantidad de levofloxacino cargado en la estructura mesoporosa del andamio MGHA. Parámetros texturales (superficie específica, volumen de poro, diámetro de poro) antes y después de la carga.

Muestras	% Levo	S_{BET} (m^2/g)	V_p (cm^3/g)	D_p (nm)
MGHA	-	123	0.2	10.0
MGHA-levo	3	40	0.1	9.3

Para confirmar cualitativamente la presencia de levofloxacino en los andamios así como los cambios estructurales y composicionales del andamio tras el proceso de carga, los andamios se han caracterizado por FTIR y XRD (**Figura 3.5.**). Los espectros FTIR de los andamios MGHA tras la impregnación muestran bandas características de la molécula de levofloxacino a 1725 cm^{-1} del grupo carbonilo, a 2935 cm^{-1} del anillo aromático y del grupo C-H y 3266 cm^{-1} del grupo OH de grupo carboxilo. Asimismo, los estudios por XRD muestran que la incorporación de levofloxacino en la estructura del andamio no afecta ni al orden estructural (sigue manteniendo una estructura 2D hexagonal) ni a la cristalinidad de la hidroxiapatita presente en el andamio.

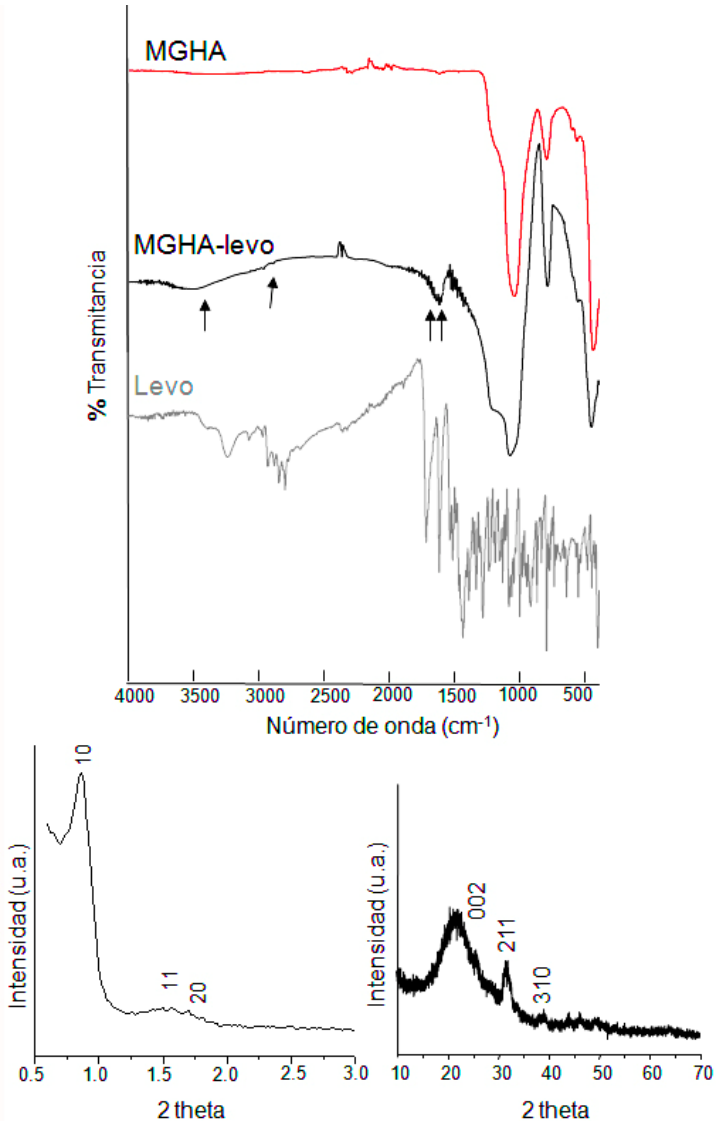

Figura 3.5. Parte superior: espectros de FTIR de los andamios MGHA antes y después de incorporar levofloxacino. El espectro correspondiente a dicho fármaco también se representa. Las flechas indican las bandas presentes en el andamio MGHA características de la molécula de levofloxacino. Parte inferior: diagramas de DRX recopilados a bajos y altos ángulos 2θ, respectivamente correspondiente a los andamios después del proceso de impregnación con levofloxacino.

Los estudios cinéticos de liberación de levofloxacino desde de los andamios MGHA se han realizado a tres diferentes pH, 5.5, 6.7 y 7.4, como valores representativos de los pH existentes en condiciones de un proceso infeccioso (5.5. y 6.7) y condiciones fisiológicas (7.4). Estos estudios se han llevado a cabo sumergiendo cada andamio cargado con levofloxacino (soportado verticalmente con un hilo de Pt) en 15 mL de PBS, ajustados a los diferentes pH, a 37ºC y en agitación orbital a 300 r.p.m.

Los ensayos se han realizado renovando diariamente el medio. El levofloxacino liberado se ha cuantificado utilizando un espectrofluorímetro Biotek Powerwave XS y la versión 1.00.14 del programa *Gen5* utilizando una $\lambda_{excitación}$ = 292 y $\lambda_{emisión}$ = 494 nm. En este caso, se calcularon diferentes rectas de calibrado a los diferentes pHs en un intervalo de concentración de 12 a 0.01 µg/mL. La **Figura 3.6.** muestra los perfiles de liberación representados por la cantidad acumulada de levofloxacino liberado en el tiempo (Q_t) con respecto a la cantidad de levofloxacino presente inicialmente en el andamio (Q_0). Los resultados ponen de manifiesto una gran influencia del pH en la liberación de levofloxacino, presentando una liberación más rápida a pH ácidos. Por el contrario, cuando el pH es el fisiológico (pH 7.4), los perfiles indican una liberación lenta y sostenida en el tiempo.

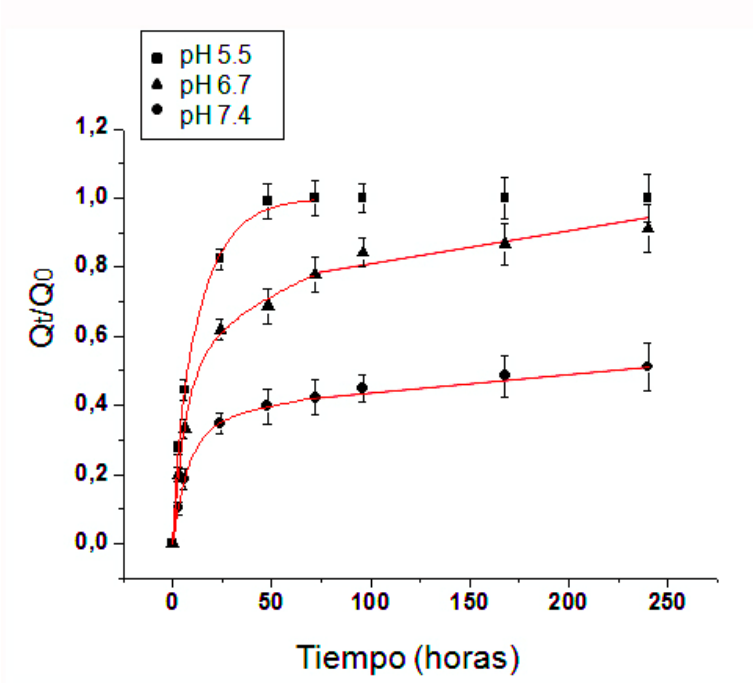

Figura 3.6. Perfiles de liberación de levofloxacino cargado en andamios MGHA a pH 5.5, 6.7 y 7.4 a 37ºC en PBS. Las curvas representan la acumulación de levofloxacino liberado (Q_t) con respecto a la cantidad inicial presente en el andamio (Q_0) en función del tiempo de ensayo. Se observan notables diferencias en las cinéticas de liberación del fármaco en función del pH.

Numerosos estudios han mostrado que las cinéticas de liberación desde matrices mesoporosas se rigen principalmente por procesos de difusión del fármaco en la matriz y se ajustan por lo general al modelo de Higuchi [49, 31]. Las investigaciones se han centrado en conseguir una disminución de la liberación inicial desmesurada "*efecto*

burst" producida por lo general en estas matrices mesoporosas, mediante la funcionalización de la superficie de la matriz para favorecer su interacción con el fármaco y de esta manera obtener una liberación más sostenida en el tiempo [31]. Así, los perfiles de liberación de estas matrices se han ajustado a dos cinéticas de liberación; una regida por la difusión y otra regida por la interacción del fármaco con la matriz. En el presente estudio los perfiles de liberación a pH 7.4 no presentan el característico "*efecto burst*" propio de las matrices mesoporosas con la misma estructura tipo hexagonal tipo SBA-15 [50], poniéndose de manifiesto una interacción entre el fármaco y la matriz que es pH dependiente. Los perfiles de liberación han sido ajustados de acuerdo a un modelo cinético simple con tres parámetros que combina tanto la interacción reversible fármaco-vehículo como la difusión de éste desde la matriz [51]. Este modelo se ha utilizado para una gran cantidad de matrices, incluyendo liposomas, nanopartículas mesoporosas, nanocápsulas poliméricas, etc, y es aplicable cuando hay una combinación de ambos procesos (difusión e interacción matriz/fármaco) y en sistemas de liberación que son regidos por un estímulo externo como la temperatura y el pH. El modelo se basa en la **ecuación 3.1.**

$$\frac{Q_t}{Q_0} = \frac{k_{off}}{k_{on}+k_{off}}\left(1 - e^{-k_s t}\right) + \frac{k_{on}}{k_{on}+k_{off}}\left(1 - e^{-k_{off} t}\right) \qquad \textbf{Ecuación 3.1.}$$

Q_t/Q_0 corresponde a la cantidad acumulativa de droga liberada con respecto a la cantidad de droga presente inicialmente en la matriz por unidad de tiempo, k_s corresponde a la constante de difusión, y k_{off} y k_{on} corresponden a las constantes de disociación/asociación fármaco-matriz. La droga que no interacciona con la matriz se regirá por la k_s, mientras que la droga que interacciona con esta se regirá por k_{off}. Con este modelo además puede calcularse la diferencia de energía libre entre la forma libre de fármaco y el unido, que corresponde a ΔG expresado en la **ecuación 3.2.** y que determinará el *efecto burst* inicial:

$$\Delta G = -k_B T \ln\left(\frac{k_{on}}{k_{off}}\right) \qquad \textbf{Ecuación 3.2.}$$

k_B es la constante de Boltzmann y T la temperatura absoluta del sistema en grados Kelvin.

La **Tabla 3.2.** representa los parámetros estimados desde el ajuste cinético basado en la **ecuación 3.1.** en función del pH. Como puede observarse, a medida que disminuye el pH los valores de k_s, ΔG y k_{off} aumentan, indicando una mayor proporción de fármaco libre y una menor de interacción entre el fármaco y la matriz. Estos resultados podrían explicarse en función de las diferentes especies iónicas del fármaco a los diferentes pH, las cuales podrían interaccionar de modo diferente con la matriz.

Tabla 3.2. Parámetros estimados del ajuste cinético basado en la ecuación 3.1.

pH	K_{off} ($^{h-1}$)	K_s ($^{h-1}$)	ΔG(10^{-21} J)	R^2
7.4	0.002	0.121	2.71	0.997
6.5	0.011	0.155	4.19	0.996
5.5	0.067	0.435	19.15	0.999

Estudios antimicrobianos de los sistemas levofloxacino-andamio MGHA frente a E. coli y S. aureus

La actividad antimicrobiana *in vitro* de los andamios 3D MGHA conteniendo levofloxacino se ha realizado para determinar la efectividad del sistema frente a una suspensión bacteriana de *S. aureus* (de la cepa colección ATCC 29213). *S. aureus* es una bacteria Gram negativa presente en osteomielitis severa, lo que justifica su utilización como modelo experimental para el presente estudio. Esta bacteria fue crecida hasta la alcanzar la fase exponencial (con un valor de densidad óptica de 1.0 u.a. a λ = 600 nm) en un medio de cultivo bacteriano Todd Hewitt Broth (THB, Sigma-Aldrich, USA), a 37ºC y en condiciones de agitación orbital a 200 r.p.m durante toda la noche. Transcurrido el tiempo, la suspensión bacteriana se centrifugó a 3500 r.p.m., lavándose 3 veces el pellet con PBS y posteriormente resuspendiéndose en PBS hasta alcanzar una densidad óptica de 0.5 MACFARLAM que corresponde a una concentración de *S.*

aureus de 10^8 CFU. Una vez calculada la concentración bacteriana, los andamios MGHA con levofloxacino se incubaron en 15 mL de PBS conteniendo $6x10^5$ bacterias/mL a 37ºC en agitación orbital (200 r.p.m.). Diariamente, se renovó el medio bacteriano siguiendo este mismo procedimiento y recogiendo previamente el líquido incubado. Con el fin de determinar la efectividad del sistema, se ha realizado un estudio directo sobre la superficie del andamio mediante la tinción de la superficie y estudio por microscopia confocal **(Figura 3.7.)** y se ha determinado la cantidad de bacterias presentes en el fluido.

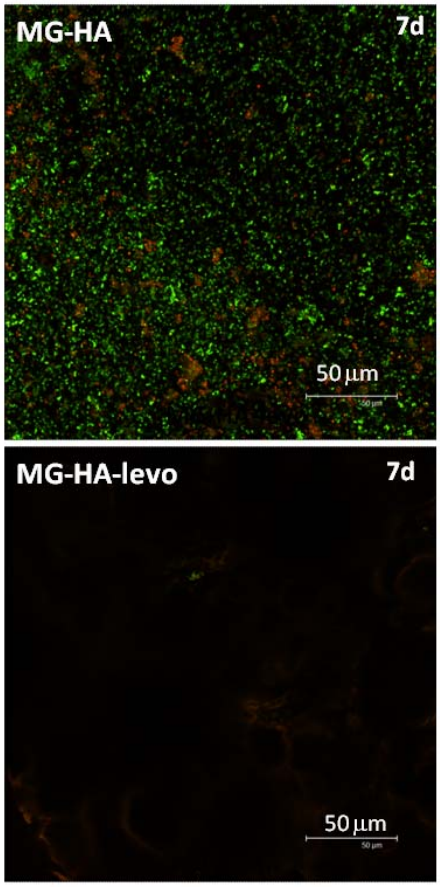

Figura 3.7. Imágenes por microscopia de confocal mostrando la superficie del los andamios 3D MGHA sin y con levofloxacino cargado, tras 7 días de ensayo antimicrobiano con *S. aureus.*

Para determinar la cantidad de bacterias presentes en el líquido se realizó un recuento en agar de las unidades formadoras de colonias (CFU) de las bacterias

adheridas al andamio. Con este propósito, durante un período de 16 días, 0.1 mL de la suspensión bacteriana en presencia del material se sembraron en placas de agar que fueron cultivadas a 37ºC durante 24 horas. La aparición de CFU sobre el agar indicó la pérdida de efectividad de la matriz. Por el contrario, las placas que no presentaban crecimiento bacteriano indicaban la efectividad del material conteniendo el levofloxacino. La actividad antimicrobiana de levofloxacino se evaluó en el rango de 30 μg/mL a 0.02 μg/mL, obteniéndose un valor de CMI de 0.06 μg /mL.

Estudios de biocompatibilidad de los sistemas levofloxacino-andamio MGHA con osteoblastos

Para comprobar la ausencia de posibles efectos citotóxicos del levofloxacino liberado desde los andamios MGHA sobre células óseas, se han realizado estudios de biocompatibilidad con osteoblastos humanos Saos-2 tratados 24 horas con extractos procedentes de dichos andamios tras incubación en 15 ml de DMEM durante 3 y 24 h a pH 7.4. Como parámetros de biocompatibilidad se han evaluado ciclo celular, viabilidad, apoptosis, proliferación y contenido intracelular de especies reactivas de óxigeno (ROS). Los métodos utilizados se describen en el **ANEXO II**.

La **Figura 3.8.** muestra los resultados obtenidos tras analizar el ciclo celular de osteoblastos Saos-2 tratados con el medio que contiene la dosis de levofloxacino liberada a las 3 h y 24 h desde los andamios MGHA impregnados con el fármaco.

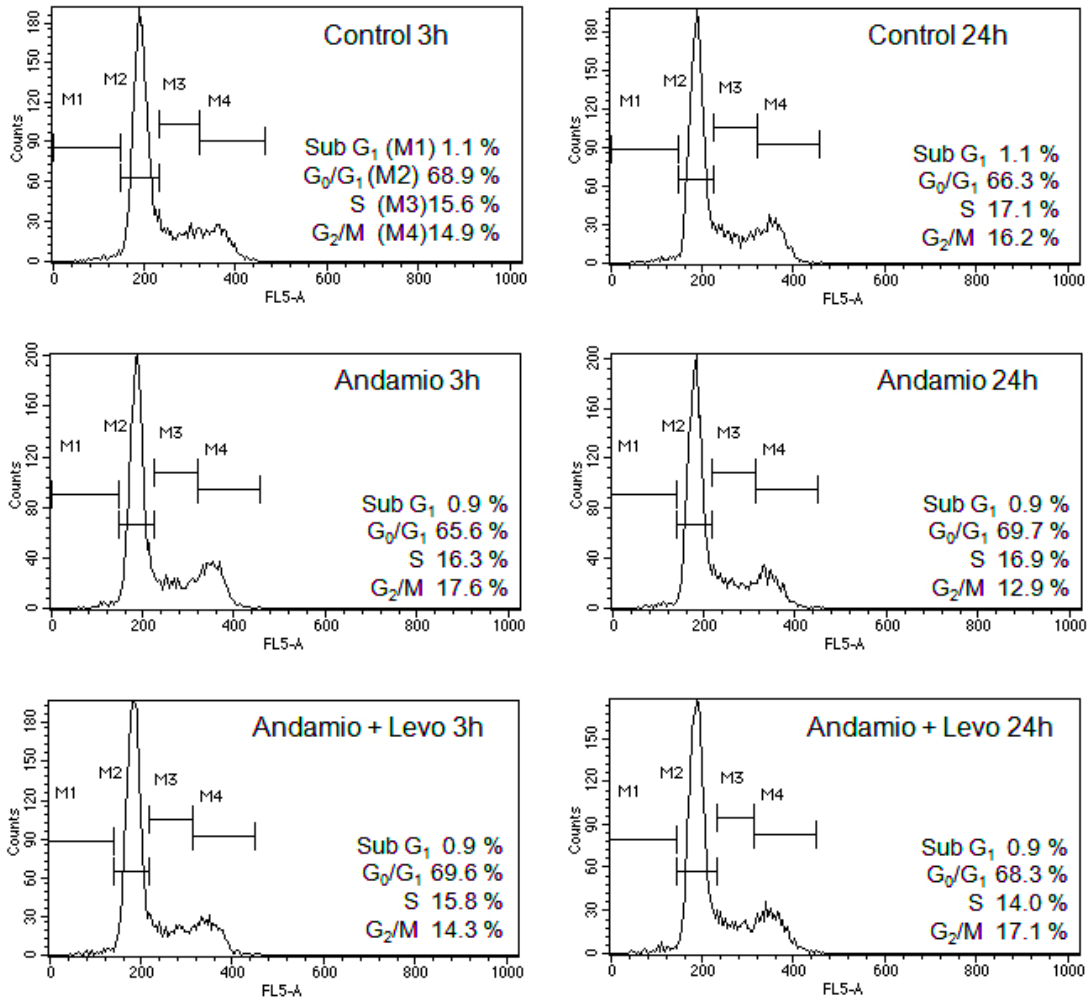

Figura 3.8. Efecto de la dosis de levofloxacino liberado a las 3 y 24 h sobre el ciclo celular de osteoblastos Saos-2.

Los resultados indican que la dosis de levofloxacino liberada desde los andamios MGHA a las 3 h y 24 h no altera el ciclo celular de osteoblastos Saos- 2.

La **Tabla 3.3.** muestra los valores de viabilidad y apoptosis obtenidos tras el tratamiento de osteoblastos Saos-2 con extractos de andamios MGHA cargados con levofloxacino tras 3 h y 24 h de liberación.

Tabla 3.3. Efecto de la dosis de levofloxacino liberado a las 3 y 24 h sobre los porcentajes de viabilidad y apoptosis de osteoblastos Saos-2.

Parámetro celular	3 horas			24 horas		
	Control	Andamio	Andamio + Levo	Control	Andamio	Andamio + Levo
Viabilidad (%)	97.7 ± 4.9	96.7 ± 4.8	97.2 ± 4.9	92.6 ± 4.6	95.8 ± 4.8	94.1 ± 4.7
Apoptosis (%)	1.1 ± 0.1	0.9 ± 0.04	0.9 ± 0.04	1.1. ± 0.1	0.9 ± 0.04	0.9 ± 0.04

No se observan alteraciones significativas en los porcentajes de viabilidad celular ni en los de apoptosis, con respecto a la muestra control. Estos resultados indican que la dosis de levofloxacino liberada en los tiempos estudiados no es citotóxica, ya que no produce muerte celular.

Para evaluar el efecto sobre la proliferación y el posible estrés oxidativo inducido sobre los osteoblastos por la dosis de fármaco liberado a partir de los andamios MGHA, se analizaron el número de células y la concentración intracelular de ROS tras el tratamiento con extractos de 24 h, al ser mayor la dosis liberada a este tiempo. Los resultados obtenidos (**Tabla 3.4.**) indican que a pesar de que la dosis de levofloxacino liberada desde andamios MGHA-levo no es citotóxica en ninguno de los tiempos estudiados, existe un retraso significativo ($p < 0.05$) en la proliferación de osteoblastos tras ser cultivados en presencia de extractos de 24h con respecto a los cultivados con extractos sin fármaco y a la muestra control. Por otra parte, los resultados indican que la dosis de levofloxacino liberada a 24 h no produce diferencias significativas en el contenido de ROS en comparación con la muestra control, confirmando que dicha dosis no induce estrés oxidativo sobre los osteoblastos.

Tabla 3.4. Efecto de la dosis de levofloxacino liberado a las 24 h sobre la proliferación y el contenido de ROS de osteoblastos Saos-2.

Parámetro celular	24 horas		
	Control	Andamio	Andamio + Levo
Proliferación (nº células x 10^{-3})	1158 ± 53	1194 ± 54	810 ± 37
ROS (u.a.)	2171 ± 108	2028 ± 101	2037 ± 101

Los datos obtenidos confirman la biocompatibilidad de los andamios MGHA impregnados con el antibiótico levofloxacino.

Todos los resultados presentados en esta sección permiten concluir que los andamios del *nanocomposite* MGHA cargados con levofloxacino por el método de impregnación muestran una liberación sostenida en el tiempo a pH fisiológico (pH 7.4), la cual es pH dependiente. Dichos perfiles se han ajustado a un único modelo cinético que combina tanto los procesos de difusión del fármaco en la matriz como la interacción del fármaco con la matriz. En los estudios realizados a pH 7.4, 6.7 y 5.5, los resultados obtenidos muestran una liberación más rápida y progresiva a medida que disminuye el pH. Este efecto se basa en una considerable disminución de las interacciones fármaco/ matriz a los pH 5.5. y 6.7, los cuales son característicos de un proceso de infección. Los estudios de efectividad frente a *S. aureus* muestran una actividad antimicrobiana de estos sistemas durante prolongados periodos de tiempo. Asimismo, los estudios de biocompatibilidad *in vitro* con células osteoblásticas tratadas con los extractos procedentes de andamios conteniendo levofloxacino a diferentes tiempos no han mostrado ningún efecto citotóxico de estos sistemas.

3.4. Bibliografía

[1] Williams DF. On the mechanisms of biocompatibility. Biomaterials 2008, 29, 2941-53.

[2] D. Campoccia, L. Montanaro, C.R. Arciola. The significance of infection related to orthopedic devices and issues of antibiotic resistance. Biomaterials 2006, 27, 2331-2339.

[3] D. Campoccia, L. Montanaro, C.R. Arciola. A review of the clinical implications of anti-infective biomaterials and infection-resistant surfaces. Biomaterials 2013, 34, 8018-8029.

[4] J. Vila, A. Soriano, J. Mensa. Molecular basis of microbial adherence to prosthetic materials. Role of biofilms in prosthesis-associated infection. Enferm Infecc Microbiol Clin 2008, 26, 48-54.

[5] EM. Hetrick, MH. Schoenfisch. Reducing implant-related infections: active release strategies. Chem Soc Rev 2006, 35, 780-789.

[6] KC. Dee, A. Puleo, R. Bizios. An introduction to tissue-biomaterial interactions. New York: Wiley-Liss, 2002.

[7] C. R. Arciola, D. Campoccia, P. Speziale, L. Montanaro, J. W. Costerton. Biofilm formation in *Staphylococcus* implant infections. A review of molecular mechanisms and implications for biofilm-resistant materials. Biomaterials 2012, 33, 5967-5982.

[8] P. D. Fey, M. E. Olson. Current concepts in biofilm formation of *Staphylococcus epidermidis*. Future Microbiol 2010, 5, 917-933.

[9] D. R. Monteiro, L. F. Gorup, A. S. Takamiya, A. C. Ruvollo-Filho, E. R. de Camargo, D. B. Barbosa. The growing importance of materials that prevent microbial adhesion: antimicrobial effect of medical devices containing silver. Int J Antimicrob Agents 2009, 34, 103-110.

[10] C. C. de Carvalho. Biofilms: recent developments on an old battle. Recent Pat Biotechnol 2007, 1, 49-57.

[11] D. T. Tsukayama, R. Estrada, R. B. Gustilo. Infection after total hip arthroplasty. A study of the treatment of one hundred and six infections. J Bone Joint Surg Am 1996, 78, 512-523.

[12] L. Montanaro, P. Speziale, D. Campoccia, S. Ravaioli, I. Cangini, G. Pietroloca, S. Giannini, C. R. Arciola. Scenary of *Staphylococcus* implant infections in orthopedics. Future Microbiol 2011, 6, 1329-1349.

[13] Y. Bustanji, C. R. Arciola, M. Conti, E. Mandello, L. Montanaro, B. Samorí. Dynamics of the interaction between a fibronectin molecule and a living bacterium under mechanical force. Proc Natl Acad Sci USA 2003, 100, 13292-13297.

[14] C. R. Arciola, Y. Bustanji, M. Conti, D. Campoccia, L. Baldassarri, B. Samori, L. Montanaro. Staphylococcus epidermidis-fibronectin binding and its inhibition by heparin. Biomaterials 2003, 24, 3013-3019.

[15] P. Speziale, G. Pietrocola, S. Rindi, M. Provenzano, G. Provenza, A. Di Poto, L. Visai, C. R. Arciola. Structural and functional role of *Staphylococcus aureus* surface components recognizing adhesive matrix molecules of the host. Future Microbiol 2009, 4, 1337-1352.

[16] O.C. Farokhzad, R. Langer. Impact of nanotechnology on drug delivery. ACS Nano, 2009, 3, 51-59.

[17] J.M. Rosenholm, C. Sahlgren, M. Linden. Towards multifunctional, targeted drug delivery systems using mesoporous silica nanoparticles-opportunities & challenges. Nanoscale 2010, 2, 1870-1883.

[18] M. Vallet-Regí, E. Ruiz-Hernández. Bioceramics: from bone regeneration to cancer nanomedicine. Adv. Mater. 2011, 23, 5177-5218.

[19] T. Yanagisawa, T. Shimizu, K. Kuroda, C. Kato. The preparation of alkyltrimethylammonium–kanemite complexes and their conversion to microporous materials. Bull. Chem. Soc. Jpn. 1990, 63, 988-992.

[20] C.T. Kresge, M.E. Leonowicz, W.J. Roth, J.C. Vartuli, J.S. Beck. Ordered mesoporous molecular sieves synthesized by a liquid-crystal template mechanism. Nature 1992, 359, 710-712.

[21] M. Vallet-Regí, A. Rámila, R.P. del Real, J. Pérez-Pariente. A new property of MCM-41: Drug Delivery System. Chem. Mater. 2001, 13, 308-311.

[22] B. G. Trewyn, S. Giri, I. I. Slowing, V. S.-Y. Lin. Mesoporous silica nanoparticle based controlled release, drug delivery, and biosensor systems. Chem. Commun. 2007, 31, 3236-3245.

[23] K. Ariga, A. Vinu, J.P. Hill, T. Mori. Coordination chemistry and supramolecular chemistry in mesoporous nanospace. Coord. Chem. Rev. 2007, 251, 2562-2591.

[24] C.-Y. Lai, B.G. Trewyn, D.M. Jeftinija, K. Jeftinija, S. Xu, S. Jeftinija, V. S.-Y. Lin. A mesoporous silica nanosphere-based carrier system with chemically removable

CdS nanoparticle caps for stimuli-responsive controlled release of neurotransmitters and drug molecules. J. Am. Chem. Soc. 2003, 125, 4451-4459.

[25] A. L. Doadrio, E. M. B. Sousa, J. C. Doadrio, J. Pérez-Pariente, I. Izquierdo-Barba, M. Vallet-Regí. Mesoporous SBA-15 HPLC evaluation for controlled gentamicin drug delivery. J. Control Release, 2004, 97, 125-132.

[26] M. Vallet-Regí, F. Balas, D. Arcos. Mesoporous Materials for Drug Delivery. Angew. Chem. Int. Ed. 2007, 46, 7548-7558.

[27] F. Qu, G. Zhu, H. Lin, J. Sun, D. Zhang, S. Li, S. Qiu. Drug Self-Templated Synthesis of Ibuprofen/Mesoporous Silica for Sustained Release. Eur. J. Inorg. Chem. 2006, 19, 3943-3947.

[28] Y-H. Son, M. Park, Y. B. Choy, H.R. Choy, D.S. Kim, K.C. Park, J-H. Choy. One-pot synthetic route to polymer–silica assembled capsule encased with nonionic drug molecule. Chem. Commun. 2007, 2799-2801.

[29] C. Charnay, S. Bqu, C. Tourné-Péteilh, L. Nicole, D. A. Lerner, J.M. Devoisselle. Inclusion of ibuprofen in mesoporous templated silica: drug loading and release property. Eur. J. Pharm. Biopharm. 2004, 57, 533-540.

[30] Q. Ji, M. Miyahara, J.P. Hill, S. Acharya, A. Vinu, S.B. Yoon, J.-S. Yu, K. Sakamoto, K. Ariga, J. Am. Chem. Soc. 2008, 130, 2376.

[31] M. Colilla, I. Izquierdo-Barba, M. Vallet-Regí. Novel biomaterials for drug delivery. Expert Opin. Ther. Patents 2008, 18, 639-656.

[32] M. Manzano, M. Vallet-Regí. New developments in ordered mesoporous materials for drug delivery. J. Mater. Chem. 2010, 20, 5593-5604.

[33] D. Campoccia, L. Montanaro, P. Speziale, C.R. Arciola. Antibiotic-loaded biomaterials and the risk for the spread of antibiotic resistance following their prophylactic and therapeutic clinical use. Biomaterials 2010, 31, 6363-6377.

[34] M. Vallet-Regí, M. Colilla, B. González. Medical application of organic-inorganic hybrid materials within the field of silica-based bioceramics. Chem. Soc. Rev. 2011, 40, 596-607.

[35] S-H. Wu, Y. Hung, C-Y. Mou. Mesoporous silica nanoparticles as nanocarriers. Chem. Commun. 2011, 47, 9972-9985.

[36] M. Vallet-Regí, M. Manzano, J.M. González-Calbet, E. Okunishid. Evidence of drugs confinement into silica mesoporous matrices by Stem CS Corredted Microscopy. Chem. Commun. 2010, 46, 2956 - 2958.

[37] C. Gao, I. Izquierdo-Barba, I. Nakase, S. Futaki, J. Ruan, K. Sakamoto, Y. Sakamoto, K. Kuroda, O. Terasaki, S. Che. Mesostructured silica based delivery system for a drug with a peptide as a cell-penetrating vector. Microporous Mesoporous Mater. 2009, 122, 201-207.

[38] R.N. Greenberg, M.T. Newman, S. Shariaty, R.W. Pectol. Ciprofloxacin, lomefloxacin or levofloxacin as treatment for chronic osteomyelitis. Antimicrob. Agents Chemother. 2000, 44, 164–166.

[39] H. A. Okerin, I. M. Arhewoh. Analytical profile of fluoroquinolone antibacterials I. Ofloxacin. Africa J. Biotech 2008, 7, 670-680.

[40] Y. Wang, W.R.G. Baeyens, C. Huang, G. Fei, L. Hem, J. Ouyang. Enhanced separation of seven quinolones by capillary electrophoresis with silica nanoparticles as additive. Talanta 2009, 77, 1674-1667.

[41] S. Pavlukhina, Y. Lu, A. Patimetha, M. Libera, S. Sukhishvili. Polymer multilayers with pH-triggered release of antibacterial agents. Biomacromolecules 2010, 11, 3448–3456.

[42] K.-T. Peng, C.-F. Chen, I.M. Chu, Y.-M. Li, W.-H. Hsu, R.W.-W. Hsu, P.-J. Chang. Treatment of osteomyelitis with teicoplanin-encapsulated biodegradable thermosensitive hydrogel nanoparticles. Biomaterials 2010, 31, 5227–5236.

[43] S. Sirivisoot, R. Pareta, T.J. Webster. Electrically controlled drug release from nanostructured polypyrrole coated on titanium. Nanotechnology 2011, 22, 8: 08510, ISSN 09574484.

[44] B.B. Md. Systemic response to inflammation. Nutr. Rev. 2007, 65, S170–S172.

[45] L. Marnell, C. Mold, T.W. Du Clos. C-reactive protein: ligands, receptors and role in inflammation. Clin. Immunol. 2005, 117, 104–111.

[46] A.C. Issekutz, S. Bhimji. Role for endotoxin in the leukocyte infiltration companying *Escherichia coli* inflammation. Infect. Immun. 1982, 36, 558–566.

[47] L. Ma, M. Liu, H. Liu, J. Chen, D. Cui. *In vitro* cytotoxicity and drug release properties of pH- and temperature-sensitive core-shell hydrogel microspheres. Int. J. Pharm. 2009, 385,86–91.

[48] P. Loïc, A. Gilles, J. Cédric, B. Brouillaud, V. Héroguez, M. C. Durrieu. pH-controlled delivery of gentamicin sulfate from orthopedic devices preventing nosocomial infections. Journal of Controlled Release 2012, 162, 373–381.

[49] T. Higuchi. Mechanism for sustained-action medication. J Pharm Sci 1963, 52, 1145-1147.

[50] M. Vallet-Regí, F. Balas, M. Colilla, M. Manzano. Bioceramics and pharmaceuticals: a remarkable synergy. Prog Solid State Chem 2007, 9, 768-776.

[51] L. Zeng, L. An, X. Wu. Modeling Drug-Carrier Interaction in the Drug Release from Nanocarriers. Journal of Drug Delivery, 2011, Article ID 370308, 15 pages. doi:10.1155/2011/370308.

Conclusiones

Conclusions

CONCLUSIONES

Capítulo 1

En la presente Tesis Doctoral se ha llevado a cabo la síntesis, caracterización y evaluación de un nuevo material *nanocomposite* denominado MGHA, formado por un vidrio mesoporoso en el sistema SiO_2-CaO-P_2O_5 con nanopartículas de apatita nanocristalina embebidas homogéneamente en las paredes del vidrio mesoporoso.

La síntesis de este nuevo material se basa fundamentalmente en el proceso de preparación de vidrios mesoporosos con dos modificaciones específicas: (i) aceleración de la formación sol-gel de la apatita mediante acidificación del sistema y (ii) utilización del surfactante *F127* el cual, además de actuar como agente director de la estructura, ejerce una acción de estabilización del sistema permitiendo una incorporación homogénea de las nanopartículas de apatita dentro de las paredes de naturaleza amorfa del vidrio mesoporoso.

La incorporación de estas nanopartículas no afecta a las propiedades texturales y estructurales del vidrio mesoporoso ni a su comportamiento bioactivo. Asimismo, la presencia de apatita nanocristalina incrementa la biocompatibilidad del material y estimula notablemente la proliferación celular.

Capítulo 2

Este nuevo material *nanocomposite* ha sido conformado por la técnica de prototipado rápido (*robocasting*) en andamios 3D de porosidad jerarquizada e interconectada con posible aplicación en regeneración tisular ósea. Dichos andamios presentan: (i) una red ordenada de macroporos de un diámetro de 500 μm, consecuencia del diseño asistido por ordenador en formato CAD de la propia técnica de *robocasting*; (ii) macroporos en el rango de 30-80 μm con interconexiones de 1-10 μm, originados durante la eliminación por calcinación del polímero biomacromolecular metilcelulosa utilizado en la preparación de estos andamios como agente estabilizador de la “pasta precursora” (iii) mesoporos ordenados con diámetro de 10 nm derivados de la eliminación del surfactante *F127* como agente director de la mesoestructura.

Los estudios realizados *in vitro* con preosteoblastos cultivados sobre andamios MGHA indican una adecuada adhesión, proliferación y diferenciación celular, además de la colonización de toda la superficie útil del andamio 3D por este tipo celular.

El estudio de la interacción de andamios MGHA con células primarias de bazo de ratón implicadas en la respuesta inmune ha demostrado que dichos andamios no producen alteraciones significativas en la activación *in vitro* de macrófagos, linfocitos B, linfocitos T ni células *natural killer* cuando estas subpoblaciones se utilizaron como modelo experimental. Estos resultados ponen de manifiesto la excelente biocompatibilidad de los andamios MGHA y permiten predecir una adecuada respuesta de los tejidos adyacentes después de su implantación *in vivo*.

La aminopropil-funcionalización de la superficie de los andamios MGHA mejora notablemente la adhesión, proliferación (2.3 veces superior) y diferenciación (4.8 veces superior) de preosteoblastos, así como la colonización celular en toda la superficie del soporte. Estos resultados son consecuencia de la participación de los grupos amino en la etapa temprana de la adhesión celular caracterizada por la adsorción inespecífica de proteínas, al igual que ocurre con secuencias peptídicas de adhesión (tipo RGD) ampliamente utilizadas en la "biodecoración" de la superficie de andamios. Este sencillo y efectivo proceso de amino funcionalización de andamios MGHA podría ser una alternativa encaminada a la mejora de las propiedades superficiales de andamios con aplicación en ingeniería tisular ósea.

Capítulo 3

Las características mesoestructurales del material *nanocomposite* MGHA permiten la incorporación y posterior liberación local de agentes antimicrobianos para la prevención y tratamiento de posibles procesos de infección derivados de los implantes.

Estudios comparativos de las diferentes metodologías de carga de agentes antimicrobianos en materiales mesoestructurados como la impregnación (IP) y la carga de fármaco asistido por surfactante (One-Pot, OP) han puesto de manifiesto: (i) el papel crítico del proceso de calcinación de estas matrices, ya que no solo implica la eliminación del surfactante y de los reactivos sino también cambios sustanciales

(detectables a nivel celular) en el entorno local de la red de sílice; (ii) diferentes repuestas celulares a estas matrices dependiendo del tipo celular (osteoblastos y fibroblastos) evidenciando que las células podrían detectar pequeños cambios en el entorno local de sílice y la presencia de etanol residual; (iii) similares perfiles de liberación de levofloxacino acorde a un modelo de difusión de Higuchi; (iv) efectividad antimicrobiana del levofloxacino liberado desde ambas matrices basadas en las diferentes metodologías estudiadas. Los resultados obtenidos en los estudios de biocompatibilidad ponen de manifiesto la necesidad de un riguroso control en el diseño de este tipo de matrices para la liberación controlada de fármacos dependiendo de su aplicación biomédica y de los tipos celulares con los que vayan a entrar en contacto.

Los andamios del *nanocomposite* MGHA cargados con levofloxacino por el método de impregnación muestran una liberación sostenida en el tiempo a pH fisiológico (pH 7.4) siguiendo un modelo simple que combina los procesos de difusión con las interacciones existentes entre fármaco y matriz. Esta liberación es pH-dependiente, presentado un incremento en sus cinéticas a pH 5.5. y 6.7, valores característicos de un proceso de infección.

La actividad antimicrobiana de los andamios MGHA con levofloxacino frente a *S. aureus* y *E. coli* demuestra una excelente efectividad prolongada durante 10 días.

Estudios de biocompatibilidad de los andamios MGHA cargados con levofloxacino no muestran ningún efecto citotóxico sobre osteoblastos Saos-2, incluso en los tiempos en los cuales se ha liberado la mayor dosis de fármaco.

CONCLUSIONS

Chapter 1

In the present Ph.D. Thesis the synthesis, characterization and evaluation of a new *nanocomposite* material denoted MGHA has been carried out. This new material is formed by a mesoporous glass in the SiO_2-CaO-P_2O_5 system with nanocrystalline apatite nanoparticles embedded homogeneously in the walls of mesoporous glass.

The synthesis of this new material was based mainly on the process of preparation of mesoporous glasses with two specific modifications: (i) acceleration of the sol-gel formation of apatite by acidification of the system and (ii) the use of surfactant *F127* which, besides acting as structure directing agent, has an action to stabilize the system allowing a homogeneous introduction of apatite nanoparticles within the walls of amorphous nature of the mesoporous glass.

The incorporation of these nanoparticles does not affect the textural and structural properties of mesoporous bioactive glass or its behaviour. The presence of nanocrystalline apatite also increases the material biocompatibility and stimulates significantly cell proliferation.

Chapter 2

This new *nanocomposite* material has been shaped by rapid prototyping technique (*robocasting*) in 3D scaffolds with hierarchical and interconnected porosity for possible application in bone tissue regeneration. These scaffolds have: (i) an ordered network of macropores with a diameter of 500 μm, due to the computer-aided design in CAD format of the *robocasting* own technique, (ii) macropores in the range of 30-80 μm with interconnections in the range of 1-10 μm, produced after calcination in order to remove the methylcellulose used in the preparation of these scaffolds as stabilizing agent of the precursor slurry (iii) ordered mesopores with a diameter of 10 nm, produced after removal of the surfactant *F127* as the mesostructure-directing agent.

In vitro studies with preosteoblasts cultured on MGHA scaffolds indicate adequate adhesion, proliferation and differentiation, in addition to the colonization of the entire useful surface of the 3D scaffold for this cell type.

The study of MGHA scaffold interaction with mouse spleen primary cells involved in the immune response has demonstrated that these scaffolds do not produce significant alterations on the *in vitro* activation of macrophages, B lymphocytes, T lymphocytes and *killer natural* cells, when these subpopulations were used as an experimental model. These results demonstrate the excellent biocompatibility of these scaffolds and predict an adequate response of adjacent tissues after implantation *in vivo*.

The aminopropyl surface functionalization of MGHA scaffolds notably improves adhesion, proliferation (2.3 fold), differentiation (4.8 fold) of preosteoblasts and cell colonization over the entire useful surface of the support. These improved results are due to the role of the amino groups in the early stage of cell adhesion, characterized by the nonspecific adsorption of proteins, as occurs with adhesion peptide sequences (RGD type), which are widely used in the "biodecoration" of the surface of the scaffolds. This simple and effective amino functionalization process of MGHA scaffolds could be an alternative aimed to improve the surface properties of scaffolds with applications in bone tissue engineering.

Chapter 3

The meso-structure features of MGHA *nanocomposite* material permit the incorporation and subsequent local release of antimicrobial agents for the prevention and treatment of infection processes caused by implants.

Comparative studies of different methodologies for loading antimicrobial agents in mesostructured materials as the impregnation method (IP) and the drug loading assisted by surfactant method (One -Pot, OP) have shown: (i) the critical role of the calcination process of these matrices, which does not involve only the removal of the surfactant and reactants but also produces substantial changes (detectable at cellular level) in the local environment of the silica network , (ii) different cellular responses to these matrices depending on cell type (osteoblasts and fibroblasts) showing that cells could detect

small changes in the local environment of silica and the presence of residual ethanol, (iii) similar levofloxacin release profiles according to Higuchi diffusion model, (iv) antimicrobial effectiveness of levofloxacin released from both matrices based on the studied methodologies. The biocompatibility results highlight the need of a rigorous control in the design of such matrices for controlled drug release depending on their biomedical application and on the cell types which will come into contact with the material.

MGHA *nanocomposite* scaffolds loaded with levofloxacin by impregnation method show a sustained release over time at physiological pH (pH 7.4) following a simple model which combines diffusion processes with interactions between drug and matrix. This release is pH-dependent, with an increase in their kinetics at pH 5.5. and 6.7, which are characteristic values of an infection process.

The antimicrobial activity of MGHA scaffolds loaded with levofloxacin against *S. aureus* and *E. coli* demonstrates an excellent prolonged effectiveness over 10 days.

Biocompatibility studies of MGHA scaffolds loaded with levofloxacin show no cytotoxic effects on osteoblasts Saos-2, even when the highest drug dose has been released.

Anexo I

ANEXO I. TÉCNICAS DE CARACTERIZACIÓN FISICOQUÍMICA DE MATERIALES

I.1. Difracción de Rayos-X (DRX)

Los perfiles de DRX para la caracterización estructural de los materiales se han obtenido utilizando un difractómetro Philips X'Pert Plus (Eindhoven, The Netherlands) con una fuente de radiación Cu Kα ($\lambda = 1.5406$ A, 40 kV, 20 mA). Para determinar el ordenamiento mesoporoso, los perfiles de DRX se midieron en el rango de 0.6º a 10.0º (2θ) con un paso de 0.02º (2θ) y un tiempo de análisis de 5 s. Para determinar el orden estructural a nivel atómico, los análisis se realizaron en el rango de 5.0º a 80.0º (2θ) con un paso de 0.02º (2θ) y un tiempo de análisis de 10 s.

I.2. Microscopía electrónica de transmisión (MET)

Las imágenes de microscopía electrónica de transmisión se han obtenido de un microscopio JEOL 3000 FEG con una tensión de aceleración de 300 kV (Cs 0.6 mm, resolución 1.7 A) el cual lleva acoplado un analizador de energía dispersiva de rayos X (EDS) Oxford LINK y un portamuestras goniométrico de doble inclinación hasta un máximo de ± 45º. Este microscopio está instalado en el Centro Nacional de Microscopía Electrónica de la Universidad Complutense de Madrid (UCM). Las imágenes se han registrado con una cámara CCD (Modelo MultiScan 794, Gatan, 1024 x 1024 píxeles, tamaño 24 µm x 24 µm) utilizando condiciones de baja dosis. El análisis y procesado de imágenes se han realizado a través del programa *Digital Micrograph* (Gatan). Para la preparación de las muestras, se molió una pequeña cantidad en un mortero de ágata y se dispersó mediante sonicación en etanol durante 5 minutos. A continuación, una gota de dicha suspensión se depositó sobre una rendija de cobre de 3 mm de diámetro recubierta con una película de polivinil-fornal sobre la que se ha depositado una película de carbono como soporte.

I.3. Microscopía electrónica de barrido (MEB)

La microscopía electrónica de barrido se ha realizado en un microscopio electrónico JEOL JSM-6335F (Tokio, Japón) con un voltaje de aceleración de 10 kV.

Este microscopio está instalado en el Centro Nacional de Microscopía Electrónica de la UCM. Los análisis de EDS se realizaron en un sistema Oxford acoplado al microscopio Pentafet 6335F. El portamuestras es un goniómetro que permite desplazamientos en todas las direcciones. Las muestras, bien en forma de polvo o fragmentos de piezas, se pegan a un portamuestras de cobre mediante una cinta de grafito, metalizándose el conjunto con una capa muy fina de oro mediante la técnica de *sputtering* a vacío. El espesor de esta capa, que permite la observación de muestras no conductoras, asegura suficiente conductividad de las muestras evitando que su superficie se cargue con electrones.

I.4. Porosimetría de adsorción de nitrógeno

Las propiedades texturales de los materiales se han caracterizado mediante análisis de adsorción/desorción de N_2 a -196ºC en un porosímetro Micromeritics ASAP 2020 (Micromeritics Co., Norcross, USA). Antes de cada medida, entre 100-150 mg de cada muestra en forma de polvo fueron desgasificadas durante 24 h a 200ºC con un vacío inferior a 10^{-8} bar. Las muestras cargadas con biomoléculas fueron desgasificadas durante 24 h a 37ºC para evitar la degradación de la materia orgánica por efecto de la temperatura. La superficie específica se ha determinado a partir de la ecuación BET (Brunauer-Emmett-Teller) en el rango de presiones relativas P/P_0 0.05 a 0.35. La distribución de tamaño de poro (*pore size distribution, PSD*) se ha calculado a partir de análisis de la rama de adsorción de las isotermas empleando el método BJH. La posición del máximo de la distribución se ha tomado como el diámetro de poro promedio (D_p). El volumen total de poro (V_T) se ha calculado empleando el método de un solo punto a P/P_0 = 0.99. El volumen de microporo (poro con diámetros < 2 nm) se ha calculado empleando el método *t* (*t-plot*).

I.5. Porosimetría por intrusión de mercurio

Las medidas de porosidad se realizaron en un porosímetro de mercurio de modelo Micromeritics Autopore IV 9500 (Micromeritics Instrument Corporation, Norcross, GA, USA). La técnica determina el volumen de mercurio forzado a entrar en los poros como una función de la presión, la cual está relacionada con el tamaño de poro mediante la ecuación de Washburn. En esta técnica , la muestra se coloca en un

recipiente impermeable. Para desgasificar la muestra, el recipiente con la muestra en su interior es sometido a vacío y rellenado con un volumen conocido de mercurio. A continuación, se aplica de forma progresiva presión al mercurio, produciéndose una intrusión gradual de mercurio en el medio poroso evacuado, seguida de una extrusión del mismo desde la estructura porosa a medida que la presión va disminuyendo. A baja presión el mercurio está forzado a penetrar en los canales porosos de gran diámetro de la muestra. Cuando la presión se aumenta, el mercurio penetra en los poros más pequeños. El volumen de mercurio introducido en la muestra es registrado junto con el valor de la presión aplicada. Estos valores describen la curva volumen de mercurio introducido frente a la presión aplicada. Estos datos experimentales se analizan mediante la ecuación de Washburn:

$$D = (1/P)\ \gamma\ 4\cos\varphi$$

donde D es el diámetro de poro, P es la presión aplicada, γ la tensión superficial y φ el ángulo de contacto. La curva volumen-presión puede convertirse, aplicando el modelo de poros adecuado, en volumen o área de poro frente a radio de poro.

I.6. Espectroscopia infrarroja con transformada de Fourier (IRTF)

Los espectros de infrarrojo con transformada de Fourier de muestras en estado sólido se han registrado entre 4000 y 300 cm^{-1} en un espectrómetro Thermo Nicolet Nexus 470 en el modo de transmisión empleando el método de pastilla con KBr. Las muestras se prepararon mezclando en un mortero de ágata 1 mg del material en forma de polvo con 250 mg de KBr como soporte inerte, comprimiéndose en forma de discos de 13 mm de diámetro mediante una prensa uniaxial a una presión de 50 MPa.

I.7. Espectroscopia de fluorescencia de Rayos-X (FRX)

Los análisis espectroscópicos de fluorescencia de rayos-X se han llevado a cabo en un espectofotómetro Philips PANalytical Aχios, que emplea como fuente de rayos X un cátodo de rodio, utilizándose la radiación de la línea Rh kα (λ = 0.6139 A). Este equipo emplea dos cristales monocromadores, uno de LiF y otro de wolframio, que

discriminan la señal de rayos X emitida por la muestra en función de su energía. El análisis se limita a los elementos cuyo número atómico, Z, sea mayor a 6 (a partir del boro). Las muestras se comprimieron en forma de discos de 13 mm de diámetro mediante una presión uniaxial de 0.5 MPa y se depositaron sobre ácido bórico. Para la medida se han empleado portamuestras de aluminio con máscaras de 10 nm de diámetro.

I.8. Espectroscopia de energía dispersiva de rayos X (EDX)

El espectro de rayos X emitido por un material bajo el impacto de un haz de electrones focalizado contiene información relativa a la composición del sólido. Una parte de los electrones incidentes excita los átomos de la muestra, los cuales emiten sus radiaciones características, que son recogidas y analizadas por el espectrómetro de rayos X. El resto de los electrones son retrodispersados por la muestra sin pérdida apreciable de energía. La retrodispersión es proporcional al número atómico, siendo menor para los elementos cuyo número atómico es menor. La variación de la fracción del número atómico se utiliza para determinar la variación de la composición de la muestra.

Los análisis se han realizado en un sistema *Oxford Pentafet* acoplado a un microscopio de transmisión JEOL 3000 FEG. El análisis se limita a los elementos cuyo número atómico, Z, sea mayor que 12 (a partir del sodio), aunque existen ciertos tipos de ventanas de detección especiales (ATW) que permiten determinar la concentración de elementos ligeros (a partir del boro). Para una determinación cuantitativa es necesario aplicar correcciones de fluorescencia, absorción y eficiencia de detección así como una comparación con estándares conocidos.

I.9. Resonancia Magnética Nuclear de ^{29}Si, ^{31}P y ^{13}C (RMN)

El fenónemo de resonancia magnética nuclear se basa en la interacción de los momentos magnéticos de los núcleos con un campo magnético externo, lo que produce la separación de los niveles de energía asociados a las diferentes orientaciones de los momentos magnéticos respecto al campo magnético. La variación de la frecuencia de resonancia del núcleo se conoce como desplazamiento químico y es característica del entorno químico del núcleo.

La aplicación de la caracterización por RMN en materiales mesoporosos ha sido posible gracias al desarrollo de las técnicas RMN de sólidos, rotación de ángulo mágico (MAS-RMN) y polarización cruzada (CP-RMN). MAS-RMN permite reducir al mínimo la anchura de las bandas del espectro debida a las interacciones dipolares y cuadrupolares y a las anisotropías asociadas al desplazamiento químico. Consiste en la rotación rápida de la muestra entorno a un eje inclinado con un ángulo de 54º44'´respecto a la dirección del campo magnético externo. La técnica CP-RMN mejora la relación señal/ruido del espectro de núcleos con abundancia natural baja sin afectar a la resolución del espectro.

La espectroscopía ^{29}Si RMN proporciona información estructural de los materiales y permite determinar la proporción de unidades organosiloxano así como la relación de especies condensadas y no condensadas. Los centros silíceos tetrafuncionales se han nombrado con la notación convencional Q^n don Q se refiere a las especies siloxano [$Si(OSi)_n(OH)_{4-n}$], siendo n = 2-4 el número de átomos de oxígeno puente que rodean al átomo de silicio central. Las unidades estructurales Q^4 representas tetraedros SiO_4 interconectados que forman parte de las paredes de sílice. Las unidades Q^3 están asociadas con grupos Si-OH aislados tanto libres como unidos por enlace de hidrógeno. Las unidades Q^2 corresponden a grupos silanol germinales. Los espectros de resonancia magnética de estado sólido de ^{29}Si permiten analizar el entorno químico de los átomos de silicio así como el grado de funcionalización alcanzado. La técnica de polarización cruzada ^{29}Si CP MAS RMN aumenta la sensibilidad en la detección de los átomo de silicio próximos a protones y puede emplearse para estimar de manera cuantitativa los grupos Si-OH en superficie. Para obtener información cuantitativa a partir de espectros CP mediante deconvolución de la región espectral Q de los espectros experimentales en bandas gaussianas individuales Q^4, Q^3, Q^2, es preciso controlar el tiempo de contacto durante el que se transfiere polarización del núcleo ^{1}H al núcleo ^{29}Si y llevar a cabo todos los espectros en las mismas condiciones. La cantidad de grupos silanol por mol de sílice se ha calculado a partir de la siguiente ecuación:

$$[\mathrm{SiOH}] = \frac{(2 \times \%Q^2) + \%Q^3}{\Sigma(\%Q^i \times EMW_Q)}$$

donde [SiOH] es la concentración de grupos silanol expresada en mol/g y $\%Q^i$ representa la población relativa de especies Q^i (Q^4, Q^3, Q^2). El peso molecular efectivo

de cada especie (EMW_Q) se define como la suma del peso molecular de los átomos que contribuyen a cada especie, contando con que en los enlaces siloxano (Si-O-Si), los átomos de oxígeno que conectan especies se cuentan como medio.

Los experimentos de resonancia magnética nuclear de ^{29}Si y ^{31}P tanto polarización cruzada (CP) como rotación de ángulo mágico (MAS) se realizaron en un espectrómetro Bruker AV-400-WB a 79.49 y 161.97 MHz para ^{29}Si y ^{31}P, respectivamente. La velocidad de giro fue de 10 kHz para el ^{29}Si y de 6 kHz para el ^{31}P. Tetrametilsilano (TMS) y 85% de H_3PO_4 fueron utilizados como estándar para las medidas ^{29}Si y ^{31}P, respectivamente. Los espectros se registraron con un tiempo de contacto de 1 ms. El período de tiempo entre las sucesivas acumulaciones fue de 5 y 4 s para las medidas ^{29}Si y ^{31}P, respectivamente.

Los experimentos de resonancia magnética nuclear de ^{13}C se realizaron en un espectrómetro Bruker 200 RMN a 75.45 MHz. La velocidad de giro fue de 12 kHz. El período de tiempo entre las sucesivas acumulaciones fue de 3 ms.

I.10. Análisis termogravimétrico y térmico diferencial (TGA/DTA)

El TGA da una medida cuantitativa de la ganancia o pérdida de peso de un material en función de la temperatura y se puede llevar a cabo en distintas atmósferas de trabajo. El DTA mide cambios de energía, es decir, si un proceso es endotérmico o exotérmico con respecto a una muestra de referencia. Los análisi TGA/DTA se han realizado en un equipo Perkin-Elmer Diamond entre 30 y 1000ºC en un flujo constante de aire de 100 mL/min con una rampa de calentamiento de 10ºC/min. Las determinaciones se efectuaron en crisoles de platino.

I.11. Microanálisis elemental de C, H, N

La determinación del contenido de carbono, hidrógeno y nitrógeno de las muestras se ha realizado en un equipo LECO CHNS-932. El análisis se lleva a cabo mediante la combustión de la muestra en oxígeno y los gases resultantes (CO2, H2O y N2) se llevan a unas condiciones dadas de presión, temperatura y volumen. Los productos gaseosos se separan mediante una columna cromatográfica y se miden como

función de la conductividad térmica. Tras la calibración del equipo con patrones conocidos, la cuantificación se realiza en porcentaje en peso, empleando una técnica termogravimétrica.

I.12. Potencial zeta (ζ)

Las medidas de potencial ζ se realizaron en un equipo Malvern Zetasizer Nano Series acoplado a un valorador automático MPT-2. Se prepararon suspensiones de 10 mg de material en forma de polvo en 20 mL de una solución KCl 20 mM como electrolito soporte. Las curvas de potencial ζ se monitorizaron en el rango de pH de 2 a 10. El pH se ajustó añadiendo cantidades adecuadas de HCl o NaOH 0.01 M. Es interesante destacar que en el rango de pH estudiado la sílice es insoluble.

I.13. Elipsometría

La cantidad de proteína depositada sobre la superficie de las muestras fue determinada por elipsometría utilizando un Optrel Multiskop equipado con un láser de argon de 100 mW. Todas las medidas se llevaron a cabo a 532 nm, con un ángulo de incidencia de 67.66º en 5 mL de tampón bajo condiciones de agitación (300 rpm). Para monitorizar los cambios en el estado de polarización de la luz reflejada en una superficie, en ausencia y en presencia de una capa adsorbida, se ha obtenido el índice de refracción medio (*n*) y el espesor de la capa adsorbida (*d*). A partir del espesor de la capa y del índice de refracción, se obtiene la cantidad adsorbida (τ), acorde con la siguiente fórmula:

$$\Gamma = \frac{(n - n_0)}{\mathrm{d}n/\mathrm{d}c} d$$

donde n_0 es el índice de refracción de la solución, y *dn/dc* el aumento del índice de refracción (0.154 $cm^3\ g^{-1}$). Se han realizado rutinariamente correcciones para los cambios en el índice de refracción causados por los cambios en la temperatura y en la concentración excesiva de electrolitos.

Para la realización de las medidas experimentales por elipsometría se prepararon superficies de sílice hidrofílicas cargadas negativamente a partir de obleas de silicio

pulido tipo-p, dopadas con boro. Las superficies fueron limpiadas en una mezcla de 25% NH_4OH, 30% H_2O_2 y H_20 (1:1:5 volumen) a 80ºC durante 5 min, seguido de otra limpieza en una mezcla de 32% HCl, 30% H_2O_2 y H_2O (1:1:5 volumen) a 80ºC durante 5 min. A continuación, las obleas de silicio puro fueron lavadas dos veces con agua y etanol. Este procedimiento permitió obtener superficies hidrofílicas con un ángulo de contacto agua-aire menor de 10º. A continuación, el material fue depositado sobre estas obleas mediante el procedimiento *dip-coating*, con una velocidad de 2500 mm s^{-1}, utilizando un sol precursor envejecido durante 24h a temperatura ambiente. Finalmente, los recubrimientos se secaron a 100ºC durante 1h y posteriormente calcinados a 700ºC durante 1h para obtener el material sobre el que estudiar la adsorción de proteínas.

Anexo II

ANEXO II. TÉCNICAS DE CULTIVO Y EVALUACIÓN DE LA RESPUESTA CELULAR A BIOMATERIALES

II.1. Cultivo celular

El cultivo de tipos celulares específicos en presencia de los biomateriales permite evaluar *in vitro* el comportamiento de las células con las que van a entrar en contacto tras su implantación y constituye una etapa indispensable previa a la experimentación *in vivo*. El tipo celular elegido para los estudios *in vitro* dependerá de la aplicación para la que ha sido diseñado el biomaterial. Los estudios con cultivos celulares permiten un mayor grado de control y la valoración de numerosos parámetros celulares para conocer la respuesta que podría producirse *in vivo.*

En el presente trabajo se han realizado diferentes estudios con fibroblastos, preosteoblastos, osteoblastos, linfocitos T, linfocitos B, macrófagos y células *natural killer* para los que ha sido necesario el cultivo en diferentes condiciones de acuerdo a las necesidades y características de cada tipo celular, como se recoge en cada uno de los capítulos de la presente Tesis Doctoral. Los materiales ensayados se han puesto en contacto con las células en forma pulverizada, discos, andamios y extractos obtenidos a diferentes tiempos, realizando diferentes análisis relacionados con la adhesión, proliferación, diferenciación celular y citotoxicidad. El cultivo de células en presencia de biomateriales permite además analizar diferentes indicadores de su respuesta mediante técnicas de citometría de flujo y microscopía confocal (apartados **II.2.** y **II.3.**).

II.2. Citometría de flujo

La citometría de flujo es una herramienta de análisis que permite discriminar partículas microscópicas o células de diferente tamaño y con distinta fluorescencia. Esta técnica es ampliamente utilizada de forma rutinaria en muchos laboratorios clínicos y de investigación para medir y cuantificar propiedades fenotípicas, bioquímicas y/o moleculares de células individualizadas mediante la utilización de fluorocromos y sondas fluorescentes específicas de muy diversos parámetros celulares.

La principal característica de la citometría es que puede ofrecer de forma muy rápida un análisis multiparamétrico aportando información simultánea de distintas características de cada una de las partículas o células analizadas. Los parámetros analizables por citometría de flujo son: i) los asociados a la dispersión de luz que producen las partículas o células (*light scatter*) directamente relacionados con el **tamaño y la complejidad** y ii) las distintas **fluorescencias asociadas** a la partícula o célula. El análisis se realiza a velocidades de miles de células/segundo, lo que permite obtener datos de elevada fiabilidad estadística, así como identificar poblaciones representadas en baja frecuencia dentro de la población global. Otra importante característica de la citometría de flujo es que el análisis se realiza célula a célula de forma individualizada por lo que las células objeto de estudio deben encontrarse en suspensión. Finalmente, es importante destacar que existe una restricción respecto al tamaño de las partículas objeto de análisis, ya que éstas deben tener tamaños comprendidos entre las 0.5-100 μm. La **figura II.1.** representa un esquema del fundamento básico de la técnica citometría de flujo.

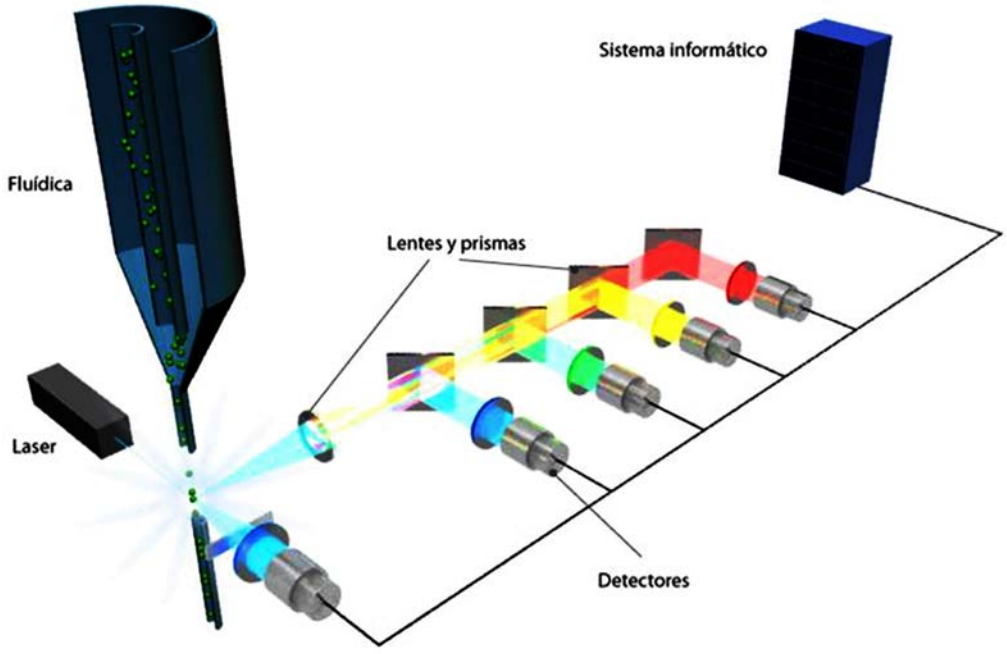

Figura II.1. Esquema del principio de la citometría de flujo. Imagen obtenida en biotechspain.com

Durante esta Tesis Doctoral, la citometría de flujo ha sido utilizada para el estudio del tamaño y la complejidad celular a partir de las propiedades de dispersión de luz *forward scatter* y *side scatter* respectivamente así como para el análisis de diferentes parámetros mediante la utilización de sondas fluorescentes específicas: INDO-1 AM para el estudio del contenido de calcio intracelular; yoduro de propidio para valorar la viabilidad celular; *Hoechst* 33258 para el estudio de la apoptosis y del ciclo celular y sonda DCFH/DA (2,7-diacetato de diclorofluoresceína) para la valoración del contenido de especies reactivas de oxígeno (ROS). Todos los parámetros han sido estudiados utilizando los citómetros de flujo LSR y FACScalibur de Becton Dickinson ubicados en el Centro de Citometría y Microscopia de Fluorescencia de la Universidad Complutense de Madrid (Centro de Asistencia a la Investigación UCM).

II.3. Microscopía confocal

El microscopio confocal emplea una técnica óptica de imagen que permite capturar planos o secciones ópticas de la muestra de forma que posteriormente se pueden reconstruir imágenes tridimensionales de ésta. Los principales elementos que definen a un microscopio confocal son el láser y el *pinhole* espacial (diafragma). El *pinhole* es una apertura localizada delante del fotomultiplicador que elimina la luz desenfocada o destellos de la lente, por lo que evita el paso de fluorescencia de las regiones de la muestra que no están en foco. La luz que proviene de regiones localizadas por encima o por debajo del plano focal no converge en el *pinhole* y por tanto no es detectada por el fotomultiplicador (**Figura II.2.**)

Las principales ventajas del microscopio confocal son:

- Evita el cruce de canales (canal rojo y verde) debido a que la excitación por medio del láser monocromo hace que los fluorocromos se **exciten secuencialmente**.
- Permite una perfecta colocalización. El dispositivo *pinhole* permite capturar la luz que procede de un solo plano, de forma que si existe colocalización, ésta es real.

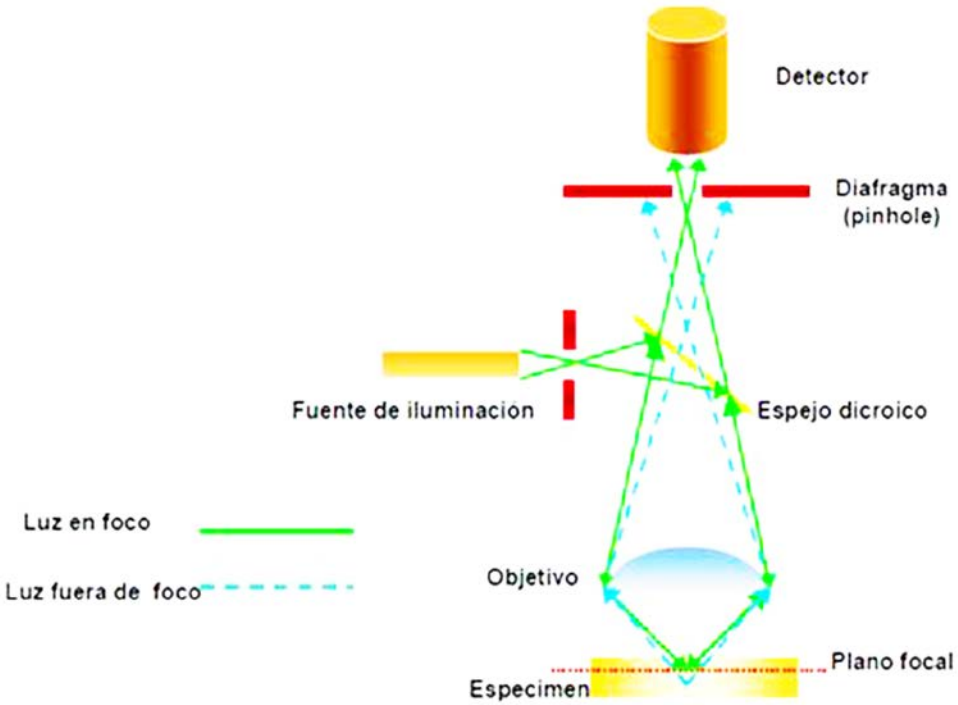

Figura II.2. Esquema del principio de la microscopia confocal. La luz procedente de los puntos fuera del plano focal es eliminada por el *pinhole*. Imagen obtenida en www.imp.mx

Durante esta Tesis Doctoral, la microscopia confocal ha sido utilizada para el estudio de distintos componentes celulares mediante inmunotinciones con marcadores fluorescentes específicos como Alexa/Phalloidina para teñir los filamentos de actina del citoesqueleto y DAPI para tinción del núcleo celular. Todos los estudios han sido realizados utilizando el microscopio confocal LEICA SP2 instalado en el Centro de Citometría y Microscopia de Fluorescencia de la Universidad Complutense de Madrid (Centro de Asistencia a la Investigación UCM).

Anexo III

ANEXO III. CULTIVOS MICROBIOLÓGICOS

Durante el desarrollo de la presente Tesis Doctoral se ha puesto en funcionamiento un laboratorio básico con niveles de bioseguridad 1 y 2 para la realización de los cultivos microbiológicos. Dicho laboratorio ha sido diseñado cumpliendo los requisitos obligatorios propios del nivel de bioseguridad 2.

La seguridad biológica o bioseguridad, es la aplicación del conocimiento, de las técnicas y de los equipos necesarios para prevenir la exposición del personal, del área de laboratorio y del medio ambiente a agentes potencialmente infecciosos o biopeligrosos. El nivel de bioseguridad 2 (grupo de riesgo 2: riesgo individual moderado, riesgo poblacional bajo) hace referencia a aquellos agentes patógenos que pueden provocar enfermedades humanas o animales pero que tienen pocas probabilidades de entrañar un riesgo grave para el personal de laboratorio, la población, el ganado o el medio ambiente. La exposición en el laboratorio puede provocar una infección grave, pero existen medidas preventivas y terapéuticas eficaces y el riesgo de propagación es limitado.

Las directrices para laboratorios básicos – niveles de bioseguridad 1 y 2 - se exponen a continuación:

Acceso

1. El símbolo y signo internacional de peligro biológico deberá colocarse en las puertas de los laboratorios donde se manipulen microorganismos del grupo de riesgo 2 o superior.
2. Sólo podrá entrar en las zonas de trabajo del laboratorio el personal autorizado.
3. Las puertas del laboratorio se mantendrán cerradas.
4. No se autorizará ni permitirá la entrada de niños en las zonas de trabajo del laboratorio.

Protección personal

1. Se usarán en todo momento monos, batas o uniformes especiales para el trabajo en el laboratorio.

2. Se usarán guantes protectores apropiados para todos los procedimientos que puedan entrañar contacto directo o accidental con materiales potencialmente infecciosos. Una vez utilizados, los guantes se retirarán de forma aséptica y a continuación se lavarán las manos.
3. El personal deberá lavarse las manos después de manipular materiales infecciosos, así como antes de abandonar las zonas de trabajo del laboratorio.
4. Se usarán gafas de seguridad u otros dispositivos de protección cuando sea necesario proteger los ojos y el rostro de salpicaduras y fuentes de radiación ultravioleta artificial.
5. Estará prohibido usar las prendas protectoras fuera del laboratorio, por ejemplo en cantinas, cafeterías, oficinas, bibliotecas, salas para el personal y baños.
6. No se usará calzado sin puntera.
7. En las zonas de trabajo estará prohibido comer, beber, fumar, aplicar cosméticos o manipular lentes de contacto.
8. Estará prohibido almacenar alimentos o bebidas para consumo humano en las zonas de trabajo del laboratorio.
9. La ropa protectora de laboratorio no se guardará en los mismos armarios o taquillas que la ropa de calle.

Procedimientos

1. Estará estrictamente prohibido pipetear con la boca.
2. No se colocará ningún material en la boca ni se pasará la lengua por las etiquetas.
3. Todos los procedimientos técnicos se practicarán de manera que se reduzca al mínimo la formación de aerosoles y gotículas.
4. Se limitará el uso de jeringuillas y agujas hipodérmicas.
5. Todos los derrames, accidentes y exposiciones reales o potenciales a materiales infecciosos se comunicarán al supervisor del laboratorio. Se mantendrá un registro escrito de esos accidentes e incidentes.
6. Se elaborará y seguirá un procedimiento escrito para la limpieza de todos los derrames.
7. Los líquidos contaminados deberán descontaminarse (por medios químicos o físicos) antes de eliminarlos por el colector de saneamiento. Puede ser necesario un sistema de tratamiento de efluentes, según lo que indique la evaluación de riesgos del agente con el que se esté trabajando.

8. Los documentos escritos que hayan de salir del laboratorio se protegerán de la contaminación mientras se encuentren en éste.

Zonas de trabajo del laboratorio

1. El laboratorio se mantendrá ordenado, limpio y libre de materiales no relacionados con el trabajo.
2. Las superficies de trabajo se descontaminarán después de todo derrame de material potencialmente peligroso y al final de cada jornada de trabajo.
3. Todos los materiales, muestras y cultivos contaminados deberán ser descontaminados antes de eliminarlos o de limpiarlos para volverlos a utilizar.
4. El embalaje y el transporte de material deberán seguir la reglamentación nacional o internacional aplicable.
5. Las ventanas que puedan abrirse estarán equipadas con rejillas que impidan el paso de artrópodos.

Diseño e instalaciones del laboratorio

Al diseñar el laboratorio y asignarle determinados tipos de trabajo, se prestará especial atención a aquellas condiciones que se sepa que plantean problemas de seguridad. Entre ellas figuran:

1. La formación de aerosoles.
2. El trabajo con grandes cantidades o altas concentraciones de microorganismos.
3. El exceso de personal o de material.
4. La entrada de personas no autorizadas.
5. El circuito de trabajo: utilización de muestras y reactivos concretos.

Características de diseño

1. Se dispondrá de espacio suficiente para realizar el trabajo de laboratorio en condiciones de seguridad y para la limpieza y el mantenimiento.
2. Las paredes, los techos y los suelos serán lisos, fáciles de limpiar, impermeables a los líquidos y resistentes a los productos químicos y desinfectantes normalmente utilizados en el laboratorio. Los suelos serán antideslizantes.
3. Las superficies de trabajo serán impermeables y resistentes a desinfectantes, ácidos, álcalis, disolventes orgánicos y calor moderado.

4. La iluminación será adecuada para todas las actividades. Se evitarán los reflejos y brillos molestos.

5. El mobiliario debe ser robusto y debe quedar espacio entre mesas, armarios y otros muebles, así como debajo de los mismos, a fin de facilitar la limpieza.

6. Habrá espacio suficiente para guardar los artículos de uso inmediato, evitando así su acumulación desordenada sobre las mesas de trabajo y en los pasillos. También debe preverse espacio para el almacenamiento a largo plazo, convenientemente situado fuera de las zonas de trabajo.

7. Se preverán espacio e instalaciones para la manipulación y el almacenamiento seguros de disolventes, material radiactivo y gases comprimidos y licuados.

8. Las taquillas para guardar la ropa de calle y los objetos personales se encontrarán fuera de las zonas de trabajo del laboratorio.

9. Los locales para comer y beber y para descansar se dispondrán fuera de las zonas de trabajo del laboratorio.

10. En cada sala del laboratorio habrá lavabos, a ser posible con agua corriente, instalados de preferencia cerca de la salida.

11. Las puertas estarán debidamente protegidas contra el fuego; se cerrarán automáticamente, preferentemente.

12. En el nivel de bioseguridad 2 se dispondrá de un autoclave u otro medio de descontaminación debidamente próximo al laboratorio.

13. Los sistemas de seguridad deben comprender medios de protección contra incendios y emergencias eléctricas, así como duchas para casos de urgencia y medios para el lavado de los ojos.

14. Hay que prever locales o salas de primeros auxilios, convenientemente equipados y fácilmente accesibles.

15. Debe disponerse de un suministro de electricidad seguro y de suficiente capacidad, así como de un sistema de iluminación de emergencia que permita salir del laboratorio en condiciones de seguridad.

16. Es esencial un suministro fiable y adecuado de gas. La instalación debe ser objeto del debido mantenimiento.

Manipulación de desechos

Se considera desecho todo aquello que debe descartarse. En los laboratorios, la descontaminación y la eliminación de desechos son operaciones estrechamente relacionadas. En el trabajo cotidiano, son pocos los materiales contaminados que es preciso retirar del laboratorio o destruir. La mayor parte de la cristalería, los instrumentos y la ropa del laboratorio vuelve a utilizarse o se recicla. El principio básico es que todo el material infeccioso ha de ser descontaminado, esterilizado en autoclave o incinerado en el laboratorio.

Descontaminación

El tratamiento en autoclave de vapor constituye el método de elección para todos los procesos de descontaminación. El material destinado a la descontaminación y eliminación debe introducirse en recipientes (por ejemplo en bolsas de plástico resistentes al tratamiento en autoclave) que tengan un código de color para indicar si el contenido ha de pasar al autoclave o a la incineración.

Procedimientos de manipulación y eliminación de material y desechos contaminados

Deberá adoptarse un sistema de identificación y separación del material infeccioso y sus recipientes. Se seguirán las normas nacionales e internacionales y se tendrán en cuenta las siguientes categorías:

1. Desechos no contaminados (no infecciosos) que puedan reutilizarse o reciclarse o eliminarse como si fueran «basura» en general.
2. Objetos cortantes y punzantes contaminados (infecciosos): agujas hipodérmicas, bisturís, cuchillas, vidrio roto; se recogerán siempre en recipientes a prueba de perforación dotados de tapaderas y serán tratados como material infeccioso.
3. Material contaminado destinado al tratamiento en autoclave que después pueda lavarse y volverse a utilizar o reciclarse.
4. Material contaminado destinado al tratamiento en autoclave y a la eliminación.
5. Material contaminado destinado a la incineración directa.

MANUAL DE BIOSEGURIDAD EN EL LABORATORIO. *Tercera Edición.* ***ORGANIZACIÓN MUNDIAL DE LA SALUD.*** *Ginebra, 2005. ISBN 92 4 354650 3.*

Anexo IV

ANEXO IV. OTRAS PUBLICACIONES DEL DOCTORANDO RELACIONADAS CON ESTA TESIS DOCTORAL

- M. Vila, **M. Cicuéndez**, J. Sánchez-Marcos, V. Fal-Miyar, M. Manzano, C. Prieto, M. Vallet-Regí. ***Electrical stimuli to increase cell proliferation on carbon nanotubes/mesoporous silica composites for drug delivery. J Biomedical Research (A), 2012, 101, 213-21.***

- M. Cicuéndez, I. Izquierdo-Barba, M. Vila, S. Sánchez-Salcedo, M. Vallet-Regí. ***Biological performance of HA-biopolymer foams: in vitro cell response. Acta Biomaterialia, 2012, 8, 802-810.***

- M. Vila, S. Sánchez-Salcedo, **M. Cicuéndez**, I. Izquierdo-Barba, M. Vallet-Regí. ***Novel biopolymer-coated hydroxyapatite foams for removing heavy-metals from polluted water. Journal of Hazardous Materials, 2011, 192, 71– 77.***

- S. Sánchez-Salcedo, M. Vila, I. Izquierdo-Barba, **M. Cicuéndez**, M. Vallet-Regí. ***Biopolymer-coated hydroxyapatite foams: A new antidote for heavy metal intoxication. Journal of Materials Chemistry, 2010, 20, 6956–6961. Front Cover.***

El desarrollo de nuevos biomateriales se basa en la innovación multidisciplinar y en cierta medida en la capacidad de "imaginar" sus aplicaciones. La multidisciplinaridad es un requisito esencial de la investigación biomédica que avanza rápidamente gracias a la convergencia de diferentes áreas como la física, matemáticas, ingeniería, biología y medicina.

En la presente Tesis Doctoral se ha realizado la síntesis, caracterización química y evaluación biológica de un nuevo *nanocomposite* MGHA, formado por partículas de hidroxiapatita nanocristalina embebidas en una matriz mesoporosa. Dicho material ha sido preparado en forma pulverizada y como andamios macroporosos 3D, analizando su interacción con diferentes tipos celulares implicados en la formación de tejido óseo (preosteoblastos, osteoblastos, fibroblastos) y en la respuesta inmune (macrófagos, linfocitos T y B, células *natural killer*). Asimismo se ha llevado a cabo la carga y liberación de levofloxacino en el material MGHA, evaluando su acción sobre *Staphylococcus aureus* y *Escherichia coli* y la influencia del pH en la cinética de liberación.